LBL-28126

Lawrence Berkeley Laboratory
UNIVERSITY OF CALIFORNIA

Materials & Chemical Sciences Division

Vibrational State-Resolved Differential Cross Sections for the $D + H_2 \rightarrow DH + H$ Reaction

R.E. Continetti
(Ph.D. Thesis)

November 1989

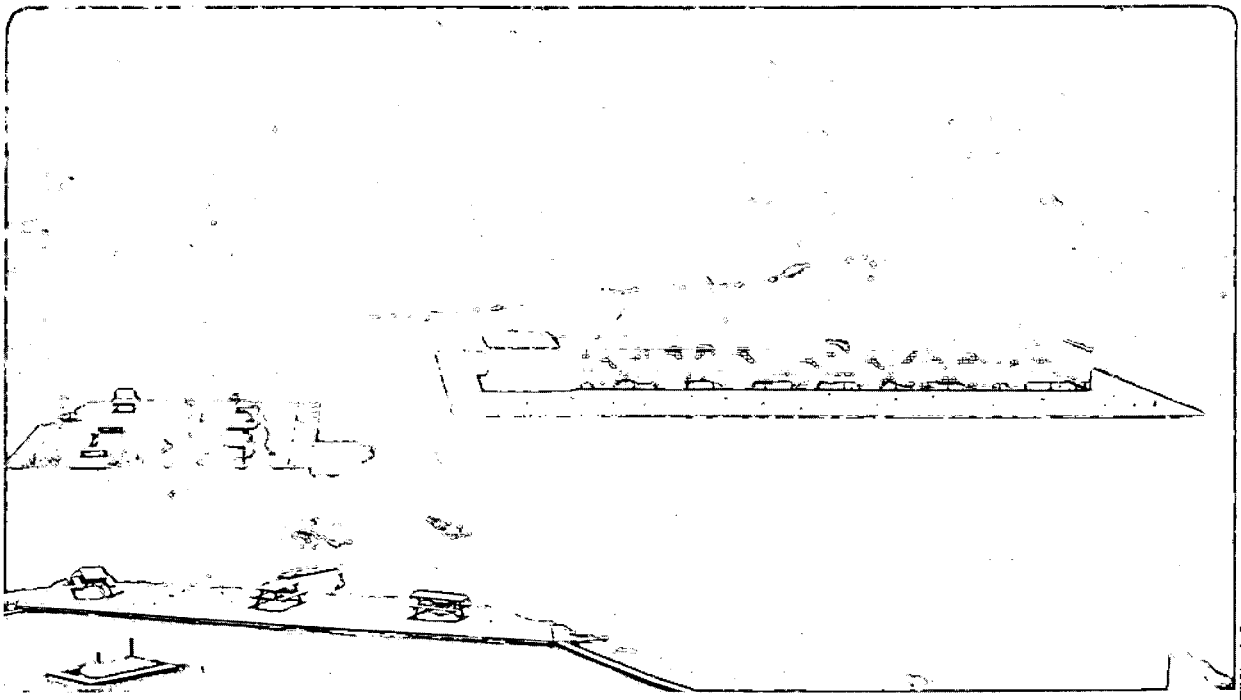

LOAN COPY
Circulates
for 2 weeks
Bldg. 50 Library.
LBL-28126
Copy 2

Prepared for the U.S. Department of Energy under Contract Number DE-AC03-76SF00098.

DISCLAIMER

This document was prepared as an account of work sponsored by the United States Government. While this document is believed to contain correct information, neither the United States Government nor any agency thereof, nor the Regents of the University of California, nor any of their employees, makes any warranty, express or implied, or assumes any legal responsibility for the accuracy, completeness, or usefulness of any information, apparatus, product, or process disclosed, or represents that its use would not infringe privately owned rights. Reference herein to any specific commercial product, process, or service by its trade name, trademark, manufacturer, or otherwise, does not necessarily constitute or imply its endorsement, recommendation, or favoring by the United States Government or any agency thereof, or the Regents of the University of California. The views and opinions of authors expressed herein do not necessarily state or reflect those of the United States Government or any agency thereof or the Regents of the University of California.

LBL-28126

Vibrational State-Resolved Differential Cross Sections for the $D + H_2 \rightarrow DH + H$ Reaction

Robert Elliot Continetti

Materials and Chemical Sciences Division
Lawrence Berkeley Laboratory
1 Cyclotron Road
Berkeley, California 94720

DISSERTATION

Submitted in partial satisfaction for the requirements for the degree of

DOCTOR OF PHILOSOPHY

in

CHEMISTRY

in the

GRADUATE DIVISION

of the

UNIVERSITY OF CALIFORNIA at Berkeley

November 1989

This report has been reproduced directly from the best available copy

Vibrational State-Resolved Differential Cross Sections

for the $D + H_2 \rightarrow DH + H$ Reaction

by

Robert Elliot Continetti

Abstract

In this thesis, crossed-molecular-beams studies of the reaction $D + H_2 \rightarrow DH + H$ at collision energies of 0.53 and 1.01 eV are reported. Chapter One provides a survey of important experimental and theoretical studies on the dynamics of the hydrogen exchange reaction. Chapter Two discusses the development of the excimer-laser photolysis D atom beam source that was used in these studies and preliminary experiments on the $D + H_2$ reaction. In Chapter Three, the differential cross section measurements are presented and compared to recent theoretical predictions. The measured differential cross sections for rotationally excited DH products showed significant deviations from recent quantum scattering calculations, in the first detailed comparison of experimental and theoretical differential cross sections. These results indicate that further work on the H_3 potential energy surface, particularly the bending potential, is in order.

Yuan T. Lee

Table of Contents

Abstract 1

Dedication viii

Acknowledgements ix

Chapter 1. Dynamics Studies of the Elementary Reaction $D + H_2 \rightarrow DH + H$

1. Introduction 1
2. $H + H_2 \rightarrow H_2 + H$; Historical Survey 3
   - 2.1 The 1930's 4
   - 2.2 The 1960's 4
   - 2.3 The 1970's 6
   - 2.4 The 1980's 9
3. The Future 17

References 19

Chapter 2. Development of the $D + H_2 \rightarrow DH + H$ Reactive Scattering Experiments

1. Introduction 26
2. H/D-Atom Beam Sources 27
   - 2.1 Thermal Dissociation Sources 28
   - 2.2 Electrical Discharge Sources 30
   - 2.3 Ion Beam Neutralization Sources 31
   - 2.4 Hot Atom Sources 33

3. Photolytic Atomic Beams....35
4. Crossed-Molecular-Beams Scattering Apparatus....39
4.1 Detector....40
4.2 Signal-processing Electronics....41
4.3 Vacuum System....42
5. Reactive Scattering with a Photolytic D-Atom Beam: Feasibility 44
5.1 D-Atom Production and Transport....44
5.2 Generation of the H_2 Molecular Beam....48
5.3 Crossed-Beams Interaction and Product Detection....51
6. D + H_2 Version I....53
6.1 Photolytic D-Atom Beam....54
6.2 H_2 Molecular Beam....56
6.3 Modulated DH Background Sources....57
6.4 Conclusions....58
7. D + H_2 Version II....59
7.1 D-Atom Beam Source Chamber....60
7.2 D-Atom Beam Characteristics....61
7.2.1 Beam Intensity....61
7.2.2 Pulsed Beam/Photolysis Laser Time Delay Effects....62
7.2.3 Rydberg D Atom TOF Spectra....63
7.2.4 Contamination by fast DH and D_2....65
7.3 H_2 Beam Source Chamber....67
7.4 H_2 Beam Characteristics....69
7.5 Modulated DH Background Sources....69

7.6 $D + H_2 \rightarrow DH + H$ Scattering Results/ Conclusions.....71

References.....74

Figure Captions.....80

Figures.....86

Chapter 3. Vibrational State-Resolved Differential Cross Sections for the Reaction $D + H_2 \rightarrow DH + H$

1. Introduction.....107

1.1 Dynamical Observables.....109

1.2 Recent Theoretical Studies.....112

2. Experimental.....114

2.1 Apparatus.....114

2.1.1 General Description.....114

2.1.2 D-Atom Beam Source.....116

2.1.3 H_2 Beam Source.....118

2.2 DH Product TOF Measurements.....119

3. Results.....122

3.1 Reactive Scattering TOF Data.....122

3.2 Modulated Background.....124

3.2.1 H_2 Beam Modulated Background.....124

3.2.2 D-Atom Beam Modulated Background.....126

3.3 Correction of the Reactive Scattering TOF Data.....129

3.4 Laboratory Angular Distributions.....131

4. Analysis.....132

4.1 Direct Inversion 133

4.2 Monte Carlo Simulation 134

4.3 E_c = 1.01 eV Reactive Scattering Simulation 138

4.3.1 Best-Fit DCS at E_c = 1.01 eV 141

4.3.2 Integral Cross Sections at E_c = 1.01 eV 144

4.4 E_c = 0.53 eV Reactive Scattering Simulation 147

4.4.1 Best-Fit DCS at E_c = 0.53 eV 148

4.4.2 Integral Cross Sections at E_c = 0.53 eV 149

4.5 DH Product CM Velocity-Flux Contour Maps 150

5. Discussion 151

5.1 Comparison with other Crossed-Molecular-Beams Studies 151

5.2 Comparison with DH Product-State Distribution Measurements 153

5.3 Implications for the H_3 Potential Energy Surface 154

6. Conclusions 158

References 160

Tables 164

Figure Captions 168

Figures 178

Appendix A. Transformation of Center-of-Mass Differential Cross Sections to the Laboratory Frame

1. Introduction 234

2. The Monte Carlo Approach 237

3. The LabAvg Program 240
4. Conclusions 247
References 248
Figure Captions 250
Figures 253

Appendix B. Pulsed Molecular Beams

1. Introduction 263
2. Experimental 265
   2.1 Commercial Piezoelectric Pulsed Valves 265
   2.2 Custom Piezoelectric Pulsed Valve 265
   2.3 Corrosive Gas Applications 267
   2.4 Cryogenic Pulsed Valve 268
3. Conclusions 270
References 270
Figure Captions 272
Figures 273

Appendix C. Pulsed Beam Diagnostics

1. Introduction 275
2. Fast Ion Gauge Measurements 278
   2.1 Method 278
   2.2 Results 279
3. Beam TOF Measurements 283
   3.1 Method 283

3.2 Results 286
3.2.1 300 K H_2 Beam Source 287
3.2.2 Cryogenic H_2 Beam Source 289
4. Ion Gauge Manometer Measurements 291
4.1 Method 291
4.2 Results 293
5. Conclusions 293
References 294
Figure Captions 296
Figures 301

Appendix D. The Synthesis of Deuterium Iodide

1. Introduction 316
2. Materials of Construction 316
3. Reagents 318
4. Synthetic Protocol 318
4.1 Manifold Preparation 319
4.2 Loading of Reagents 319
4.3 Synthesis 320
4.4 Product Collection 322
5. Results 323
References 324
Figure Caption 325
Figure 326

This thesis is dedicated to the memory of my father,

Reno A. Continetti.

Acknowledgements

The scientific guidance, encouragement, patience and motivation of Professor Yuan T. Lee made the experiments described in this thesis possible. Yuan never failed to come up with several ways of improving any experimental setup, and his insights into the dynamics of chemical reactions were invaluable. Working with Yuan over the past six years has been a great experience, and I am sure that the many lessons I have learned in his laboratory will serve me well.

Barbara Balko, through her hard work and dedication, helped make the final D + H_2 experiments possible. Although many modifications to the machine had to be made, and many experiments had to be done before the light at the end of the tunnel appeared, Barbara never lost her enthusiasm, or her willingness to work for 36 hours in a row.

Collaboration with Dr. John Zhang and Professor Bill Miller made the final D + H_2 scattering experiments much more meaningful, as they generated theoretical predictions of the reaction dynamics at the experimental energies. Drs. Bob Walker and Russ Pack of Los Alamos introduced me to the wonders of Monte Carlo simulation, which was used in the detailed comparison of our results with the theoretical predictions.

In my first four years at Berkeley, I learned many things about the reactive scattering of halogen atoms and methyl radicals with Gary Robinson. Gary also worked with me on the first attempt at studying the D + H_2

reaction. Dr. Gil Nathanson, with his boundless enthusiasm and scientific insights, joined the 35" machine team for the final methyl radical scattering experiments.

Dr. Thomas Trickl brought his pulsed valve design to the Lee group in 1986. Without this tool, the final D + H_2 experiments would have been very difficult indeed. His advice and comments on modifications of the pulsed valves for these experiments were most helpful.

Without the assistance of many skilled machinists, I would probably still be in the laboratory. In particular, Andy Anderson, Scott Bonnilla, Hans Graetsch, Dave Murai, Chuck Souders, Bob Waite, and George Weber of the Chemistry Dept. Machine Shop all played central roles in the fabrication of the beam source chambers for the final D + H_2 experiments. Tom Lawhead built the DI synthesis manifold, and was always helpful when we broke it and needed those emergency repairs. Tony Moscarelli of LBL taught me many things about working in the machine shop, which gave me a better perspective of just what I was asking of the shop. Fred Vogelsberg of LBL was always of great assistance with any electronics problems.

The great trauma of the move from LBL to Giauque Hall in 1986 was mitigated by the advice and assistance of Harry Chiladakis, who is also the master of mechanical pump troubleshooting and could answer <u>any</u> questions about the status of the laboratory's physical plant. The LBL riggers, headed by Bob Everett and Oliver Wiggins, did all the hard work moving the molecular beam machines. Thanks go to Rick Brudzynski for suggesting that I handle the final coordination of the move to campus, and once again to Yuan, for his

confidence. All the members of the Lee group made the move a little less painful by cooperating and adjusting their busy schedules so that the move could be made in short order.

The Lee group is so large (and full of talented people!) that all due acknowledgements cannot possibly be made here. Many former group members, including Laurie Butler, Dr. Jeremy Frey, Tim Minton, Mitchio Okumura, Ralph Page, Paul Weiss and Alec Wodtke helped to teach me the many facets of molecular beam research and expand my scientific horizons. I used to wonder how research would continue after all these skilled people graduated. With Professor Qihe Zhu, Xinsheng Zhao, Eric Hintsa, and Dr. Atsushi Yokoyama, I made some forays into the world of polyatomic photodissociation, when the beams weren't crossing. Dr. Deon Anex and Professor Bill Jackson also provided me with some interesting photodissociation problems, 'in my spare time'. Pam Chu deserves great thanks for her efforts at setting up and running our microvaxes, with James Chesko carrying on these noble duties. I had many fruitful conversations with Dr. Manfred Vodegel about the reactive scattering of D + H_2. Dr. Di-jia Liu was an excellent office-mate, and could answer almost any spectroscopy question.

Dr. Lloyd Currie of NIST provided me with my first opportunity to work in a physical chemistry laboratory, and Professor Kit Bowen at Johns Hopkins introduced me to experimental chemical physics. To them and the other dedicated educators I have met over the years I am indebted.

Ann Weightman plays an important role in the conduct of research in the Lee group, from expediting those critical equipment orders to guiding

confused graduate students through the bureaucratic morass. Her skills were especially helpful during the move to campus, and I thank her for all the assistance and advice she has given me over the years.

My mother has always encouraged my efforts and supported my education, and I must also thank my brother Michael, who provided me with an intellectually stimulating environment while growing up out on the farm. Finally, my wife, Sharon, has contributed to the success of my graduate studies in more ways than I can begin to name, and I thank her for her sacrifices, love, and assistance over the years.

My last year of graduate studies was supported by an Amoco graduate fellowship through the Department of Chemistry, University of California at Berkeley. This work was supported by the Director, Office of Basic Energy Sciences, Chemical Sciences Division of the U.S. Department of Energy under Contract No. DE-AC03-76SF00098.

Chapter 1

Dynamics Studies of the Elementary Reaction $D + H_2 \rightarrow DH + H$

1. Introduction

Chemists have long sought an understanding of both the rate and dynamics of chemical reactions. Systematic studies of chemical kinetics date back more than 100 years to the time of Arrhenius[1]. Since the advent of quantum mechanics in the 1920's a detailed picture of the dynamics of chemical reactions has been pursued. Consideration of the problem of chemical reactions quickly revealed that the simplest reaction,

$$H + H_2 \rightarrow H_2 + H \qquad (1)$$

was the most tractable system for application of the new concepts. During the 1930's experimental chemical physicists soon undertook the first studies of the kinetics of this elementary reaction, and thus began a fruitful theoretical/experimental interplay that continues to the present day. The simplicity of this three-electron three-proton system has given it a central role in the development of theoretical models of chemical dynamics. In fact, only for the H_3 system have potential energy surfaces (PES's) of 'chemical' accuracy, within a few tenths of a kcal/mole, been calculated.[2,3,4] Experimental study of this reaction is made difficult by the large barrier to reaction (0.425 eV on the LSTH surface)[3], which results in a low reactive cross section (≈ 1 Å^2). In practice most experimental techniques are restricted to studying isotopic variants of this reaction, such as the reaction

$$D + H_2 \rightarrow DH + H \qquad (2),$$

which is the subject of this thesis. These isotopic variants pose a somewhat more difficult problem in theoretical studies due to the non-symmetric particle arrangements before and after the reactive collision.

In the last 5 years a wide variety of detailed dynamical data on isotopic variants of the H_3 system, such as product-state distributions and doubly differential cross sections (product flux as a function of recoil velocity and angle) at several collision energies, has become available. Detailed microscopic data of this sort can finally test the theoretical predictions of a wide variety of observable quantities for this fundamental reaction. These developments, coupled with the great recent progress in quantum reactive scattering methods, have finally made it possible to compare state-resolved differential cross section (DCS) measurements with fully converged three-dimensional (3-D) quantum state-resolved DCS calculations[5] performed on accurate *ab initio* PES's[2,3,4] over the entire experimentally accessible energy range.

In this thesis, extensive crossed-molecular-beams DCS measurements with vibrational state resolution for backward-scattered DH products in the center-of-mass (CM) frame for the reaction $D + H_2 \rightarrow DH + H$ at nominal CM collision energies of 0.53 and 1.01 eV are reported. A comparison is made with the fully converged 3-D quantum reactive scattering DCS calculations of Zhang and Miller,[5] resulting in one of the most detailed experimental/theoretical intercomparisons for this elementary reaction to date. These measurements are very sensitive to the theoretical predictions and should stimulate further theoretical studies of the sensitivity of the differential cross section to features of the potential energy surface.

Comparisons of this sort are a vital step in the continuing search for an accurate PES and an accurate understanding of the dynamics of this most fundamental of all bimolecular chemical reactions.

In this introductory chapter, a brief survey of the history and current status of the experimental and theoretical understanding of this reaction is presented. During the last 15 years, several important reviews of theoretical[6] and experimental[7] progress in the study of the dynamics of this reaction have appeared, and reference should be made to these for an exhaustive history of the dynamics of the H_3 system.

2. $H + H_2 \rightarrow H_2 + H$: Historical Survey

The interplay between experiment and theory that has led to our current state of knowledge concerning this and other elementary reactions is best understood with a brief historical survey. The tractability of dynamics calculations on the H_3 system have allowed it to play a unique role in the development of the theory of chemical dynamics. Recent advances in experimental techniques have provided new physical observables such as product-state distributions and differential cross sections, motivating theoreticians to refine their techniques and present ever more accurate PES's and dynamics calculations. Now, at the end of the 1980's, we are witnessing a rapid convergence of both accurate theory and experiment concerning the dynamics of this fundamental reaction. The account that follows highlights some of the important advances made in both theoretical understanding and experimental measurement of the dynamics of this chemical reaction.

2.1 The 1930's

The basis of much of our modern understanding of chemical reaction dynamics is found in the concept of the electronically adiabatic PES for a chemical reaction first presented by London.[8] Within the framework of the Born-Oppenheimer approximation[9], London presented a semi-empirical formula for the PES governing the nuclear motions for a simple system like $H + H_2 \rightarrow H_2 + H$. Prior to this development, it wasn't clear why an exchange reaction of this sort could proceed with an activation energy less than the molecular bond dissociation energy. London's surface illustrated how a reaction could proceed with a much lower activation energy, due to the formation of the new chemical bond as the old bond broke. By 1931, Eyring and Polanyi had extended this approach further and numerically calculated PES's for several systems of chemical interest[10]. The first classical trajectory study of the dynamics of the hydrogen exchange reaction, (or <u>any</u> chemical reaction), was performed on such a surface by Hirschfelder, Eyring and Topley[11]. In response to these theoretical developments, the first experimental rate constant and activation energy measurements for this system were carried out by monitoring the ortho-para conversion of H_2 and D_2 due to the exchange reaction.[12]

2.2 The 1960's

By the early 1960's considerable improvement was made in the calculation of both semi-empirical and *ab initio* PES's. The review of Truhlar and Wyatt tells the story of the extensive work on the PES during

this period[6b]. The availability of high speed computers made possible more refined trajectory studies of the dynamics of a variety of chemical reactions. For the H_3 system, an improved semi-empirical potential energy surface, Porter and Karplus' surface PK2, was presented in 1965[13], which still appears in some dynamics studies today[14,15]. Early applications of high-speed computers to quasi-classical trajectory (QCT) reaction dynamics studies[16] led to the first extensive 3-D QCT study of the dynamics of $H + H_2$ by Porter, Karplus and Sharma[17].

Experimental studies of reaction dynamics were undergoing a period of great expansion at this time[18]. In 1955 the first crossed-molecular-beams studies were performed by Datz and Taylor[19] on the reaction $K + HBr \rightarrow KBr + H$ using the hot-wire surface-ionization detector, and several groups were pursuing reactive scattering studies by the 1960's. By 1964 two groups had reported preliminary product angular distributions for the reaction $D + H_2 \rightarrow DH + H$[20] and $H + D_2 \rightarrow HD + D$[21] using electron-impact ionization mass-spectrometric detection of the molecular product. These studies were the first reactive scattering experiments on non-Alkali metal systems. These experiments were not particularly successful, and further work on non-Alkali metals was generally not done until the first truly successful 'universal' crossed-molecular-beams apparatus was built.[22] These early molecular beam studies were part of the impetus for the first QCT calculations of differential cross sections for the hydrogen exchange reactions by Brumer and Karplus, however.[23] During the same time period, Polanyi's group made great progress in the development of the infrared chemiluminescence technique for the determination of nascent product vibration-rotation (v,J) distributions for many halogen/hydrogen halide/hydrogen atom reactions of the form H +

X_2, XY and X + H_2, HX, HY where X and Y represent different halogens.[18a] Since the highly excited HX products of these generally exothermic reactions could emit IR radiation, careful measurement of the IR emission spectrum allowed the product (v,J) distributions to be mapped out. In order to understand these results, Polanyi's group and others calculated semi-empirical London-Eyring-Polanyi-Sato (LEPS) surfaces for these systems and a large number of QCT studies of energy disposal in the products were performed.[18a,24] For the hydrogen exchange reaction, however, detailed product-state distributions would have to wait until the 1980's due to the lack of IR emission from H_2, DH or D_2.

Refined rate constants also became available during the 1960's due to the Electron Spin Resonance (ESR) studies of Schulz and Leroy[25], then Westenberg and deHaas[26], with later measurements also made by LeRoy's group[27]. Numerous approximate theoretical calculations of the rate constants have been made, and today there is reasonable agreement between theory and experiment for the rate constant for the reaction D + H_2(v=0) $\rightarrow$ DH + H[7]. Kuppermann and White also performed the first bulk measurement of the experimental energetic threshold (0.33 $\pm$ 0.02 eV) for the reaction D + H_2 $\rightarrow$ DH + H using photolytically produced D atoms[28], a technique which has played an important role in the expansion of our experimental knowledge of the dynamics of this reaction in the 1980's.

2.3. The 1970's

During the 1970's, theoretical and experimental progress became, to some extent, uncoupled. On the theoretical side, great progress was made.

The calculation of the 'chemical accuracy' LSTH (Liu-Siegbahn-Truhlar-Horowitz) *ab initio* PES for the H_3 system was completed by 1978.[2] The first fully converged 3-D quantum close-coupling (CC) scattering calculations were reported at total energies in the range 0.3 to 0.7 eV[29,30], and the first predictions of observable quantum-mechanical dynamic resonances were made[31]. 3-D quantum scattering calculations at the higher energies which are more accessible in dynamics experiments were not yet feasible, however. Due to the computational intensity of the 3-D quantum scattering calculations, significant efforts were also made to develop approximate treatments of the dynamics of this simple system which could reproduce the exact calculations, in the hope that such methods would be applicable to more complicated systems. Indeed, DCS calculations at higher total energies were needed to compare with experimental rate constants and molecular-beam scattering data that was becoming available in this time frame. A series of approximate quantum-mechanical distorted-wave Born approximation (DWBA) studies of the $D + H_2 \rightarrow DH + H$ system were initiated in 1975 by Tang and Choi[32] providing differential cross sections on several PES's at total energies up to 0.5 eV. The application of various dimension-reducing approximations to the quantum-mechanical CC scattering calculations was begun by Elkowitz and Wyatt[33] (J_z conserving approximation) and Kuppermann[34] (coupled states approximation). The infinite order sudden approximation (IOSA) was extended to reactive scattering by the late 1970's[35]. An excellent review of the current status of these various approximate approaches to quantum reactive scattering calculations has recently appeared.[36]

Once the accurate LSTH PES became available, Mayne and Toennies carried out a systematic QCT study of the H_3 system and its isotopic variants

on this accurate PES.[37] This extensive body of information, which was later extended to include calculations for a distribution of reactant states[38], was essential for comparison with differential cross sections for $D + H_2 \rightarrow DH + H$ and $D + H_2(v=1) \rightarrow DH + H$ measured by Toennies' group.[39,40]

Slow progress was made in experimental measurements of the differential cross section for $D + H_2 \rightarrow DH + H$ in the 1970's. Fite's group reported the first extensive DCS measurements for $D + H_2 \rightarrow DH + H$ at a nominal collision energy of 0.48 eV (corresponding to 0.75 eV total energy).[41] These experiments used an effusive D atom beam, with correspondingly poor velocity resolution and crude (phase-sensitive detection) velocity analysis of the scattered products. Due to the temperature limitations imposed by oven materials for the thermal dissociation of H_2, the nominal energy of 0.48 eV represents an upper limit to the collision energies obtainable via this approach. The measured DCS was shown to peak in the 'backwards' direction in the CM, relative to the incident D atom, as expected for a direct reaction near threshold. Crossed-beams studies of the reactions $H,D + T_2$ were also reported by Kwei's group which took advantage of selective chemisorption of product T atoms on MoO_3.[42] These experiments also used effusive atomic beams, and the detection scheme precluded velocity analysis. Due to the wide range of collision energies present in both of these experiments, and the lack of product velocity analysis, comparison with the DCS predictions available at that time gave no real quantitative information, but did show qualitative agreement in the form of the product angular distributions (backward scattered in the CM).

Integral cross-section measurements were also improved during this decade. Early work by Harrison[43] was followed up by experiments in

Herschbach's group in the late 1960's.[44] Fite's group extracted some absolute cross-section data from their work[41]. Toennies' group later did a more detailed study of the integral cross section and recalibrated the reactive differential cross sections of Geddes, Krause and Fite by a factor of 0.73 to give an integral reactive cross section of $\sigma = 0.35 \pm 0.18$ Å^2 at the nominal collision energy of 0.48 eV.[45,46]

Measurements of the rate constants for the ground state reaction D + $H_2(v=0) \rightarrow DH + H$ had, as mentioned above, converged by the mid 1970's. Attention then began to focus on the reaction of vibrationally excited H_2 reagent. Several experimental measurements were reported[47,48,49,50] all of which indicated rate constants much greater than any theoretical predictions. There are significant experimental difficulties associated with the production of $H_2(v=1)$ reagent, and with time the measurements of this rate constant have been monotonically decreasing, into closer agreement with theoretical predictions.[7,51] The disagreement between theory and experiment for this reaction has been controversial to the present day. Due to the 'unconverged' status of the experimental data , it is apparent that the definitive experimental measurement of the rate of the reaction $D + H_2(v=1) \rightarrow DH + H$ remains to be done.

2.4 The 1980's

In the last few years, as mentioned in the introduction, we have witnessed an unprecedented advance in both theory and experiment for the H_3 system. In both cases, the advances are chiefly due to progress in the appropriate 'technologies'. Supercomputers, coupled with the development

and application of improved algorithms for the solution of the full quantum-mechanical close coupling equations have finally permitted fully converged 3-D quantum scattering calculations for any of the isotopic variants of the H_3 system[5]. The effort continues to find ever faster algorithms for the solution of the exact quantum-scattering problem with several groups (and approaches) currently involved in the effort[52]. The H_3 system naturally continues to be a testing ground for many approximate dynamical methods, which have been recently reviewed[36,6c,6d]. Product-state distributions have been calculated using the QCT technique for the $H + D_2$ and $D + H_2$ reactions for comparison with the detailed experimental measurements of these quantities which have become available.[53] In addition to the earlier work by Mayne and Toennies[37], QCT calculations of the DCS for $D + H_2$ have been done by Blais and Truhlar[54] and Aoiz and coworkers.[55] Approximate QM-DCS calculations have appeared using the Reactive Infinite-Order Sudden Approximation (RIOSA)[56] and a new dimensionality reducing approximation, the Fixed Angle Reactor Model (FARM)[57].

The most exciting development has been Zhang and Miller's development of the S-matrix Kohn Variational Principal technique.[5] With this approach, fully converged 3-D quantum calculations of the DCS are now possible over the entire experimentally accessible energy range.[5] Close collaboration with Miller's group resulted in their calculation of the DCS at the two nominal energies of our experiment, with a grid of 13 other energies. Since these are the first converged 3-D quantum scattering results, we have limited the comparison of our experimental DCS measurements to this 'benchmark'. It is important to note that for the $H + H_2 \rightarrow H_2 + H$ reaction,

Zhang and Miller's results have now been duplicated by two other groups using different approaches.[58]

A new *ab initio* PES has recently appeared (the Double Many Body Expansion, or DMBE surface).[4] The DMBE surface is a new analytic representation of the PES for the H_3 system that takes into account the potential energy of configurations at high energies near the first conical intersection at ≈ 3.5 eV total energy. While this surface fits the calculated *ab initio* points better at high energies, near threshold the LSTH surface still provides a better fit.[4] Integral cross section calculations which have been done on the two surfaces so far have not shown great differences[59], but no exact 3-D quantum calculations of the DCS have yet been performed on the DMBE surface.

Toennies' group, as mentioned above, has made a number of significant experimental contributions to our knowledge of the differential cross sections for the D + H_2 system in this decade. To reach collision energies beyond those accessible with thermal D-atom beams[41] an arc-heated D-atom beam source was developed which achieved gas temperatures from 10,000 to 30,000 K[39,60]. This source enabled nominal collision energies of up to 1.5 eV to be probed, however, it had the disadvantages of poor velocity resolution ($\Delta v/v \approx 1$) and poor long term stability (≤ 50 hour operation time). The velocity resolution precluded measurement of vibrational state-resolved DCS's. This experiment is a landmark, however, in that it is the first crossed-molecular-beams scattering measurement of the doubly differential cross section (product velocity and angular distributions). Comparison with the QCT predictions of Mayne and Toennies[37] showed good qualitative agreement[39,60]. Measurements of the DCS for the reaction of D + H_2(v=1) at

a nominal collision energy of 0.33 eV have also been reported by Toennies group.[40,61] These results constitute the first crossed-molecular-beams data on this reaction, and have showed favorable comparison with QCT and RIOSA predictions. Absolute cross sections in good agreement with the theoretical predictions were obtained. The $H_2(v=1)$ was produced in a heated tungsten oven followed by a supersonic expansion, and therefore, in addition to a large amount of $H_2(v=0)$ in the beam, there was a broad distribution of reagent rotational states[61]. This limits the comparison of these results with exact 3-D quantum calculations, as it is still prohibitively expensive to perform these calculations over a wide range of collision energies for an ensemble of reactant states.

The continued development of the laser has been the predominant reason for the exciting advances in our ability to measure product-state distributions and differential cross sections for this system. The availability of powerful pulsed UV lasers at a number of wavelengths has provided a great opportunity for further application of the classic photochemical approach[62] to hot atom generation in the 1 to 3 eV translational energy range.[63] These new UV light sources have made the generation of large quantities of energetic H and D atoms with well-defined velocity distributions possible. Non-linear laser-based spectroscopic methods such as Coherent Anti-Stokes Raman Scattering (CARS) spectroscopy[64] and various multi-photon ionization (MPI) schemes for the sensitive state-selective detection of H_2 and its isotopic variants[65] have provided nascent product-state distributions for the $H + D_2$, $D + H_2$, and $H + H_2$ reactions. An MPI technique has also produced preliminary results on the detection of the HD_2 transition state.[66] New measurements of the total reactive cross sections for $H + D_2$ and H + HD have

been made with a vacuum ultra-violet laser-induced fluorescence technique.[67]

The status of product-state distribution measurements was covered in Valentini's review in 1988[7] , but there are continued advances in this area. Zare's group first reported MPI measurements of the DH product-state distribution for the H + D_2 reaction in 1984 at nominal collision energies of 0.55 and 1.30 eV.[65] Valentini's group nearly simultaneously reported the first CARS measurements for this reaction at the same collision energies.[64] The 'low' sensitivity of the CARS technique requires that these experiments be done in the bulk at moderately high pressures (≈ 5 torr total pressure HI/D_2). These measurements are time-resolved, however, and the delay between the HI photolysis and the CARS DH probe lasers can be made as short as desired, limited only by the width of the laser pulses (≈ 5 nsec). Product-state distributions measured with delays of 5 nsec are believed to accurately represent the nascent 'single-collision' product-state distributions. While qualitative agreement between the two techniques was observed some discrepancies outside of the respective experimental errors remained. The extraction of product-state distributions from the CARS spectra is believed to be well understood, but for the MPI results an accurate calibration was deemed necessary, and to this end a tungsten oven was constructed to produce a thermal population of DH to accurately calibrate the MPI technique against.[68] After these small corrections were made, good agreement between the two techniques was noted[69]. The MPI technique is considerably more sensitive than CARS, and therefore the reaction may be studied in the better defined environment of the free jet with a generally higher signal-to-noise ratio.[70]

The CARS studies have been extended to both inelastic and reactive collisions of H + D_2 at several collision energies, determining absolute product-state integral cross sections.[71] To date these measurements have been chiefly compared with QCT results[52] and have shown good qualitative agreement. The QCT results tend to show somewhat higher rotational excitation than the measurements, however. In an exciting development, product-state distributions for H + o-H_2 $\rightarrow$ p-H_2 + H were measured as a function of collision energy, and sharp features in these excitation functions for v=1 product at energies close to the predicted quantum mechanical resonances for this system were observed.[72] Previously, the only phenomenon attributable to dynamical resonances were observed in the vibrational state resolved DCS for the reaction F + H_2 $\rightarrow$ HF + H[73]. Although resonances were first observed in low dimensionality quantum calculations of the excitation function for the H + H_2 system[31], it was felt that the large number of partial waves contributing to the reaction in 3-D would wash out any such features in a product-state distribution measurement. The recent exact 3-D quantum results of Zhang and Miller show that in fact the resonances in the excitation functions should 'wash out', at least on the LSTH potential energy surface.[74] This discrepancy remains an unresolved question at this point. Questions regarding the accuracy of the LSTH surface in the regions most pertinent to the formation of the quasi-bound states which produce the resonances remain to be answered. In addition, replication of the experimental results with another technique has yet to be done. Initial evidence for a resonance near the DH(v=1) product threshold for the reaction D + H_2 $\rightarrow$ DH + H was also recently obtained.[75]

The MPI technique has recently begun producing new results as well, including product-state distributions at higher collision energies.[76] This technique has now been applied to the measurement of the D + H_2(v=1,J=1) reaction[77], with the study of more ro-vibrational state-selected reactions possible in the near future. With the availability in the near future of exact quantum calculations for the various isotopic variants of H_3 over the energy range of experimental interest, we can finally look forward to a detailed intercomparison of experimental and theoretical product-state distributions.

A landmark crossed-molecular-beams DCS measurement for the D + $H_2 \rightarrow$ DH + H reaction at a collision energy of 0.95 eV using a similar technique to that described in this thesis was first reported by Buntin, Giese and Gentry in 1987.[78] Photolysis of D_2S at 193 nm was used to generate a pulsed D-atom beam with a well-defined velocity distribution. These photolytic D atoms were then scattered off of a pulsed H_2 molecular beam, with the velocity of the DH products recorded at specific laboratory angles by measuring the time-of-flight (TOF) of the DH products with mass-spectrometric detection. For the first time, vibrational state-resolved DCS measurements were made on the D + H_2 reaction. Gentry's apparatus has rotatable beam sources and a fixed detector, a geometry that has some advantages and some disadvantages when compared to the fixed beam source, rotatable detector geometry used in our laboratory. An advantage is that the crossing angle of the beams may be changed, thereby allowing adjustment of the collision energy of the experiment. In principle, with such a geometry, after fixing the beam crossing angle, both beam sources may be rotated together relative to the fixed detector, allowing measurement of the product angular and velocity distributions. This becomes much less feasible,

however, when an excimer laser is coupled to one of the sources and counting times of up to 42 hours/angle are necessary.[76] The extremely short pulse-length pulsed beams used allowed high signal-to-noise ratios to be achieved per laser shot without differential pumping. The lack of differential pumping limited the repetition rate of the experiment to 2 Hz, however. This extremely low duty cycle, coupled with the difficulty associated with rotation of the beam sources precluded the acquisition of extensive product-angular distributions. Buntin reported several more experiments at collision energies of 0.85, 0.95, 1.05 and 1.20 eV with detection at a single angle, chosen to measure the resolvable back-scattered DH(v=1)/DH(v=0) products.[76] A detailed comparison of these results with theoretical predictions has not yet appeared, however, a Monte Carlo algorithm was used to extract the experimental (v,J) distributions for the backward scattered DH products.

Finally, we come to the crossed-beams measurements described in this thesis. Using the photolysis of DI at 248 nm to produce D atoms with translational energies of $\approx$ 1 and 2 eV the vibrational state-resolved differential cross sections for the reaction $D + H_2 \rightarrow DH(v) + H$ at nominal collision energies of 0.53 and 1.01 eV have been measured using a crossed-molecular-beams apparatus with a rotatable mass-spectrometric detector. The backward scattered DH(v=0)/DH(v=1) product states are well resolved over a range of CM angles. TOF distributions at 22 angles were measured at 1.01 eV, with 12 measured at 0.53 eV. Although two velocity groups of D atoms are produced in the photodissociation of DI, these may be separated in space to a large degree due to the different symmetries of the electronic transitions producing the ground and spin-orbit excited state I atoms (parallel and perpendicular to the diatom bond, respectively). This convenient fact

allowed changing the collision energy of the experiment by merely changing the direction of linear polarization of the photolysis laser. In Chapter Three these results will be presented and compared with the extensive exact 3-D quantum calculations of Zhang and Miller. The agreement between the calculations and the experiment is in many ways remarkable, indicating that our theoretical understanding of this reaction is indeed quite impressive. There are, however, systematic deviations between experiment and theory, but with modifications to the theoretical differential cross sections good agreement is obtained. The necessary changes do not significantly alter the product rotational distributions. The sensitivity of these DCS measurements raises further questions about the global accuracy of the existing *ab initio* PES's, and provides the most important detailed test of the H_3 PES to date.

3. The Future

At this point, it appears that the problem of performing exact 3-D quantum-scattering calculations on the H_3 system has been solved. With respect to chemical dynamics as a whole, there will certainly be continued efforts to accelerate exact 3-D calculations, extend the calculations to more complex systems, and improve the approximate methods for dynamics calculations. Quantum chemists are now in a position to provide us with more accurate potential energy surfaces[79], which the DCS measurements described in this thesis and the apparent observation of the dynamical resonances in Valentini's laboratory[72] indicate may be in order.

On the experimental front, work remains to be done. The measurements reported in this thesis and those of Buntin, et. al.[78], have

provided vibrational state-resolved DCS measurements, however, it is not clear that the conventional 'universal' electron-impact-ionization-detection technique can be reasonably extended to provide rotational-state resolution. More detailed studies of the reaction of state-selected reagents also remain to be done. The initial results on the detection of the H_3 transition state from Polanyi's group[66] raise the possibility that the H_3 transition state itself may be amenable to direct study someday. The future will most certainly bring laser-based state-resolved DCS measurements, possibly using higher sensitivity MPI techniques for the molecular product, or more exotic approaches for detection of H atoms.[80] Presumably, when accurate, fully (v,J) state-resolved differential cross sections for the entire CM distribution are measured as a function of collision energy, any observable quantum-mechanical resonance phenomena should be revealed, and the experimental determination of the dynamics of this elementary reaction will be complete. Perhaps one more decade will see this culminating result appear in the literature.

1 S. Arrhenius, Z. Phys. Chem., **4**, 226 (1889).

2 a) B. Liu, J. Chem. Phys., **58**, 1925 (1973).

b) P. Siegbahn and B. Liu, J. Chem. Phys., **68** ,2457 (1978).

3 D.G. Truhlar and C.J. Horowitz, J. Chem. Phys., **68**, 2466 (1978); J. Chem. Phys., **71**, 1514 (1979).

4 A.J.C. Varandas, F.B. Brown, C.A. Mead, D.G. Truhlar, and N.C. Blais, J. Chem. Phys., **86**, 6258 (1987).

5 J.Z.H. Zhang and W.H. Miller, J. Chem. Phys., **91**, 1528 (1989).

6 a) D.G. Truhlar and R.E. Wyatt, " History of H_3 Kinetics ", Ann. Rev. Phys. Chem., **27**, 1 (1976).

b) D.G. Truhlar and R.E. Wyatt, " H + H_2: Potential-Energy Surfaces and Elastic and Inelastic Scattering", Adv. Chem. Phys., **36**, 141 (1977).

c) G.C. Schatz, " Recent Quantum Scattering Calculations on the H + H_2 Reaction and its Isotopic Counterparts", in The Theory of Chemical Reaction Dynamics, ed. D. C. Clary, NATO Adv. Res. Wkshp., D. Reidel , Dordrecht, Holland, (1986), pp. 1- 26.

d) G.C. Schatz, " Quantum Effects in Gas Phase Chemical Reactions", Ann. Rev. Phys. Chem. , **39**, 317 (1988).

7 J.J. Valentini and D.L. Phillips, "Experimental and Theoretical Studies of the Dynamics of the Hydrogen Exchange Reaction: Maturation of a Prototype", in Advances in Gas Phase Photochemistry and Kinetics, Vol. 2: Bimolecular Collisions, M.N.R. Ashfold and J. E. Baggott, Eds., Royal Society of Chemistry, London, 1988.

8 F. London, Z. Elektrochem., **35**, 552 (1929).

9 M. Born and J.R. Oppenheimer, Ann. Physik, **84**, 457 (1927).

[10] H. Eyring and M. Polanyi, Z. Physik. Chem. **B12**, 279, (1931).

[11] J.O. Hirschfelder, H. Eyring, and B. Topley, J. Chem. Phys., **4** , 170 (1936).

[12] a) A. Farkas, Z. Phys. Chem., **B10**, 419 (1930).

b) K.H. Geib and P. Harteck, Z. Phys. Chem. Bodenstein Festband, (1931), p. 849.

c) A. Farkas and L. Farkas, Proc. Roy. Soc. London, **A152**, 124 (1935).

[13] R.N. Porter and M. Karplus, J. Chem. Phys., **40**, 1105 (1964).

[14] H.R. Mayne and J.P. Toennies, J. Chem. Phys. **70**, 5314 (1979).

[15] E. Pollak, Int. J. Chem. Kin., **18**, 1087 (1986).

[16] a) F. T. Wall, L.A. Hiller, Jr., and J. Mazur, J. Chem. Phys. **29**, 255 (1958).

b) *ibid.*, **35**, 1284 (1961).

[17] M. Karplus, R.N. Porter and R.D. Sharma, J. Chem. Phys. **43**, 3259 (1965).

[18] a) J.C. Polanyi, Chemica Scripta, **27**, 229 (1987).

b) D.R. Herschbach, Chemica Scripta, **27**, 329 (1987).

[19] E. H. Taylor and S. Datz, J. Chem. Phys., **23**, 1711 (1955).

[20] S. Datz and E. H. Taylor, J. Chem. Phys., **39**, 1896 (1963)

[21] W.L. Fite and R.T. Brackmann,in Atomic Collision Processes, ed. by M.R.C. McDowell, North Holland, Amsterdam (1964), pp. 955-963.

[22] a) Y.T. Lee, J.D. McDonald, P.R. LeBreton and D.R. Herschbach, Rev. Sci. Inst., **40**, 1402 (1968).

b) Y.T. Lee, Chemica Scripta, **27**, 215 (1987).

[23] P. Brumer and M. Karplus, J. Chem. Phys., **54**, 4955 (1971).

[24] a) J.C. Polanyi and J.L. Schreiber, Physical Chemistry, An Advanced Treatise, **vol. VIA**: Kinetics of Gas Reactions ,ed. H. Eyring, W. Jost and D. Henderson, Academic Press, New York (1974), Ch. 6, p. 383.

b) P.J. Kuntz, Dynamics of Molecular Collisions, Part B, (ed. by W.H. Miller), Plenum Press, New York (1976), Ch.2, p. 53.

[25] W.R. Schulz and D.J. LeRoy, J. Chem. Phys., **42**, 3869 (1965).

[26] A.A. Westenberg and N. deHaas, J. Chem. Phys., **47**, 1393 (1967).

[27] a) K.A. Quickert and D.J. LeRoy, J. Chem. Phys., **53**, 1325 (1970), *ibid.*, 54, 5444E (1971).

b) D.N. Mitchell and D.J. LeRoy, J. Chem. Phys., **58**, 3449 (1973).

[28] A. Kuppermann and J.M. White, J. Chem. Phys., **44**, 4352 (1966).

[29] a) A. Kuppermann and G.C. Schatz, J. Chem. Phys., **62**, 2502 (1975).

b) G. C. Schatz and A. Kuppermann, J. Chem. Phys., **65**, 4642 (1975), *ibid.*, **65**, 4668 (1975).

[30] R.B. Walker, E.B. Stechel and J.C. Light, J. Chem. Phys., **69**, 2922 (1978).

[31] S.F. Wu and R.D. Levine, Molec. Phys., **22**, 881 (1971).

[32] a). K.T. Tang and B.H. Choi, J. Chem. Phys., **62**, 3642 (1975).

b). B.H. Choi, R.T. Poe and K.T. Tang, J. Chem. Phys., **69**, 411 (1978).

c). Y.Y. Yung, B.H. Choi and K.T. Tang, J. Chem. Phys., **72**, 621 (1980).

d). J.C. Sun, B.H. Choi, R.T. Poe and K.T. Tang, J. Chem. Phys., **73**, 6095 (1980).

e). J.C. Sun, B.H. Choi, R.T. Poe and K.T. Tang, J. Chem. Phys., **79**, 5376 (1983).

[33] A.B. Elkowitz and R.E. Wyatt, Mol. Phys., **31**, 189 (1976).

[34] A. Kuppermann, G.C. Schatz, and J. Dwyer, Chem. Phys. Lett., **45**, 71 (1977).

[35] a).J.M. Bowman and K.T. Lee, J. Chem. Phys., **68**, 3940 (1978).

b).V. Khare, D.J. Kouri and M. Baer, J. Chem. Phys., **71**, 1188 (1979).

[36] a). the DWBA is reviewed in;

K.T. Tang, "Approximate Treatments of Reactive Scattering: The T-Matrix Approach", in Theory of Chemical Reaction Dynamics, Vol. 2, ed. by M. Baer, CRC Press, Boca Raton, Fla USA, (1985), pp. 125 - 180.

b). the IOSA is reviewed in;

J. Jellinek and D. J. Kouri, "Approximate Treatments of Reactive Scattering: Infinite Order Sudden Approximation", in Theory of Chemical Reaction Dynamics, Vol. 2, ed. by M. Baer, CRC Press, Boca Raton, Fla USA, (1985), pp. 1 - 123.

[37] a) H.R. Mayne, J. Chem. Phys., **73**, 217 (1980).

b) G.D. Barg, H.R. Mayne and J.P. Toennies, J. Chem. Phys., **74**, 1017 (1981).

c) H.R. Mayne and J.P. Toennies, J. Chem. Phys., **75**, 1794 (1981).

[38] N. Sathyamurthy and J.P. Toennies, Chem. Phys. Lett., **143**, 323 (1988).

[39] R. Goetting, H. R. Mayne and J. P. Toennies, J. Chem. Phys., **85**, 6396 (1986), J. Chem. Phys., **80**, 2230 (1984)L.

[40] a) R. Goetting, J.P. Toennies and M. Vodegel, Int. J. Chem. Kin., **18**, 949 (1986).

b) R. Goetting, V. Herrero, J.P. Toennies and M. Vodegel, Chem. Phys. Lett., **137**, 524 (1987).

[41] J. Geddes, H.F. Krause, and W.L. Fite, J. Chem. Phys., **56**, 3298 (1972), *ibid.*, **42**, 3296L (1970), *ibid.*, **59**, 566E (1972).

[42] a). G.H. Kwei, V.W.S. Lo, and E.A. Entemann, J. Chem. Phys. **59**, 3421 (1973).

b). G.H. Kwei and V.W.S. Lo, J. Chem. Phys., **72**, 6265 (1980).

[43] H. Harrison, J. Chem. Phys., **37**, 1164 (1962).

[44] a). M.A.D. Fluendy, R.M. Martin, E.E. Muschlitz, and D.R. Herschbach, J. Chem. Phys., **46**, 2172 (1967).

b). W.C. Stwalley, A. Niehaus, and D.R. Herschbach, J. Chem. Phys., **51**, 2287 (1969).

[45] R. Gengenbach, Ch. Hahn, and J.P. Toennies, J. Chem. Phys., **62**, 3620 (1975).

[46] W. Bauer, R.W. Bickes Jr., B. Lantzsch, J.P. Toennies, and K. Walaschewski, Chem. Phys. Lett., **31**, 12 (1975).

[47] R.F. Heidner III and J.V.V. Kasper, Chem. Phys. Lett., **15**, 179 (1972).

[48] E.B. Gordon, B.I. Ivanov, A.P. Perminox, V.E. Balalev, A.N. Ponomarev and V.V. Filotov, Chem. Phys. Lett., **58**, 425 (1978).

[49] a) M. Kneba, U. Wellhausen and J. Wolfrum, Ber. Bunsenges. Phys. Chem., **83**, 940 (1979).

b) U. Wellhausen and J. Wolfrum, Ber. Bunsenges. Phys. Chem., **89**, 314 (1985).

[50] a). G.P. Glass and B.K. Chaturvedi, J. Chem. Phys., 77, 3478 (1982).

b). V.B. Rozenshtein, Y.M. Gershenzon, A.V. Ivanov, S.I. Kucheryavii, and S. Ya. Umanskii, Chem. Phys. Lett., **105**, 423 (1984).

c). V.B. Rozenshtein, Y.M. Gershenzon, A.V. Ivanov, S.D. Il'in, S.I. Kucheryavii, and S. Ya. Umanskii, Chem. Phys. Lett., **121**, 89 (1985).

[51] T. Dreier and J. Wolfrum, Int. J. Chem. Kin., **18**, 919 (1986).

[52] a). F. Webster and J.C. Light, J. Chem. Phys., **90**, 265 (1989), *ibid.*, **90**, 300(1989).

b). K. Haug, D.W. Schwenke, Y. Shima, D.G. Truhlar, J.Z.H. Zhang and D.J. Kouri, J. Phys. Chem., **90**, 6757 (1986).

c). D.E. Manolopoulos and R.E. Wyatt, Chem. Phys. Lett., **152**, 23 (1988).

[53] a) N.C. Blais and D.G. Truhlar, Chem. Phys. Lett., **102**, 120 (1983).

b) N.C. Blais, D.G. Truhlar, and B.C. Garrett, J. Chem. Phys., **82**, 2300 (1985).

[54] N.C. Blais and D.G. Truhlar, J. Chem. Phys., **88**, 5457 (1988).

[55] F.J. Aoiz, V.J. Herrero, and V. Saez, Chem. Phys. Lett., **161**, 270 (1989).

[56] N. Abu Salbi, D.J. Kouri, Y. Shima and M. Baer, J. Chem. Phys., **82**, 2650 (1985).

[57] B.M.D.D. Jansen op de Haar and G.G. Balint-Kurti, J. Chem. Phys., **90**, 888 (1989).

[58] a). D.E. Manolopoulos and R. E. Wyatt, Chem. Phys. Lett., **159**, 123 (1989).
b). J.M. Launay and M. Le Dourneuf, Chem. Phys. Lett., in press.

[59] S.M. Auerbach, J.Z.H. Zhang and W.H.Miller, in preparation.

[60] R. Goetting, Ph. D. thesis, Goettingen, 1985.

[61] M. Vodegel, Ph. D. thesis, Goettingen, 1987.

[62] R.R. Williams and R.A. Ogg, J. Chem. Phys., **15**, 691 (1947).

[63] G.W. Flynn and R.E. Weston, Jr., Ann. Rev. Phys. Chem., **37**, 551 (1986).

[64] D.P. Gerrity and J.J. Valentini, J. Chem. Phys., **81**, 1290 (1984).

[65] E.E. Marinero, C.T. Rettner, and R.N. Zare, J. Chem. Phys., **80**, 4146 (1984).

[66] B.A. Collings, J.C. Polanyi, M.A. Smith, A. Stolow and A.W. Tarr, Phys. Rev. Lett., **59**, 2551 (1987).

[67] G.W. Johnston, B. Katz, K. Tsukiyama and R. Bersohn, J. Phys. Chem., **91**, 5445 (1987).

[68] K.-D. Rinnen, D.A.V. Kliner, and R.N. Zare Israel J. Chem., (1989) In Press.

[69] a). R.S. Blake, K.-D. Rinnen, D.A.V. Kliner and R.N. Zare, Chem. Phys. Lett., **153**, 365 (1988).
b). K.-D. Rinnen, D.A.V. Kliner, R.S. Blake and R.N. Zare, Chem. Phys. Lett., **153**, 371 (1988).

[70] K.-D. Rinnen, D.A.V. Kliner, R.S. Blake and R.N. Zare, Rev. Sci. Inst., **60**, 717 (1988).

[71] a) D.P. Gerrity and J.J. Valentini, J. Chem. Phys., **82**, 1323 (1985).

b) D.P. Gerrity and J.J. Valentini, J. Chem. Phys., **83**, 2207 (1985).

c) J.J. Valentini and D.P. Gerrity, Int. J. Chem. Kin., **18**, 937 (1986).

d) H.B. Levene, D.L. Phillips, J.-C. Nieh, D.P. Gerrity and J.J. Valentini, Chem. Phys. Lett., **143**, 317 (1988).

72 J.-C. Nieh and J.J. Valentini, Phys. Rev. Lett., **60**, 519 (1988).

73 a) D.M. Neumark, A.M. Wodtke, G.N. Robinson, C.C. Hayden and Y.T. Lee, Phys. Rev. Lett., **53**, 2226 (1984).

b) D.M. Neumark, A.M. Wodtke, G.N. Robinson, C.C. Hayden and Y.T. Lee, J. Chem. Phys., **82**, 3045 (1985).

c) D.M. Neumark, A.M. Wodtke, G.N. Robinson, C.C. Hayden, K. Shobatake, R.K. Sparks, T.P. Schafer and Y.T. Lee, J. Chem. Phys., **82**, 3067 (1985).

74 J.Z.H. Zhang and W.H. Miller, Chem. Phys. Lett., **153**, 465 (1988).

75 D.L. Phillips, H.B. Levene and J.J. Valentini, J. Chem. Phys., **90**, 1600 (1988).

76 K.-D. Rinnen, D.A.V. Kliner, R.S. Blake, Chem. Phys. Lett., **153**, 371 (1988).

77 D.A.V. Kliner, and R.N. Zare, J. Chem. Phys., submitted.

78 a) S.A. Buntin, C.F. Giese and W.R. Gentry, J. Chem. Phys., **87**, 1443 (1987).

b). S.A. Buntin, Ph. D. Thesis, Univ. of Minnesota, (1987).

79 R.N. Barnett, P.J. Reynolds and W. A. Lester, Jr., J. Chem. Phys., **82**, 2700 (1985).

80 K.A. Welge, XII International Symposium on Molecular Beams, Abstracts of Invited Talks and Contributed Papers (May 29-June 2, 1989, Perugia, Italy), p. I.10.

Chapter 2

Development of the D + H_2 → DH + H Reactive Scattering Experiments

1. Introduction

The reactive scattering experiments described in this thesis were performed in three distinct phases. A significant amount of development work was required in this study, since scattering experiments with a photolytic D-atom beam had not been done previously. In this chapter, various approaches to H/D-atom beam generation are briefly reviewed, the photolytic D-atom beam source is assessed and the crossed-molecular-beams scattering apparatus on which the experiments were performed is described. This is followed by a discussion of the feasibility of photolytic beam scattering experiments, and, finally, the results of the first two iterations of the D + H_2 experiment will be presented, with the focus on the characteristics of the photolytic D-atom beam.

Reactive scattering experiments with crossed-molecular-beams involve the interaction of two collimated, velocity-selected atomic or molecular beams in a well-defined interaction region, followed by analysis of the product identity, scattering angle, intensity, and kinetic energy. The kinetic energy of the products is determined by measurements of the particle velocity using the time-of-flight (TOF) method, in which the time it takes for a particle to fly a known distance is recorded. For a known total available energy, conservation of energy then determines the product internal energy. The

collision energy associated with the interaction of the beams is determined by the velocity distributions and crossing angle of the beams. Thus, generation of collimated atomic and molecular beams is critical to the successful scattering experiment. Beams of stable molecules and rare gases are relatively easy to generate; basically all that is needed is a pinhole and a vacuum chamber. Reactive species pose a more difficult problem, since they are by definition 'transient'. A suitable D-atom source was therefore of central importance in the D + H_2 scattering experiments. The most suitable method for producing a high energy D-atom beam with a narrow energy distribution is currently laser photolysis of a suitable hydride molecule. This technique is discussed in detail in this chapter.

2. H/D-Atom Beam Sources

Experimental studies of hydrogen atom reactions have traditionally been fraught with difficulty. Due to the reactivity of H atoms and the typical strength of chemical bonds with the H atom the generation of reactant H atoms is not an easy task. The first H-atom source used was an electrical discharge, the "Wood's tube" of the 1920's.[1] More sophisticated RF, microwave and arc discharge sources have seen use over the years, in both crossed beams and bulk gas studies. Sources based on the thermal dissociation of H_2 have been used in many studies, but the translational energies obtainable by such techniques are limited by the construction materials available that can withstand the high temperatures associated with the thermal dissociation of H_2. Charge-exchange sources have been studied due to their application as a tool for heating nuclear plasma fusion reactors.[2]

Tritium atoms produced as a product of radioactive decay have been used in many bulk studies of hot atom chemistry.[3] Another classic hot atom technique, the production of energetic atoms by photodissociation[4], has seen a resurgence today due to the availability of high power UV lasers. Excimer laser photolysis of DI at 248 nm is the approach we have used in these experiments. A brief review of some of the alternative approaches is presented, followed by a more detailed discussion of photolytic sources for energetic hydrogen atoms.

2.1 Thermal Dissociation Sources

One of the most straightforward approaches to the generation of atomic beams is through thermal dissociation of the parent homonuclear diatomic molecule. Due to the strong bond energy of H_2, (4.478 eV)[5] this approach is limited by the availability of construction materials able to withstand the high temperatures required to achieve a significant fraction of dissociation (≈ 2800 K for H_2). Tungsten metal best fulfills the requirements, as it maintains mechanical strength for relatively long periods of time at temperatures up to 3000 K.[6] In the case of the hydrogen exchange reaction, due to the high barrier and small reduced mass of the D - H_2 reactants, high reagent velocities are required for appreciable reaction to occur. The most probable velocity in an effusive beam in thermal equilibrium with an oven is given by

$$v_{mp} = \sqrt{\frac{3kT}{m}} \qquad (1).^{7}$$

Thus, a D-atom beam produced by thermal dissociation of H_2 at 2800 K would be expected to have a most probable velocity of 5.9×10^5 cm/sec. Assuming that a beam of this sort was perpendicularly crossed with a supersonic beam of H_2 having a most probable velocity of 2.7×10^5 cm/sec, a nominal collision energy of 0.22 eV would result, which is below the threshold energy for the D + H_2 exchange reaction. The distribution of collision energies in such experiments is quite broad, however, with many higher energy collisions occurring. Early crossed-molecular-beams studies of the D + H_2[8,9a], H + D_2[9b] and T + H_2[10] reactions were done with thermal oven beams of H, D and T. Thermal dissociation sources are more useful for the study of hydrogen atom reactions with low activation energies (i.e., < 0.5 eV)[11,12]. Seeded supersonic beams of H/D atoms have been generated in a high-pressure tungsten oven, however, the beam velocity limitation imposed by the oven material still restricts the collision energies attainable.[13] The seeded-supersonic-beam technique, which is frequently used for the acceleration of heavy particles by seeding a small fraction of the heavy component in a light buffer gas and taking advantage of the aerodynamic acceleration in the expansion[14] will not work for H or D atoms, due to the lack of lighter buffer gases. For our purposes, the low collision energy and broad collision energy distribution inherent in thermal dissociation beam sources ruled out this approach in the measurement of vibrational state resolved differential cross sections for the D + H_2 reaction.

2.2 Electrical Discharge Sources

The first H-atom source was the Wood's discharge tube of the 1920's, which was applied to spectroscopic studies of the H atom.[1] Various electrical discharge sources have received considerable use since then, for both low and high energy H atom beams. Both RF[15] and microwave discharges[16] have been used in low-energy molecular beam scattering experiments with H/D atoms. These sources can be operated at low temperatures with dissociation fractions varying between 30 - 100 %[16a]. Once again, sources of this type are most useful for reactions with a low activation energy, due to the low beam velocities. The velocity distributions are also quite broad, as the sources must be operated at relatively low pressures (typically less than 2 torr). The low-temperature microwave-discharge source has seen application in a crossed-molecular beams study of the vibrationally excited $D + H_2(v=1) \rightarrow DH + H$ reaction, which has a considerably lower activation energy than the exchange reaction with $H_2(v=0)$.[16a]

High-temperature arc discharges provide one of the best 'conventional' continuous-molecular-beam sources for H-atom scattering studies in the 1 to 10 eV range. Sources of this type were first developed by Knuth and coworkers[17], and applied to the production of H atoms by Way, Yang and Stwalley[18]. More recently, Goetting, Mayne and Toennies applied a modified source of this design to the study of the $D + H_2$ reaction at a nominal collision energy of 1.5 eV[19], and a source of this type was also developed for the production of metastable H_3.[20] In these sources locally high temperatures (plasma temperatures up to 30000 K) are created in the arc struck between a

tungsten cathode and anode, which has the nozzle drilled into it.[21] Efficient cooling of the source is required to prevent meltdown and large power supplies are required to operate sources of this type. An additional complication associated with discharges of this type is that metastable species such as H_3 may contaminate the beam[19]. The source characteristics (temperature and velocity distribution) are also critically dependent on the assembly of the components, and are often not reproducible, requiring re-characterization of the beam velocity distribution upon each re-assembly. Given that the lifespan of such sources is only on the order of 50 hours[19], this is a serious limitation. The beam velocity distributions are also very broad. The D-atom source used by Goetting and coworkers[19], for example, had a peak D-atom kinetic energy of $\approx$ 3.8 eV, with a velocity distribution characterized by a mach number $M \approx 1$. Beam sources of this type can yield high intensity D-atom beams (up to 10^{22} atoms$\cdot$sr^{-1} $\cdot$sec^{-1}), but, due to the breadth of the velocity distribution and the technical difficulties associated with the construction of mechanical velocity selectors for particles with velocities in excess of 10^6 cm/sec,[22] such sources are not suitable for the measurement of vibrational-state resolved differential cross sections for the D + H_2 reaction.

2.3 Ion Beam Neutralization Sources

Charge exchange and other types of ion beam neutralization sources have not been applied to the study of collision processes in the energy range of 'chemical' interest, (less than 10 eV). They could, in principle, be applied in the future. Neutralization of ion beams provides an interesting approach

to the preparation of energetic neutral particle beams since the precursor ion beam energy distribution may be conveniently manipulated with electromagnetic optics. The chief difficulty associated with the use of such techniques in the energy range < 10 eV is the limitation imposed on the precursor ion beam size and density by the space charge within the beam.[23] The use of the merging beams technique, which has been extensively applied to ion-molecule reactions[24], could bring techniques of this sort into use for dynamics studies of chemical reactions at energies less than 10 eV. Neutralization of 40-50 keV proton beams in Cs vapor has an important technological application to the heating of tokamak fusion reactors[2], and considerable work has been dedicated to the development of such neutral particle beams. The energy range and large physical dimensions of such beams are inappropriate for chemical dynamics studies, however.

Another interesting approach is the neutralization of H^- beams by photodetachment, i.e.,

$$H^- + h\nu \rightarrow H + e^- \quad \text{E. A.} = .75 \text{ eV} \qquad (2).$$

This technique was applied by two groups in the 1970's[25,26] to the study of various collisional processes in the 50 eV to 3 keV energy range. Van Zyl, Utterback and Amme[25] claimed useful beam intensities at energies down to 10 eV. The long term success of these efforts was apparently not very good, however, as this group later reported on the development of a new type of thermal dissociation oven for H atoms.[27] With the improved photodetachment light sources available today, perhaps such techniques will see more use in the future.

2.4 Hot Atom Sources

Much of the pioneering work on the kinetics of high energy chemical reactions was performed using two novel reactive atom sources. Radioactive decay of various isotopes can yield high kinetic energy atoms from the nuclear recoil. A large number of bulk kinetic studies have been done on the reactions of ^{11}C, ^{18}F and ^{3}H, (tritium) using this hot atom approach. The common reaction producing tritium, for example, is

$$n^0 + {}^3He \rightarrow {}^3H + H^+ + 0.19\ MeV \qquad (3).^3$$

These extremely high energy tritium atoms are presumably produced as ions, and are subsequently neutralized and thermalized by collision with an inert gas buffer until the energy range where chemical reactions occur is reached. After reaction with a dilute substrate occurs, the final products are analyzed, and the product yields are correlated with complicated kinetic schemes that model the reactions in the bulk sample. Such methods as applied to H atom reactions have been reviewed by Wolfgang.[3] Nuclear recoil sources of this sort are not applicable to the single-collision conditions of crossed-molecular-beams experiments.

The other classic hot atom chemistry technique involves the production of energetic atoms by the photodissociation of appropriate molecular precursors. Photodissociation of the hydrogen halides HI and HBr was adopted simultaneously with the development of the above-mentioned nuclear recoil sources as a source of energetic H atoms of well defined kinetic

energy in the 1 - 3 eV range.[4] The chief advantage of the photolytic source is that the kinetic energy of the H atom is determined by the difference between the photon energy and the dissociation energy of the parent molecule. Thus, the kinetic energy of the atoms may be varied by changing the photon energy and/or the precursor molecule. For bulk studies, the well-defined initial energy removes some of the uncertainty in reaction collision energy that is inherent in the moderation of the extremely energetic nuclear-recoil particles. The techniques used in the classic photochemical bulk kinetic studies were similar to those used in the nuclear recoil studies, namely the determination of product yields and relation of these yields to a kinetic scheme for the (complicated) bulk system.

Up until the early 1970's, considerable work was done using this classic technique. As mentioned in Chapter 1, this approach was used in the first experimental determination of the energetic threshold for the D + H_2 reaction by Kuppermann and White.[28] This approach to hot atom generation saw progressively less use until the development of powerful UV pulsed lasers in the 1980's. With excimer lasers, Nd:Yag lasers and even tunable UV dye lasers it is now possible to produce large quantities of H or D atoms by photolysis of the hydrogen halides HX (X = Br,I typically due to the low absorption cross sections for HCl and HF at attainable wavelengths), and, quite frequently, hydrogen sulfide (H_2S). The simultaneous development of more sensitive laser-based state-selective detection techniques for various molecules has allowed an explosion of work on energy transfer and reaction dynamics in the 1980's, including the efforts by Valentini and Zare on the HD_2 , HH_2 and DH_2 systems cited in Chapter 1. The wide range of bulk dynamical studies that have ensued have been recently reviewed.[29]

3. Photolytic Atomic Beams

Extension of the photolysis technique to the production of atomic beams for use in reactive scattering studies poses a more difficult problem, since the resulting beam intensities are quite low. Figure 2-1 gives a schematic view of a laser-generated photolytic-atomic-beam experiment. Buntin, Giese and Gentry first applied this technique to the generation of a D-atom beam for reactive scattering in 1987, using the 193 nm photolysis of D_2S[30]. Though difficult, creation of a spatially defined atomic beam does have special advantages, (in addition to allowing the measurement of differential cross sections), particularly when the hydrogen halides are used as the atomic precursor. Bulk kinetic or dynamical studies using HX precursors are typically complicated by the occurrence of two distinct photodissociation pathways,

$$HX + h\nu \rightarrow H(^2S) + X(^2P_{1/2}) \qquad (4),$$

and

$$HX + h\nu \rightarrow H(^2S) + X(^2P_{3/2}) \qquad (5)$$

producing ground and spin-orbit excited halogen atoms.[31] For X = I, the spin-orbit splitting is 0.94 eV, while for X = Br, the splitting is only 0.46 eV.[32] The branching ratio between these states is wavelength dependent. For HI/DI at 248 nm the branching ratio [I]/[I*] is approximately equal to one.[33]

Fortunately, the electronic transitions associated with the different spin-orbit states generally have different symmetry with respect to the diatom bond; for the $X(^2P_{1/2})$ channel the transition moment is parallel to the bond, while for the $X(^2P_{3/2})$ channel, the transition moment is perpendicular to the bond.[33] For the parallel transition, the photofragment angular distribution is proportional to $\cos^2\theta$ for a prompt dissociation, where θ is the angle between the electric vector of the photodissociation laser and the diatom bond. For the perpendicular transition, the photofragment angular distribution will be proportional to $\sin^2\theta$.[34] Thus, by using a polarized dissociation laser, the two different energy H atoms resulting from (4) and (5) may be, to a large degree, separated in space.[35]

The ideal precursor for a photolytic atomic beam source is a diatomic molecule which undergoes direct dissociation on a repulsive excited-state surface correlating with a single set of atomic fragments. A diatom precursor will yield the best velocity resolution for the photolytic beam because there are no internal degrees of freedom (other than electronic) with which to partition the excess energy in the photodissociation process. In this ideal case, then, the center-of-mass (CM) translational energy of the atomic species is determined by the conservation of linear momentum in the CM to be

$$E_H = \left(1 - \frac{m_H}{m_X}\right) E_{tr} \qquad (6)$$

where the translational energy E_{tr}, is given by

$$E_{tr} = E_{h\nu} - \Delta D^0_{0,HX} + E_{rot,\,HX} \qquad (7),$$

where $E_{h\nu}$ is the photon energy, $\Delta D^0_{0,HX}$ is the bond dissociation energy for the HX molecule, and $E_{rot,HX}$ is the rotational energy of the parent molecule. Due to the extreme mass ratio m_H/m_X in the hydrogen halides, virtually all of the total available energy ends up in H atom translation. In principal this technique provides the best way to produce monoenergetic H atom beams. The only spread in CM energy from the photodissociation process itself comes from the bandwidth of the laser and any parent rotational energy. An additional spread in the LAB velocity distribution, and hence LAB energy, comes from the parent molecule velocity vector distribution. For HX, though, the H atom recoil velocity is > 50 times larger than the parent velocity, and the spread in parent velocities will be much less than that. For a diatomic molecule, all of the parent rotational energy will end up in fragment translation. In the case of a polyatomic precursor, this will not, in general, be true. The use of polyatomic precursors is chiefly complicated by the fact that the polyatomic fragment produced in conjunction with the atomic species will have, in addition to electronic degrees of freedom, rotational and vibrational degrees of freedom with which the total available energy E_{tot} may be partitioned, i.e.,

$$E_{tr} = E_{h\nu} - \Delta D^0_{0,HR} + E_{int,\,HR} - E_{int,R}. \qquad (8).$$

Additionally, the polyatomic fragment may itself undergo photodissociation leading to a further spread in the observed laboratory velocity distribution if secondary H atoms are produced. At higher laser fluences multiphoton ionization of the precursor molecules may also become a competitive pathway with photodissociation, however, studies of the H-atom-yield laser-

fluence dependence showed that this was not a dominant pathway for HI or DI.

Due to limitations in both photolysis laser power and laser optics damage thresholds, the photodissociation cross section of the precursor should be reasonably large ($> 1 \times 10^{-19}$ cm^2) to allow for a significant fraction of dissociation at reasonable laser fluences. The laser may be focussed to achieve higher fluences, but by doing this, the total number of precursor molecules irradiated will decrease as the photolysis volume decreases. For molecules with larger dissociation cross sections, the laser may be operated with only mild focussing, yielding a higher atomic beam intensity.

One other general resolution consideration that is important in using a pulsed-photolytic-atom beam is that of <u>temporal</u> resolution. The temporal resolution of the pulsed beam is determined by the length of the laser pulse ($\approx$ 20 nsec for an excimer laser), the size of the photolysis volume, and the lab velocity distribution of the photolytic atoms. The angular resolution of the photolytic beam is also affected by the size of the photolysis volume, since the goal of a crossed-beams experiment of this sort is to produce atoms at the photolysis volume, collimate the recoiling atoms and cross them with a molecular beam in an interaction volume of finite size as shown in Figure 2-1. If the size of the photolysis volume is increased, the distribution of particle flight times from a point in the source to a point at the target will be broadened. Thus, for a large photodissociation-cross-section precursor, the beam intensity may be increased by defocussing the laser, but the temporal and angular resolution of the beam will decrease.

In the quest for high intensity pulsed photolytic beams, however, it is difficult to obtain 'ideal' conditions. The comments above did not address

effects which arise due to clusters or collisional phenomena in the photolytic beam source. In practice, the target beam pressure has to be raised to a significant value (> 5 x 10^{14} molec·cm^3) to produce beams of sufficient intensity in order to observe scattered products with universal mass spectrometric detection. At such high densities, some collisions will occur in the photolysis volume. Additionally, precursor clusters may be present in the target pulsed beam, which may result in a broadening of the observed velocity distribution. Effects of this sort were readily apparent in our studies, particularly the chemical reactions

$$\begin{aligned} D + HI &\rightarrow DH(v,J) + I \\ H + DI &\rightarrow DH(v,J) + I \end{aligned} \qquad (9).$$

These reactions proved to be troublesome due to the fact that the DH(v,J) product had high velocities and arrived in the same time frame as the DH product from the $D + H_2 \rightarrow DH + H$ reaction. These phenomena will be discussed in more detail later in this chapter and in Chapter Three.

4. Crossed-Molecular-Beams Scattering Apparatus

Molecular beam scattering became a general tool for studies of the chemical reaction dynamics of neutral species with the advent of the 'universal' crossed-molecular-beams machine. Earlier scattering experiments concentrated on the reactions of alkali metals since these species were specifically detectable with sensitive hot-wire surface-ionization detectors.[36] The first truly successful 'universal' crossed-molecular-beams

apparatus was that built by Lee, et. al.[37], which employed fixed differentially pumped continuous atomic/molecular beam sources and a rotatable mass spectrometer. This design has been very successful and has been used to study a wide range of elastic, inelastic and reactive scattering processes.[38] The apparatus used in this work is a large, high-resolution version of the original machine described in detail in ref. 37 .[39] Although the apparatus was originally designed to use continuous molecular beam sources, adaptation to use in pulsed molecular beam experiments was not difficult. The basic product detection principles remain unchanged, with the only major modifications occurring in the molecular beam source chambers. These will be reviewed in more detail later in this Chapter and in Chapter Three.

4.1 Detector

The detector is a triply differentially pumped rotatable ultra-high vacuum (UHV) quadrupole mass spectrometer using a scintillation-based ion-counting detection scheme[40]. A schematic of the detector is shown in Figure 2-2. An electron-impact ionizer based on the original design of Brink[41] is used to create positive ions from the scattered neutral particles that pass through three collimating apertures. These positive ions are then extracted and separated according to mass-to-charge (m/e) ratio with an Extrel quadrupole mass spectrometer adapted to the detector chamber. A new high frequency inductor circuit (Extrel Model 012-10 High-Q Head) was used with the mass spectrometer to allow good mass separation for low m/e ions at high ion energies (ion energy ≈ 100 V), achieving higher ion transmission for m/e = 1, 2, 3 and 4.[42] With a scintillation-based ion detector, a positive ion is

first converted into several secondary electrons by accelerating the ion into a -35 kV cathode. The secondary electrons are accelerated in this same field into an aluminum coated scintillator. The photons produced enter an RCA 8850 photomultiplier tube (PMT), which produces pulses of several hundred millivolts with a FWHM of ≈ 25 nsec. The aluminum coating (≈ 500 Å [37]) on the scintillator prevents scattered laser light or photons emitted by the hot ionizer filament from reaching the PMT. Scintillation detectors of this type offer the advantages of higher gain and higher permissible count rates compared to more conventional nude electron multipliers.

4.2 Signal Processing Electronics

Pulse counting of the ion signal is done to obtain the TOF spectrum of the neutrals, which yields the product velocity distribution. In continuous-beam scattering experiments, a chopping wheel modulates the product signal. In the present experiments, the modulation is provided by the firing of the photolysis laser which produces the D atoms. The ion-produced pulses are first passed through a discriminator (LeCroy LRS 621BL Quad Discriminator) where low voltage pulses corresponding to single-photon events and shot noise in the PMT are rejected. The inverted output of the discriminator is then amplified and shaped by a LRS 333 dual bipolar amplifier (LeCroy), producing pulses of ≈ 3 V, 25 nsec FWHM which are then sent to a custom built multi-channel scaler (MCS) with 4096 channels and a minimum channel time width (dwell time) of 0.15 μsec and a dead time between channels of ≈ 20 nsec.[43] The MCS can handle count rates up to ≈ 1 MHz. Count rates in excess of 1 MHz can cause saturation of the MCS. An LSI 11/73

microcomputer is interfaced with the MCS via a CAMAC crate. The MCS dumps the TOF data to the microcomputer after each user-specified number of laser shots.

4.3 Vacuum System

The crossed-molecular-beams machine is a fine showcase of vacuum technology. The differentially pumped beam source chambers typically run in the 10^{-4} to 10^{-5} torr range, with large source throughputs supported by high pumping speeds obtained with untrapped 10" Varian VHS-10 diffusion pumps (DP's), (pumping speed S = 6,000 liters·sec^{-1} for H_2 without a gate valve), often backed by a Roots-blower mechanical pumping system. Differential pumping on each of the source chambers is provided by one 4" VHS-4 DP (S ≈ 600 liters·sec^{-1} for H_2 with a gate valve) each. The pumping arrangement for the source chambers are described in greater detail later. The main chamber, where the beams cross, is pumped by two VHS-10 DP's and one 6" VHS-6 DP. An additional 15" VHS-400 DP (S ≈ 10,000 liters·sec^{-1} for H_2) was added to the scattering chamber by machining a large hole in the chamber door and attaching the pump with a 16" stainless steel tee. In addition, the main scattering chamber is cryo-pumped with a large Ni-plated Cu cold shield, (cooled to 77K with liquid nitrogen), which surrounds the chamber. This does not help in the pumping of H_2, but for condensible species extremely high pumping speeds are achievable. The scattering chamber reaches ultimate pressures in the 10^{-8} torr range. With the D and H_2 beams running, the main chamber pressure was typically ≈ 1 x 10^{-6} torr H_2. The main chamber is separated from the UHV detector by a sliding O-ring

sealed gate valve, so the chamber may be routinely vented without affecting the detector pressure.

The detector is comprised of three differential pumping regions, as illustrated in Figure 2-2. Scattered molecules enter the first chamber (region I, $P_I \approx 10^{-9}$ torr) through the first collimating slit, pass through a second collimating slit into the second chamber (region II, $P_{II} \approx 10^{-10}$ torr) then through the final collimator into the ionization chamber (region III, $P_{III} \approx 10^{-11}$ torr). The flight path from the COR to the ionizer is ≈ 34 cm. The positive ions are extracted from the ionizer into the mass spectrometer/ion counting system which resides in region II. This 'nested' geometry allows un-ionized scattered particles to pass straight through region III, thereby reducing the base pressure at the mass of interest. On the original machine these regions were pumped with ion and sublimation pumps. Currently, region I is pumped by a Perkin Elmer Ultek 220 liters·sec^{-1} triode ion pump/Boostivac titanium sublimator which is especially useful for pumping H_2. Region II is also pumped by a 220 liters·sec^{-1} ion pump, backed by a Seiko-Seiki STP-400 magnetically-suspended turbomolecular pump ($S \approx 300$ liters·sec^{-1} for H_2, with a compression ratio of 10^3 for H_2). Region III is pumped by another Seiko-Seiki STP-400 turbo and a 220 liters·sec^{-1} ion pump. Region III is also cryogenically pumped, as the entire chamber consists of a liquid-nitrogen cooled OFHC copper dewar. The STP-400 pumps are then backed by one more STP-400 pump, and finally by the main scattering chamber. The turbomolecular pumps are especially effective at reducing the rare-gas background in the detector.

5. Reactive Scattering with a Photolytic D-Atom Beam: Feasibility

The magnitude of the signal intensities and signal-to-noise (S/N) ratios achievable in a scattering experiment using a photolytic beam source may be estimated with a simple S/N calculation. A brief review of this calculation will give the reader an idea of the practical problems associated with this technique and its potential for further use. Conceptually, the D + H_2 reactive scattering experiment has four fundamental parts: (1) generation of the D-atom beam by photodissociation of DI at 248 nm, (2) generation of the H_2 molecular beam, (3) interaction of the two beams, and (4) detection of the scattered particles. Each of these problems will be considered below.

5.1 D-atom Production and Transport

A high-power UV laser is essential for the generation of photolytic atomic beams of sufficient intensity to perform crossed-beams DCS measurements by 'conventional' electron-bombardment mass spectrometric detection. In recent years several light sources that may satisfy this requirement have become available, most notably harmonics of the pulsed Nd:YAG solid state lasers and pulsed rare gas-halide excimer lasers. For the reactive scattering experiments a high duty cycle was desired, thus, the excimer laser was chosen as the light source. Repetition rates into the hundreds of Hz are possible with such lasers, as opposed to ≈ 10 Hz typical repetition rate for most Nd:YAG based systems. The final set of D + H_2 scattering experiments were done using a Lambda Physik EMG-202MSC

excimer laser, which, when in new or rebuilt condition and run in conjunction with a gas processor, could produce 375 mJ/pulse at 248 nm (37.5 W at 100 Hz) or 250 mJ/pulse at 193 nm (25 W at 100 Hz) for many hours without optics maintenance. The excimer laser output was plane-polarized using a ten-plate Brewster-angle stack transmission polarizer constructed with 0.16 mm thick Suprasil-A plates (Esco). This polarizer attenuated ≈ 55% of the incident beam, leaving light with > 95% polarization at 248 nm.[44] The laser beam was focussed by two Suprasil cylindrical lenses, one of which formed the window into the scattering chamber, providing 4 more optic element surfaces, with ≈ 5% reflection loss per surface. A reasonable value for the laser energy delivered to the DI beam/laser interaction region with this configuration is; 300 mJ/pulse x .45 x $(.95)^4$ = 110 mJ/pulse of polarized light. This corresponds to (.110 J) x (5.03×10^{22} cm^{-1}/Joule) x (one 248 nm photon/40,377 cm^{-1}) ≈ 1.4×10^{17} photons/ 20 nsec pulse. In practice the laser was focussed to a 3 mm x 3 mm spot. This gives a fluence of 1.5×10^{18} photons/cm^2·pulse, or 7.6×10^{25} photons/cm^2·sec during the pulse. The rate at which the molecules absorb photons and dissociate is given by:

$$\dot{N} \propto \sigma \cdot I \cdot N \qquad (10)$$

where N is the initial number of molecules, σ is the absorption cross section in cm^2, [45]and I is the photon flux. This expression may be integrated to yield an expression for the undissociated molecules;

$$\frac{N_f}{N_0} = \exp(-\sigma I \tau) \qquad (11),$$

where τ is the laser pulse length.[35] According to equation 11, approximately 45% of the molecules are dissociated under these conditions . Focussing the laser to a 2 x 2 mm spot increases the dissociation fraction to ≈ 75 %, but decreasing the irradiation volume decreases the total number of irradiated molecules and reduces the total number of dissociated molecules to around 1/2 of that obtained with the 3mm x 3mm laser spot.

Once the D atoms are produced, transport to the crossed-beams collision volume must be effected with as little interference as possible. Any collisions that occur may broaden the velocity distribution and thereby negate the benefits of using the photolytic D-atom source. In addition, reactive processes may occur with undissociated precursor molecules, resulting in unwanted contaminants in the atomic beam. For these reasons, it is important to estimate the upper limits on the precursor density. With a pulsed free jet it is possible to generate instantaneous pressures significantly in excess of 1 torr (3.5×10^{16} molecules·cm^{-3} at 298 K) within a few nozzle diameters of the source[46], so molecular beam intensity is not a problem here. The largest cross section scattering process in a target beam of DI is elastic scattering between D and DI or I atom. In the case of D + I scattering a hard-sphere collision diameter of ≈ 3.4 Å is estimated[47], which yields a hard-sphere collision cross section of ≈ 35 Å^2 . The attenuation of an incident beam of intensity I_0 by a stationary scattering gas is given by Beer's Law;

$$\frac{I}{I_0} = \exp(-\sigma n l) \qquad (12)$$

where n is the number density of the scatterer, σ is the cross section in cm^2 and l is the path length in cm.[48] For $n\sigma l = 1$, the density at which 1/e of the

incident beam is scattered is seen to be $\approx 1 \times 10^{15}$ cm^{-3} for l = 0.3 cm. For the reactive process D + DI $\rightarrow D_2$ + I the cross section is ≈ 2 Å^2 [49], so at this density approximately 6 % of the atoms could be expected to react in this manner. In the case under consideration the atoms are produced throughout the 'scattering' volume, so for some particles the path length l is much shorter, and this treatment overestimates the amount of scattering. In any case, though, it is clear that at densities significantly in excess of 1×10^{15} molecules/cm^3, collisional effects will begin to play an important role in the degradation of the quality of the atomic beam velocity distribution. For the purposes of this S/N calculation we will consider a precursor molecule density of 8×10^{14} molecules·cm^{-3} in a volume of 0.027 cm^3 giving 2.2×10^{13} target molecules of which ≈ 50 % are dissociated. Of the 1.1×10^{13} atoms produced, ≈ 40 % will undergo velocity changing collisions, and due to the branching ratio between the reactions given in equations 4 and 5, only ≈ 50% of them will have the desired velocity initially. Thus, $\approx 2 \times 10^{12}$ D atoms with the desired velocity are produced in the photolytic source volume per laser shot.

The transport of the D atoms to the crossed-beams interaction region is an important parameter of the experiment. As the distance between the photolytic volume and the scattering volume increases, the angular resolution of the D-atom beam increases, however, the D-atom beam density decreases as $1/r^2$. The distance between the nominal D-atom source point and the nominal scattering volume point in these experiments was 4.8 cm, with the D-atom beam collimated to give a nominal point source angular resolution of 5.7°.[50] The distribution of photofragment recoil directions in space is not isotropic, and is described by

$$I(\theta) = \frac{1}{4\pi}\,(1 + \beta \cdot P_2(\cos\theta)) \qquad (13)^{34}.$$

In this equation, θ is the angle between the photofragment recoil in the CM and the electric vector of the dissociation laser and $P_2(\cos\theta)$ is the Legendre polynomial of degree 2 in $\cos\theta$. Using a polarized dissociation laser, the angular distribution of photofragments resulting from a transition moment perpendicular to the diatom bond is characterized by $\beta = -1$, while for a parallel transition, $\beta = 2$. Integration of the photofragment angular distribution over the solid angle subtended by the scattering volume shows that the fraction of the D atoms subtended by the scattering volume for a perpendicular transition is 1.2×10^{-3}. Thus, the number of D atoms which may be delivered to the crossed-beams interaction region per laser shot is $\approx 2.4 \times 10^9$. These atoms will cross the the plane of the interaction region in a short time, say ≈ 1 μsec, so the instantaneous intensity will be 2×10^{15} atoms·sec^{-1}, or $\approx 2 \times 10^{17}$ atoms·sr^{-1}·sec^{-1}.

5.2 Generation of the H_2 Molecular Beam

Due to the low intensity of the D-atom beam, the H_2 molecular beam must be more intense than a typical molecular beam to obtain reasonable signal levels. There are two considerations regarding the H_2 beam intensity; (1) isotopic DH[51] increasing the background signal at m/e = 3 (DH^+, and/or $H_2 + H_2^+ \rightarrow H_3^+ + H$ [52]), and (2) the possibility of multiple collisions in the crossed-beams interaction region. The first consideration may be largely mitigated through the use of pulsed molecular beams and judicious

differential pumping of the beam source and detector chambers. The second consideration is more fundamental, though, and yields a clear upper limit to the target H_2 number density.

Using Beer's law, the H_2 density at which 10% of the incident D-atom beam reacts is calculated to be 3.5×10^{15} cm^{-3}, or 0.1 torr, for an interaction length of 0.3 cm and a reactive cross section of ≈ 1 Å^2 [53]. A more important factor, though, for detection of the DH product is the probability that it may undergo secondary velocity-changing collisions. The DH-H_2 hard-sphere collision cross section is approximately 12 Å^2 [54], while the total effective cross section has been measured to be ≈ 150 Å^2 in the 0.3 eV collision energy range[55]. Ten percent attenuation of the DH products due to hard-sphere collisions corresponds to an H_2 density of $\approx 3 \times 10^{14}$ cm^{-3}, while the same attenuation from all processes contributing to the total effective cross section occurs for H_2 densities of $\approx 2 \times 10^{13}$ cm^{-3}. Very large number densities of H_2 may easily be obtained with an unskimmed free jet. The attenuation of photolytically produced DH in the D-atom beam by the H_2 crossed beam was typically between ten and fifteen percent in the final experimental configuration. Under the experimental conditions used in the final measurements, no H_2 pressure dependence was observed in the reactive scattering TOF spectra, indicating that secondary collisions of DH product were not important. Evidently, secondary collisions that lead to a significant broadening of the product velocity distributions are better characterized by the smaller hard-sphere cross section. An H_2 density of 1×10^{14} cm^{-3} (3×10^{-3} torr) corresponds to ≈ 0.15 % of the incident D-atom beam reacting to yield DH product.

Consideration of the pumping speed and the source chamber operating pressure indicates that densities of this magnitude are obtainable with pulsed beam techniques. The throughput equation for the beam source may be written

$$\dot{n} = n \cdot S \cdot \frac{1}{f} \tag{14}$$

where n is the steady state number density in the source, S is the source pumping speed in $cm^3 \cdot sec^{-1}$, 1/f is the duty cycle of the pulsed beam and $\dot{n}$ is the number flow rate of particles into the source chamber. The duty cycle can be measured accurately by the methods of Appendix C, or approximated as a square wave of length 100 μsec and repetition rate 100 Hz. S can be determined from manufacturer-quoted pumping speeds, taking into account special features of the apparatus that may reduce S. Typical molecular beam source operating conditions are $n = 7.0 \times 10^{12}$ cm^{-3} (2×10^{-4} torr), $S = 6 \times 10^6$ $cm^3 \cdot sec^{-1}$ for H_2 with an untrapped VHS-10 diffusion pump, and $1/f \approx 100$. This yields a particle flow rate of $\approx 4 \times 10^{21}$ sec^{-1}. The ideal free jet intensity per steradian corresponding to this flow rate is given by

$$I_0 = \frac{\kappa \cdot \dot{n}}{\pi} \tag{15}$$

where κ is a peaking factor (κ = 1.38 for a diatomic molecule).[56] Thus, we get a free jet intensity of 1.8×10^{21} $sr^{-1} \cdot sec^{-1}$ in the absence of beam/skimmer interactions. For a crossed-beams interaction region of area 0.3 x 0.3 cm located 3.2 cm away from the nozzle, the intensity will be 1.5×10^{19} $cm^{-2} \cdot sec^{-1}$.

For H_2 travelling at 2.7×10^5 cm·sec^{-1} this corresponds to a density of $\approx 5 \times 10^{13}$ cm^{-3}. The peak density in a real pulsed beam will be higher than this, however, since the temporal density profile of the beam is not constant, as assumed in this calculation.

5.3 Crossed-Beams Interaction and Product Detection

The expression for the rate of collisions in two crossed molecular beams is given by

$$Z = n_D \cdot n_{H_2} \cdot v_{rel} \cdot \sigma(v_{rel}) \cdot \Delta V \qquad (16),$$

where n_D and n_{H_2} are the number densities of the two components, v_{rel} is the relative velocity associated with the collision, σ is the collision cross section, and ΔV is the volume in which the two beams interact.[57] In the case of fast D-atom collisions, $v_{rel} \approx v_D$, so this equation may be recast;

$$Z_{DH} = (n_D \cdot v_D \cdot A) \cdot n_{H_2} \cdot \sigma \cdot l = I_D \cdot (n_{H_2} \cdot \sigma \cdot l) \qquad (17),$$

where l is the collision volume length, A is the area as seen by the incident D-atom beam of intensity I_D atoms entering the interaction volume per pulse, and Z_{DH} is the number of DH products produced per pulse. Given $I_D \approx 2.4 \times 10^9$ atoms·pulse^{-1}, $n_{H_2} = 1 \times 10^{14}$ molecules·cm^{-3}, the reactive cross section σ = 1 Å^2, and l = 0.3 cm, Z_{DH} is found to be 7.2×10^6 DH/pulse. The kinematics of the D + H_2 reaction at $\approx$ 1 eV dictate that the products are scattered into $\approx 70°$ in the laboratory frame, whereas the detector effectively subtends $\approx 1.7°$. If we

assume that the products are then isotropically scattered in the entire angular range accessible in the laboratory we see that

$$N_{det} \approx f_{det} \cdot Z_{DH} \approx 4.3 \times 10^4 \text{ DH/pulse} \qquad (18)$$

enter the mass spectrometer ionizer, where f_{det} is the fraction of products which enter the detector. For the electron impact ionizer, operated at 10 mA emission, the electron flux is $I_e \approx 6 \times 10^{16}$ electrons·cm^{-2}·sec^{-1}. The fraction of molecules ionized is given by the equation

$$F_{ion} = 1 - N_f/N_0 = 1 - \exp(-\sigma_{ion} I_e \tau) \qquad (19)^{58}$$

where $\sigma_{ion} = 1$ Å^2 for $H_2 + e^- \rightarrow H_2^+ + 2\,e^-$ with an electron energy of 80 eV[59] and a residence time in the ionizer $\tau \approx (1\text{cm}/8\text{x}10^5 \text{ cm·sec}^{-1}) \approx 1\text{x}10^{-6}$ sec. This gives the fraction ionized to be $F_{ion} \approx 6 \times 10^{-6}$. If we assume T = 70% transmission through the quadrupole mass spectrometer and an ion detection efficiency = 1, we obtain the value for the number of detected DH per laser pulse;

$$N_{DH} = N_{det} \cdot F_{ion} \cdot T = (4 \times 10^4) \cdot (6 \times 10^{-6}) \cdot (0.70) \approx 0.17 \qquad (20).$$

The velocity distribution of the DH product is measured by the TOF method with ion counting. If a multichannel scaler (MCS) with a time resolution of 1 μsec is used, the collision kinematics dictate that the signal can be expected to be distributed over ≈ 110 channels, and, if it is isotropically distributed, 1.5×10^{-3} DH counts/pulse·channel can be expected. Since the

experiment can be run at 100 Hz, the final signal intensity is .15 DH count/channel·sec. After 2.8 hours ($\approx 1 \times 10^6$ pulses), 1,500 signal counts can be expected per channel. The inherent detector background is rather high, $\approx$ 1.5 kHz for m/e = 3. In the final experiments, with both molecular beams turned on, the background count rate at m/e = 3 ranged from 1.5-3.0 kHz. For an S/N = 100 , counting times of $\approx$ 36 hours would be required, assuming Poisson counting statistics.

This S/N calculation indicates that this experiment is quite difficult, yet feasible. The clearest opportunity for future improvement is in the detection efficiency for the DH product. Improvements in the efficiency of electron-impact ionizers is unlikely, but, careful optimization of the overall ionizer/quadrupole mass spectrometer system may yield improvements on the percent scale. One of the benefits of the electron-impact ionizer is that it allows for 'universal' detection. More detailed future studies on this system may require specific state-selective detection techniques.

6. D + H_2 Version I

The experimental set-up used in the first efforts to obtain the vibrational state-resolved differential cross sections for the D + $H_2 \rightarrow$ DH + H reaction is shown in Figure 2-3. In this version of the experiment both the pulsed photolytic D-atom beam and the pulsed room-temperature H_2 molecular beam propagated in the plane of rotation of the detector, while the continuous precursor DI beam was directed perpendicular to this plane. Figure 2-4 shows a kinematic diagram illustrating the CM-LAB transformation for this configuration and the laboratory angular range over

which DH(v) products are scattered. The experiment was done by measuring the TOF spectra at m/e = 3 (DH^+) relative to the photolysis laser pulse as shown in Figure 2-3. This experiment did not produce significant DH scattering signal, but it did provide valuable experience which was essential in the development of the later, successful experiments. The features of the experimental setup will be reviewed here.

6.1 Photolytic D-Atom Beam

The D-atom beam source used in these experiments consisted of a continuous free-jet DI beam crossed by unpolarized 248 nm laser light produced by a Lambda Physik EMG 103MSC KrF excimer laser. The excimer laser typically produced 150 - 200 mJ/pulse at repetition rates up to 150 Hz. The laser output was focussed to a 2 mm x 2 mm spot using a 2 m focal length Suprasil cylindrical lens and a 76 cm Suprasil spherical lens. The beam source was located above the scattering plane, with the DI beam directed downward, in the direction of a cryogenically-trapped 4" DP. A 10" DP also evacuated the source chamber. One of the primary reasons for using a continuous DI beam in these experiments was to avoid using a substance as corrosive as DI with a pulsed molecular beam source. The use of a continuous DI beam was a definite disadvantage in this inherently pulsed experiment, however. With a continuous beam, higher DI-target number densities, and higher D-atom beam intensities were accompanied by a large rise in both source pressure and effusive background emanating from the source chamber. In addition, use of the beam source at higher stagnation

pressures resulted in rapid consumption of the DI reagent, which had to be synthesized as described in Appendix D.

In these experiments the laser beam crossed the DI beam 2 to 4 nozzle diameters downstream of the nozzle aperture. With the 1.0 mm nozzle, the source was typically run with DI stagnation pressures from 2 to 6 torr, while with the 0.5 mm nozzle, stagnation pressures up to 40 torr were used. The 0.5 mm nozzle gave somewhat higher D-atom beam intensities, because the size of the beam more nearly matched the size of the photolysis laser spot. The 1.0 mm nozzle produced a beam which was significantly larger than the photolysis laser. In this case, the undissociated DI molecules outside of the laser beam only served to attenuate the photolytic D atoms. The source stagnation-pressure dependence of the D-atom TOF spectra are shown in Figure 2-5. These spectra are measured with the rotatable detector directed straight into the D-atom beam, at a LAB angle of zero degrees. The two peaks observed in the spectra are due to D atoms correlating with both ground state $I(^2P_{3/2})$ and excited state $I(^2P_{1/2})$ atoms. The laboratory (LAB) velocities corresponding to the two peaks were 1.38×10^6 cm/sec and 9.8×10^5 cm/sec. The TOF spectra shown were recorded with an older 256 channel, 1 μsec/channel MCS. In the case of H/D-atom photofragment spectra the limitations of the old scaler are readily visible, as all of the signal arrives in approximately five TOF channels. Figure 2-5 shows that, at higher pressures, significant broadening of the TOF spectra, and hence, the D-atom-beam velocity distribution occurred due to various collisional processes. The broadening of the velocity distribution is undesirable in this experiment, but also unavoidable if high intensity beams are required. An interesting interpretation of these spectra is that they constitute 'snapshots' of the

evolution of the nearly monoenergetic D-atom velocity distribution[60] as collisions occur in the photolysis volume. As the stagnation pressure is increased, the number of collisions the D atom undergoes before leaving the local high pressure region in the photolysis volume increases. A detailed analysis of this interpretation was not attempted. This effect is not likely to be due to photolysis of DI clusters, as the beam has not fully cooled when it has reached a distance of only 2 to 4 nozzle diameters from the aperture[46]. The high-pressure attenuation limit of the beam intensity could not be achieved with the continuous beam source. This is illustrated in the D-atom beam intensity pressure dependence shown in Figure 2-6. It became evident at this time that definite trade-offs between beam intensity and the quality of the beam velocity distribution would be necessary to achieve reasonable reactive scattering signal intensities.

6.2 H_2 Molecular Beam

The pulsed H_2 molecular beam was generated using a commercial piezoelectric pulsed valve (Lasertechnics model LPV), with several configurations tested. A stainless-steel conical skimmer of 1.4 mm diameter was used, sometimes in conjunction with a second, larger skimmer for better collimation. Both 1.0 mm and 0.5 mm nozzle apertures were used. The highest intensity beams were achieved with nozzle - skimmer distances of $\approx$ 2 cm. The commercial pulsed valve did not fully open the 1.0 mm aperture due to limited translation of the piezoelectric translator.[61] The sealing poppet also had a tendency to bounce, producing secondary gas pulses, particularly when the valve seal was adjusted loosely enough to produce high

intensity gas pulses. In addition, the seal was prone to developing leaks as it was formed by a thin viton sheet which became deformed much more rapidly than the O-ring seal used on the home-built valves described in Appendix B[62]. H_2 pressures up to 100 psig were used. The H_2 beam source was located in a differentially pumped source chamber evacuated by a 10" and a 4" DP, backed by a Roots-blower/mechanical pump combination. One of the key differences between this experiment and the later, successful experiments is that the pulsed beam nozzle was ≈ 5 cm from the crossed-beams interaction region, whereas in the final experiments this distance was reduced to 3 cm.

6.3 Modulated DH Background Sources

In the course of these measurements two important sources of modulated m/e = 3 background were noted. One, due to the H_2 pulsed beam, appeared at flight times long after the firing of the photolysis laser (≈ 150 μsec). This was due to scattering of isotopic impurity DH out of the pulsed beam and the eventual 'filling up' of the scattering chamber with the H_2 pulse. Only the leading edge of this signal arrives fast enough to interfere with the measurement of the DH product from the D + H_2 reaction.

The second and more troublesome source of modulated background is fast DH in the D-atom beam. Although the DI purity was typically 95-97%, impurity H atoms were detectable in the photofragment spectra. This meant that the exoergic hydrogen/deuterium abstraction reactions (9) and the corresponding H/D-atom exchange reactions could occur. The abstraction reaction occurs with no barrier and has a significant cross section (≈ 2 $Å^2$).[49] Large signals at m/e = 3 (DH^+) and m/e = 4 (D_2^+), (from the corresponding

D/DI abstraction reaction), were observed the first time the D-atom beam source was run, with the detector directed straight into the D-atom beam. These signals were found to have a quadratic dependence on source stagnation pressure, as expected for a bimolecular chemical reaction. Addition of an extra collimation slit for the D-atom beam significantly reduced the amount of this signal seen at angles greater than 10°, but some DH scattered off of the beam collimation slits and was detected at all laboratory angles, even with no secondary scattering beam present. These reactive processes produce DH with a wide range of velocities, from 1×10^6 cm/sec down to very low velocities, $<< 10^5$ cm/sec. Given the exoergicity for reactions (9) of ≈ 1.4 eV, and the nominal collision energies of 1 to 2 eV, a wide variety of DH(v,J) states may be populated.[49] This may be an important interference effect in state-selective bulk studies of $D + H_2 \rightarrow DH + H$ product state distributions. This source of modulated background will be discussed further in Section 7.2.4 and Chapter Three.

6.4 Conclusions

In spite of many efforts to improve the experiment, no measurable reactive scattering was observed during the course of this first attempt at studying the $D + H_2 \rightarrow DH + H$ reaction. These early experiments indicated that using a pulsed DI beam would be desirable, and would provide higher D-atom beam intensities as well as lower source chamber pressures and lower detector background count rates. The density of the pulsed H_2 beam in these initial experiments also appeared to be inadequate, as primary beam attenuation by the secondary beam was not detectable. This problem was later

resolved by using a better pulsed molecular beam source and placing the source closer to the crossed-beams interaction region. The experiment was also hampered by the use of a differential pumping chamber previously built for continuous-molecular-beam experiments. The lessons learned in these crude experiments set the stage for the second, successful generation of experiments.

7. D + H_2 Version II

The second generation of D + H_2 scattering experiments featured several new innovations. A basic change in the geometry of the experiment was made to employ a slow out-of-plane H_2 beam which required little collimation and provided high target densities with a small total gas load on the source chamber. Figure 2-7 shows a three-dimensional schematic view of the experimental geometry. New differential pumping chambers were designed and built to correct some of the problems encountered in the first set of experiments and to provide the flexibility necessary to allow future changes for specific photolytic-atom scattering experiments. New, high-performance pulsed-molecular-beam sources with corrosive gas capabilities were constructed. These are described in Appendix B. A cryogenic pulsed beam source, described in Appendices B and C was built to produce slow, dense beams of H_2. A custom-made 0.15 μsec resolution 4096 channel scaler was implemented[43], and a new high-power Lambda Physik EMG 202MSC excimer laser capable of providing up to 450 mJ/pulse at 248 nm and 300 mJ/pulse at 193 nm was obtained. A pile-of-plates Brewster-angle transmission polarizer was built to provide polarized light at both 248 and 193 nm. The new primary

(D atom) and secondary (H_2) source chambers and the beam source characteristics are reviewed below, and some initial $D + H_2 \rightarrow DH + H$ scattering results presented at the end of the chapter. This experiment produced high S/N scattering data. The kinematics of the $D + H_2$ reaction limited the vibrational-state resolution obtainable with this setup, however, so this was not the final experimental geometry used.

7.1 D-Atom Source Chamber

The new primary source chamber was designed to support the use of a pulsed photolysis target beam in various geometries with enhanced pumping speeds and differential pumping options. The final design consisted of an inner, removable chamber nested within a larger one. The laser/target beam interaction occurred in the small chamber (the photolysis chamber), which was evacuated by a 4" DP, with additional pumping provided in the form of a liquid-nitrogen cooled cryo-panel. The cryo-panel had a total surface area of ≈ 1000 cm^2, but only half of that was effective in pumping since the panel was located close to the chamber walls. Combined with the ≈ 600 $liters \cdot sec^{-1}$ pumping speed of the 4" DP, a total pumping speed of S ≈ 6,000 $liters \cdot sec^{-1}$ for condensible gases was achieved, assuming an ideal cryo-pumping speed of 11.9 $liters \cdot sec^{-1} \cdot cm^{-2}$. [62] The volume of the chamber is V≈ 5 liters, so a chamber pumpout time[63] of $\tau = V/S \approx 1$ msec was achieved, (ten times shorter than the 10 msec period corresponding to the 100 Hz repetition rate of the experiment). The larger chamber (the source chamber), through which the pulsed beam source entered the photolysis chamber was pumped by a 10" DP and two sets of cryo-panels. The 10" D.P. had a pumping speed of ≈ 2500

liters·sec^{-1}, while the effective cryo-panel area in the source chamber was approximately 1300 cm^2. Thus, the effective pumping speed in this chamber was S ≈ 18,000 liters·sec^{-1} for condensible species. With a volume V ≈ 40 liters a pumpout time $\tau \approx 2$ msec was obtained for this chamber. The elaborate pumping setup of these chambers was necessary to achieve 100 Hz operation of the pulsed beam with virtually no continuous effusive gas load on the main scattering chamber through the atomic beam collimation apertures.

An assembly drawing of the D-atom beam source is shown in Figure 2-8. The larger chamber served as both beam source and beam catcher in this pulsed-beam experiment. The beam reentered the source chamber through aperture B after passing through the laser interaction region. If desired, the pulsed beam could be skimmed, with the skimmer placed between the source and photolysis chambers, giving a more conventional differentially pumped target beam. This configuration proved to require consumption of too much DI reagent to be a reasonable method for the generation of high-intensity atomic beams. The inner photolysis chamber can be removed to allow future experiments using the pulsed-beam source in the same plane as the rotatable detector.

7.2 D-Atom Beam Characteristics

7.2.1 Beam Intensity

The photolytic D-atom beam was produced by irradiating the DI free jet 3 mm from the nozzle with an excimer laser focussed to a 3 x 3 mm spot. Several laser/source distances, as well as both 1.0 and 0.75 mm diameter

nozzle apertures, were tried. The 0.75 mm nozzle was used for the majority of the experiments, since the consumption of DI reagent was reduced relative to the 1.0 mm nozzle, while the D-atom beam intensity was not diminished. The pulsed DI target beam was fired first, followed by the excimer laser. By varying the time delay of the laser, different target densities could be sampled at a constant source stagnation pressure, according to the temporal profile of the pulsed-beam density. With the 0.75 mm nozzle installed, and the valve properly adjusted to give high intensity pulses, the optimum stagnation pressure was observed to be ≈ 140 torr of neat DI. No clusters were directly observable in mass-spectrometric studies of neat DI beams until stagnation pressures of ≈ 600 torr were reached, but some may have been present at lower stagnation pressures, yet not detected due to fragmentation upon electron-impact ionization. The pulsed beam/laser-time-delay dependence of the integrated D-atom intensity is shown in Figure 2-9. The levelling off of the D-atom intensity at long delay times (> 200 μsec) indicated that with the pulsed beam source, D-atom intensities limited only by the photolysis laser power and the collisional processes occurring in the photolysis volume were achievable, in contrast with the earlier continuous target-beam photolysis source. Figure 2-10 shows the photolysis laser power dependence of the D-atom beam intensity, which showed no signs of saturation even at the highest fluences used in this experiment (≈ 60 MW/cm^2).

7.2.2 Pulsed Beam/Photolysis Laser Time Delay Effects

The laser-time-delay dependence of the D-atom TOF spectra measured with laser polarization parallel and perpendicular to the direction of detection

is shown in Figures 2-11 and 2-12, respectively. The TOF spectra for unpolarized, parallel and perpendicular polarizations are shown in Figure 2-13. The discrimination between the D atoms correlated with the two spin-orbit states of the I atom is not complete, as the spectra show. This effect is due to the fact that some curve crossing occurs in the dissociation process, resulting in a loss of the ideal photofragment anisotropy. Degradation of the photofragment spatial anisotropy due to collisions in the photolysis volume also occurs. In particular, the broad component underneath the two D-atom peaks in the spectra showed no polarization dependence whatsoever. In addition to collisions of the D atoms in the source region, some of the atoms with a broad velocity distribution may be produced by the $D + D'I \rightarrow DI + D'$ exchange reaction. Previous experiments[64] using a photolytic D-atom beam generated by the photolysis of D_2S also exhibited similar beam/laser delay-time-dependent TOF broadening, which was attributed to cluster formation. H_2S clusters more easily than HI. $(H_2S)_2$ has been observed in our laboratory in pulsed free jets with stagnation pressures as low as 40 torr behind a 1 mm nozzle. In addition these previous experiments used higher D_2S stagnation pressures (1 - 2 atmospheres) and a different beam source/laser geometry, making cluster photofragmentation a more probable contaminant in those experiments. The D-atom velocity distributions used in the scattering experiments will be discussed in more detail in Chapter Three.

7.2.3 Rydberg D-Atom TOF spectra

It is well known that a variety of H/D-atom Rydberg states can be produced by electron impact.[65] The possibility exists that a highly

electronically excited species may fly straight through the mass spectrometer and either field ionize when the particle reaches the field of the -35 kV cathode, or ionize upon impact with a metal surface. With the electron-impact ionizer on, but no ion transmission (ion energy = 0 V), m/e independent Rydberg D-atom (D*) TOF spectra were observed when the D-atom beam was studied. Electron-impact excitation in the ion source produced these excited atoms. The intensity of the D* signal was linearly dependent on the ionizer emission current, and linearly dependent on the photolysis-laser power, indicating that these excited atoms were not produced by multiphoton excitation of the D atoms in the photolysis source.

Given the known velocities of the D atoms produced by photofragmentation of DI at 248 nm, it is clear that the D* atoms field ionize in the vicinity of the cathode as shown in Figure 2-2. The distance between the ionizer and the cathode is ≈ 30 cm, so fast D atoms, with a velocity of ≈ 1.35×10^6 cm/sec will traverse this distance in ≈ 22 μsec. The lifetime of high-Rydberg states scales approximately as n^3,(where n is the principal quantum number), and states with large n can survive for many microseconds.[65]

The cross section σ_{ryd} for production of D* is approximately $(0.025)\sigma_{ion}$, as determined by comparing the intensities of the integrated m/e = 2 D-atom spectra and the D* spectra. This is not a very accurate number, as no lifetime correction for the Rydberg states involved, or any assessment of the affects of the various fields present in the ionizer were made. The pulsed-beam/laser-delay-time dependence of the D* TOF spectra is shown in Figure 2-14. The delay-time dependence of the intensity of the D* signal behaved the same as that of the D atoms, as shown in Figure 2-9; the intensity levelled off between 190 and 210 μsec. D_2 and DH showed a different delay-time dependence, so

the species specific D* detection scheme showed that the D-atom m/e = 2 TOF spectra were not contaminated by significant signal from the dissociative ionization of D_2 or DH

$$D_2 + e^- \rightarrow D + D^+ + 2e^- \qquad (21)$$

in the ionizer. Although high Rydberg states of H_2 have been reported in electron-impact excitation studies[66], no evidence for these states were observed in this work. The Rydberg TOF spectra do show one important difference from the m/e=2 TOF spectra in that more of the fast D atoms are evident. This effect is due to the finite lifetime of D*, which discriminates somewhat against the slower atoms.

7.2.4 Contamination by Fast DH and D_2

In addition to the degradation of the D-atom beam velocity distribution at longer pulsed-beam/laser delay times, the amount of DH and D_2 produced by D-atom abstraction reactions in the beam source increased significantly. The delay-time dependence of the DH and D_2 intensity is shown in Figure 2-15(a). The key difference to be noted between the D_2/DH pulsed beam/laser-delay-time dependence in Figure 2-15(a) and the corresponding curve for the D atoms in Figure 2-9 is that the D-atom intensity levelled off in the 190 to 210 μsec time frame, while D_2 and DH intensity continued to rise. The standard deviations of the points in the curves shown in Figures 2-9 and 2-15(a) are approximately as large as the symbols, with 3 measurements taken at each point. Due to the high degree of precision, we can infer that the significant

differences in the shapes of these curves are indicative of photodissociation in the case of D atoms, and a bimolecular chemical reaction in the case of D_2 and DH.

Interestingly, the ratio of the D_2/DH integrated intensities is also seen to be time dependent, rising from a value of ≈ 5 at short delay times to a limiting value of 15 at longer times, as shown in Figure 2-15(b). If the different isotopic abstraction reactions all have the same cross sections, a simple kinetic analysis predicts that the D_2/DH ratio should be approximately 15 at equilibrium with DI of 97% isotopic purity.[67] The reason for the observed time dependence is not clear. Representative TOF spectra of the D_2 (m/e = 4) and DH (m/e = 3) produced under typical conditions used in the generation of the D-atom beam (DI beam/laser delay = 170 μsec, 140 torr DI beam stagnation pressure) are shown in Figure 2-16. The two large spikes seen in the DH (m/e = 3) curve are from the previously discussed D* atoms. An interesting TOF spectrum of the D_2 in the beam taken under more nearly single-collision conditions (delay 225 μsec, 40 torr DI stagnation pressure) is shown in Figure 2-17. The structure observable in this spectrum is due to the production of D_2 in several vibrational states by the D + DI abstraction reaction. These results are difficult to deconvolute due to the presence of the two nominal D-atom velocities, however. A small component of this spectrum is due to the Rydberg D atoms as shown.

The relative intensity of D vs. DH was measured to be D/DH ≈ 65. The two spectra cannot be plotted on the same scale, however, as all of the D-atom signal comes in very few channels, while the DH signal is distributed over a wide number of channels as the TOF spectra show. The electron-impact-ionization cross sections at 80 eV for DH and D_2 are similar, $\sigma_{ion} \approx 1.1$ Å^2,

whereas $\sigma_{ion} \approx .6$ Å^2 for D.[68] Taking an average D-atom velocity of $\approx 1.2 \times 10^6$ cm/sec and and average DH velocity of $\approx 5 \times 10^5$ cm/sec, the ionization probability for D versus DH can be estimated using equation 19 to be $P_D/P_{DH} \approx 0.2$. The detection efficiency of D^+ is lower than DH^+ with the Daly detector, due to the different secondary electron yield of the two species, but this quantity is difficult to quantify and presumably dependent on the detector operating conditions. Thus, a lower limit for the D/DH ratio in the D-atom beam is ≈ 325, with $D/D_2 \approx 65$ under the conditions used in the scattering experiments.

7.3 H_2 Beam Source Chamber

The H_2 beam source chamber was designed to support both in and out-of-plane H_2-beam geometries. The source was pumped by a 10" DP backed by a Roots-blower mechanical-pump combination, giving a pumping speed of S $\approx$ 6,000 liters·sec^{-1} for H_2. For this iteration of the D + H_2 experiments, the 4" differential DP was replaced by a He-closed-cycle refrigerator (Air Products CS-202) for the purpose of cooling the H_2-molecular beam down to temperatures as low as 20K. The primary goal for the H_2 beam source in this experiment was to establish high H_2 densities to increase the intensity of the reactively scattered DH. The approach taken was similar to experiments done in Toennies' group (ref. 19), in that a slow H_2 beam was directed perpendicular to the primary beam/detector rotation plane. For scattering experiments involving interaction of a fast primary beam with a slow secondary beam such a geometry does not cause a significant detection problem except in cases where the secondary beam particles or the detected

products are very heavy. If the product CM recoil velocity is less than the out-of-plane component of the velocity of the CM of the colliding particles, that product will not be observed. The kinematic diagram for this collision geometry does have some problems, though, as Figure 2-18 shows. For the D + H_2 reaction, both forward- and backward- scattered products in the CM[69] will only be detectable at LAB angles near and in the D-atom beam, a situation which is not tenable with mass-spectrometric molecular-beam detectors.

The out-of-plane cryogenic H_2 beam was mounted in a stainless-steel box welded onto the front of the source chamber, as shown schematically in Figure 2-7 and in the assembly drawing, Figure 2-8. Two arrangements for this source were used. Initially an uncollimated free jet was used, with the 0.75 mm nozzle/crossed-beams interaction region distance set to 10 mm. In the second arrangement, shown in the assembly drawing Figure 2-8, a teflon shield with a copper collimator attached to the nozzle was installed to give higher angular resolution in the scattering studies. In this arrangement the nozzle/collimator distance was 15 mm and the nozzle/interaction region distance was 20 mm. After the beam passed through the crossed-beams interaction region it entered a large aperture that was intended to serve as a beam catcher. In a pulsed beam experiment, deflection shields of this sort can often serve to 'push back' beam-related background effects in time, however, in this experiment H_2 scattering out of the pulsed beam itself appeared to be one of the dominant sources of time-dependent background, and these efforts had little effect on the background. A fast ion gauge (FIG) was installed in the chamber to continuously monitor the H_2-pulsed-beam intensity, as the cold (40 K) beam had a tendency to clog as pump oil from the surrounding chamber froze onto it. Even after shielding the region with 80 K cryo-panels,

clogging of the nozzle would occur over a 6 to 8 hour time period. The FIG was invaluable in detecting the onset of clogging.

7.4 H_2 Beam Characteristics

The properties of the cryogenic H_2 beams are discussed in Appendix C. At a nominal source temperature of 40 K , the peak H_2 beam velocity is $\approx 9.5 \times 10^4$ cm/sec. Even with mild expansion conditions (H_2 stagnation pressures ranging from 45 to 90 torr), clustering of the H_2 is an important complication with the beam source held at such low temperatures. Although clusters were not directly observed to be a significant component of the skimmed, collimated 40 K H_2 beam, some were undoubtedly present. The presence of clusters in the H_2 beam may have perturbed these D + H_2 measurements. Implementation of the cryogenic H_2 beam certainly satisfied one of the chief goals of this round of experiments; attenuation of the incident D-atom beam up to 25% was possible. At such high attenuation, multiple collisions in the interaction region began to have an affect on the DH TOF spectra, so care had to be taken to keep the attenuation to less than 10%.

7.5 Modulated DH Background Sources

The same modulated background sources present in the first D + H_2 experiments continued to be a problem in this round of experiments. Laser correlated DH gave large signals at angles less than 15° from the primary beam, with no secondary beam on. Signal at long flight times from the H_2 molecular beam was likewise a problem at all LAB angles. This signal

primarily arrived after the scattered products arrived in the detector, although the separation in time scales was not as good as with the room-temperature H_2 beam. In addition, due to the high target densities (approaching 10^{15} cm^{-3}), slow signal due to multiple collisions of the DH product and possible elastic and inelastic scattering of the fast DH in the D-atom beam off of the H_2 was an added complication. Detailed studies of this crossed-beams-correlated background were not made until the final round of experiments described in Chapter Three.

One important modification in the detection scheme was made to reduce the steady state m/e = 3 signal in the detector. A chopper was mounted on front of the detector in the same configuration as used in the measurement of molecular-beam velocity distributions. Two 6.4 mm wide slots were cut in the chopping wheel. A small tube was mounted on the UHV detector gate valve which came within < 1 mm of the chopping wheel. The wheel was synchronously spun at 50 Hz, opening the detector at a frequency of 100 Hz, with the 4 mm detector aperture being fully open for ≈ 70 μsec each time the detector opened. The chopping wheel was located ≈ 4 cm from the beam crossing region, and all scattered products from the $D + H_2 \rightarrow DH + H$ reaction passed through the plane of the chopper within 20 μsec. Thus the entire experiment was run at a specific phase relative to the chopper, and the detector was effectively open only when the products were arriving. In practice, the detector was not shut off the rest of the time, but the conductance of the detector aperture was drastically reduced. This modification allowed the $D + H_2$ scattering experiments to be run with a detector background of 1.5 to 3 kHz at the beginning of a scattering

experiment, not much higher than the inherent detector m/e = 3 background count rate.

7.6 D + H_2 → DH + H Scattering Results / Conclusions

The modifications to the apparatus described in this section produced D + H_2 → DH + H scattering data with S/N ratios in good accord with the calculations presented earlier in this chapter. As an example, a raw DH (m/e = 3) product TOF spectrum at a LAB angle of 20° is shown in Figure 2-19. This TOF spectrum shows evidence for DH(v=1) product, as the fits in Figure 2-20 indicate. The two curves fit to the spectrum in Figure 2-19 show the contributions from the D-atom-beam correlated DH background (the 'fast' component) and the H_2-beam-correlated background (the 'slow' component). The fit for the H_2-beam-correlated background shows that a significant amount of fast signal was observable from this source with the cryogenic beam as opposed to the room-temperature H_2 beam results described in Chapter Three. These contributions were obtained by fitting the measured signal resulting from the D-atom beam and H_2 beams separately, then scaling the results to the raw TOF, with the constraint that the resultant signal should go to zero at flight times longer than kinematically allowed. These background effects will be discussed in more detail in Chapter Three. TOF spectra were taken at several other angles, however, these efforts were not carried through to completion, as it was clear that more success could be gained by improving the experiment as described below and in Chapter Three.

The stripped TOF spectrum is compared with the fully-converged three-dimensional quantum scattering calculations of Zhang and Miller[70] in Figure 2-20. Figure 2-20(a) shows the results of a Monte Carlo simulation (see Appendix A) of the experiment using Zhang and Miller's CM differential cross section calculations for the D + H_2 reaction. The fit shows some deficiencies for products with low CM recoil velocities, and in the long tail on the data. Using the complete results of Chapter Three, the theoretical DCS's were modified to fit the data, and Figure 2-20(b) shows the fit using the modified DCS. There is seen to be a much better agreement between this fit and the data, but the backward-scattered DH(v=0) signal is still not fit well, and the data shows a slow tail which is not explained by this DCS. The cryogenic H_2 beam may have been contaminated with some H_2 clusters so these results should not be over-interpreted.

These results served the important role of illustrating that this experiment was feasible. The quality of the spectra with respect to the resolution of DH(v=1) product in the TOF was somewhat disappointing. It became clear that the better kinematics of the in-plane scattering experiment with a room-temperature supersonic beam would provide a better opportunity for resolution of the DH (v=1) product, as consideration of the kinematic diagrams Figures 2-4 and 2-18 show. Due to the azimuthal symmetry of the scattering with respect to the relative velocity vector in crossed-molecular-beams experiments[71] there is a buildup of signal intensity where the product recoil vector lies along the relative velocity vector. In the room temperature H_2-beam in-plane experiment, the backward-scattered DH(v=0)/DH(v=1) products can be detected at these kinematically enhanced points. In any case, the large modulated background source of DH in the D-

atom beam made it desirable to move the scattered signal away from the D-atom beam. The results of Buntin, Giese and Gentry[30] had also been published by this time, which unambiguously showed that good DH(v=1)/DH(v=0) resolution was possible in the in-plane experiment. Thus, the experiment was modified to reintroduce the original in-plane H_2 beam geometry with several improvements. With the high-duty-cycle pulsed-beam apparatus, it was felt that measurement of the complete differential cross section for the D + H_2 reaction at 0.53 and 1.01 eV would be possible. This final modification proved to be quite successful, as the results presented in Chapter Three will show.

[1] R.W. Wood, Proc. Roy. Soc. **A100**, 455 (1920) and Proc. Roy. Soc. **A102**, 1 (1922).

[2] E. Speth, Rep. Prog. Phys., **52**, 57 (1989).

[3] R. Wolfgang , Prog. Reaction. Kin., **3**, 97 (1965).

[4] R.R. Williams and R.A. Ogg, Jr., J. Chem. Phys., **15**, 691 (1947).

[5] K.P. Huber and G. Herzberg, Molecular Spectra and Molecular Structure, IV. Constants of Diatomic Molecules, Van Nostrand, Reinhold and Co., New York (1979), p. 240.

[6] F. Rosebury, Handbook of Electron Tube and Vacuum Techniques, Addison-Wesley, New York, (1965), pp. 548-558.

[7] Norman F. Ramsey, Molecular Beams, Oxford Univ. Press, Oxford, (1956), Ch. II, p.21.

[8] S. Datz and E.H. Taylor, J. Chem. Phys., **39**, 1896 (1963).

[9] a). J. Geddes, H.F. Krause and W.L. Fite, J. Chem. Phys., **56**, 3298 (1972), *ibid.*, **42**, 3296L (1970), *ibid.*, **59**, 566E (1972).

b). W.L. Fite and R.T. Brackmann, in Atomic Collsion Processes, ed. M.R.C. McDowell, North Holland, Amsterdam (1964), p. 955.

[10] a). G.H. Kwei, V.W.S. Lo, and E.A. Entemann, J. Chem. Phys., **59**, 3421 (1973).

b). G.H. Kwei and V.W.S. Lo, J. Chem. Phys., **72**, 6265 (1980).

[11] J.D. MacDonald, P.R. LeBreton, Y.T. Lee and D.R. Herschbach, J. Chem. Phys., **56**, 769 (1972).

[12] H. Haberland and K. Schmidt, Chem. Phys., **2**, 342 (1973).

[13] J.W. Hepburn, D.Klimek, K.Liu, R.G. MacDonald, F.J. Northrup, and J.C. Polanyi, J. Chem. Phys., **74**, 6226 (1981).

[14] J.B. Anderson, R.P. Andres, and J.B. Fenn, Adv. Chem. Phys., **10**, 275 (1966).

[15] J.P. Toennies, W. Welz and G. Wolf, J. Chem. Phys. **61**, 2461 (1974).

[16] a). M. Vodegel, Ph. D. Thesis, Goettingen, (1988).

b). F.E. Davidson, G.L. Duncan and R. Grice, Mol. Phys., **44**, 1119 (1981).

c). E.J. Murpy and J.H. Brophy, Rev. Sci. Instrum., **50**, 635 (1979).

[17] W.S. Young, W.E. Rodgers, and E.L. Knuth, Rev. Sci. Instrum., **40**, 1346 (1969).

[18] K.R. Way, S-C. Yang, and W.C. Stwalley, Rev. Sci. Instrum., **47**, 1049 (1976).

[19] R. Goetting, H.R. Mayne and J.P. Toennies, J. Chem. Phys., **85**, 6396 (1986).

[20] J.F. Garvey and A. Kuppermann, Rev. Sci. Instrum., **57**, 1061 (1986).

[21] This is in reference to the source used in ref. 19.

[22] H.Pauly and J.P. Toennies, Methods of Experimental Physics, Atomic Interactions, Part A, ed. by B. Bederson and W.L. Fite, Academic Press, New York (1968), Ch. 3.1, p. 254.

[23] J.B. Anderson, R.P. Andres, and J.B. Fenn, Adv. At. Mol. Phys., **1**, 345 (1965).

[24] W.R. Gentry, D.J. McClure and C.H. Douglass, Rev. Sci. Inst., **46**, 367 (1975).

[25] B. Van Zyl, N.G. Utterback, and R.C. Amme, Rev. Sci. Inst., **47**, 814, (1976).

[26] W. Aberle, B. Brehm and J. Grosser, Chem. Phys. Lett., **55**, 71 (1978).

[27] B. Van Zyl and M.W. Gealy, Rev. Sci. Inst., **57**, 359 (1986).

[28] A. Kuppermann and J.M. White, J. Chem. Phys., **44**, 4352 (1966).

[29] G.W. Flynn and R.E. Weston, Jr., Ann. Rev. Phys. Chem., **37**, 551 (1986).

[30] S.A. Buntin, C.F. Giese and W.R. Gentry, J. Chem. Phys., **87**, 1443 (1987).

[31] R.D. Clear, S.J. Riley and K.R. Wilson, J. Chem. Phys., **63**, 1340 (1975).

[32] C.E. Moore, Atomic Energy Levels, NBS Circular 467, Vol. III, p. 106 (1958), and Vol. II, p. 159 (1952).

[33] G.N.A. Van Veen, K.A. Mohamed, T. Baller and A.E. DeVries, Chem. Phys., **80**, 113 (1983).

[34] R.N. Zare, Mol. Photochem., **4**, 1 (1972).

[35] J.H. Ling and K.R. Wilson, J. Chem. Phys., **65**, 881 (1976).

[36] S. Datz and E.H. Taylor, J. Chem. Phys., **25**, 389 (1956).

[37] Y.T. Lee, J.D. McDonald, P.R. LeBreton and D.R. Herschbach, Rev. Sci. Inst., **40**, 1402 (1969).

[38] Y.T. Lee, Chemica Scripta, **27**, 215 (1987).

[39] R.K. Sparks, Ph. D. Thesis, University of California, Berkeley (1979).

[40] a) N.F. Daly, Rev. Sci. Inst., **31**, 264 (1960).

b) H.M. Gibbs and E.D. Commins, Rev. Sci. Inst., **37**, 1385 (1966).

[41] G.O. Brink, Rev. Sci. Inst., **37**, 857, 1626 (1966).

[42] The transmission improvement was found to be ≈ 10 % in going from the 4 MHz Model 012-11 High-Q head at 55 V ion energy to the 5 Mhz Model 012-10 at 100 V.

[43] Built at the Lawrence Berkeley Laboratory. See P.S. Weiss, Ph.D. thesis, U. C. Berkeley, 1986. The MCS can be operated with a dwell time of 0.10 μsec, however, the dead time between channels starts to become significant.

[44] Based on studies of the polarization dependence of HI and CH_3I photodissociation. Brewster-angle-stack transmission polarizers are discussed in Handbook of Optics, ed. W.G. Driscoll, McGraw-Hill, New York, (1978), § 52, pp. 10-88 - 10-96.

[45] The absorption cross section for DI at 248 nm is $\approx 4 \times 10^{-19}$ cm^2. See J.F. Ogilvie, Trans. Farad. Soc., **67**, 2205 (1971).

[46] D.R. Miller in Atomic and Molecular Beam Methods, Vol. I, ed. G. Scoles, Oxford Univ. Press, London, (1988), Ch.2, p. 18.

[47] Using the Van der Waals' radii $r_H = 1.2$ Å and $r_I = 2.15$ Å, CRC Handbook of Chemistry and Physics, 61st Edition, R.C. Weast, ed., CRC Press, Boca Raton, Florida, (1980) p. D-194.

[48] J. B. Hasted, Physics of Atomic Collisions, 2nd Ed., American Elsevier Pub., New York (1972) ,pp. 11-15.

[49] P.M. Aker, G. Germann and J.J. Valentini, J. Chem. Phys., **90**, 4795 (1989).

[50] This is the full angle subtended by the scattering volume at a point in the D-atom source volume.

[51] The natural abundance of D is 0.015%, therefore the abundance of DH in H_2 should be 0.03%, or 300 ppm. CRC Handbook of Chemistry and Physics, 61st Edition, R.C. Weast, ed., CRC Press, Boca Raton, Florida, (1980) p. B-259.

[52] The cross section for the reaction $H_2 + H_2^+ \rightarrow H_3^+ + H$ is ≈ 70 $Å^2$ at collision energies below 1 eV (C.F. Giese, W.B. Maier II, J. Chem. Phys., **39**, 739 (1963). Goetting , Mayne and Toennies[19] attributed a significant amount of the m/e = 3 background in their experiment to this process. It seems unlikely that low energy collisions of this sort would dominate the H_2-H_2^+ collisions in the ion source, from which the ions are extracted at 100 V. In addition, strong background differences observed in para-H_2 vs. normal-H_2 in our experiments (see Chapter Three) show that the beam-

related background at m/e = 3 was predominately from isotopic DH in the H_2 beam.

53 A total reactive cross section of 1 $Å^2$ at a collision energy of 1 eV for the reaction $H + D_2 \rightarrow DH + H$ has been reported by K. Tsukiyama, B. Katz, and R. Bersohn, J.Chem. Phys., **84**, 1934 (1986). The cross section for the reaction $D + H_2 \rightarrow DH + H$ at a collision energy of 0.8 eV has been reported to be 0.8 $Å^2$ (see D.L. Phillips, H.B. Levene, and J.J. Valentini, J. Chem. Phys., **90**, 1600 (1989)).

54 A.K. McMahan, H. Beck, and J.A. Krumhansl, Phys. Rev. A, **9**, 1852 (1974).

55 R. Gengenbach, Ch. Hahn, W. Schrader and J.P. Toennies, Theoret. Chim. Acta (Berl.) **34**, 199 (1974).

56 D.R. Miller,in Atomic and Molecular Beam Methods, Vol 1., Oxford Press, London, (1988), Ch. 1, p. 33.

57 Y.T. Lee, in Atomic and Molecular Beam Methods, Vol 1., Oxford Press, London, (1988), Ch. 22, p. 553.

58 W.E. Quinn, A. Pery, J.M. Baker, H.R. Lewis, N.F. Ramsey, and J.T. LaTourrette, Rev. Sci. Inst., **29**, 935 (1958).

59 Sanborn C. Brown, Basic Data of Plasma Physics, 1966, 2nd Ed., The MIT Press, Cambridge, MA (1967), p. 141.

60 a). R.N. Porter, J. Chem. Phys., 45, 2284 (1966).

b). A. Kuppermann, J. Stevenson and P. O'Keefe, Disc. Farad. Soc., **44**, 46 (1967).

61 D. Proch and T. Trickl, Rev. Sci. Inst., **60**, 713 (1989).

62 S. Dushman, Scientific Foundations of Vacuum Technique, 2nd Ed., J. Wiley and Sons, New York, (1969), p. 91.

[63] τ is the time for the pressure to drop by 1/e. See W. R. Gentry, in Atomic and Molecular Beam Methods, Vol 1., Oxford Press, London, (1988), Ch. 3, p. 57.

[64] S.A. Buntin, Ph.D. thesis, Univ. of Minnesota, (1987).

[65] S. Fenieulle and P. Jacquinot, Adv. At. Mol. Phys., **17**, 99 (1981).

[66] J.A. Schiavone, K.C. Smyth and R.S. Freund, J. Chem. Phys., **63**, 1043 (1975).

[67] Both of the reactions (9) yield DH, increasing the final concentration relative to D_2.

[68] Atomic Data, **1**, p. 51 and p.24, (1969).

[69] Forward-scattering is typically defined to be CM angles from 0 - 90° , measured relative to the incident atom velocity in the CM, whereas back-scattering corresponds to angles from 90 - 180° in the COM.

[70] J.Z.H. Zhang and W.H. Miller, J. Chem. Phys., **91**, 1528 (1989).

[71] R.B. Bernstein, Chemical Dynamics via Molecular Beam and Laser Techniques, Oxford Univ. Press, New York (1982), pp. 68 - 73.

Chapter Two Figure Captions

Figure 2-1: Schematic diagram of a photolytic-atomic-beam scattering experiment. The photolysis laser beam crosses a photolytic atom precursor beam in a remote chamber. The collimated photolytic atoms then cross a target beam, with the scattered products detected as a function of laboratory angle Θ_{Lab}.

Figure 2-2: Schematic diagram of the triply differentially pumped quadrupole-mass-spectrometer detector. The three pumping regions I, II and III are indicated. Products are scattered from the crossed-beams interaction region at COR (the center-of-rotation) through a set of apertures, into the electron-impact ion source ION in region III. The product ions are then extracted, mass selected with the quadrupole mass spectrometer QPMS, and counted with the Daly-type scintillation ion detector as discussed in the text. The neutral particle time-of-flight (TOF) is measured over the distance d_n. Fast neutrals excited to high Rydberg states by electron-impact in the ion source may fly straight through the QPMS and ionize in the field of the high voltage cathode C, giving a TOF corresponding to the distance d_R.

Figure 2-3: Schematic diagram of the first iteration of the D + H_2 scattering experiments. A data acquisition cycle was started by firing the H_2 pulsed beam PV. After a variable delay, the excimer laser photodissociated the DI precursor. Some of the fast D atoms produced were then collimated, subsequently colliding with the H_2 beam at the

COR of the detector. Product DH scattered at LAB angle Θ_{LAB} then entered the detector, and the TOF of the DH was then recorded as a function of time after the laser shot with the multi-channel scaler (MCS).

Figure 2-4: Kinematic diagram for $D + H_2 \rightarrow DH + H$ collisions at a nominal collision energy of 1.01 eV. The velocity of the center-of-mass (CM) of the colliding particles is $\mathbf{V}_{cm}$. The relative velocity of the particles in the CM frame is the vector drawn between the tips of the $\mathbf{V}_{H2}$ and the $\mathbf{V}_{D}$ vectors. The maximum CM recoil velocities for DH(v=0,1 and 2) products are shown as circles centered on the tip of $\mathbf{V}_{cm}$.

Figure 2-5: Stagnation pressure dependence of the D-atom beam TOF spectra with the continuous DI target beam. The curves correspond to;

—— ; 40 torr DI

····· ; 20 torr DI, and

- - - - ; 10 torr DI.

Figure 2-6: Stagnation pressure dependence of the integrated D-atom beam intensity. The deviation from linearity at low pressures is due to the transition between effusive and supersonic flow as the stagnation pressure increases. Higher stagnation pressures could not be reached with the continuous DI beam source due to pumping speed limitations.

Figure 2-7: Schematic view of the second generation of $D + H_2 \rightarrow DH + H$ scattering experiments. The labels correspond to; 1) D-atom beam; 2) scattered DH product entering the electron-impact ionizer in the detector; 3) cryogenically cooled H_2 molecular beam, directed out of the plane of detector rotation; 4) DI molecular beam; 5) excimer laser beam; and 6) liquid-N_2-cooled cryo-panel.

Figure 2-8: Assembly drawing (side view) of the pulsed photolytic D-atom beam source/cryogenic H_2 beam source scattering experiment. Seven effective chambers are shown; (1) the photolysis-target beam source chamber; (2) the photolysis chamber; (3) the lower part of chamber (1); (4) H_2 beam source chamber; (5) scattering chamber; (6) H_2 beam catcher chamber; and (7) apparatus main chamber through which products fly into the rotatable detector. Chambers (4) and (5) and (6) are only separated by simple deflector shields, and are thus only separated on the time scale of the pulsed-molecular-beam duration.

The photolysis target is produced by the pulsed valve C. The target beam interacts with the excimer laser (which travels into the plane of the paper in this drawing) in chamber (2) at D, then flies into chamber (3) through aperture B. Cryopumping is provided in chambers (1) - (3) by the liquid-N_2-cooled cryo-panels marked A. Recoiling photolytic atoms are defined by the aperture E, then enter the scattering chamber (5) through slits J, crossing the cryogenically cooled H_2 beam at I. Scattered products then fly out of the scattering chamber through the slits J, and into the detector.

The H_2 pulsed-beam source F enters chamber (4), where it is cooled with a He closed-cycle-refrigerator cooled OFHC Cu block G. The beam is then collimated by an aperture mounted in a teflon wall H. The H_2 beam then left the scattering chamber through aperture K. The intensity of the cooled H_2 beam was monitored with a Fast Ion Gauge, L.

Figure 2-9; The pulsed beam/laser-delay-time dependence of the D atom beam intensity for a source stagnation pressure of 140 torr DI.

Figure 2-10; The photolysis-laser power dependence of the D atom beam intensity under standard experimental conditions. No saturation of DI photodissociation was observed. The dashed line corresponds to D atoms produced in the photodissociation yielding $I(^2P_{1/2})$. The solid line corresponds to D atoms produced in conjunction with $I(^2P_{3/2})$.

Figure 2-11; Pulsed beam/laser-delay-time dependence of the D atom TOF spectra taken with the laser E vector parallel to the direction of detection: (a) 140 μsec, (b) 170 μsec, (c) 190 μsec, and (d) 210 μsec.

Figure 2-12; Same as Figure 2-11, but with E perpendicular to the direction of detection.

Figure 2-13; D atom TOF spectra illustrating the relative intensity of D atom beams with photolysis laser (a) unpolarized, (b) polarized 'parallel' as in Fig. 2-11, and (c) polarized 'perpendicular' as in Fig. 2-12. The pulsed

beam/laser delay time is 170 μsec. The same incident laser power was used in these spectra, so the actual fluence reaching the DI beam is approximately a factor of 2.2 higher in (a).

Figure 2-14; Pulsed beam/laser-delay-time dependence of the Rydberg D atom TOF spectra with an unpolarized dissociation laser; (a) 140 μsec, (b) 170 μsec, (c) 190 μsec, and (d) 210 μsec.

Figure 2-15; (a) Pulsed beam/laser-delay-time dependence of the intensity of the DH and D_2 recoiling from the photolysis volume. The solid line corresponds to the D_2 yield. The dashed line corresponds to the DH yield.

(b) Ratio of D_2/DH integrated signal as a function of pulsed beam/laser-delay time.

Figure 2-16; TOF spectra of D_2 (m/e = 4) ; ——— and DH (m/e = 3) ; ····· recoiling from the photolysis volume under standard D atom beam operating conditions.

Figure 2-17; TOF spectrum of D_2 (m/e = 4) recorded with a lower DI target density. This spectrum was recorded for 6 hours (2×10^6 laser shots). The points show the raw data, with the solid curve showing the data after correction for the Rydberg atom contamination, which is shown as the dashed curve.

Figure 2-18; Kinematic diagram for the $D + H_2 \rightarrow DH + H$ experiment at 0.95 eV. In this configuration, the H_2 beam, with a velocity of $\approx 9.5 \times 10^4$ cm/sec, is directed out of the plane of the paper, and the relative velocity vector lies on top of the D atom velocity vector V_D, slightly out of the plane of the paper. The projection of the velocity of the CM, v_{cm}, onto the plane of detection is shown.

Figure 2-19; Raw TOF spectrum of DH (m/e = 3) from the $D + H_2 \rightarrow DH + H$ reaction at a LAB angle of 20°. Modulated background components due to the H_2 beam (– · – · –) and DH in the primary beam (- - - - -) are shown, with the sum of these two contributions shown as the solid line.

Figure 2-20; (a) Stripped TOF spectrum at 20°. The fit to the spectrum is a result of Monte Carlo simulation of the experiment with the theoretical results of Zhang and Miller. The scattered points are the data, the solid line the total fit from the simulation, with the contributions from DH (v=0) given by (- - - -) and DH (v=1) given by (– · – · –).

(b) The fit shown here is obtained using the best-fit DCS from the results in Chapter Three.

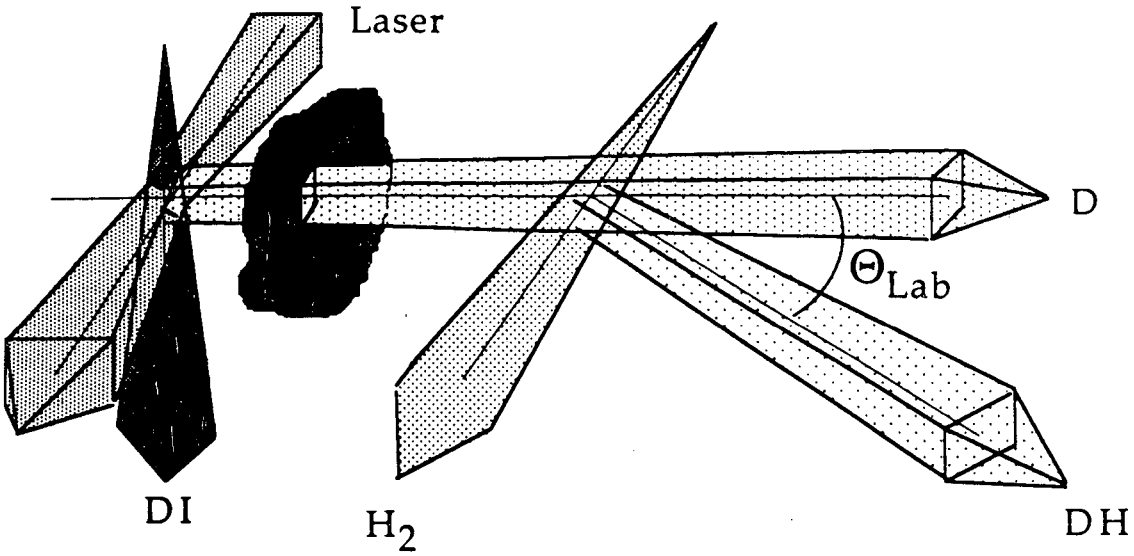

XBL 8911-4011

Figure 2

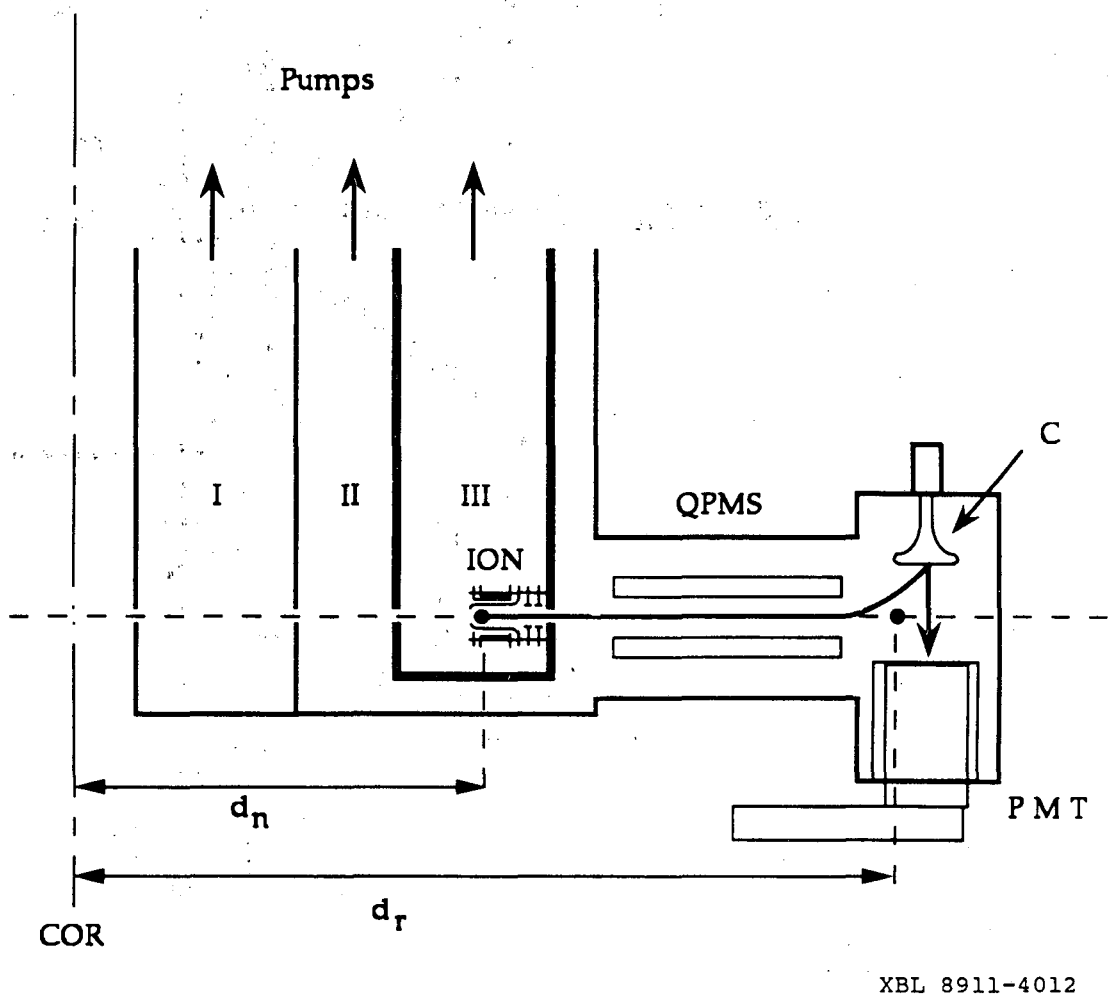

Figure 2 - 2

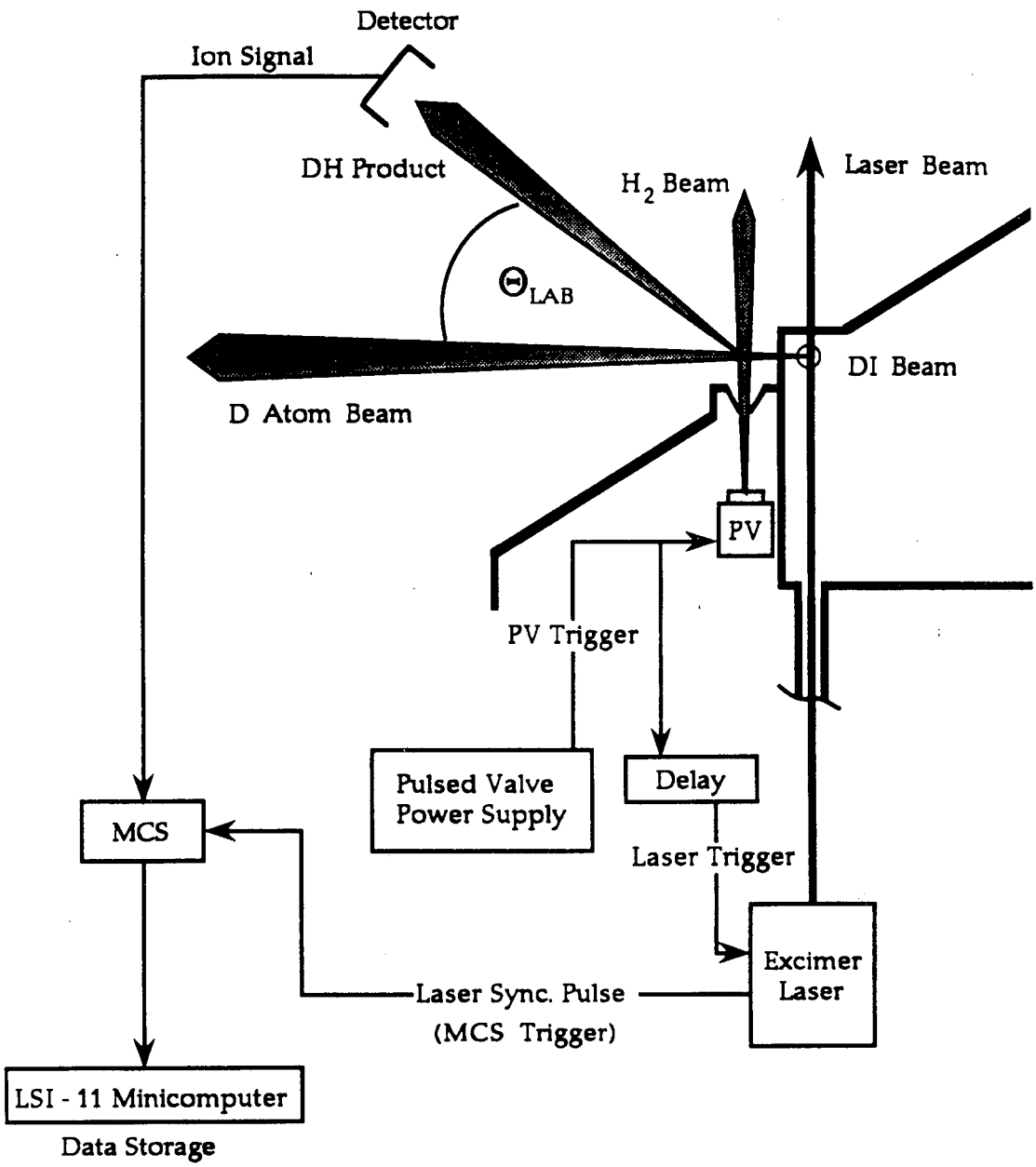

XBL 8911-4013

Figure 2 - 3

$$D + H_2 \rightarrow \underline{DH} + H$$

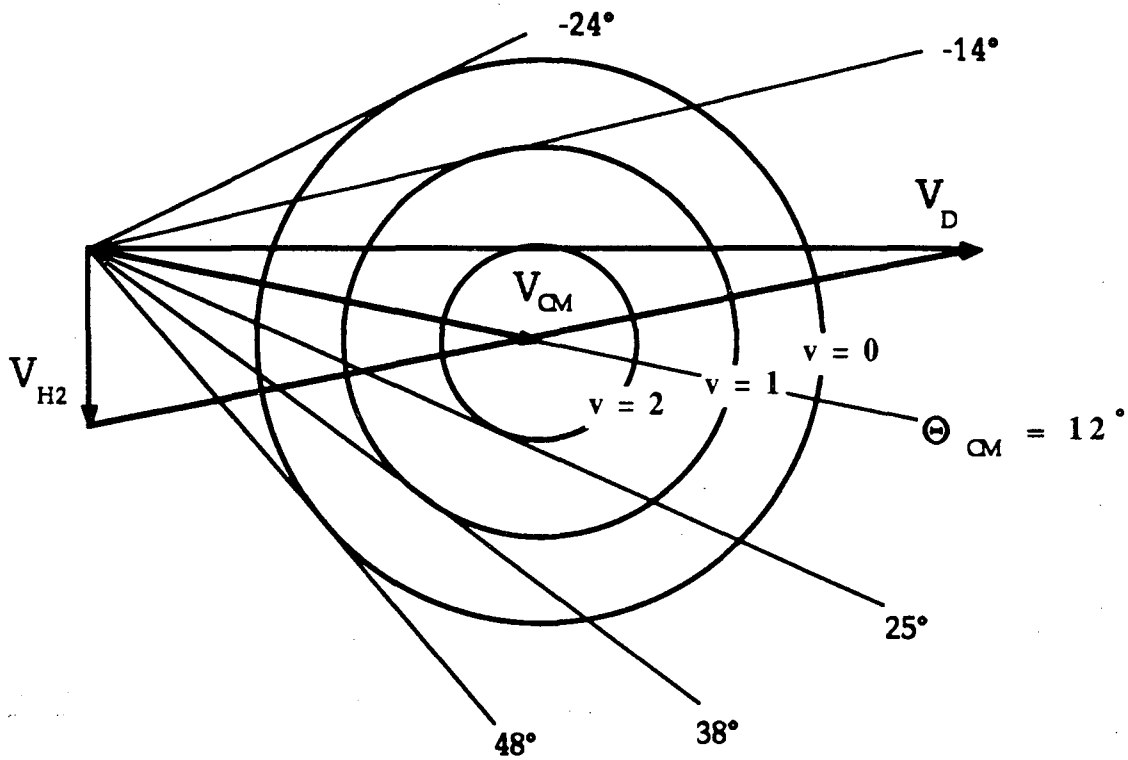

XBL 8911-4014

Figure 2 - 4

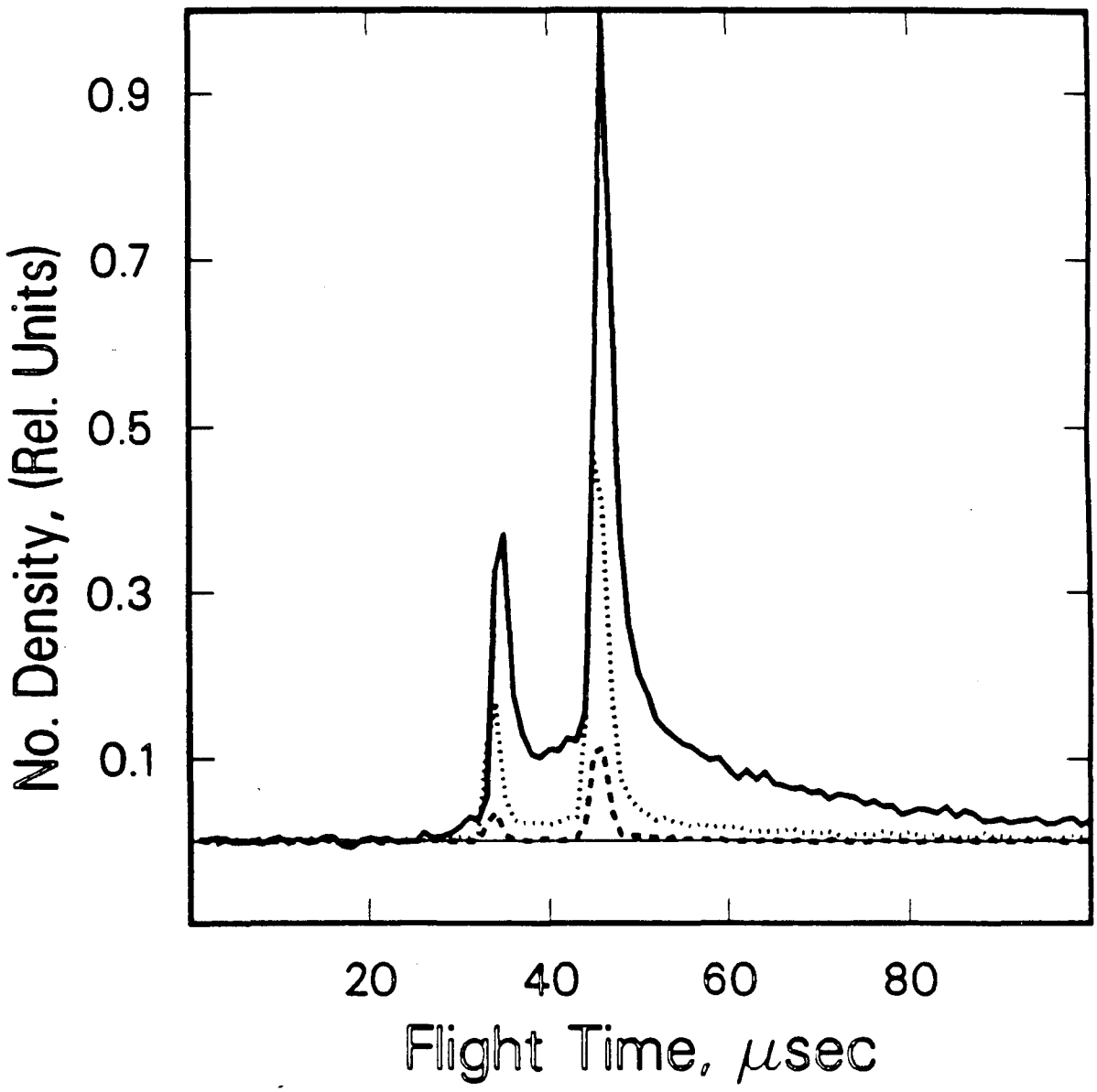

XBL 8911-4015

Figure 2 - 5

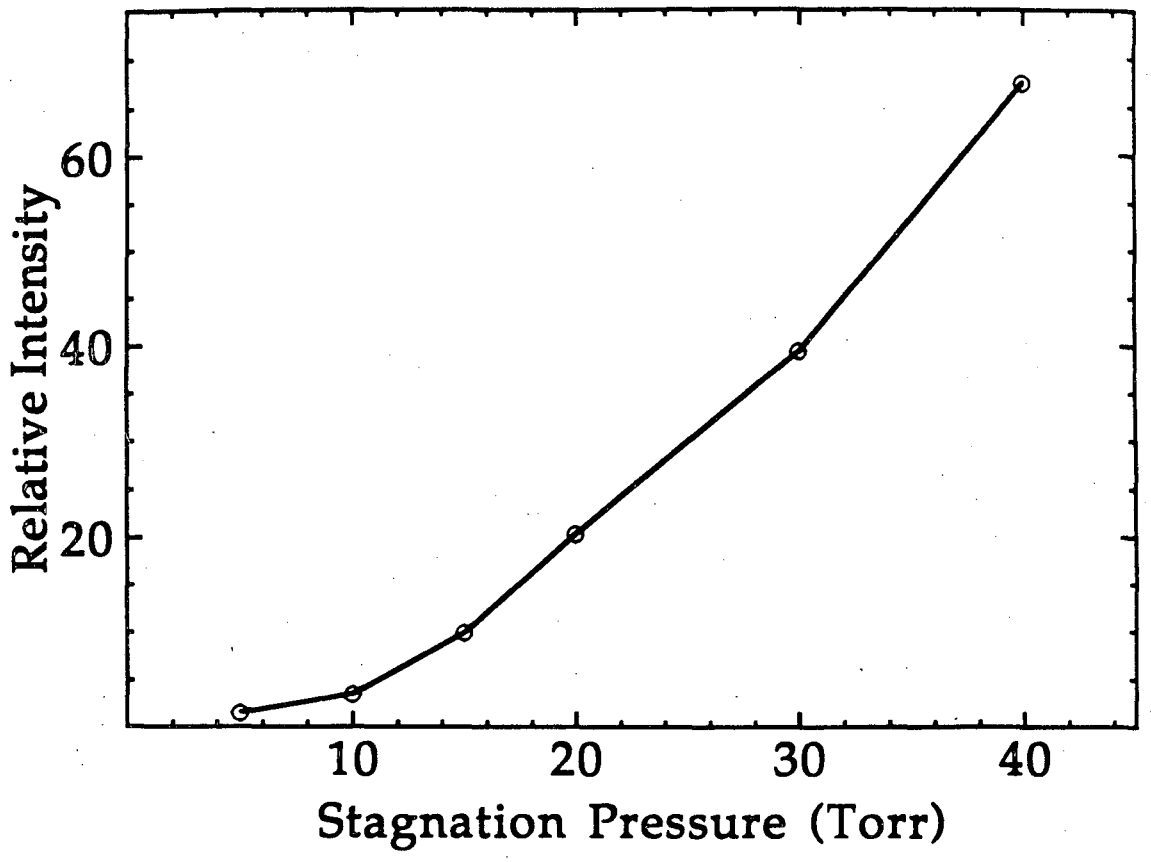

XBL 8911-4016

Figure 2 - 6

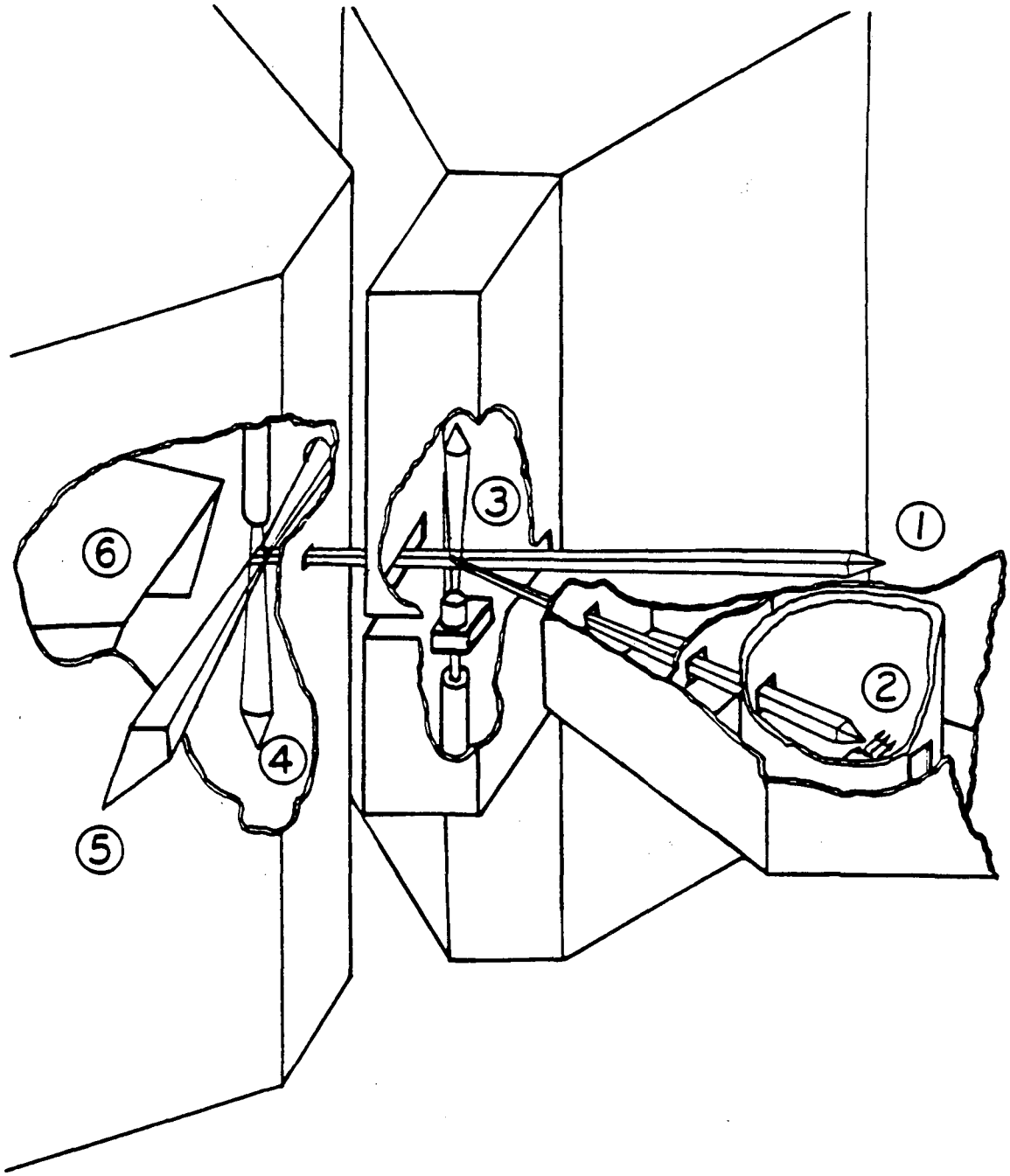

XBL 8911-4017

Figure 2 - 7

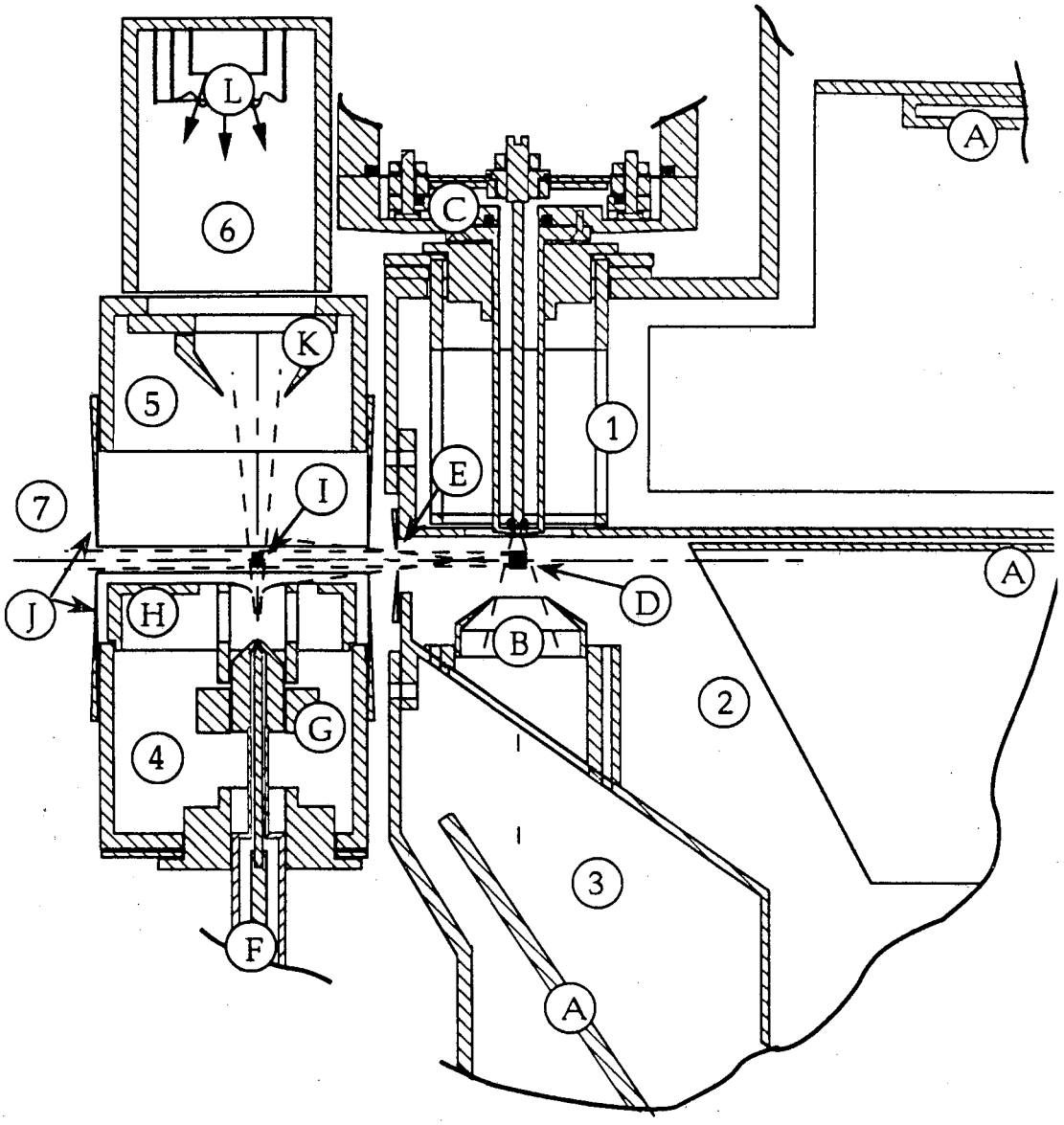

XBL 8911-4018

Figure 2 - 8

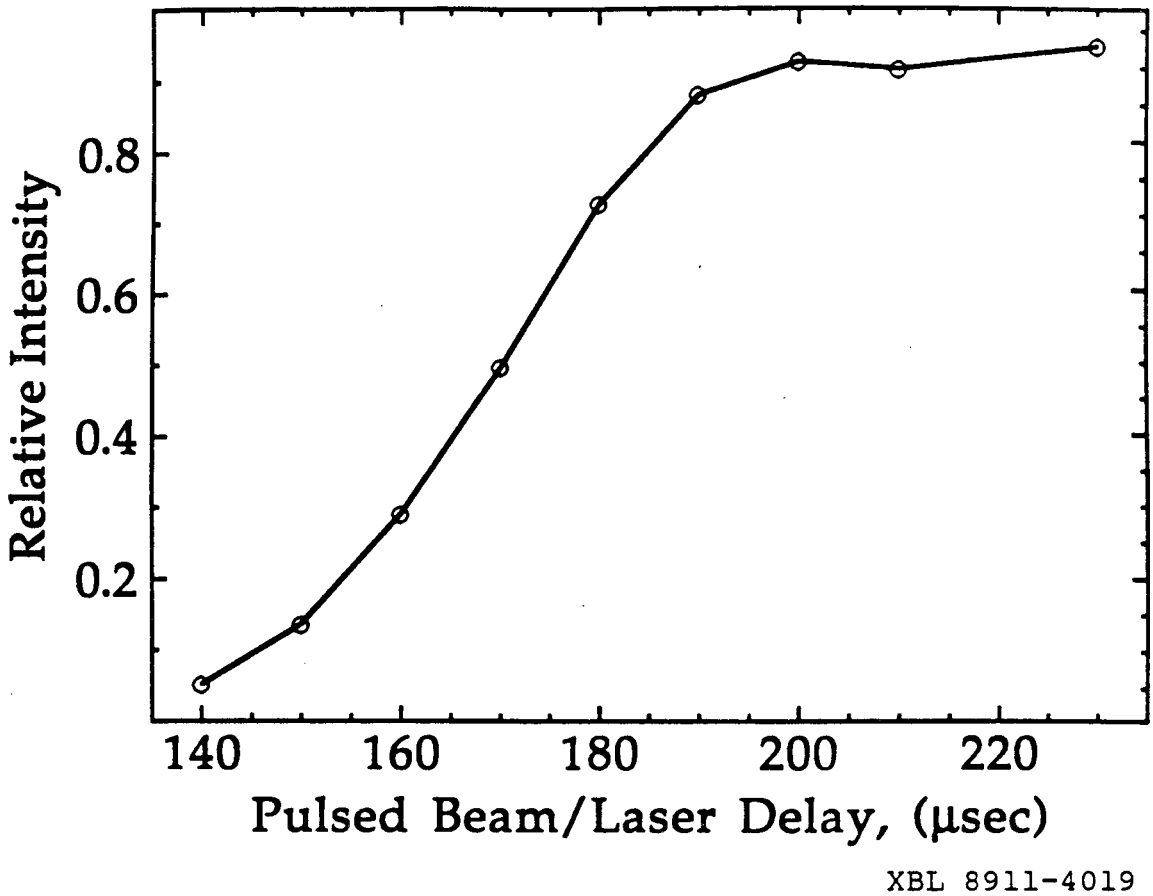
Relative Intensity
0.8
0.6
0.4
0.2
140
160
180
200
220
Pulsed Beam/Laser Delay, (μsec)
XBL 8911-4019

Figure 2 - 9

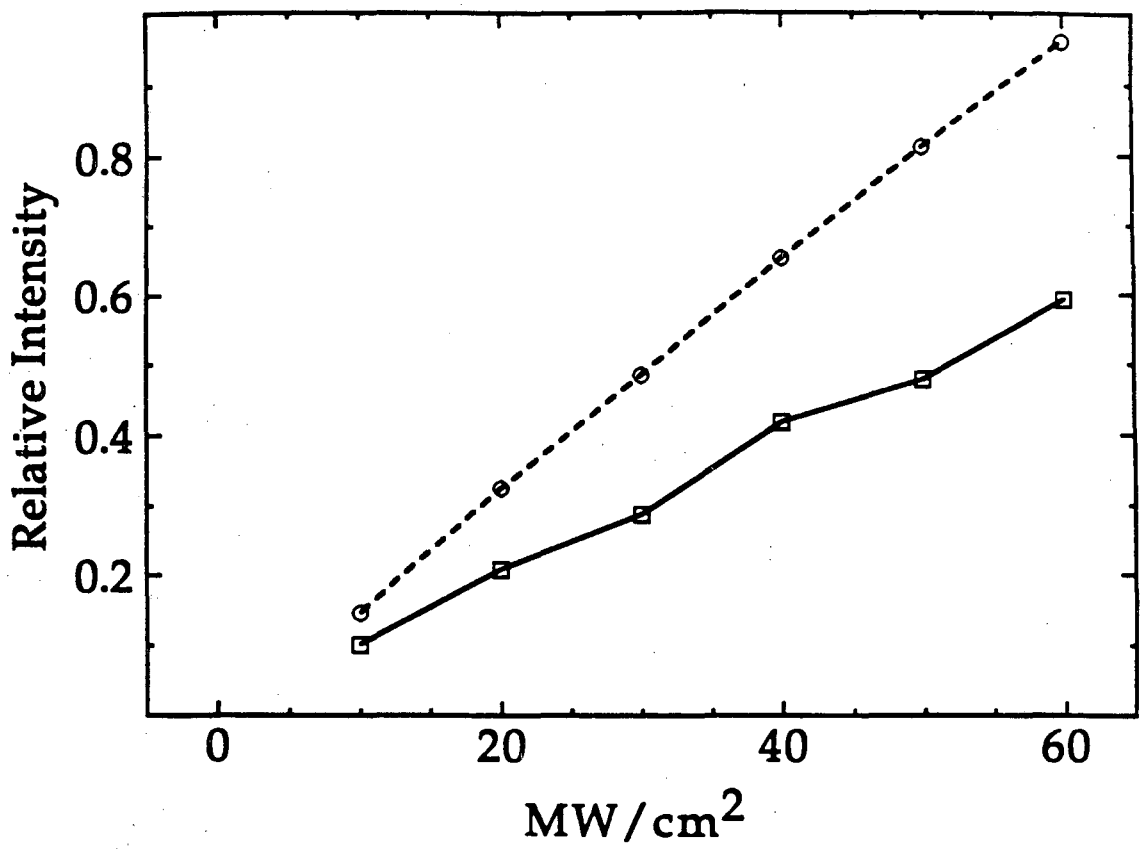

XBL 8911-4020

Figure 2 - 10

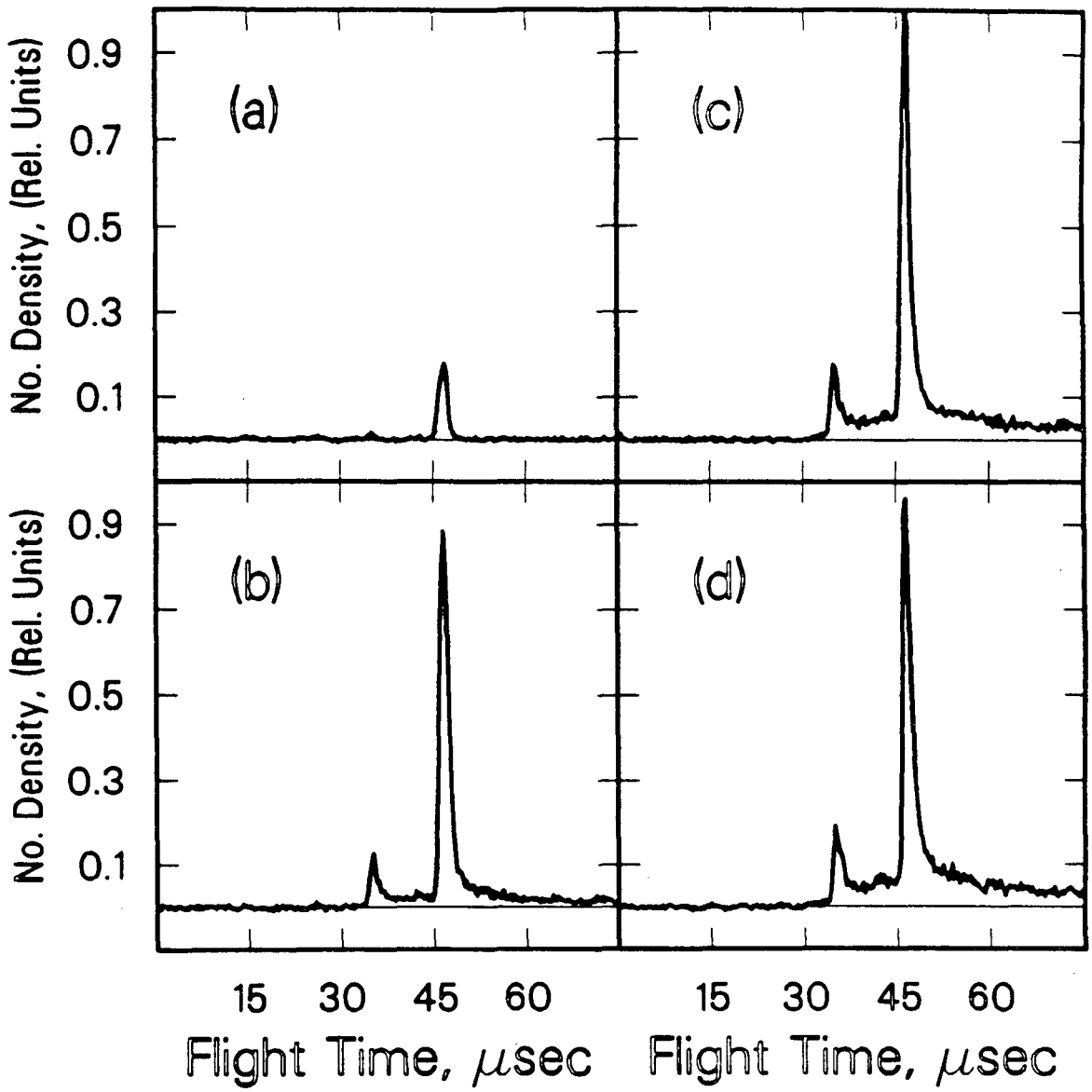

XBL 8911-4021

Figure 2 - 11

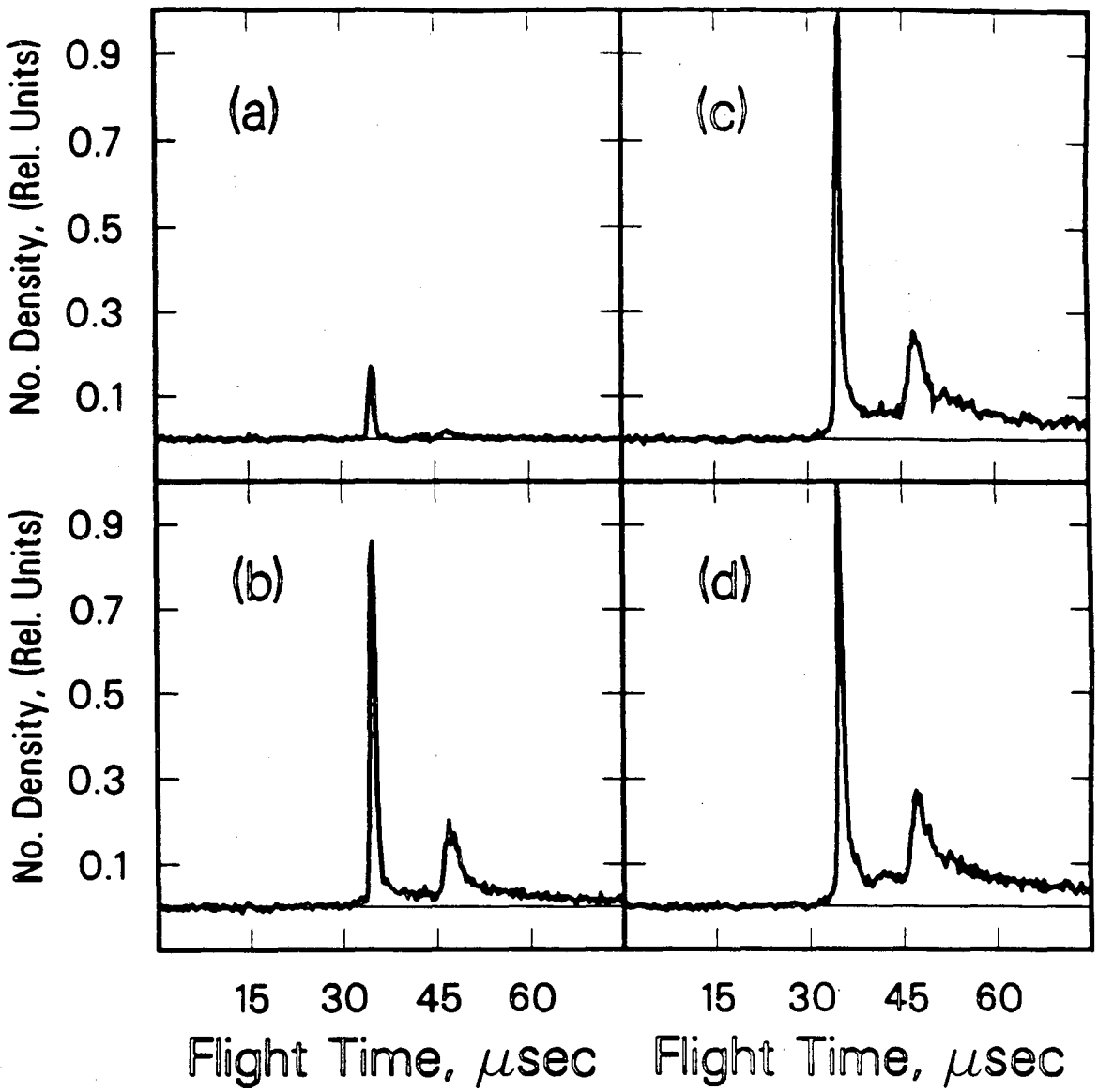

XBL 8911-4022

Figure 2 - 12

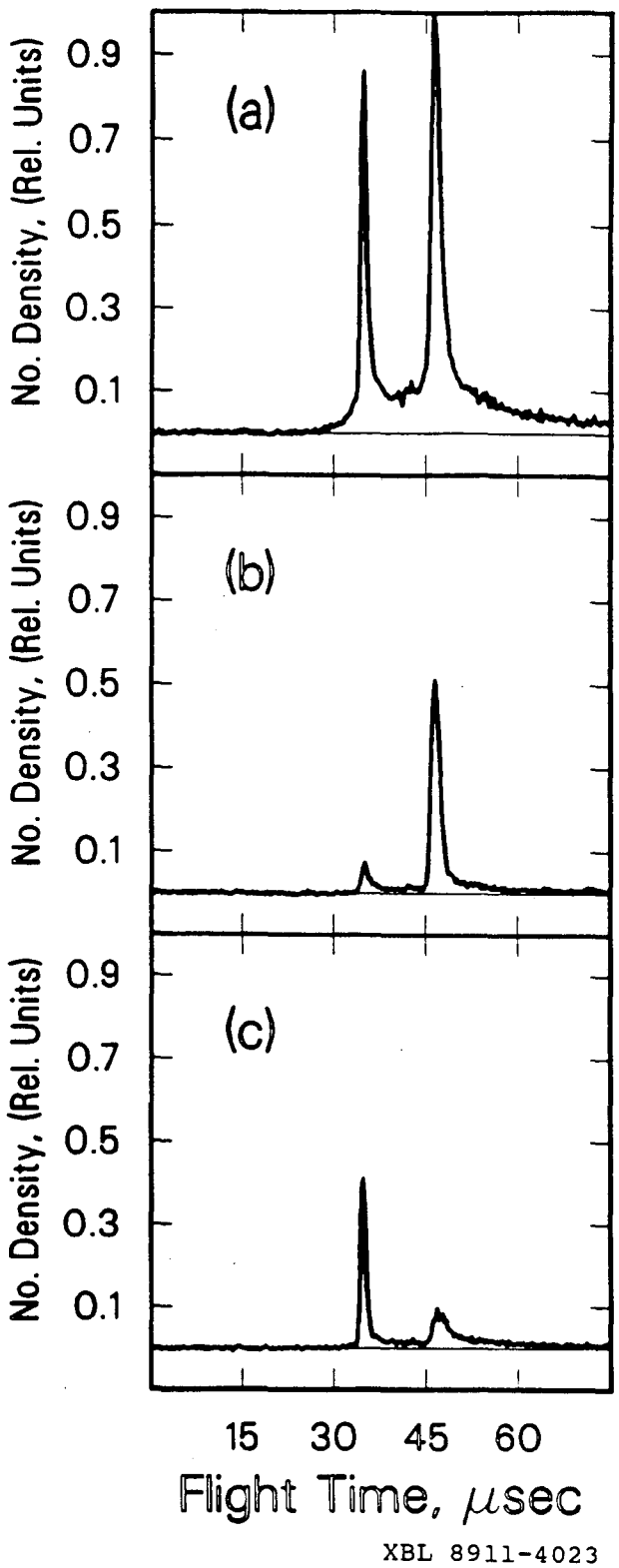
No. Density, (Rel. Units)
0.9
0.7
0.5
0.3
0.1
(a)
(b)
(c)
15
30
45
60
Flight Time, μsec
XBL 8911-4023

Figure 2 - 13

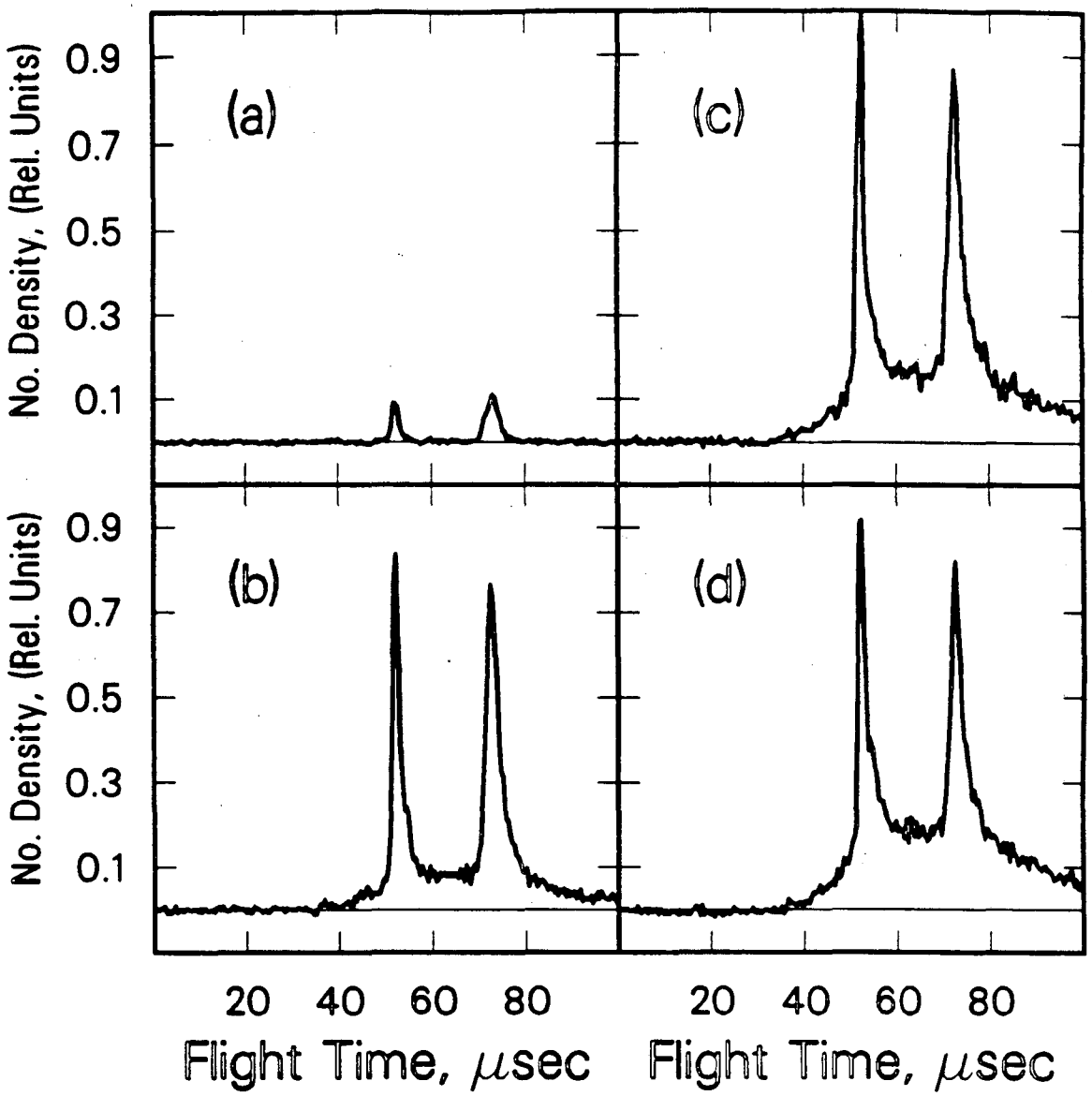

XBL 8911-4024

Figure 2 - 14

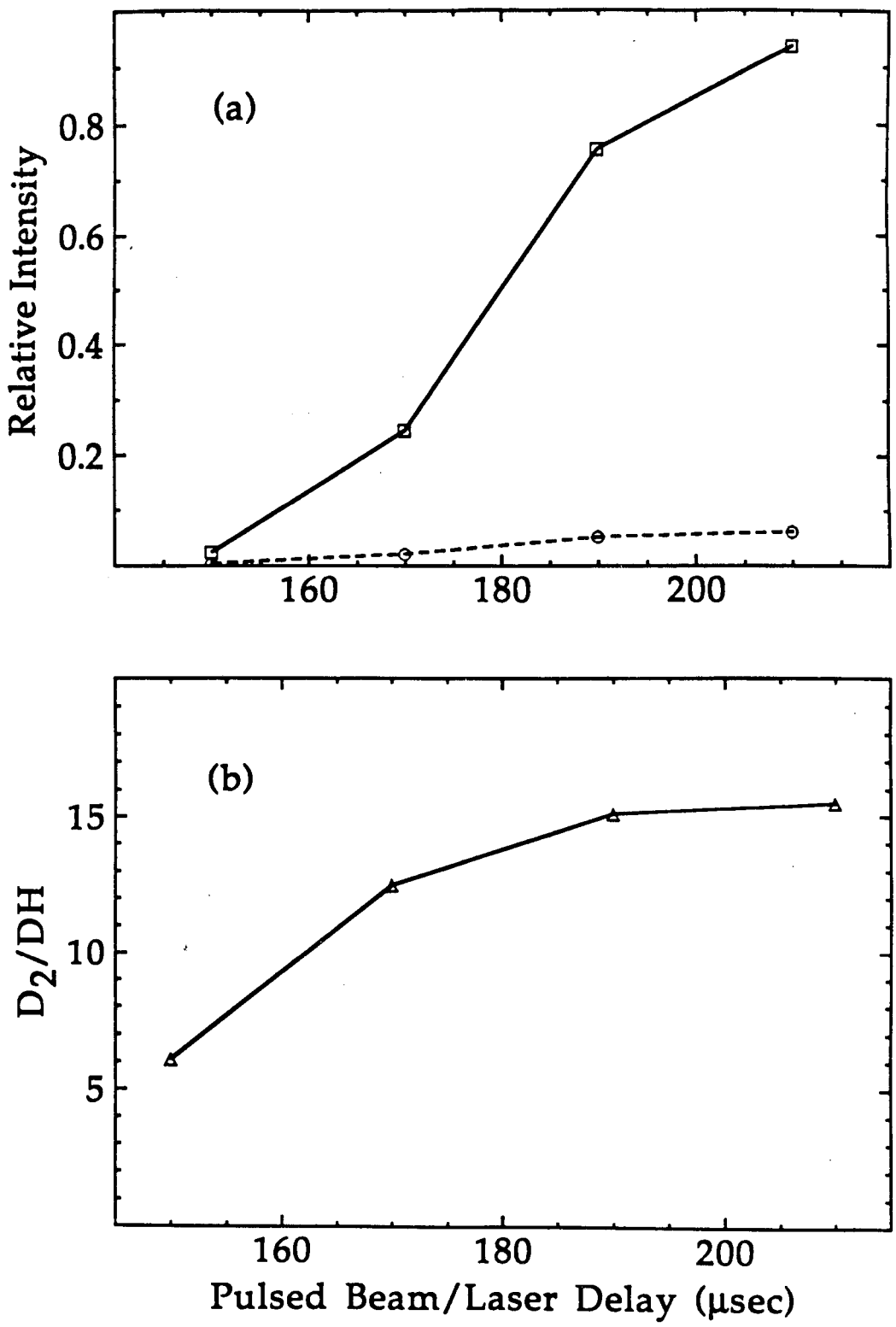

XBL 8911-4025

Figure 2 - 15

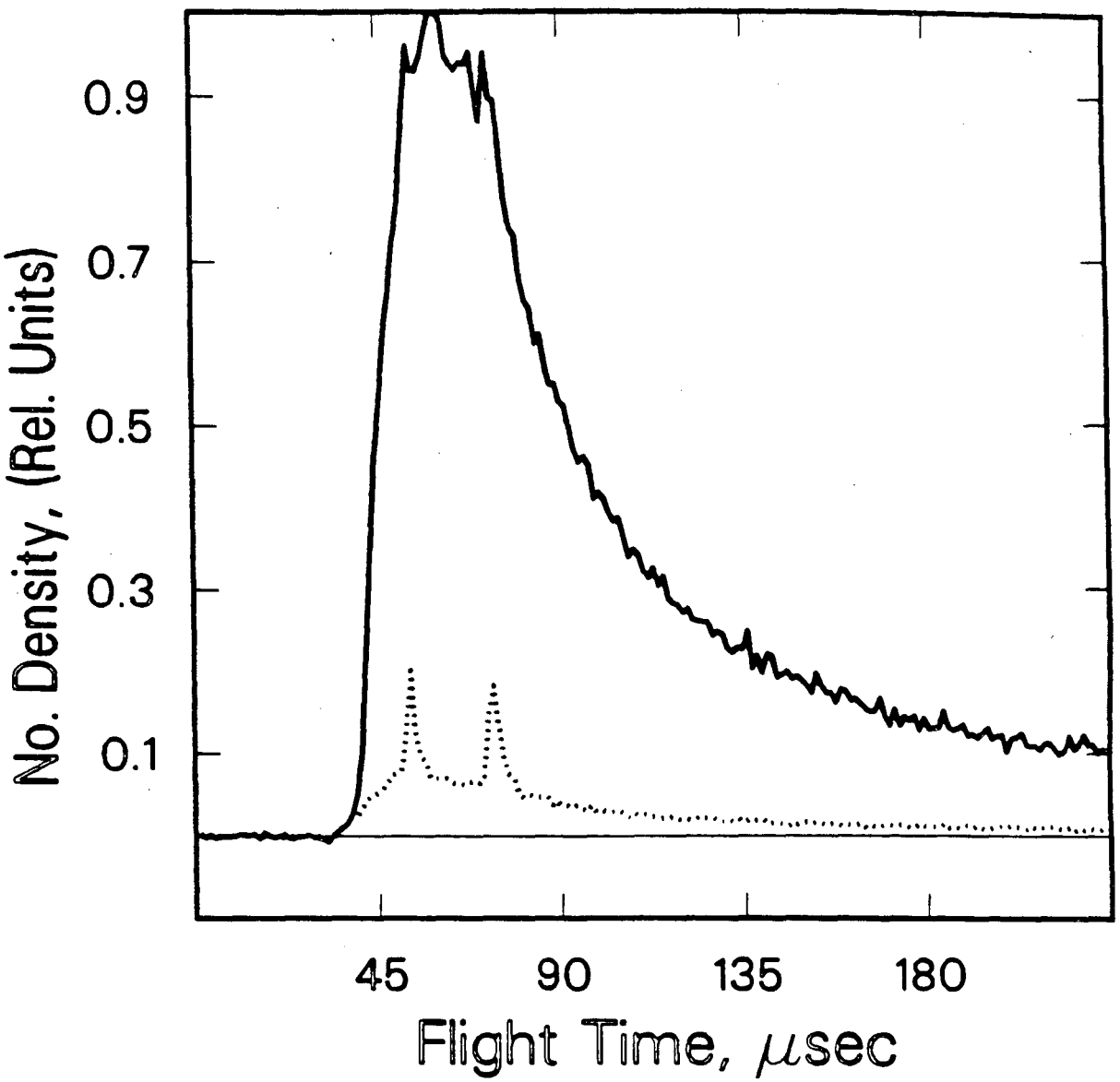

XBL 8911-4026

Figure 2 - 16

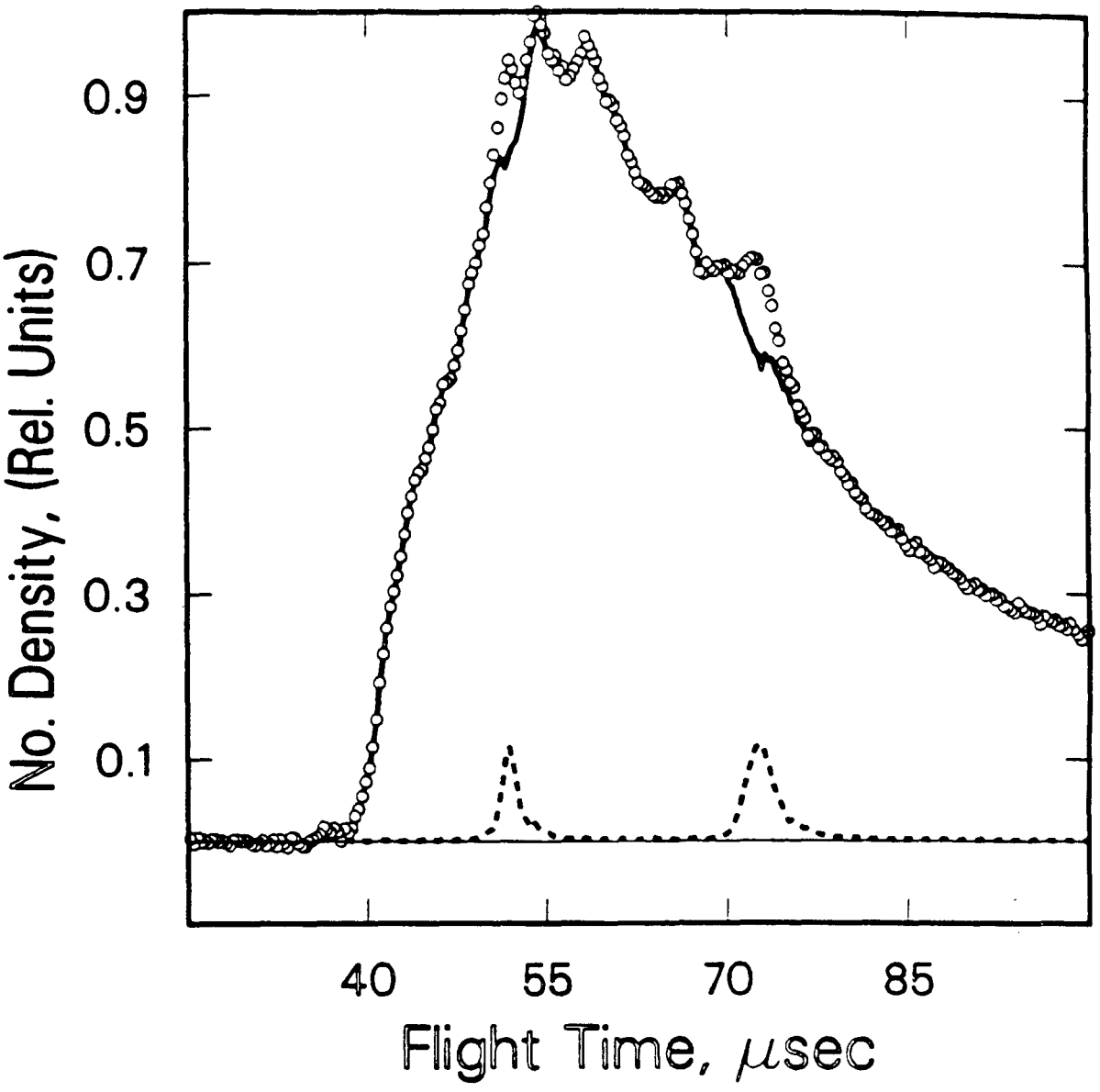

XBL 8911-4027

Figure 2 - 17

$$D + H_2 \rightarrow \underline{DH}(v) + H$$

$$E_c = 0.95 \text{ eV}$$

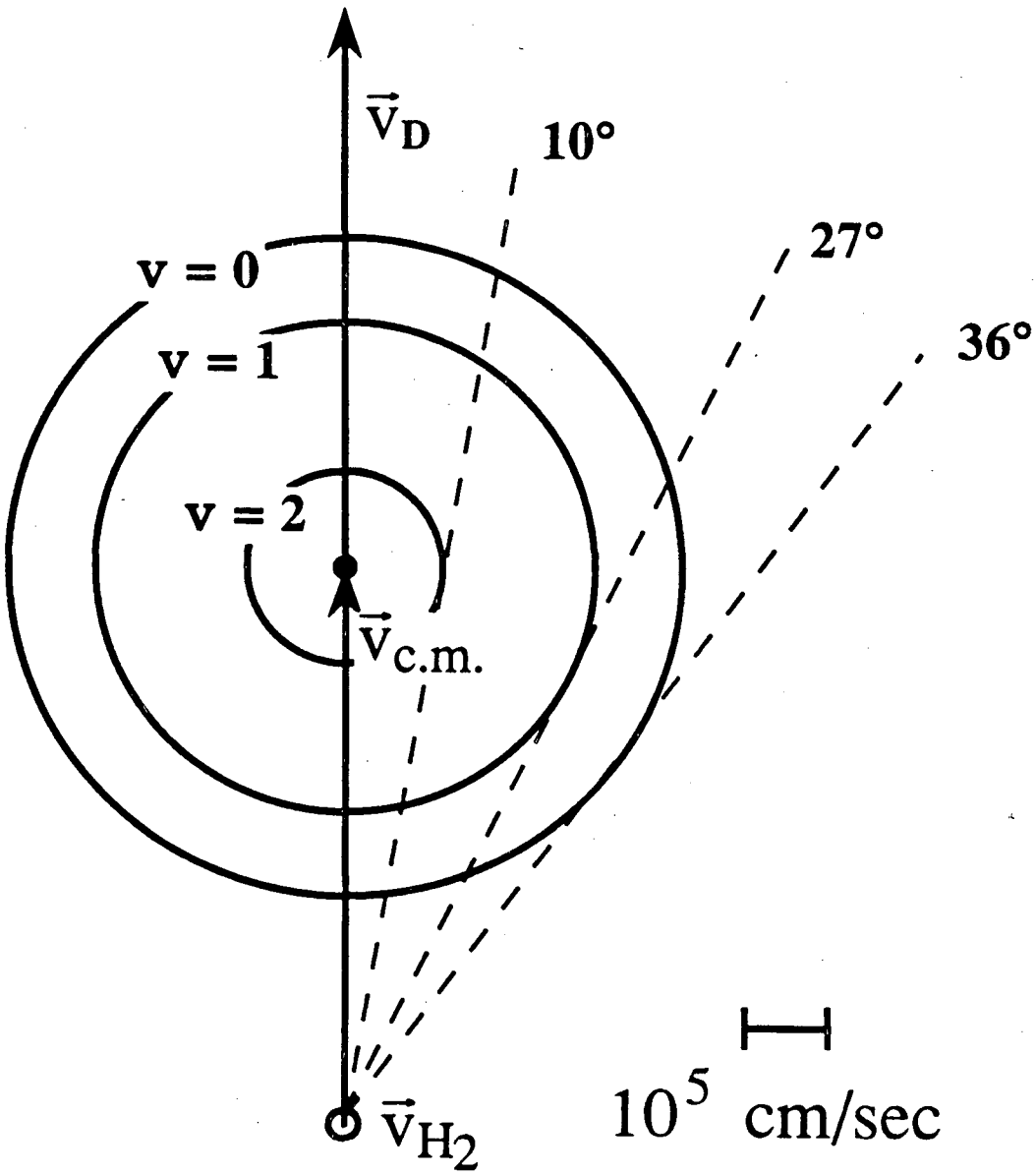

XBL 8911-4028

Figure 2 - 18

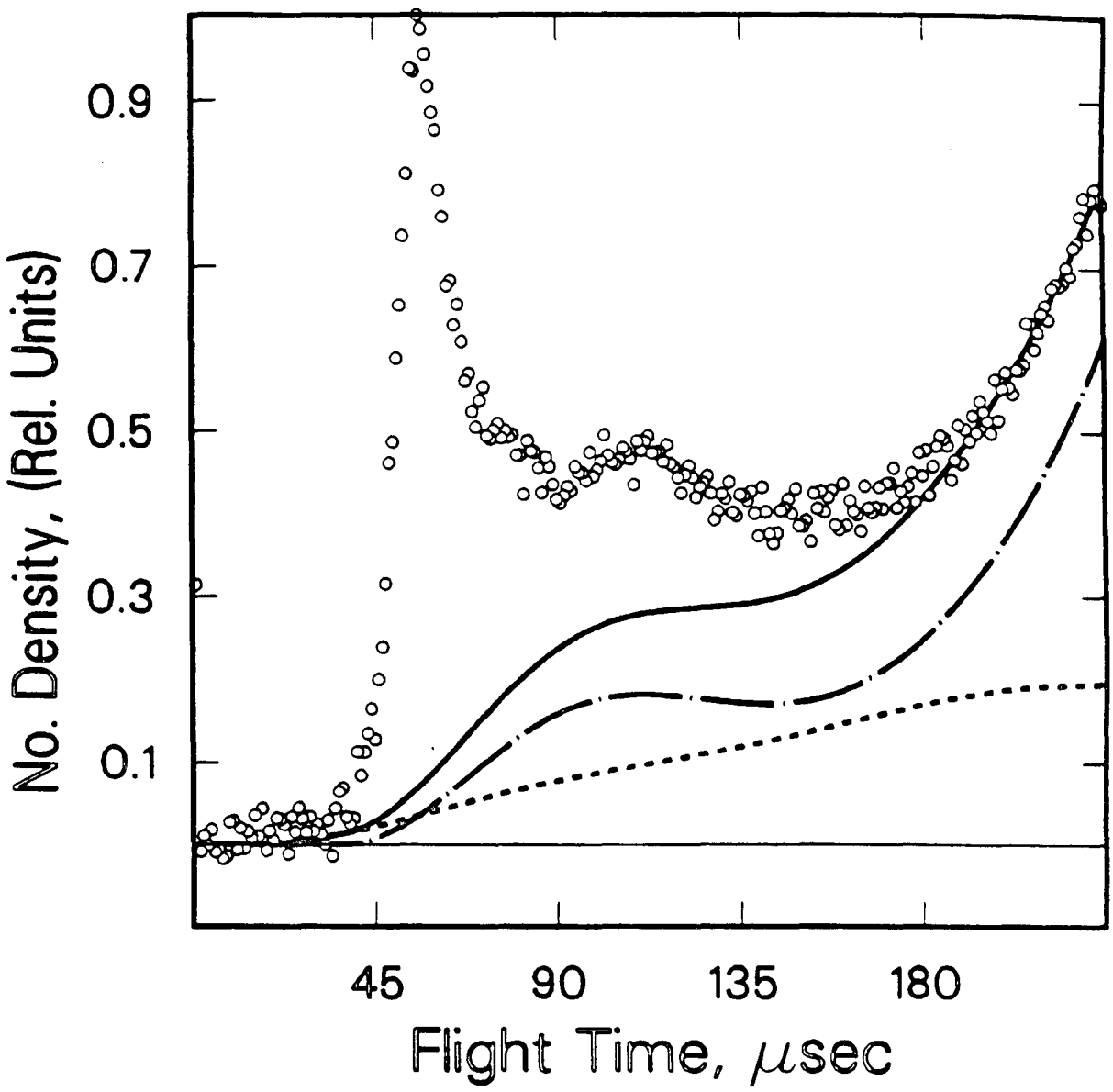

XBL 8911-4029

Figure 2 - 19

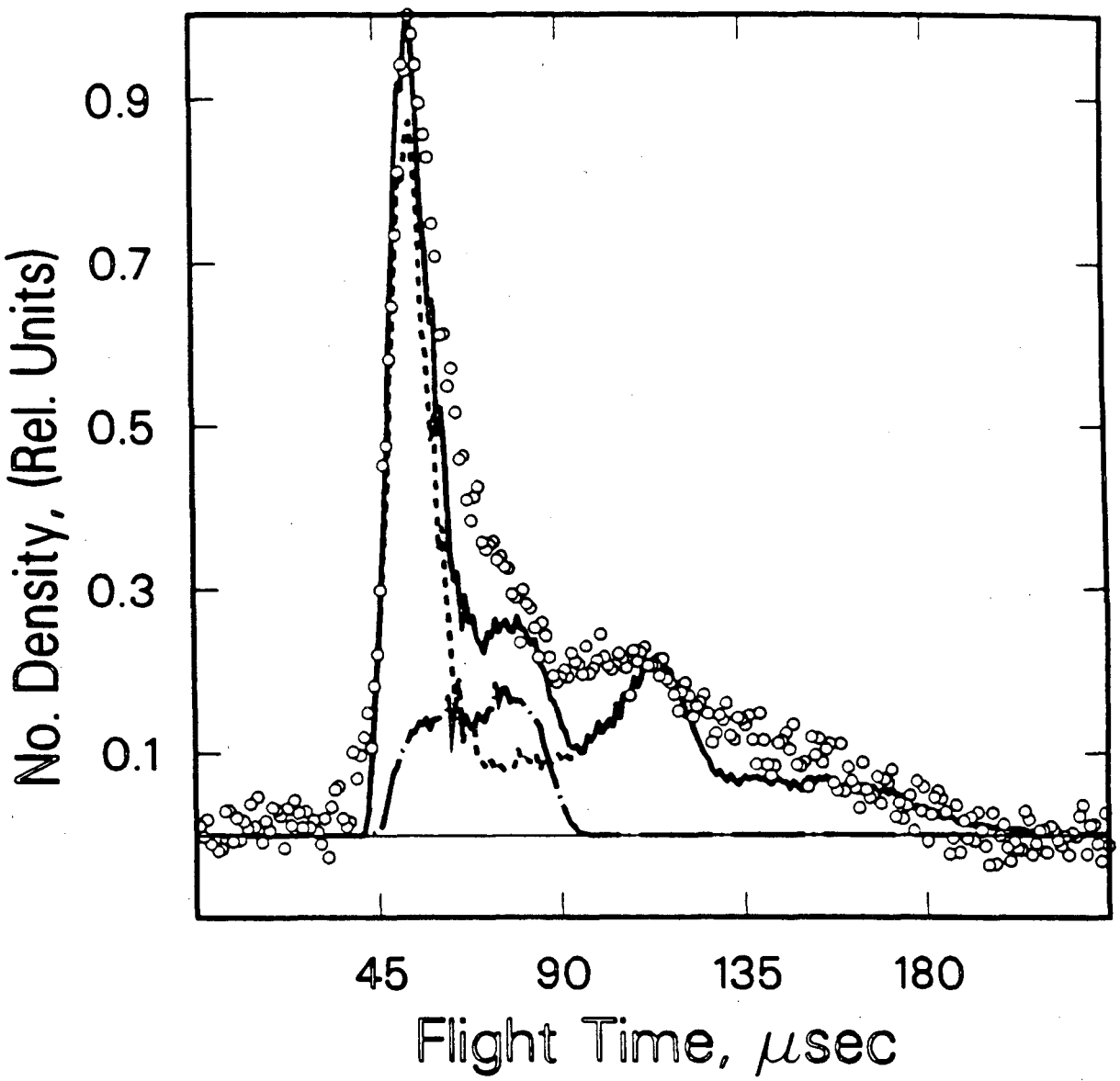

XBL 8911-4030

Figure 2 - 20a

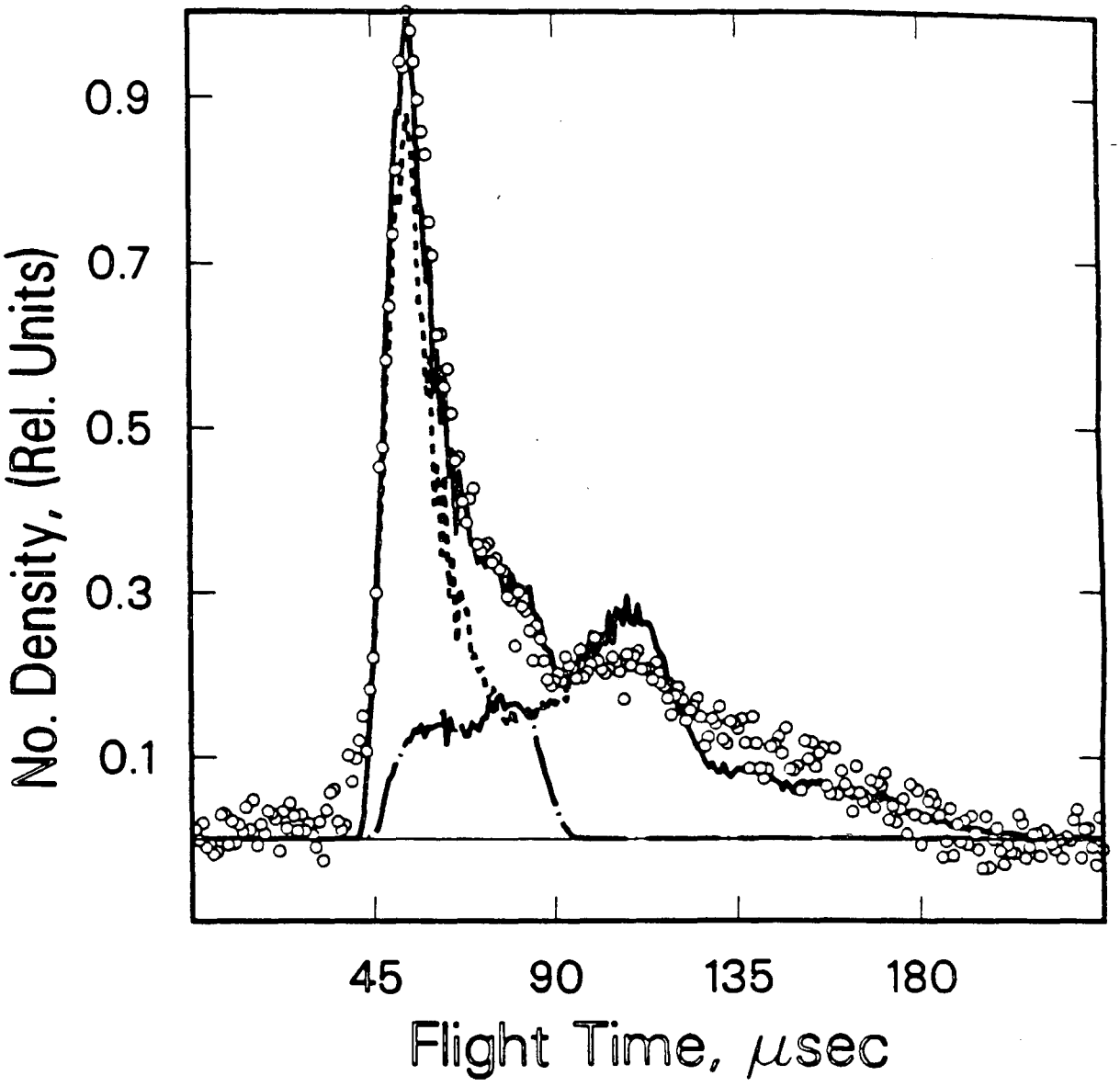

XBL 8911-4031

Figure 2 - 20b

Chapter 3

Vibrational State-Resolved Differential Cross Sections for the Reaction $D + H_2 \rightarrow DH + H$

1. Introduction

The hydrogen exchange reaction

$$H + H_2 \rightarrow H_2 + H \qquad (1)$$

is the simplest bimolecular chemical reaction between neutral species. The study of the dynamics of this reaction has played a central role in the development of our understanding of chemical reactions. As discussed in Chapter 1, many investigations, both theoretical and experimental, have been performed on this reaction and its isotopic variants. In the past, experimental difficulties prevented the acquisition of detailed dynamical data, however, with the advances made in the 1980's, this reaction is fulfilling its role as a prototype both theoretically and experimentally. Recently it has become possible to compare dynamical observables such as product-state distributions and differential cross sections with accurate three-dimensional (3-D) quantum scattering calculations[1] on the most accurate potential energy surface (PES) available for any chemical reaction, the LSTH surface for H_3[2,3]. The results presented in this chapter constitute the first direct comparison of vibrational state-resolved differential cross sections with these new theoretical calculations for the reaction

$$D + H_2 \rightarrow DH + H \qquad (2)$$

at two nominal center-of-mass (CM) collision energies, E_c = 0.53 and 1.01 eV. This comparison between theory and experiment is one of the most critical tests to date of quantum scattering calculations and the *ab initio* potential energy surface for this fundamental chemical reaction.

The asymptotic energies of the reactants and products of the D-H_2 system are known to a high degree of accuracy both experimentally and theoretically. Figure 3-1 illustrates the energetics of reaction (2), with D-H-H in a collinear configuration. From the time of the earliest PES calculations for this surface up to the most recent *ab initio* PES's, it has been realized that the minimum energy path for the reaction occurs with a collinear configuration. As the reactants deviate from a collinear configuration, the barrier to reaction rapidly increases. The nominal experimental collision energies and the DH product vibrational states accessible are shown in Figure 3-1. The large barrier to reaction (0.42 eV in the collinear geometry)[4] necessitates the use of a fast D-atom beam to attain the required collision energies. In this work fast D atoms were generated by the UV photodissociation of DI, as described in Chapter 2. Although this technique of hot atom generation has seen a wide range of application in the 1980's, this work is only the second successful effort to use photodissociation products as an atomic beam source.[5]

This chapter will first give a brief review of recent experimental and theoretical advances in the study of the H_3 system. The D + H_2 $\rightarrow$ DH(v) + H differential cross section (DCS) measurements are then discussed in section 2, with the experimental data presented in section 3. Section 4 deals with the analysis of the data and presents the comparison of these measurements with the recent 3-D quantum-mechanical reactive scattering calculations of Zhang and Miller[1]. Finally, section 5 concludes with a comparison of these results

with other experiments and the implications of this study on the PES for the H_3 potential energy surface.

1.1 Dynamical Observables

As experimental techniques have improved, an increasing number of dynamical observables have become available. As reviewed in Chapter 1, the earliest experimental studies of reaction (1) involved the measurements of reaction rate constants under bulk gas-phase conditions. Rate constant measurements continue to play an important role in chemical dynamics because they test the PES near threshold.[6,7] This region is difficult to probe by other means, and is the region in which quantum-mechanical tunneling is most important for a chemical reaction.

Product-state distributions provide the next level of detail in the elucidation of the dynamics of a chemical reaction. The first product-state distribution measurements for the H_3 system were done in the early 1980's using two laser-based state-selective detection techniques, Coherent Anti-Stokes Raman Scattering (CARS)[8] and Resonance-Enhanced Multiphoton Ionization (REMPI)[9]. These techniques were first applied to the measurement of the product-state distributions for the H + D_2 reaction at collision energies of 0.55 and 1.35 eV. These measurements have since been extended to a wider range of collision energies[10,11] and the isotopic variants H + p-H_2 [12] and D + H_2 .[13,14] Nascent product-state distribution measurements have been compared to the predictions of quasiclassical trajectory (QCT) calculations[15], and, for the H + p-H_2 system, fully converged 3-D quantum scattering calculations.[16] The QCT calculations and the

measurements generally show good agreement, however, the QCT rotational distributions are somewhat 'hotter' than those measured by both CARS and MPI. The product-state distributions measured with these two experimental techniques agree within experimental error for the H + D_2 reaction at E_c = 1.35 eV. [17]

The detailed correlation between the features of the PES and the product-state distributions is not well known. The observation of features in the energy dependence of the reactive cross sections which could be attributed to Feshbach resonances would provide a critical test of both the *ab initio* PES and dynamics calculations.[18] These resonances have been predicted to occur, leading to 'quasi-bound' collision complexes which survive for a very short period of time in a reaction that is otherwise a direct encounter. In a study of the H + p-H_2 reaction, Valentini and coworkers measured the energy dependence of the H_2(v,J) reactive cross sections. Striking features in the excitation function were observed near the predicted resonance energies on the LSTH surface.[19] Encouraging agreement with unconverged QM scattering calculations was observed, however, the fully converged 3-D H + H_2 calculations of Zhang and Miller[16] indicate that the resonance features seen in lower-dimensionality calculations and unconverged 3-D calculations should 'wash-out' in three dimensions. Studies of the PES sensitivity of the resonances have thus far failed to indicate better agreement with the measurements of Valentini and coworkers[20], and this remains an area of controversy today. If reactive resonances are observable in product-state distributions, such measurements may play an important role in the complete characterization of the PES for the H_3 reaction.

Measurements of the energy dependence of state-resolved differential cross sections will yield the most detailed experimental picture of the dynamics of a chemical reaction. The PES, which governs the interaction of the particles during the collision, determines the phase-shift of the scattering wavefunction, and thus, the angular dependence of the DCS in the center-of-mass frame. A direct comparison of state-resolved DH(v,J) differential cross sections with theoretical results is desirable, since the DCS should be the dynamical observable most sensitive to the features of the PES. Several measurements of the DCS for the $D + H_2 \rightarrow DH + H$ reaction have been performed in the last 26 years[21,22,23,24], however, resolution of product vibrational states was achieved only recently by Buntin, Giese and Gentry.[5,25] In their study, DCS data for single laboratory scattering (LAB) angles was obtained as a function of collision energy from 0.85 to 1.20 eV. The resolution was sufficient to resolve the vibrational states of backward-scattered DH(v,J) product. The LAB angles were chosen to measure the DCS in a fixed CM angular range as a function of energy. The eventual goal of measuring the energy dependence of individual rotational state-resolved differential cross sections has yet to be realized. An innovative laser-based H atom detection scheme has been developed that may be used in the future to achieve this goal.[26]

The measurement of experimentally observable manifestations of dynamical resonances constitutes another very sensitive dynamical observable, as previously mentioned. The first clear experimental evidence for the occurrence of dynamical resonances was observed in anomalous forward-scattering in the vibrational state-resolved DCS for HF(v=3) in the $F + H_2 \rightarrow HF + H$ reaction.[27] In principle, measurement of the energy

dependence of the state-resolved DCS in the $D + H_2 \rightarrow DH + H$ reaction will provide information on the energies at which the resonances occur, and hence, information on the nature of the transition state. This goal is beyond the scope of the present experiments, however. Efforts have also been made to directly detect the HD_2 transition state using MPI techniques.[28] Despite promising preliminary results, however, this work has yet to yield any information concerning the transition state in the H_3 system.

1.2 Recent Theoretical Studies

In the last several years, great progress has been made in reactive scattering dynamics calculations. This progress has been quite timely, given the advances made in the experimental probing of the dynamics of the hydrogen exchange reaction. The essential element in any dynamics calculation is the quality of the PES on which the process occurs, and for the H_3 system the high quality *ab initio* LSTH surface has been available since 1978. This surface is thought to be accurate to within < 1 kcal/mole (0.04 eV) near threshold for the reaction.[2,3] Further calculations at non-linear reactant geometries have been performed to check the global quality of the initial fit to the *ab initio* data points, and have been found to be in good accord.[4] Recently a new fit to the PES, known as the DMBE surface, has been derived. This surface takes into account several new *ab initio* energies for nonlinear H_3 geometries and the interaction of the ground electronic surface with the first electronically excited state.[29] The overall agreement between the two surfaces is quite good, although the DMBE surface has a collinear barrier to reaction that is 0.15 kcal/mole lower, which is in accord with the newest *ab*

initio calculations. Quantum Monte Carlo techniques have also been used to calculate the collinear barrier height for the reaction, indicating a barrier to reaction of 0.42 eV in accordance with the most recent *ab initio* calculations.[30,31] The good agreement between the available *ab initio* PES's has provided a firm foundation upon which QCT calculations and various approximate quantum scattering calculations have been done. The most significant uncertainties in the PES presently involve non-linear H_3 geometries, which may need to be sampled more thoroughly in future studies. Now that exact 3-D quantum scattering calculations have become possible, and with the more critical experimental tests of the reaction dynamics that are being done, attention may turn again to the calculation of better *ab initio* PES's for the H_3 system.

Since the LSTH surface became available, several QCT studies of the dynamics of the H_3 system have been performed. For the D + H_2 reaction in particular, Mayne and Toennies[32], Blais and Truhlar[33], and Aoiz, et. al.[34] have performed dynamical calculations on the D + H_2 isotopic variant of the H_3 system. The QCT calculations show good qualitative agreement with Zhang and Miller[1]. The comparison of the experimental results described in this chapter will be limited to the exact 3-D quantum scattering calculations, since these calculations represent the most complete set of theoretical predictions for the D + H_2 reaction over the experimentally relevant energy range.

The first fully converged 3-D close-coupling (CC) quantum scattering calculations were done on reaction (1) for total energies (collision energy + zero point energy of the reactants) E_{tot} < 0.7 eV in the mid-1970's.[35] The extension of accurate 3-D quantum scattering calculations to higher energies

and the more complicated, non-symmetric isotopic reactions such as D + H_2 was not successfully made until 1989[1], although great progress was made in the intervening period in the development of accurate approximate calculations, as noted in Chapter 1. With the results of Zhang and Miller, then, for the first time we have the opportunity to compare accurate dynamics calculations with high resolution experiments over the entire experimentally accessible energy range. This is a unique opportunity in chemical dynamics, and for this reason the comparison between the DCS measurements reported here and Zhang and Miller's results will be the main focus of this chapter.

2. Experimental

2.1 Apparatus

2.1.1 General Description

Using the technique of crossed-molecular beams scattering with mass-spectrometric detection, we have measured the vibrational state-resolved DCS for the D + $H_2 \rightarrow$ DH + H reaction. The DH product velocities were measured by the time-of-flight (TOF) method. A high-resolution universal crossed-molecular-beams apparatus was used in these studies. The general features of this apparatus have previously been discussed in detail.[36] A description of the modifications made in the course of these measurements was given in Chapter 2, but the salient points will be reviewed here. A schematic view of the experimental geometry is shown in Figure 3-2, and a

detailed scale drawing of the scattering region geometry is shown in Figure 3-3. An excimer laser beam crossed a DI target beam, producing a pulse of D atoms that was subsequently collimated by a set of defining apertures. At the center-of-rotation (COR) of the UHV detector, the D-atom beam crossed a pulsed H_2 molecular beam orthogonally in the main scattering chamber, which had a working pressure of $\approx 1 \times 10^{-6}$ torr H_2 with both the DI photolysis target beam and the H_2 molecular beam running. The scattered DH products entered the detector by first passing through a slot in a synchronized chopping wheel and then a small tube attached to the face of the detector. This served to gate the detector opening, reducing the gas load on the detector and thus, the background count rate at m/e = 3. A schematic timing diagram for the experiment is shown in Figure 3-4.

The apparatus is equipped with a triply differentially pumped UHV quadrupole mass-spectrometric detector which rotates in the plane defined by the atomic and molecular beams. Scattered products entering the detector were collimated by a set of 3 apertures, giving a nominal detector angular resolution of 1.25°. DH products flew 34.3 cm from the COR to the electron-impact ionizer. The uncertainty in the flight path was about .75 cm, predominantly due to the size of the ionizer. The DH products were ionized, mass selected with a quadrupole mass spectrometer and counted with a Daly-type ion counting assembly.[37] A custom-built 4096 channel multi-channel-scaler (MCS) recorded the TOF of the ions relative to the dissociation laser pulse. An LSI-11/73 microcomputer interfaced to the MCS via a CAMAC crate controlled data acquisition.

2.1.2 D-Atom Beam Source

The D-atom beam was produced by crossing an intense 248 nm pulse from a Lambda Physik EMG 202 MSC excimer laser (operating on the KrF excimer line) with a pulsed beam (FWHM ≈ 225 μsec) of deuterium iodide (DI) produced by expansion of 140 torr DI through a 0.75 mm aperture. The time- and source pressure-dependent behavior of the D-atom beam is discussed in Chapter 2. The DI pulsed beam source is described in more detail in Appendices B and C.

The output of the excimer laser was polarized by a 10-plate brewster angle stack polarizer. The polarizer attenuated ≈ 55 % of the beam, leaving light with better than 95 % polarization. Under typical operating conditions, the laser generated 300 mJ/20 nsec pulse, delivering ≈ 140 mJ of polarized 248 nm radiation to the photolysis volume. The performance of the excimer laser was improved by using an Applied Photonics C-5000 gas processor. With the gas processor in use, constant laser power could be maintained with the laser's ILC feedback circuit (Lambda Physik) in excess of 1 million shots (≈ 3 hours at 100 Hz). Two uncoated fused silica cylindrical lenses, f = 19 cm and f = 24 cm were used to focus the 2.5 x 1.0 cm rectangular output beam of the excimer laser to 3 x 3 mm at a distance of 3 mm from the nozzle aperture. Collisions still occur this close to the nozzle, broadening the D-atom velocity distribution. However, due to beam intensity requirements it was necessary to operate the beam source in this configuration.

The D-atom beam was then collimated by three apertures to a nominal point-source angular divergence of ≈ 6°. The size and positions of these

apertures was as follows; 1) a set of vertical slits of width 4 mm placed 5.5 mm from the center of the photolysis volume; 2) a 3 x 3 mm defining slit made of razor blades placed a distance of 22.9 mm from the center of the photolysis volume, and 3) a 3.5 mm (in the plane of the beams) x 4 mm defining slit placed a distance of 34.8 mm from the center of the photolysis volume. The distance from the center of the photolysis volume to the COR of the detector was 48.3 mm.

TOF spectra of the D-atom beams produced with the laser polarization parallel and perpendicular to the direction of beam propagation and detection are shown in Figure 3-5. The fit to the data points was generated with a modified version of the LabAvg Monte Carlo simulation program described in Appendix A. This program also generated a D-atom number-density velocity distribution corrected for all apparatus averaging effects which was used in the simulation of the reactive scattering data. The velocity distributions corresponding to Figure 3-5 are shown in Figure 3-6. The peak velocity for the perpendicular polarization was 1.38×10^6 cm/sec with a FWHM of $+.01/ -.04 \times 10^6$ cm·sec^{-1}, while for the parallel polarization the peak velocity was 9.77×10^5 cm·sec^{-1} with a FWHM of $+ 0.08/ - 0.20 \times 10^5$ cm·sec^{-1}. Photofragmentation of DI and the other hydrogen halides under single collision conditions was used to calibrate the TOF measurements. The peak D-atom velocities observed in the high-intensity D-atom beam used in the scattering studies are ≈ 1.5 % higher than the single-collision values due to collisional effects in the photolysis free-jet source.

The differential pumping chamber used for generation of the D-atom beam was discussed in detail in Chapter 2. It consisted of a large chamber, pumped by a VHS-10 10" diffusion pump (DP) and two liquid-N_2-cooled cryo-

panels, with a smaller photolysis chamber nested within. The photolysis chamber was pumped by a VHS-4 4" DP and one liquid-N_2-cooled cryo-panel. The cryo-panels reduced the rate at which pump oil and iodine fouled the f=19 cm lens, which formed the vacuum seal through which the laser beam passed. For a condensible photolysis target gas like DI, very high pumping speeds were obtained with this arrangement.

2.1.3 H_2 Beam Source

These experiments employed a room-temperature pulsed H_2 beam source with the H_2 beam in the plane of detection. The chamber used in the experiments with the cryogenically cooled H_2 source described in Chapter 2 was modified for this experiment. The source chamber was pumped by a VHS-10 10" DP backed by a Roots-blower mechanical pump combination, and a VHS-4 4" DP. The box which previously held the pulsed beam source and scattering volume viewing slits was opened, and the H_2 pulsed beam source mounted in the differential pumping chamber in a more standard crossed-beams configuration as shown in Figure 3-3.

A 0.5 mm diameter nozzle placed 18 mm from a 1.5 mm diameter home-made electroformed skimmer was used to generate the H_2 beam. The distance from the skimmer opening to the crossed-beams interaction region was 12.5 mm. The pulsed H_2 beam had an angular FWHM of 8°, as reported in Appendix C. With a stagnation pressure of 1200 torr, velocity distributions for normal-H_2 (n-H_2) characterized by (α,S) = (1.98 , 13.9) were observed, while for para-H_2 (p-H_2) velocity distributions characterized by (α,S) = (1.87, 15.0) were observed. The fitting parameters α and the speed ratio, S, are

defined in Appendix C. The velocity distributions were measured with a synchronous TOF technique, which enabled measurement of the velocity distribution at different times in the gas pulse. As discussed in Appendix C, the p-H_2 beam had approximately 20 to 30 % H_2 (J = 2) in it, with the balance in J = 0. The pulsed-beam temporal profile in the free jet had a FWHM of ≈ 175 μsec, while the portion of the beam transmitted through the skimmer had a FWHM of ≈ 80 μsec. Para-H_2 was made by the U.C. Berkeley Dept. of Chemistry Low Temperature Laboratory.

2.2 DH Product TOF measurements

The D + H_2 experiment was characterized by low signal intensities. TOF spectra for DH (m/e = 3) were recorded as a function of LAB scattering angle at nominal collision energies E_c = 0.53 and 1.01 eV. The highest signal intensities observed were ≈ 2 x 10^{-3} ion counts/0.9 μsec time bin/laser shot. To complete the DCS measurements, the experiment had to operate reliably for long periods of time. Once the operating conditions had been optimized, ≈ 210 hours of actual reactive scattering data for the D + p-H_2 reaction and ≈ 120 hours of data for the D + n-H_2 reaction were acquired over a period of three months.

The pulsed-molecular-beam sources in particular performed very reliably in the final experiments. The H_2 beam source produced in excess of 250 million cycles without failure or readjustment. The DI beam source piezoelectric crystal performance degraded with time and had to be replaced after ≈ 100 million cycles, but otherwise even this corrosive-gas pulsed beam source performed reliably. The performance of the excimer laser degraded

significantly over the course of these measurements, however. Initially, the laser was able to deliver 350 mJ/pulse of unpolarized 248 nm radiation at a repetition rate of 100 Hz for up to 30 hours without cleaning of the output coupler and high reflector. By the end of the study the laser was delivering only ≈ 250 mJ/pulse, and the output coupler or the high reflector had to be cleaned alternately every 12 hours. The excimer laser lenses also required routine maintenance. After an experimental run of ≈ 80 hours, the lens transmission would decrease to ≈ 2/3 of its normal, 'clean' value. The scattering chamber had to be vented for lens cleaning.

An experiment began with measurement of the D-atom beam intensity. With the mass spectrometer pointed into the D-atom beam, the intensity and appearance of the D-atom photofragment spectra were monitored. The D-atom beam intensity was also monitored periodically as the run progressed. Attenuation of the D-atom beam by the H_2-molecular beam was then measured to check the H_2 beam intensity and verify that the experimental timing was correct. The measured attenuation of the D-atom beam by the H_2 beam was typically 5 % or less in the final experiments.

Once the two beams were crossing with the desired phase, reactive scattering data acquisition was begun. Data was first acquired at a reference LAB angle for 2×10^5 pulses (33.3 minutes at a data acquisition rate of 100 Hz). LAB angles of 27.5° and 32° were used as reference angles for the E_c = 1.01 eV reaction, while 40° was used as the reference angle for the E_c = 0.53 eV reaction. TOF spectra at three other LAB angles were then measured, followed by the reference angle. This cycle was then repeated until the laser gas needed changing (≈ 3 to 5 hours). Either nominal collision energy could be chosen by simply rotating the transmission polarizer, without any laser

realignment required. Two background measurements were also done routinely. The signal at m/e = 3 coming solely from the D-atom beam was measured without the H_2 beam running. This measurement was done occasionally, with typically at least one LAB angle recorded per laser gas fill. While the laser gas was being changed, the signal due to the H_2 beam alone was measured. Separate studies of the background sources associated with the D-atom and H_2 beams were also made.

The laser power was kept constant by the ILC feedback circuit on the excimer laser. The H_2 and DI beam source stagnation pressures were monitored with Baratron (MKS) capacitance manometers. The H_2 beam source pressure was adjusted with a vacuum regulator, while the DI beam source pressure was kept stable with a variable temperature cryogenic bath and a needle valve. DI of ≈ 97 % isotopic purity was synthesized as described in Appendix D. The DI cylinder was kept at a temperature of - 55°C. When the DI feed line or the DI pulsed-beam source was disassembled, passivation of the line was necessary to reduce isotopic contamination of the DI by exchange with H in atmospheric water vapor. This was accomplished by exposing the line to D_2O vapor, followed by repeated filling/evacuation cycles with DI.

Due to the low signal levels, the quality of the data was strongly dependent on the background count rate in the mass spectrometer at m/e = 3. With the gated detection scheme that was used, a count rate of 1.8 kHz at m/e = 3 was achieved at the beginning of an experimental run. The inherent m/e = 3 background in the detector alone gave count rates of ≈ 1.5 kHz. As a long experimental run progressed, the count rate would slowly rise, due to the

buildup of DH in the chamber. After 40 to 50 hours of continuous measurements, for example, the m/e = 3 count rate would reach 2.5 - 3 kHz.

3. Results

3.1 Reactive Scattering TOF Data

The raw data obtained for the D + p-H_2 reaction in two of the six long experimental runs are shown in Figures 3-7 to 3-10. In Figure 3-7, TOF spectra at m/e = 3 for the reaction at E_c = 1.01 eV are shown, while in Figure 3-8, the data for the E_c = 0.53 eV reaction are shown. These results represent the most complete single experiment performed, which lasted 110 hours and generated ≈ 70 hours worth of reactive scattering TOF data. The data are normalized to the signal observed in 2 x 10^5 laser shots, with the constant background subtracted. The reference spectrum at 32°, for example, represents 4 x 10^6 laser shots. These spectra are six channel averages of the 0.15 μsec dwell-time raw data, so each point on the spectra represents the signal arriving in a 0.9 μsec wide TOF bin. In Figures 3-9 and 3-10, data taken in a shorter experiment at fewer LAB angles for E_c = 1.01 and E_c = 0.53 eV is shown. These spectra are also normalized to 2 x 10^5 laser shots/TOF. The laser power was ≈ 15 % lower in this run, and the DI beam/ laser delay was 160 μsec (10 μsec shorter than the data shown in Figure 3-7). The shorter delay and lower laser power resulted in less laser-correlated DH background in the spectra. The D-atom-beam velocity distribution was not significantly different from the ones shown in Figures 3-6(a) and 3-6(b).

The raw data are contaminated by two types of modulated background. The large signal at long flight times in all the spectra is correlated with the H_2 molecular beam, and does not depend on the presence of the crossed D-atom beam. As the H_2 beam enters the scattering chamber, some collisions occur in the beam, scattering H_2 (and isotopic impurity DH) into the detector. Eventually, the H_2 beam scatters off the various surfaces in the chamber and into the detector, contributing to the signal at longer flight times. This background signal generally arrives at longer flight times than the reactively scattered signal, except in the case of the slow products of the $E_c = 0.53$ eV reaction.

The other source of modulated background is fast DH in the D-atom beam, formed by D/H abstraction reactions with DI/HI in the photolysis source, as discussed in Chapter 2. This signal is observed at all LAB angles even without a crossed-beam scattering target, although the intensity diminishes at LAB angles greater than 15°. The intensity of this background signal is dependent on the presence of a crossed beam, however, as some of the fast DH is elastically and inelastically scattered into wider LAB angles. At LAB angles less than 15° this is a significant problem, as a fast elastic scattering peak is observed which is difficult to model or measure independently of the D + H_2 experiment. For LAB angles greater than 20°, however, test measurements with fast D_2 + H_2 scattering and fast DH + He scattering show that the observed signal with the crossed beam on is very broad with no discernable structure, and can therefore be well accounted for by measuring the DH from the D-atom beam alone. The curves that are fit to the raw data in Figures 3-7 to 3-10 represent the contributions of these two background sources, as described below.

The initial plan in these experiments was to focus on the D + n-H_2 → DH + H reaction, since p-H_2 is more difficult to obtain and great differences between the reactivity of n-H_2 and p-H_2 were not expected. However, as Figure 3-11 shows, a significant difference was observed in the raw TOF spectra for D + n-H_2 and D + p-H_2. The reactive signal intensity did not differ for n-H_2 or p-H_2, but, the H_2 beam-correlated background was significantly lower in the D + p-H_2 experiment under otherwise identical operating conditions. Possible explanations for this effect are considered below.

3.2. Modulated Background

3.2.1 H_2 Beam Modulated Background

TOF data with only the H_2 beam running was collected for all LAB angles, and subsequently fit to allow correction of the raw reactive scattering TOF data. A linear polynomial least-squares fit, (typically using a 9th order polynomial), was used to fit the H_2 beam data at each LAB angle. Any spurious oscillations in the leading baseline of the polynomial fit were removed. The fits were checked to ensure that they accurately represented the slope of the increasing signal, as this was critical for successful correction of the reactive scattering TOF spectra. Figure 3-12(a) shows an example of the fit to the m/e = 3 H_2-beam-correlated background at a LAB angle of 27.5°. In each experimental run, TOF spectra of this background source were measured to insure that the shape of the TOF signal did not change. The relative intensity of this background source did not vary significantly from run-to-run. The intensity of the H_2-beam-correlated background increased

considerably beyond 50°, causing a significant rise in the detector m/e = 3 count rate, which made scattering measurements increasingly difficult at wider LAB angles.

The difference observed in the modulated background at m/e=3 from the n-H_2 and p-H_2 beam was apparently due to a depletion of DH in the p-H_2. The DH intensity along the beam centerline was observed to be ≈ 18% lower in the p-H_2 beam. It is possible that the p-H_2 was depleted in the higher boiling-point isotopic DH during preparation. This possibility was ruled out by comparing the beam TOF of an old p-H_2 sample (prepared two months earlier) with a fresh p-H_2 sample and a n-H_2 sample. The old p-H_2 beam (now n-H_2) was observed to have the same velocity distribution and DH intensity as a standard n-H_2 beam. The p-H_2 was stored in aluminum cylinders, which reduced the rate of o-p interconversion and should have kept any isotopic exchange processes to a minimum. Another possible explanation of this effect is that the cross section for the rotational de-excitation of H_2 is significantly higher for DH-H_2 collisions than H_2-H_2 collisions. Normal-H_2 has a population of ≈ 67 % H_2 (J=1) and only 11% in H_2 (J=2) at room temperature. The H_2(J=1) molecules cannot rotationally relax in the expansion. Para-H_2, on the other hand, has ≈ 47% H_2 (J=2) at room temperature, so significant rotational relaxation occurs in the expansion of p-H_2. Rotationally inelastic collisions between DH and H_2 may scatter a significant amount of the DH out of the p-H_2 beam in the free jet expansion. A detailed, state-selective study of this effect should resolve the origin of the DH depletion once and for all.

3.2.2 D-atom Beam Modulated Background

The most important source of modulated background in this experiment was fast DH present in the D-atom beam. Exoergic H/D-atom abstraction reactions with unphotolyzed DI/HI precursor molecules generated DH with a wide distribution of velocities and internal energies.[38, 39] Due to the large velocities of the DH (up to 10^6 cm·sec^{-1}), signal from this source made contributions to the TOF spectra in the same time frame as the reactively scattered DH. Careful analysis of this signal was therefore necessary to allow proper correction of the raw reactive scattering TOF spectra. The intensity of this background signal was strongly dependent on the time delay between the firing of the DI pulsed beam and the photolysis laser. In addition, the signal was dependent on the laser power. For this reason, the magnitude of this background signal tended to vary, so measurements had to be made during every experiment. The final D-atom collimation slit placed 35 mm from the photolysis source helped suppress this signal at wider LAB angles significantly, but it was not possible to eliminate this signal entirely. Reactions of the D-atom beam at surfaces inside the scattering chamber and the detector almost certainly contributed to this background at longer flight times.

To account for this background component in the reactive scattering TOF's, the signal measured with only the D-atom beam on was recorded and fit in the same manner as the H_2 beam background. A TOF spectrum showing the DH from the D-atom beam at a LAB angle of 17° along with the

fit used is shown in Figure 3-12(b). The shape of this signal did not change considerably beyond 20°, although the intensity decreased.

Examination of the reactive scattering TOF data showed that the DH scattered out of the H_2 beam and the fast DH present in the D-atom beam could not account for all of the modulated background. The kinematics of the $D + H_2$ reaction dictate that the slowest DH products at $E_c = 0.53$ eV have a velocity of $\approx 2 \times 10^5$ cm·sec^{-1}, which corresponds to a TOF of 175 μsec. Lower energy collisions also occur due to the D-atom beam velocity distribution, but at flight times in excess of 200 μsec, the reactive scattering signal must go to zero. The only possible additional source of m/e = 3 signal with velocities fast enough to come under the leading edge of the reactive TOF signal was elastic and inelastic scattering of DH in the D-atom beam off of the H_2 beam. Although the DH concentration in the D-atom beam was more than two orders of magnitude less than the D-atom concentration, the elastic scattering cross section is significantly higher, so observation of some elastic scattering is not surprising. Due to the broad DH velocity distribution (see Chapter 2), the scattering signals resulting from DH-H_2 collisions were expected to be broad and featureless.

Two kinds of test experiments were done to assess the nature of the contribution from this 'beams-crossing' background signal. The first test measurement performed involved crossing the D-atom beam with the H_2 beam, with TOF spectra at m/e = 4 recorded. The signals observed corresponded to fast D_2 in the D-atom beam scattering off of H_2. The kinematics for this collision are somewhat different from those for DH-H_2 collisions. In particular, since the product mass ratio $H_2/D_2 = 1/2$ as opposed to $H_2/DH = 2/3$, the scattered D_2 has a smaller CM velocity and is scattered in

a smaller solid angle in the laboratory frame. This accentuates the observed signal. Figure 3-13 shows the differences and relative magnitudes of the m/e = 4 signals observed at LAB angles of 10° and 20° with the D-atom beam running and the H_2 beam both on and off. Signal due to scattering of the D_2 is observed at 10°, arriving at earlier flight times than the signal measured with the D-atom beam only. At a LAB angle of 20°, however, little difference is observed between the two spectra, and it is clear that a significant elastic scattering peak is not observed. This result indicated that, while elastic scattering was a significant contaminant in the reactive scattering TOF spectra at small LAB angles, the 'beams-crossing' background at wider LAB angles could be fit well using the broad background signal measured with only the D-atom beam running.

The second test measurement involved crossing the D-atom beam with He, with the mass spectrometer tuned to m/e = 3. The kinematics for DH + He collisions result in a less intense LAB scattering signal being observed compared to that expected in the DH-H_2 system, due to the He/DH mass ratio of 4/3. Figure 3-14 shows the magnitude of the TOF signals observed for reactively scattered D + p-H_2 → <u>DH</u> + H compared to DH + He → <u>DH</u> + He at a LAB angle of 27.5°. As the TOF spectra show, some broad DH signal is observed in the DH + He collisions, but the magnitude is significantly lower than that recorded in the reactive scattering of D + H_2. The solid-line fit to the DH + He spectrum was generated using the DH TOF spectra measured with only the D-atom beam running. The fit is quite good, specifically, no significant signal was observed from DH + He scattering at this LAB angle at flight times less than 80 μsec, which is where the most

significant differences between the theoretical predictions and the experiment lie.

3.3 Correction of the Reactive Scattering TOF Data

The test measurements indicated that elastic and/or inelastic scattering of DH in the D-atom beam was a significant problem at the smallest LAB angles (10 °), rapidly decreasing in severity. By the time $\Theta_{LAB} = 20°$ was reached, no significant elastic scattering peak was observable, although an increase in the overall broad TOF signal intensity occurred. This signal was fit well by the DH TOF measured with no crossed beam. Substitution of a pure DH beam for the photolytic D-atom beam was not possible, since the DH produced in the photolytic source had a very broad, non-thermal velocity distribution. The DH impurity in the D-atom beam is also characterized by a wide distribution of DH vibrational and rotational states that are unique to the D/H atom abstraction reactions.[38,39]

The raw reactive scattering TOF spectra were corrected for the modulated background signal by scaling the fits to the background TOF spectra at the individual LAB angles to the DH reactive scattering data at flight times beyond those kinematically allowed in the D + H_2 reactive collisions. The fact that the two significant background contributions were measurable allowed the correction of the TOF spectra to be made with confidence. A computer program was written that found the best fit of the two background components using the constraint that the resultant signal was zero at long flight times. The TOF spectra at a given LAB angle for a given experimental run were combined before stripping the background from

the data. Since the intensity of the D-atom-beam-correlated background tended to vary between experiments, the results from individual experiments were stripped individually and then added together to give the final TOF spectra.

The kinematic diagram for the $E_c = 1.01$ eV reaction is shown in Figure 3-15. This velocity vector diagram illustrates the CM→LAB transformation for this reaction and allows qualitative interpretation of the LAB TOF spectra. The corrected TOF spectra at $E_c = 1.01$ eV are shown in Figure 3-16. These spectra represent the summed results of the six major experimental runs for D + p-H_2. Consideration of Figure 3-15 shows that at a LAB angle of 27.5°, for example, four peaks might be observed in a TOF spectrum, corresponding to the forward and backward scattered DH vibrational states. Examination of the TOF spectra indicate that the backward scattered DH(v=0) and DH(v=1) states are resolved, most notably from 23° to 32° (see Figure 3-30 also). The high LAB-velocity forward-scattered signal is compressed into fewer TOF channels, though, and the resolution is not sufficient to resolve the DH(v) states in the forward direction. At the LAB angles closer to the D-atom beam (10°, 12° and 14°), a very fast narrow peak corresponding to DH scattered as far forward as $\theta_{cm} = 20°$ is observed, followed by a large, broad signal due to the elastic scattering of DH in the primary beam. At wide angles ($\Theta_{LAB} = -14°$ and 50°, for example), the forward/backward structure in the TOF spectra disappears as the edge of the CM recoil velocity circle is reached. In general, the shape of the slow TOF signal in the small LAB angle data has the greatest uncertainty due to the significant background corrections which were necessary in the angular range < 20°.

The kinematic diagram for the E_c = 0.53 eV reaction is shown in Figure 3-17. The corrected TOF spectra at E_c = 0.53 eV are shown in Figure 3-18. In spite of the much lower reactive cross section at this lower energy, the signal in this crossed-molecular-beams experiment is quite intense. This is due to the favorable kinematics that result from the smaller CM recoil velocities of the products. DH (v=1) has a small yield at this nominal collision energy, but a weak feature attributable to this state is observed at LAB angles less than 32°. The amount of fast, forward scattered product is much lower at this collision energy.

3.4 Laboratory Angular Distributions

The LAB angular distributions were generated by integrating the corrected TOF spectra. The extensive raw data set shown in Figures 3-7 and 3-8 was used after the background components were stripped off. For the angular distribution, each corrected 2×10^5 shot TOF spectrum was integrated individually, with the intensities time-normalized to the reference angles previously mentioned. The LAB angular distributions for the E_c = 1.01 and 0.53 eV reactions are shown in Figures 3-19 and 3-20. The error bars represent 90% confidence limits on 3 to 4 data points per angle. In the E_c = 1.01 eV angular distribution, the ratio of the intensities of the reference angles, 27.5° and 32°, are best known, as these angles were measured in every experiment.

Qualitative examination of Figures 3-19 and 3-20 show that the angular distribution broadens considerably at the higher collision energy. Detailed analysis of the scattering results will be presented in the next section. Evidence of the elastic scattering of DH at LAB angles less than 15° is seen in

the E_c = 1.01 eV angular distribution. At the LAB angles greater than 15°, the background subtraction procedure removed all of this elastic scattering signal.

4. Analysis

The analysis and interpretation of crossed-molecular beams scattering data involves the determination of the DCS from the LAB data. The possible CM recoil velocities for the DH(v) products are shown in Figures 3-15 and 3-17 for the two nominal collision energies studied. The kinematic diagrams show that at most LAB angles, the CM→LAB transformation is double-valued, i.e., at a given LAB angle, both forward and backward scattered DH products are observed. Forward/backward scattering of the DH product is conventionally defined relative to the incident D-atom velocity vector in the CM, with backward scattering corresponding to θ_{cm} = 180°, where θ_{cm} is defined in Figure 3-15.

Accurate inversion of scattering data to the CM frame is a difficult proposition. Due to the finite resolution of the crossed beams and the detection scheme, the actual collision events are described by a multitude of kinematic diagrams. Use of a single-kinematic-diagram transformation from the LAB to the CM can yield qualitative insights to the nature of the DCS, especially in cases where the kinematics of the reaction are dominated by a well defined beam.[40] This approach and the results obtained with it will be described in Section 4.1. Methods to directly deconvolute the LAB scattering data from the effects of the finite experimental resolution have been

discussed by Siska.[41] This approach has problems with any noise in the scattering data, however, and has not seen considerable use.

The most common approach to analyzing scattering data is the forward convolution method, wherein predicted or guessed CM angular and velocity distributions are numerically averaged over the apparatus distributions and compared to the LAB data.[42] For the D + H_2 experiments, a Monte Carlo simulation program was used for detailed comparison of the LAB data with the theoretical predictions of Zhang and Miller, and, subsequently used to generate the best-fit DCS for the data. These results will be discussed in Section 4.2., and the rest of the chapter.

4.1 Direct Inversion

As discussed by Wolfgang and Cross,[40] the LAB-frame and CM velocity-flux distributions are related by

$$\frac{I(v)}{v^2} = \frac{I(u)}{u^2} \qquad (3).$$

In this equation, v and u are the LAB and CM velocities of the products, respectively, and I(v) and I(u) are the associated velocity-fluxes associated with them. Using this relation, the individual TOF spectra were normalized to the LAB angular distribution, transformed to the quantity $I(v)/v^2$, plotted on the kinematic diagram as a function of LAB angle and velocity, then represented as a contour plot of the velocity-flux distribution weighted by $1/u^2$. Prior to inversion, the data was subjected to nine-point polynomial smoothing[43], since the direct inversion is very sensitive to noise in the data.

A contour map of this type is often referred to as a 'Cartesian' plot, since it shows the flux per unit area in Cartesian LAB and CM velocity coordinate systems. This view of the data cannot, however, correct for the beam angular and velocity distributions and the detector resolution.

The direct-inversion Cartesian contour map for the D + H_2 reaction at E_c = 1.01 eV is shown in Figure 3-21. At this collision energy, the DCS is observed to peak at θ_{cm} = 125°. A wider range of collision geometries can overcome the higher non-collinear barrier at higher collision energies, resulting in more forward scattering. The minor DH (v=1) channel cannot be seen with the resolution of this contour map. The E_c = 0.53 eV Cartesian contour plot is shown in Figure 3-22. At this low collision energy, the DCS for DH products peaks in the backward direction (θ_{cm} = 180°) . This is the expected result for a direct chemical reaction dominated by collinear geometries, such as the D + H_2 reaction at low collision energies. This experiment is the first to directly measure the change from backward scattering at low collision energies to sideways peaking at higher collision energies. These qualitative results at the two collision energies show good accord with the theoretical results of Zhang and Miller, with the predictions showing a backward-peaking DCS at E_c = 0.51 eV, with the peak moving forward to 120° at E_c = 0.98 eV.

4.2 Monte Carlo Simulation

For this fundamental elementary reaction, it is important to undertake a detailed comparison of the experimental results with the available theoretical predictions. In particular, collaboration with Zhang and Miller

resulted in the generation of theoretical DCS's for this isotopic variant of the H_3 reaction over the experimentally relevant energy range. To effect this comparison, a detailed Monte Carlo simulation of the LAB data was undertaken using the complete $D + H_2(0,0) \rightarrow DH(v,J) + H$ DCS results of Zhang and Miller. This experiment achieved vibrational-state resolution, and the vibrational state TOF contours contain significant information on the rotational state distribution as a function of angle. Due to the large spacing of the DH product quantum states, it was imperative to treat the DCS in a discrete, state-resolved fashion for a legitimate comparison with the predictions, as opposed to an approximate treatment of the CM velocity-angle distributions as continuous functions.

An importance-sampling Monte Carlo algorithm based on the treatment of the CM→LAB transformation described by Pack[44] was used for the forward convolution of the state-to-state DCS's. This program, which is discussed in more detail in Appendix A[45], took into account all aspects of the experimental averaging. The velocity and angular distributions of both beams, the resolution effects associated with the finite size of the D-atom source volume, the collision volume, and the detector ionization volume were treated explicitly. The LAB signal due to each state-to-state reactive cross section ($f \leftarrow i$) was calculated in turn, giving simulated TOF and angular distributions for comparison with the experimental data. In short, the calculated TOF signal in an MCS channel centered in time at t_n at a nominal LAB angle Ω_0 for a given DH(v,J) final state is given by the integral

$$\overline{N}_{fi}^{lab}(\Omega_0,t_n) = \int dv_1 \int dv_2 \int d\vec{r}_S \int d\vec{r}_C \int d\vec{r}_D \cdot$$
$$[U(t_{n+} - t_f) - U(t_{n-} - t_f)] \cdot$$
$$P_1(v_1) \cdot P_2(v_2) \cdot P_S(\vec{r}_S) \cdot P_C(\vec{r}_C) \cdot P_D(\vec{r}_D) \cdot N_{fi}^{lab}(\vec{v}_1,\vec{v}_2,\Omega) \qquad (4).$$

In this equation, the vectors $\vec{r}_S$, $\vec{r}_C$, and $\vec{r}_D$ refer to points in the D-atom source, scattering volume, and detection volume, respectively. The magnitude of the reagent velocities are given by v_1 and v_2, with the vectors defined by the chosen points in the apparatus volumes. The probability distribution functions for each of these variables, P(x), are inputs to the program. The U's are Heaviside step functions, which indicate that the signal goes in channel n if the flight time is between t_{n+} and t_{n-}, which define the width of the MCS channel in the simulation. The kinetic energy and TOF for the product molecule are determined by the incident particle velocities and any energy consumed or released in the reactive process yielding the final state under consideration, *f* . Finally, the number-density LAB-DCS associated with the particular reagent velocities and product recoil velocity is obtained from the theoretical DCS using the relation

$$N_{fi}^{lab}(\vec{v}_1,\vec{v}_2,\Omega_0) = \frac{v_{rel} \cdot v_{lab}}{u_3^2 \cdot |\cos \zeta|} I_{fi}^{cm}(v_{rel},\theta_{cm}) \qquad (5).$$

In this equation, v_{rel} is the magnitude of the relative velocity, which weights the kinematic diagrams by the collision frequency. v_{lab} is the detected product LAB recoil velocity, u_3 is the detected product CM velocity, and ζ is the angle between these two vectors. These factors correspond to the Jacobian

for the CM→LAB transformation for discrete exit channel velocities with number density detection.[44] The input from Zhang and Miller's calculations is the DCS for a specific DH(v,J) state as a function of scattering angle and relative velocity (or, total energy); $I_{fi}^{cm}(v_{rel},\theta_{cm})$.

In an ideal experiment, the DCS would need to be known at only the two nominal collision energies to allow comparison with the experimental data. In fact, as Figure 3-6 shows, the D-atom velocity distribution has two sharp peaks associated with the two spin-orbit states of I produced, with a broad, underlying component due to collisions in the source volume. Thus, accurate simulation of the data requires a knowledge of the energy dependence of each of the DH(v,J) differential cross sections. Zhang and Miller have provided the DH(v,J) differential cross sections at 15 total energies ranging from 0.40 eV to 1.35 eV, and with this wealth of high quality theoretical predictions, a legitimate comparison with the LAB data was possible. The total energies at which the DCS was available were 0.40, 0.45, 0.50, 0.55, 0.60, 0.65, 0.70, 0.75, 0.78, 0.85, 0.93, 0.98, 1.03, 1.09, 1.25 and 1.35 eV. The grid of theoretical predictions was sparser at the higher energies, where the calculations are considerably more computationally intensive. A finer grid of theoretical predictions over the entire energy range would be desirable for future comparisons. Using a bicubic-spline fitting procedure, continuous DCS surfaces as a function of total energy and CM scattering angle were produced. With these surfaces, the Monte Carlo program could look up the DCS for any collision and product recoil angle encountered in the simulation. The DCS surfaces used in the comparison, which are the spline-fits to Zhang and Miller's predictions are shown in Figure A-5 for reference. As described in Appendix A, the quality of the spline fit to the input data was shown to be

excellent, both in energy and angle. These surfaces, and the energy dependences of the state-to-state differential cross sections that they reveal are quite interesting, and illustrate the quantity of theoretical predictions Zhang and Miller have supplied. Several of the DH(v,J) differential cross section surfaces share certain topologies in the energy dependence, and we can look forward to a future time when all of these features and their relation to the PES will be understood.

To check the accuracy of the Monte Carlo simulation program and the molecular beam apparatus, a study of the elastic scattering of H + He was made. Elastic scattering of D atoms at m/e = 2 was not possible due to the large detector background. H atoms were produced by photolysis of HI, with the apparatus geometry the same as that used in the D + H_2 experiments. The H atom velocity distribution was produced by a Monte Carlo simulation of the H atom TOF, as described for the D-atom beam in the experimental section. In Figure 3-23, the results of the simulation of the H + He TOF spectra are shown. The good agreement indicates that the simulation program and the scattering apparatus were both in good working order.

4.3 E_c = 1.01 eV Reactive Scattering Simulation

The results of the Monte Carlo simulation of the TOF spectra at E_c = 1.01 eV using the DCS results of Zhang and Miller are shown in Figure 3-17. The comparison of the calculated and experimental LAB angular distributions are shown in Figure 3-19. The LAB angular distribution is normalized by the average scaling factor for the two LAB angles, 27.5° and 32°, as these are the best known experimental intensities. The calculated and

experimental TOF spectra, however, are normalized to the peak intensities in each spectrum, with the relative intensities of the TOF spectra normalized to the measured LAB angular distribution. The simulation of the LAB angular distribution does not show major differences with the experimental data, given the signal-to-noise of the data. The statistical error in the Monte Carlo simulation is in all cases much smaller than the experimental errors, and is not indicated in the figures. The TOF spectra provide a more detailed comparison of the differential cross sections. Significant differences are observed between theory and experiment at several LAB angles. The overall fit to the LAB TOF data is quite impressive, however. In particular, the shape of the fast, forward scattered signal and the relative intensities of the forward/backward scattering in the simulation fit the experimental results very well.

The most striking differences between the calculated and experimental TOF's are seen at LAB angles from 20° to 40°. At angles within this range, significantly more signal was observed at flight times corresponding to rotationally excited DH(v,J) products at CM angles mostly in the backward hemisphere ($\theta_{cm} > 90°$). At the LAB angles less than 20°, a similar difference due to an increasing amount of DH elastic scattering at the small LAB angles is observed. The important point, here, though, is that the relative intensity of the differences for LAB angles greater than 20° increased as the detector moved to angles farther away from the D-atom beam, where elastic scattering of DH from the D-atom beam was shown to be insignificant. In Figure 3-24, corrected TOF spectra for the D + n-H_2 reaction are shown at several LAB angles, with the same type of systematic difference observed as in the D + p-H_2 data.

One feature that is evident in all of the E_c = 1.01 eV TOF spectra is a long tail in the data, extending out to flight times of ≈ 200 μsec. This signal is the result of the presence of slower D atoms in the beam and the broad, underlying component in the D-atom velocity distribution. At LAB angles beyond 40°, in particular, this slow component in the reactive signal becomes very significant, since the signal from the E_c = 0.53 eV reaction peaks strongly at larger LAB angles, whereas the E_c = 1.01 eV reaction signal intensity is decreasing. The effect of the D-atom velocity distribution on the TOF data is dependent upon the DH(v,J) final state under consideration. Collision energy distributions weighted by the theoretical DCS were generated to illustrate this effect. In Figure 3-25, these distributions are compared to an unweighted collision energy distribution. As the figure shows, the low J DH(v=0) product states have a significantly higher reactive cross section at the lower collision energies, accentuating the effect of the slow D atoms on the reactive signal. For higher DH(v,J) states, the energetic threshold for reaction acts as an energy selector, and only the faster D atoms react. The unweighted peak collision energy is 1.01 + .04 / - .06 eV. In the simulation, the few collisions that occurred with E_c > 1.1 eV were treated as having the same DCS as 1.1 eV collisions.

The Monte Carlo code can also produce other diagnostic distributions, such as the distribution of beam crossing angles, and the nominal CM scattering angles that a given LAB scattering angle corresponds to. The beam crossing angle had a value of 90° ± 10° at the FWHM. For DH(v=0,J=0) product at a LAB angle of 27.5°, the forward scattered component had an average CM scattering angle of 63 ° ± 7° (one std. deviation), while the backward scattered component had a nominal CM scattering angle of 157° ±

12°. The distribution of CM angles corresponding to a given LAB angle is a function of internal state. For example, the average forward/backward scattering angles of DH (v=1, J= 0) product at Θ_{LAB} = 27.5° were 80° ± 13° and 170° ± 10°, respectively.

Several attempts were made to fit the data by simply altering the integral cross sections for the DH(v,J) states. Both the LAB angular distribution and the TOF spectra were sensitive to changes in the peak of the rotational state distributions by ± 1 quanta. The differences between the simulation and the TOF spectra were not remedied by these changes. Increasing the DH(v=1) and DH(v=2) integral cross sections filled in some of the 'missing' signal in the theoretical predictions. This reduced the quality of the fit for the slower, backward scattered DH(v=1) in the well-resolved spectra at Θ_{LAB} = 27.5°, 30° and 32°. Thus, it was concluded that changes in the state-to-state differential cross sections were necessary to fit the LAB data.

4.3.1 Best-Fit DCS at E_c = 1.01 eV

The DH(v,J) states responsible for the differences between theory and experiment may be determined by examination of the kinematic diagram for the E_c = 1.01 eV D + H_2 collisions (Figure 3-15). Even though rotational states are not resolved, the fact that vibrational states are resolvable shows that the experimental resolution is high enough to identify the DH(v,J) states in question. For example, measurements at Θ_{LAB} = 27.5° were taken because the best possibility for rotational-state resolution occurred at this angle. Referring to Figure 3-15 shows that the DH(v=0,J=10) circle is cut at θ_{cm} = 95° (TOF ≈ 50 μsec), then the DH (v=0,J=11) state is cut tangent to the maximum-CM-recoil-

velocity circle, at θ_{cm} = 120-140° (TOF ≈ 55 - 65 μsec). Finally, DH (v=0,J=10) is sampled again at θ_{cm} = 165° (TOF ≈ 75 μsec). In addition, DH(v=1,J=5) is nearly coincident in TOF with DH(v=0,J=10), DH (v=1,J=6) comes between DH(v=0,J=10) and DH(v=0,J=11), and DH(v=1,J=7) has a slightly smaller CM recoil velocity than DH(v=0,J=11). These coincident states made resolution of the DH(v,J) states impossible with a non-state-selective detector. In practice, of course, there is a significant broadening of the LAB data due to the various apparatus functions, but this gives an idea of the approach taken to identify the specific DH(v,J) differential cross sections which showed differences between theory and experiment.

The differences between theory and experiment were fit using the Monte Carlo simulation program iteratively. This involved changing the appropriate DH(v,J) DCS's and rerunning the simulation for each iteration. The success of the changes was indicated by comparison with the LAB TOF and angular distributions. The TOF spectra were used as the most important criteria in the iterative fitting process, as the signal-to-noise ratios for these spectra are typically higher than for the LAB angular distribution. The LAB angular distribution was very useful for ruling out certain changes in the DCS, however. The DCS was only modified at the point closest to the nominal collision energy, E_{tot} = 1.25 eV, corresponding to a collision energy of E_c = 0.98 eV, so references to the comparison with the theoretical predictions will refer to this energy. In the simulation process, new DCS surfaces such as those shown in Figure A-5 were generated to model the entire experimental collision energy distribution. Since significant differences between theory and experiment were observed at angles beyond those where DH(v=1) and DH(v=2) made significant contributions, it was clear that the DH(v=0)

differential cross sections needed to be modified. The approach taken was that DH(v=0,J) DCS's were modified to fit the data first, with DH(v=1) and DH(v=2) DCS's used only when necessary.

The best-fit to the TOF data is shown in Figure 3-26, while Figure 3-27 shows the fit to the LAB angular distribution. The TOF spectra are fit much better by the simulation with the best-fit DCS. The LAB angular distribution fit is not better than the original simulation, however, but is not unreasonable. In the TOF spectra, the differences between simulation and experiment for the rotationally excited DH(v,J) products that arrive in the middle of the TOF spectra at LAB angles greater than 20° are removed with the modified DCS. The DH(v=2) integral cross section was also increased by a factor of three at E_{tot} = 1.25 and 1.35 eV in order to fit a weak feature attributable to DH(v=2) in the TOF spectra at LAB angles from 20° to 25°.

In Figure 3-28, the best-fit DCS results at E_{tot} = 1.25 eV are shown together with the predictions of Zhang and Miller. The largest deviations between theory and experiment are observed for DH(v,J) final states from (v=0 , J=3) to (v=0 , J=11). Significant deviations were also observed for (v=0 , J=12) and (v=1, J= 0-8). The DCS curves for a given DH(v) state are plotted on the same scale to provide an idea of the significance of each state to the overall dynamics of the reaction. Due to the energy dependence of the reactive cross sections and the presence of the lower velocity D atoms in the beam, the fits to the TOF spectra are sensitive to the relative magnitudes of the different DH(v,J) excitation functions. The higher DH(v,J) states are detected with greater sensitivity in a crossed-molecular-beams experiment due to the smaller CM recoil velocities and the nature of the CM→LAB

transformation (see equation 5). For this reason, the changes in these DCS's, while small on a relative scale, were important for obtaining the best-fit.

The best-fit curves show that the higher DH(v,J) DCS's are generally broadened in the backward hemisphere ($\theta_{cm} > 90°$). More forward scattering, at CM angles as small as $\theta_{cm} = 60°$, was also observed for several states, most notably DH(v=0,J=5 to 11). The best-fit DH(v=1,J) DCS's were in all cases more backward-peaked than the theoretical predictions. Due to the number of DH(v,J) states involved and the lack of rotational-state resolution in the experiment, these best-fit state-to-state differential cross sections cannot be said to be unique. The relative magnitude and CM angular range of the corrections to the theoretical DCS are accurate representations of the significance of the differences observed between the theoretical predictions and the LAB data. Changes in the shape of these curves on the order of ± 10 % led to a decrease in the overall quality of the fit.

4.3.2 Integral Cross Sections at $E_c = 1.01$ eV

Integration of the best-fit DCS curves yields the DH(v,J) rotational distributions shown in Figure 3-29, with the values given in Table 3-1. The relative integral cross sections are obtained from the DCS by numerical integration[46];

$$\sigma = \int_0^{\pi} \sigma(\theta)\sin\theta d\theta \qquad (6).$$

The integral cross sections are much less sensitive to the differences between theory and experiment than the DCS. For DH(v=0) product , <J> = 6.7 for the best-fit DCS, while Zhang and Miller's result is <J> = 6.3. Thus, the experimental result shows more rotational excitation. Once the best-fit DCS was found, the easiest way to illustrate the sensitivity of the LAB data to the DCS was to alter the integral cross sections, keeping the shapes of the best-fit DCS's constant. This approach was tried with the theoretical DCS as mentioned above, but changes in the theoretical integral cross sections could not fit the data. Two arbitrary rotational distributions ('Cold' and 'Hot'), shown in Figure 3-29 and given in Tables 3-1 and 3-2 were used, which shifted the peak of the best-fit DH(v,J) rotational distributions by ± 1 quantum. As the TOF spectra at Θ_{LAB} = 27.5° and 32° shown in Figure 3-30 indicate, using these alternate rotational distributions noticeably degraded the fit to the data. The cold rotational distribution (<J> = 6.2, peak J = 6) showed too much backward-scattered DH(v=0) and DH(v=1) in the TOF spectra. The fit to the angular distribution (shown in Figure 3 - 27) was actually a little better than the best-fit DCS, however. The hot rotational distribution (<J> = 7.1, peak J = 8) caused the vibrational resolution for the DH(v=1) and DH(v=0) to wash out significantly in the 27.5° spectrum. In addition, the hot rotational distribution had a significantly poorer fit to the angular distribution than the best-fit DCS.

The experimental DH(v=1)/DH(v=0) branching ratio is lower than predicted by the calculations of Zhang and Miller. Table 3-3 shows that experimentally, the v=1/v=0 ratio was 0.11, while the calculations predict v=1/v=0 = 0.13. This difference is probably not significant, however, due to the stated bias in the fitting procedure towards DH(v=0,J) states. The

DH(v=2,J) integral cross section three times higher than predicted was needed to fit the data from LAB angles of 20° to 25°. The nominal collision energy is very close to the DH(v=2) energetic threshold, so the integral cross section was increased at both E_{tot} = 1.25 eV and 1.35 eV. One possibility that must be kept in mind in this case is that the electron-impact ionization cross section for DH(v=2) may be significantly larger than that for DH(v=0) and DH(v=1). In the case of vibrational excitation of the parent molecule (DH), fragmentation to daughter ions often becomes more important, however , which would decrease the detection efficiency for DH(v=2). There is no detailed data available on the relative electron-impact cross sections for vibrationally excited DH.

The most significant possible source of error in these measurements is the correction of the TOF data with the measured modulated background signals. The detailed test measurements on the background sources that were performed have allowed correction of the data with the true functional form of the modulated background. Possible systematic errors arising from this part of the data processing will not be considered further. Second, the ambiguities involved in generating the best-fit state-to-state differential cross sections from the rotationally unresolved TOF data are difficult to quantify. Significant changes in the magnitudes of the corrections to the various DH(v,J) DCS's cannot fit the data, but it would be difficult to express this in a compact form given the number of states involved.

4.4 E_c = 0.53 eV Reactive Scattering Simulation

The results of the Monte Carlo simulation at the nominal collision energy of E_c = 0.53 eV are shown in Figure 3-18, with the comparison of the LAB angular distributions shown in Figure 3-20. The fit to the LAB angular distribution is quite good, given the signal-to-noise ratio of the experimental data. In the case of the TOF spectra, however, once again significant differences between the simulation and the experimental data are observed (see Figure 3-18). The data at all LAB angles less than 45° tend to show more signal at small CM velocities, near the 'middle' of the TOF signals, than the theoretical predictions suggest. The forward/backward scattering intensities show very good agreement, as do the shape of the forward scattered rising edge of the signal and the backward scattered falling edge. TOF data for the D + n-H_2 reaction at several LAB angles are shown in Figure 3-31. The simulations of these spectra show similar differences with the TOF data that are similar to those observed in the D + p-H_2 experiment, although the differences are larger in magnitude for the D + n-H_2 experiment at the lower collision energy. Efforts made to fit the data by changing the integral cross sections, keeping the shapes of the theoretical DCS's constant, were once again unsuccessful.

The effect of the D-atom velocity distribution on the TOF spectra was observed to a greater extent in the E_c = 0.53 eV spectra. At $\Theta_{LAB} < 32°$, two fast, forward scattered peaks were observed. Simulation of the data showed that the fastest of the two peaks is due to the forward scattered DH formed by collisions at energies near E_c = 1.01 eV due to the fast D atoms present in the

D-atom beam. Figure 3-32 shows the cross-section-weighted collision energy distributions for several of the DH product states in this lower energy experiment. The peak at the nominal E_c of 0.53 eV has a FWHM of +.024/-.048 eV. The reactive collisions occurring for the excited DH(v,J) products are significantly skewed to higher energies.

4.4.1 Best-Fit DCS at E_c = 0.53 eV

Iterative use of the Monte Carlo simulation program allowed the best-fit DCS for the DH(v,J) states at E_c = 0.53 eV to be determined as described above. The changes in the theoretical DCS were made at E_{tot} = 0.78 eV (E_c = 0.51 eV), which was the closest point to the peak collision energy in the theoretical calculations. In Figure 3-33, the best fits to the TOF spectra for the D + p-H_2 reaction are shown. Figure 3-34 shows the best fit to the LAB angular distribution. The differences between the theoretical simulation and the TOF spectra seen in Figure 3-18 are largely removed by the modified DCS, and the best-fit LAB angular distribution also fits the experimental data well. The remaining differences between theory and experiment are due to the strong energy dependence of the reactive cross sections for the higher J DH(v,J) products. Using the changes made to the theoretical DCS at 0.51 eV only to fit the differences between the experiment and simulation TOF's resulted in a nearly perfect fit to the data, however, inclusion of these changes into the complete energy-dependent theoretical predictions resulted in the fits shown in Figure 3-33, which still exhibit some differences between theory and experiment at, for example, LAB angles of 30°, 32° and 40°. In Figure 3-35, the best-fit DCS curves at E_c = 0.51 eV are plotted together with the theoretical

results of Zhang and Miller. Changes in the DCS for higher energy collisions has a significant effect on the simulation of the E_c = 0.53 eV data. This was not true for the E_c = 1.01 eV data. The largest changes in the DCS were made for the product DH (v=0, J= 4 - 7) states in the backward hemisphere (θ_{cm} > 90°). The changes made are not largest at θ_{cm} = 180°, however, indicating that at this lower energy, slightly more sideways scattering is occurring than the calculations of Zhang and Miller indicate.

4.4.2 Integral Cross Sections at E_c = 0.53 eV

The relative DH(v,J) integral cross sections obtained by integration of the best-fit DCS at E_c = 0.53 eV are shown in Figure 3-36 and listed in Table 3-4. Once again, the experimental result shows more rotational excitation than the theoretical predictions. For the experimental rotational distribution, <J> = 3.6, while Zhang and Miller's results indicated <J> = 3.0. The fact that the magnitude of the differences in rotational distributions is larger in the lower collision energy experiment is probably due to the strong collision energy dependence for all of DH(v,J) states, particularly the higher rotational states which are near or below threshold at the nominal collision energy. The strong collision energy dependence of the 0.53 eV simulation makes these results less reliable than the 1.01 eV results. The TOF spectrum shown in Figure 3-37 at Θ_{LAB} = 32° illustrates the sensitivity of this data to a changes in the integral cross section, using a rotational distribution with a peak shifted one quantum higher (see Figure 3-36 and Table 3-4). As the spectrum shows, the hotter rotational distribution gave a broader forward-scattered peak that was inconsistent with the data.

4.5 DH Product CM Velocity-Flux Contour Maps

Cartesian CM velocity-flux contour maps were generated from the theoretical and experimental results to graphically illustrate the general trends observed in this study. These maps are recognized as one of the best ways to illustrate in one figure the full results of a molecular beam scattering experiment. These plots represent contours of the quantity $I(u)/u^2$ plotted using a surface generation routine. These maps were made using the DCS's for all the DH(v,J) states at the nominal collision energies only, so they do not show the broadening effects of the D-atom velocity distribution, which is present in the direct-inversion contour maps in Figures 3-21 and 3-22. The results for E_C = 1.01 eV are shown in Figure 3-38, while the results for E_C = 0.53 eV are shown in Figure 3-39. The contours are spaced by 0.15 in the maps, with the peaks scaled to 1. Inspection of these maps show quite clearly the broadening of the rotational distribution in the backward hemisphere that was observed at both collision energies. They also illustrate the trend from backward to sideways scattering as the collision energy increased, similar to the approximate direct-inversion contour maps. Since these plots are weighted by $1/u^2$, they exaggerate the contributions from the smaller u DH products. For example, intensity is observed within the DH(v=2) product circle in Figure 3-38(a), even though DH(v=2) only accounted for 0.5 % of the DH product.

5. Discussion

5.1 Comparison with other Crossed-Molecular-Beams Studies

As mentioned in the introduction, several crossed-molecular-beams studies of the D + H_2 reaction have been performed. The early work of Fite and coworkers[22] was a 'primitive' molecular beam experiment by modern standards: an effusive D-atom beam was used and DH product velocity distributions were measured in a very crude way. The results of their experiment at a mean collision energy of 0.48 eV showed that the DH product DCS was strongly backward-peaking, in agreement with the present results at 0.53 eV. Goetting, Mayne and Toennies[24a] performed the first doubly differential cross section measurements in which the DH-product TOF spectra were measured at several LAB angles. Deconvolution of their experimental data was hampered by an extremely broad D-atom velocity distribution produced in an arc-discharge. The data showed that the DCS for the D + H_2 reaction was peaked at a CM angle of $\approx 90°$ at the mean collision energy of E_c = 1.5 eV. The results were also shown to be in good agreement with QCT calculations by Mayne and Toennies.[32] These results show more forward scattering than the present results at E_c = 1.01 eV, which is not surprising considering the higher mean collision energy. The broad D-atom velocity distribution in these measurements prevented the resolution of product DH vibrational states.

The work of Buntin, Giese and Gentry was the first experiment to produce vibrational state-resolved differential cross sections for the D + H_2 reaction. As mentioned in the introduction, TOF spectra at single LAB angles

were measured at collision energies of 0.85, 0.95 and 1.05 eV, and at two LAB angles at 1.20 eV.[5,25] The angles were chosen to measure the backward scattered DH products. The DH product vibrational states were well resolved at 0.85 and 0.95 eV. At the higher energies, the DH(v) states were not clearly resolved in the TOF spectra, presumably due to enhanced DH product rotational excitation smearing out the DH(v) signal.[25] The experiments of Buntin, et. al., used rotatable beam sources, with variable intersection angle, to change the collision energy. For this reason, the kinematics are different from the present study, so a direct comparison of the TOF spectra is not possible.

Rotational distributions were extracted from the data of Buntin, et. al. using a Monte Carlo simulation to generate DH(v,J) final state TOF signal-shapes coupled with a least squares fitting routine which adjusted the intensity of each DH(v,J) state to achieve a best-fit to the data. The collision energy dependence of the DH(v,J) reactive cross sections was treated using the total integral cross section from QCT studies, which is not a very good approximation in light of Zhang and Miller's calculations. This treatment was also complicated by the fact that a background subtraction of arbitrary functional form was done on the data, since no information concerning the background TOF signals in their experiment was available. The rotational distributions extracted from the 0.95 eV data, in particular, are not in good agreement with Zhang and Miller's predictions[1] or the present experiments. The treatment of the modulated background in Buntin's experiment is presumably the primary cause of this discrepancy. Now that the detailed predictions of Zhang and Miller are available, a more accurate simulation of Buntin's experiments should be possible, taking into account the collision

energy dependence of the reactive cross section for each DH(v,J) state. When this simulation is done, a better comparison of the present experiments with the results of Buntin, Giese and Gentry will be possible.

5.2 Comparison with DH Product-State Distribution Measurements

Two studies of the DH(v,J) product-state distribution in the D + H_2 reaction have been reported. Valentini's group[13] measured product-state distributions for DH(v=0,J) and DH(v=1,J) at collision energies of 0.67 and 0.79 eV. These energies lie between the two nominal collision energies studied in the present experiments, and due to the strong energy dependence of the DH(v,J) cross sections it is difficult to make any direct comparisons of the experiments. The measured DH(v=0,J) state distributions showed more intensity than predicted by Zhang and Miller for $J < 4$, while the measured DH(v =1,J) distributions showed more rotational excitation than Zhang and Miller's results.[1] The measured DH(v=1) cross section was observed to decrease as the collision energy was raised from 0.69 to 0.78 eV. This was interpreted as being due to a Feshbach resonance producing DH(v=1) at the lower collision energy. This behavior was not observed in Zhang and Miller's study.

Recent work in Zare's laboratory[14] on the reaction D + H_2 (v=1,J=1) $\rightarrow$ DH + H has also yielded measurements for the D + $H_2 \rightarrow$ DH + H reaction at collision energies ranging from E_c = 0.98 to 1.06 eV. The experimental product-state distributions for DH(v=1,J) compare very well with the results of Zhang and Miller at E_{tot} = 1.32 eV.[47] The range of nominal collision energies in this experiment is due to the fact that the laser used to photolyze

the DBr precursor of the D atoms is also used in the vibrotational state-selective detection of DH, and must therefore be tuned to a slightly different wavelength for each DH(v,J) product state detected. The crossed-molecular-beams results reported in this chapter for the minor DH(v=1) product has a greater uncertainty associated with it due to the non-state-selective detection scheme, so, although the differences observed in the present study for the DH(v=1,J) distribution are larger than those measured by Kliner and Zare, this may not be significant. Further measurements of the $D + H_2 \rightarrow DH(v=0,J) + H$ product-state distributions will be necessary for a detailed comparison with our results.

5.3 Implications for the H_3 Potential Energy Surface

The best-fit DCS results presented at E_c = 1.01 eV and 0.53 eV represent the first direct comparison of experimental differential cross sections with accurate quantum scattering calculations. The results of Zhang and Miller[1], which were instrumental in the simulation of the LAB data, are the first fully-converged 3-D quantum mechanical scattering results for the $D + H_2$ reaction. Integral cross sections calculated by Zhang and Miller for the $H + H_2$ reaction have been duplicated by two other groups, using different techniques.[48] The $D + H_2$ system is more difficult to treat than $H + H_2$, however, due to the loss of particle symmetry and the need for calculations at higher total angular momenta to achieve convergence in 3-D, and these results have yet to be duplicated. It appears, though, that the technique gives accurate results, so it will be assumed that the calculations represent the true dynamics of the $D + H_2$ reaction on the LSTH surface. Therefore, the

interpretation of the present experimental results will focus on the implications of the experimental results for the PES.

Two points must be kept in mind regarding the significance of the comparison of the present experimental results with Zhang and Miller's theoretical predictions. First, the grid of total energies at which theoretical predictions were available was sparser at the higher energies. If the state-to-state differential cross sections do not vary smoothly between the calculated points, the simulation of the experimental data will be sensitive to the density of the energy grid of the theoretical predictions. As the calculations become more efficient, or computers become faster, any questions concerning the effects of the energy-grid of the theoretical predictions will be answered. Second, in the D + p-H_2 scattering experiment, 20 to 30 percent of the H_2 reagent was in J = 2, while the theoretical predictions are for H_2(J=0). Significant changes in DCS are not expected in going from H_2(J=0) to H_2(J=2). Recent QCT calculations have shown a decrease in reactive cross section for the D + H_2(v=1,J) reaction as J increases, but the DCS did not change significantly between reactant H_2(v=1,J=0) and H_2(v=1,J=4).[34] In addition, the experimental results showed that the TOF spectra did not change significantly in the D + n-H_2 reaction, for which ≈ 75% of the H_2 is in J = 1.

At E_c = 0.53 eV, the experimental results indicate that DH(v=0, J = 3-7) DCS's peak farther away from direct backward scattering, as the contour maps in Figure 3-39 show. The implications of these results for the H_3 PES are clear; partial waves with larger angular momentum contribute to the reaction at this energy. The classical picture corresponding to this result is that larger impact parameters lead to reaction, resulting in higher product rotational excitation. A 'softer' bending potential for the H_3 complex near E_{tot} = 0.78 eV

could be responsible for allowing collisions of this sort to lead to reaction. Due to the collision energy dependence of the reactive cross sections, some of the differences between the predictions of Zhang and Miller and the best-fit DCS at E_c = 0.51 eV should be distributed over the DCS's for higher energy collisions. The qualitative result that more sideways scattering is occurring at lower collision energies than predicted remains unaffected by these considerations, however.

At the higher collision energy, E_c = 1.01 eV, the experimental results once again show more product rotational excitation, with broadening of the DH(v=0,J) DCS's, mostly in the backward hemisphere. As the contour maps in Figure 3-38 show, however, a significant enhancement of the forward scattered DH was also observed. The DH(v=1,J) DCS's were seen to be more sharply backward peaked than the DH(v=0,J) states, which is not unreasonable, since typically smaller impact parameter collisions result in vibrational excitation, leading to backward scattering in the CM. Once again, the bending potential and the effect it has on D-H_2 as the reactants approach and on DH-H as the products recoil is likely to be responsible for the differences observed between the theoretical and experimental DH(v,J) differential cross sections. In this case, the observation of more backward scattering indicates that perhaps a stiffer bending potential at E_{tot} = 1.25 eV is resulting in higher product rotational excitation at these energies. This is somewhat counter-intuitive, and indicates that the influence of the bending potential may be different in the entrance and exit channels. The results at this collision energy do not show the same sensitivity to the experimental collision energy spread, since the nominal collision energy is well above threshold for most of the DH(v,J) states. Regrettably, measurements of the

DCS for a non-central potential like that operative in a chemical reaction cannot be inverted directly to yield the inter-particle potential, so further scattering calculations on new *ab initio* potential energy surfaces will need to be done to assess the significance of the differential cross sections reported here.

While theoretical studies of the effect of the bending potential on state-to-state differential cross sections have yet to be done, some information on the effect on product-state distributions is available. Blais, Truhlar and Garrett examined the H + D_2 product-state distributions produced by QCT calculations on two potential energy surfaces, the LSTH surface[1,2] and an identical surface for collinear geometries, with a softer bending potential.[49] More rotational excitation was observed on the modified LSTH surface, but the mean DH product CM scattering angle did not change. More recently, a 3-D quantum scattering study of the PES sensitivity of the product-state distributions for the H + H_2 reaction has been performed.[20] This work compared the energy dependence of the H_2(v=1,J=1,3) cross sections obtained on the LSTH and DMBE *ab initio* surfaces. These surfaces differ somewhat at the collinear saddle point, with more significant differences for bent geometries, with the DMBE surface having the softer bending potential. The energy dependence of the reactive cross sections was not observed to change significantly, but the calculated cross sections were somewhat higher on the DMBE surface, due to the lower barrier height. Future studies of the sensitivity of state-to-state DCS's to changes in the PES will be of most interest for comparison with the present experimental results.

The DH(v=2,J) integral cross sections at $E_c > 0.98$ eV were three times greater in the best-fit to the experimental data than predicted by Zhang and

Miller. The predictions indicate that < 0.2 % of the DH products at E_{tot} = 1.25 eV are in DH(v=2), so a factor of three change in the DH(v=2) product yield does not significantly change the overall picture of the dynamics of the D + H_2 reaction. This crossed-molecular-beams experiment is very sensitive to the low recoil velocity DH(v=2), and, assuming that no significant difference in ionization efficiency for these products occurs, this difference is significant. However, since DH(v=2) is only produced in the highest energy collisions, the DH(v=2) signal is very dependent on the energy dependence of the reactive cross section and the collision energy distribution in the experiment. Perhaps the predicted DH(v=2) integral cross sections would increase significantly on the DMBE surface, giving better accord with this experiment.

6. Conclusions

The crossed-molecular-beams experiments described in this chapter were difficult. Future improvements of both the sensitivity and resolution of these experiments, which used non-state-selective mass spectrometric detection of reaction products, will be a difficult proposition. The next generation of differential cross section measurements for this elementary reaction will require rotational-state resolution to make a more critical comparison with the rapidly advancing field of theoretical chemical dynamics. Sensitive laser-based, state-selective detection techniques hold the most promise for the advances required to achieve this goal.

The results presented in this chapter constitute the highest-resolution, most complete differential cross section measurements to date for the fundamental elementary reaction D + $H_2 \rightarrow$ DH + H. This is the first

scattering experiment to have sufficient collision-energy tunability to directly measure the shift from backward scattering at low collision energies to increased sideways scattering as the collision energy increases. This work also marks the first direct comparison of DCS measurements with fully converged 3-D quantum scattering calculations[1] performed on the accurate *ab initio* LSTH PES, which is the best known for any chemical reaction. The LAB data show a level of overall agreement with the theoretical predictions of Zhang and Miller that indicates that the theoretical understanding of this reaction and the PES which governs it is good over the entire experimentally accessible energy range. Significant differences between the theoretical and best-fit DCS's for rotationally excited product DH(v,J) states were observed at both collision energies, however, that indicate that the bending potential of the PES may need to be reexamined in greater detail. Future theoretical studies of the sensitivity of the DH(v,J) differential cross sections to the PES and the calculation of new *ab initio* PES's with emphasis on the quality of the H_3 bending potential should answer some of the questions raised by these differential cross section measurements.

1 J.Z.H. Zhang and W.H. Miller, J. Chem. Phys., **91**, 1528 (1989).

2 a). B. Liu, J. Chem. Phys., **58**, 1925 (1973).

b). P. Siegbahn and B. Liu, J. Chem. Phys., **68**, 2457 (1978).

3 D.G. Truhlar and C.J. Horowitz, J. Chem. Phys., **68**, 2466 (1978); *ibid.*, **71**, 1514 (1979).

4 B. Liu, J. Chem. Phys., **80**, 581 (1984).

5 S.A. Buntin, C.F. Giese and W.R. Gentry, J. Chem. Phys., **87**, 1443 (1987).

6 T. Dreier and J. Wolfrum, Int. J. Chem. Kin., **18**, 919 (1986).

7 D.G. Truhlar and R.E. Wyatt, Ann. Rev. Phys. Chem., **27**, 1 (1976).

8 D.P. Gerrity and J.J. Valentini, J. Chem. Phys., **81**, 1290 (1984).

9 a). E.E. Marinero, C.T. Rettner and R.N.Zare, J. Chem. Phys., **80**, 4146 (1984).

b). K.D. Rinnen, D.A.V. Kliner,R.S. Blake and R.N. Zare, J. Chem. Phys., In Press.

10 a). D.P. Gerrity and J.J. Valentini, J. Chem. Phys., **82**, 1323 (1985).

b). D.P. Gerrity and J.J. Valentini, J. Chem. Phys., **83**, 2207 (1985).

c). J.J. Valentini and D.P. Gerrity, Int. J. Chem. Kin., **18**, 937 (1986).

d).H.B. Levene, D.L. Phillips, J.-C. Nieh, D.P. Gerrity and J.J. Valentini, Chem. Phys. Lett., **143**, 317 (1988).

11 a). R.S. Blake, K.-D. Rinnen, D.A.V. Kliner and R.N. Zare, Chem. Phys. Lett., **153**, 365 (1988).

b). K.-D. Rinnen, D.A.V. Kliner, R.S. Blake and R.N. Zare, Chem. Phys. Lett., **153**, 371 (1988).

12 J.-C. Nieh and J.J. Valentini, Phys. Rev. Lett., **60**, 519 (1988).

13 D.L. Phillips, H.B. Levene and J.J. Valentini, J. Chem. Phys., **90**, 1600 (1988).

14 D.A.V. Kliner and R.N. Zare, J. Chem. Phys., In Press.

15 a). N.C. Blais and D.G. Truhlar, Chem. Phys. Lett., **102**, 120 (1983).

b). N.C. Blais, D.G. Truhlar and B.C. Garrett, J. Chem. Phys., **82**, 2300 (1985).

16 J.Z.H. Zhang and W.H. Miller , Chem. Phys. Lett., **153**, 465 (1988).

17 K.-D. Rinnen, D.A.V. Kliner and R.N. Zare, J. Chem. Phys., In Press

18 A. Kuppermann, in Potential Energy Surfaces and Dynamics Calculations, ed. by D.G. Truhlar, Plenum Press, New York (1981), p. 375.

19 J.-C. Nieh and J.J. Valentini, Phys. Rev. Lett., **60**, 519 (1988).

20 S.M. Auerbach, J.Z.H. Zhang, and W.H. Miller, In Preparation.

21 a) S. Datz and E.H. Taylor, J. Chem. Phys., **39**, 1896 (1963).

b) W.L. Fite and R.T. Brackmann, in Atomic Collision Processes, ed. by M.R.C. McDowell, North Holland, Amsterdam (1964), pp. 955-963.

22 J. Geddes, H.F. Krause, and W.L. Fite, J. Chem. Phys., **59**, 3421 (1973), *ibid.*, 59, 566 (1972).

23 G.H. Kwei and V.W.S. Lo, J. Chem. Phys., **72**, 6265 (1980).

24 a) R. Goetting, H.R. Mayne and J.P. Toennies, J. Chem. Phys., **85**, 6396 (1986).

b) R. Goetting, V.Herrero, J.P. Toennies and M. Vodegel, Chem. Phys. Lett., **137**, 524 (1987).

25 S.A. Buntin, Ph. D. Thesis, Univ. of Minnesota, (1987).

26 K.A. Welge, XII Intl. Symp. on Molecular Beams, Abstracts of Invited Talks and Contributed Papers (May 29-June 2, 1989, Perugia, Italy), p. I.10.

27 D.M. Neumark, A.M. Wodtke, G.N. Robinson, C.C. Hayden and Y.T. Lee, Phys. Rev. Lett., **53**, 2226 (1984).

28 B.A. Collings, J.C. Polanyi, M.A. Smith, A. Stolow and A.W. Tarr, Phys. Rev. Lett., **59**, 2551 (1987).

29 A.J.C. Varandas, F.B. Brown, C.A. Mead, D.G. Truhlar and N.C. Blais, J. Chem. Phys., **86**, 6258 (1987).

30 D.M. Ceperly and B.J. Alder, J. Chem. Phys., **81**, 5833 (1984).

31 R.N. Barnett, P.J. Reynolds and W.A. Lester, Jr., J. Chem. Phys., **82**, 2700 (1985).

32 a) H.R. Mayne, J. Chem. Phys., **73**, 217 (1980).

b) G.D. Barg, H.R. Mayne and J.P. Toennies, J. Chem. Phys., **74**, 1017 (1981).

c) H.R. Mayne and J.P. Toennies, J. Chem. Phys., **75**, 1794 (1981).

33 N.C. Blais and D.G. Truhlar, J. Chem. Phys., **88**, 5457 (1988).

34 F.J. Aoiz, V.J. Herrero and V. Saez, Chem. Phys. Lett., **161**, 270 (1989).

35 G.C. Schatz and A. Kuppermann, J. Chem. Phys., **65**, 4642 (1975), *ibid.*, **65**, 4668 (1975).

36 Y.T. Lee, J.D. McDonald, P.R. LeBreton and D.R. Herschbach, Rev. Sci. Inst., **40**, 1402 (1968).

37 a). N.F. Daly, Rev. Sci. Inst., **31**, 264 (1960).

b). H.M. Gibbs and E.D. Commins, Rev. Sci. Inst., **37**, 1385 (1966).

38 P.M. Aker, G. Germann and J.J. Valentini, J. Chem. Phys., **90**, 4795 (1989).

39 D.A.V. Kliner, K.-D. Rinnen and R.N. Zare, J. Chem. Phys., **90**, 4625 (1989).

40 R. Wolfgang and R.J. Cross, Jr., J. Phys. Chem., **73**, 743 (1969).

41 P.E. Siska , J. Chem. Phys., **59**, 6052 (1973).

42 E.A. Entemann, Ph.D. Thesis, Harvard University (1967).

43 A. Savitzky and M.J.E. Golay, Anal. Chem., **36**, 1627 (1964).

44 R. T. Pack, J. Chem. Phys., **81**, 1841 (1984).

45 The LabAvg program is an enhanced version of a program originally obtained from Dr. R.B. Walker, Los Alamos National Lab.

46 D.M. Neumark, A.M. Wodtke, G.N. Robinson, C.C. Hayden and Y.T. Lee, J. Chem. Phys., **82**, 3045 (1985).

47 W. H. Miller, pvt. communication

48 a). D.E. Manolopoulos and R.E. Wyatt, Chem. Phys. Lett., **159**, 123 (1989).
b). J.M. Launay and M. Le Dourneuf, Chem. Phys. Lett., in press.

49 N.C. Blais, D.G. Truhlar and B.C. Garrett, J. Chem. Phys., **82**, 2300 (1985).

Table 3-1: Relative DH(v=0,J) Total Cross Sections at E_{tot} = 1.25 eV

DH(v,J)	Best Fit	Z&M	Cold	Hot
0,0	0.05	0.06	0.07	0.05
0,1	0.13	0.18	0.17	0.12
0,2	0.24	0.34	0.32	0.24
0,3	0.33	0.43	0.47	0.31
0,4	0.48	0.55	0.66	0.42
0,5	0.68	0.74	0.85	0.57
0,6	0.88	0.91	1.00	0.82
0,7	1.00	1.00	0.96	0.99
0,8	0.84	0.95	0.78	1.00
0,9	0.69	0.74	0.56	0.94
0,10	0.51	0.40	0.40	0.76
0,11	0.32	0.14	0.22	0.45
0,12	0.05	0.03	0.04	0.07
<J>	6.7	6.3	6.2	7.1

Table 3-1. Relative DH(v=0,J) integral cross sections in arbitrary units for the D + H_2 reaction at a total energy of 1.25 eV, (E_c = 0.98 eV). The theoretical predictions at this energy were modified to fit the experimental results at a nominal E_c = 1.01 eV. The best-fit integral cross sections are given in the first column, with the theoretical integral cross sections of Zhang and Miller[1] given in the second column. Two arbitrary rotational distributions used in the sensitivity tests of the data are shown as 'Cold' and 'Hot'.

Table 3-2; Relative DH(v=1,J) Total Cross Sections at E_{tot} = 1.25 eV

DH(v,J)	Best Fit	Z&M	Cold	Hot
1,0	0.24	0.21	0.46	0.16
1,1	0.60	0.59	0.76	0.42
1,2	0.85	0.84	1.00	0.60
1,3	1.00	1.00	0.87	0.77
1,4	0.97	0.87	0.64	1.00
1,5	0.65	0.61	0.48	0.85
1,6	0.37	0.34	0.29	0.51
1,7	0.21	0.14	0.17	0.30
1,8	0.12	0.03	0.01	0.20
1,9	<0.01	<0.01	<0.01	<0.01
1,10	<0.01	<0.01	<0.01	<0.01
<J>	3.4	3.2	2.9	3.9

Table 3-2. Integral cross sections for DH(v=1,J) at E_{tot} = 1.25 eV; see Table 3-1 caption.

Table 3-3. Relative DH(v) Total Cross Sections at E_{tot} =1.25 eV

DH(v)	Best Fit	Z&M
0	1.0	1.0
1	0.11	0.13
2	.005	0.002

Table 3-3. Relative DH(v) cross sections at E_{tot} = 1.25 eV compared with the results of Zhang and Miller.

Table 3-4. Relative DH(v=0,J) Total Cross Sections at E_{tot} = 0.78 eV

DH(v,J)	Best Fit	Z&M	Hot
0,0	0.26	0.26	0.14
0,1	0.67	0.71	0.44
0,2	0.94	0.96	0.49
0,3	0.94	1.00	0.70
0,4	1.00	0.79	0.89
0,5	0.78	0.51	1.00
0,6	0.71	0.24	0.95
0,7	0.37	0.09	0.66
0,8	<0.01	0.02	0.19
0,9	<0.01	<0.01	<0.01
<J>	3.6	3.0	4.4

Table 3-4. Integral cross sections for DH(v=0,J) at E_{tot} = 0.78 eV, (E_c = 0.51 eV) used to fit the low collision energy data at a nominal E_c = 0.53 eV. The arbitrary rotational distribution marked 'Hot' was used in the sensitivity tests of the data.

Chapter 3 Figure Captions

Figure 3-1. Energetics of the D + H_2 → DH + H reaction, showing the collision energies studied in this experiment and the accessible DH vibrational states.

Figure 3-2. Schematic perspective view of the experimental geometry. The output of an excimer laser ,1, was polarized with a transmission polarizer, 2. The laser beam then entered the molecular beam machine, crossing a pulsed beam of DI, 3. The DI/laser interaction occurred in a differential pumping chamber, with cryo-panels, 4, assisting in the evacuation. The recoiling D atoms were collimated, forming the D-atom beam 6, which crossed the H_2 molecular beam 8, produced in a separate differential pumping chamber by the pulsed valve 7. DH products, 10, scattered into the mass-spectrometric detector, and were ionized in the electron-impact ionizer 9.

Figure 3-3. Assembly drawing showing the photolytic D-atom beam source, the H_2 beam source, crossed-beams interaction region and the entrance to the mass-spectrometric detector. Four separate chambers are shown, (1) the photolysis chamber, where the D atoms are produced, (2) the H_2 source chamber, (3) the main scattering chamber, where the beams cross, and, (4) the first region of the rotatable detector.

The excimer laser beam A entered the photolysis chamber, crossing the DI beam, which was directed into the beam catcher C, at D. Cryo-panels B assisted in pumping of the photolysis chamber. The

recoiling D atoms were collimated by three defining slits E, with the resultant D-atom beam I crossing the H_2 molecular beam at F. The H_2 molecular beam H is produced by the pulsed valve M and collimated by the skimmer G. The entrance to the detector was gated by the chopper/tube assembly J. The chopper was synchronously spun with a motor assembly K mounted on the detector. DH products L entered the first region of the detector, en route to the mass spectrometer.

Figure 3-4. Schematic diagram of the data acquisition scheme. The chopper wheel is synchronously spun. A photodiode mounted on the chopper assembly produced a clock pulse upon which the rest of the experimental timing was based. This pulse was sent to DDL 1, a digital delay generator which then triggered the DI pulsed beam. After a suitable delay the H_2 beam was triggered by DDL 2. The Laser was triggered last, by DDL 3. The DI/H_2/Laser delays had to be set to ensure that DI, H_2 and the opening on the chopper wheel were all in the correct phase to allow the D atoms to fly from the photolysis source, and the subsequently scattered DH product to enter the detector before the chopper closed. A synchronization pulse from the Laser triggered the multichannel scaler MCS for acquisition of the TOF data.

Figure 3-5. (a) D-atom TOF with the solid curve fit generated by Monte Carlo simulation program. The E vector of the excimer-laser light is parallel to the direction of detection, giving the nominal collision energy of 0.53 eV, (upper frame).

(b) D-atom TOF with **E** perpendicular to the direction of detection, giving the nominal collision energy of 1.01 eV,(lower frame).

Figure 3-6. (a) D-atom number density velocity distribution corresponding to the TOF spectrum in Fig. 3-5(a), (upper frame).

(b) D-atom number density velocity distribution corresponding to the TOF spectrum in Fig. 3-5(b), (lower frame).

Figure 3-7. Typical raw TOF spectra (m/e = 3) for the E_c = 1.01 eV D + H_2 reaction from the most complete experimental run. The LAB angles are marked on the spectra. The curves fit to the data represent the modulated background contributions to the signal: —— ; total modulated background; ····· ; D-atom-beam modulated background; - - - - - - ; H_2-beam modulated background.

Figure 3-8. Typical raw TOF spectra (m/e = 3) for the E_c = 0.53 eV reaction from the same experimental run as Figure 3-7. See caption for Figure 3-7 for curve definitions.

Figure 3-9. Raw TOF spectra (m/e = 3) for the E_c = 1.01 eV reaction recorded in a different experimental run, with lower laser power and a shorter DI beam/laser delay. The spectra at 10°, 15.5° and 18.5° were measured only in this run. See caption for Figure 3-7.

Figure 3-10. Raw TOF spectra (m/e = 3) for the E_c = 0.53 eV reaction recorded in the last experimental run. The spectra at 23° and 25° were measured only in this run. See caption for Figure 3-7.

Figure 3-11. Raw TOF spectra (m/e = 3) for the reaction D + n-H_2 → DH + H at E_c = 1.01 eV (open circles) compared with the reaction D + p-H_2 → DH + H at a LAB angle 27.5° (solid curve). The reactive scattering signal was not measurably different, but a significant difference was observed in the large peak at long times-of-flight which was produced by the H_2 beam alone.

Figure 3-12(a). TOF spectrum showing the fit to the m/e = 3 DH background produced by a p-H_2 beam at a LAB angle of 27.5°. The solid line fit to the data was generated with a 9th order polynomial.

(b). TOF spectrum at a LAB angle of 17° showing the fit to the m/e = 3 background produced by DH in the D-atom beam without a crossed beam on. The polynomial fit is shown as the solid line. The scaling between these two figures is arbitrary.

Figure 3-13. TOF spectra at m/e = 4, measured with the D-atom beam (D_2) crossing the H_2 beam at LAB angles of 10° in (a) and 20° in (b). The open points represent the signal observed with both beams on. The solid points represent the signal observed with only the D-atom beam running.

Figure 3-14. TOF spectra at m/e = 3, measured for D + p-H_2 → <u>DH</u> + H reactive scattering at E_c = 1.01 eV (solid curve) and DH + He → <u>DH</u> + He (solid points). The dashed curve fit to the DH + He TOF spectrum was generated using the DH signal measured with only the D-atom beam running.

Figure 3-15. Kinematic diagram for the D + H_2 → DH + H reaction at E_c = 1.01 eV. This velocity vector diagram shows the relationship between the CM frame and the LAB frame. The concentric circles centered at the origin of the CM frame represents the maximum CM recoil velocities for DH products in v = 0 , 1 and 2. The CM recoil velocities for DH(v=0,J=10 and 11) products are also shown.

Figure 3-16. Corrected TOF spectra at m/e = 3 for the D + p-H_2 → <u>DH</u> + H reaction at E_c = 1.01 eV. The LAB scattering angles are marked on the spectra. The solid line fit to the spectra shows the results of the Monte Carlo simulation of the data with the theoretical results of Zhang and Miller[1]. The contributions from DH(v=0) are shown as ····· ; DH(v=1) - - - - - . At LAB angles from 20° to 25°, a small contribution from DH(v=2), which appears as a solid curve, is seen near 65 μsec. At LAB angles from 20° to 40°, the simulation shows less signal in the 50 to 80 μsec range than the data.

Figure 3-17. Kinematic diagram for the D + H_2 → DH + H reaction at a collision energy of 0.53 eV. CM product recoil velocities for DH(v=0,J=0), DH(v=1,J=0) and DH(v=0, J=6 and 7) are shown.

Figure 3-18. Corrected TOF spectra at m/e = 3 for the D + p-H_2 → DH + H reaction at E_c = 0.53 eV. See Figure 3-16 caption for definition of the curves fit to the data. Significant differences between the simulation and the LAB data are seen for LAB angles from 23° to 47.5° in the 60 to 110 μsec flight-time range.

Figure 3-19. LAB angular distribution at E_c = 1.01 eV generated by integrating the corrected TOF's. The solid line shows the results of the Monte Carlo simulation with the theoretical predictions. The curves fit to the data are; DH(v=0) - - - - - ; DH(v=1) - - - - ; DH(v=2) – – – –.

Figure 3-20. LAB angular distribution at E_c = 0.53 eV generated by integrating the corrected TOF's. The curves fit to the data are; DH(v=0) - - - - - ; DH(v=1) - - - - .

Figure 3-21. Direct inversion Cartesian plot of the velocity-flux distribution for the D + H_2 reaction at E_c = 1.01 eV. The contour plot is superimposed on the kinematic diagram.

Figure 3-22. Direct inversion Cartesian plot of the velocity-flux distribution for the D + H_2 reaction at E_c = 0.53 eV. The contour plot is superimposed on the kinematic diagram.

Figure 3-23. Monte Carlo simulation of H + He → <u>H</u> + He (m/e = 1) at LAB angles of 10° and 15°. The open points represent the LAB TOF data and

the solid curve shows the results of the simulation. At 10°, some underlying broad signal due to H_2 impurity in the H-atom beam is seen.

Figure 3-24. Corrected TOF spectra for the E_c = 1.01 eV D + n-H_2 reaction at several LAB angles. Curves fit to the data have same meaning as in Figure 3-16.

Figure 3-25. Collision energy distribution generated by the Monte Carlo program. (a) unweighted $P(E_c)$, with the D-atom velocity distribution corresponding to E_c = 1.01 eV. (b) $P(E_c)$ weighted by $\sigma(E_c)$ for DH (v=0, J=0) product. (c) $P(E_c)$ weighted by $\sigma(E_c)$ for DH(v=0,J=7) product. (d) $P(E_c)$ weighted by $\sigma(E_c)$ for DH(v=1,J=0) product. (e) $P(E_c)$ weighted by $\sigma(E_c)$ for DH(v=1,J=5) product. (f) $P(E_c)$ weighted by $\sigma(E_c)$ for DH(v=2,J=0) product.

Figure 3-26. Best fit to the TOF spectra for D + p-H_2 at E_c = 1.01 eV. Curves fit to the data have same meaning as in Figure 3-16.

Figure 3-27. Best fit to the LAB angular distribution for D + p-H_2 at E_c = 1.01 eV shown as the solid curve fit to the data. The - - - - - curve shows the fit with the 'Cold' rotational distribution, (see Table 3-1). The - - - - curve shows the fit with the 'Hot' rotational distribution.

Figure 3-28. Best-fit CM differential cross sections at E_{tot} = 1.25 eV. The solid curves show the predictions of Zhang and Miller, while the dashed

curves show the DCS which gave the best fit to the experimental data. The set of curves for DH(v=0) and DH(v=1) are normalized separately.

Figure 3-29. Best-fit DH(v,J) integral cross sections at E_c = 0.98 eV, compared with the results of Zhang and Miller. The normalization of the curves is arbitrary. Solid curve with open circles are the results of Zhang and Miller. The dashed line with squares are the best fit results. The – – – – curve represents the 'Hot' distribution; the - - - - - curve represents the 'Cold' rotational distribution.

Figure 3-30. TOF spectra at Θ_{LAB} = 27.5° and 32° for E_c = 1.01 eV. The simulation using the best fit DCS is shown as the solid line; the simulation with the 'Cold' distribution is given by the - - - - curve , the simulation with the 'Hot' distribution is given by the – · – · – curve.

Figure 3-31. Corrected TOF spectra for the E_c = 0.53 eV D + n-H_2 reaction at several LAB angles. Curves fit to the data have same meaning as in Figure 3-16.

Figure 3-32. Collision energy distribution generated by the Monte Carlo program. (a) unweighted $P(E_c)$, with the D-atom velocity distribution corresponding to E_c = 0.53 eV. (b) $P(E_c)$ weighted by $\sigma(E_c)$ for DH (v=0, J=0) product. (c) $P(E_c)$ weighted by $\sigma(E_c)$ for DH(v=0,J=7) product. (d) $P(E_c)$ weighted by $\sigma(E_c)$ for DH(v=1,J=0) product.

Figure 3-33. Best fit to the TOF spectra for D + p-H_2 at E_c = 0.53 eV. Curves fit to the data have same meaning as in Figure 3-16.

Figure 3-34. Best fit to the LAB angular distribution for D + p-H_2 at E_c = 0.53 eV. The solid line shows the best-fit DCS simulation, while the dashed line shows the simulation with the 'Hot' rotational distribution.

Figure 3-35. Best-fit CM differential cross sections at E_{tot} = 0.78 eV. The solid curves show the predictions of Zhang and Miller, while the dashed curves show the best-fit to the experimental data.

Figure 3-36. Best-fit DH(v=0,J) integral cross sections at E_c = 0.51 eV, compared with the results of Zhang and Miller. The solid curve with open circles represents the results of Zhang and Miller, the dashed curve with squares is the best-fit DCS, and the – – – – curve is the 'Hot' rotational distribution.

Figure 3-37. TOF spectrum at Θ_{LAB} = 32° for E_c = 0.53 eV, showing results of the simulation using the best-fit DCS, shown as the solid line, the results of Zhang and Miller are given by the - - - - curve , and the 'Hot' distribution is given by the – · – · – curve.

Figure 3-38(a). Cartesian CM velocity-flux contour map using the best-fit DCS at E_c = 0.98 eV. The incident D atom and H_2 molecule velocity vectors in the CM are shown, as well as the possible CM recoil velocities for DH(v=0,1 and 2). Significantly increased backward scattering of

internally excited DH product is shown, as well as more forward scattering, mostly in DH(v=0), when compared with the theoretical results in (b).

(b). Cartesian CM velocity-flux contour map using the theoretical DCS of Zhang and Miller.

Figure 3-39(a). Cartesian CM velocity-flux contour map using the best-fit DCS at E_c = 0.51 eV. More rotationally excited DH is observed in the backward hemisphere compared to the theoretical DCS in (b).

(b). Cartesian CM velocity-flux contour map using the theoretical DCS of Zhang and Miller.

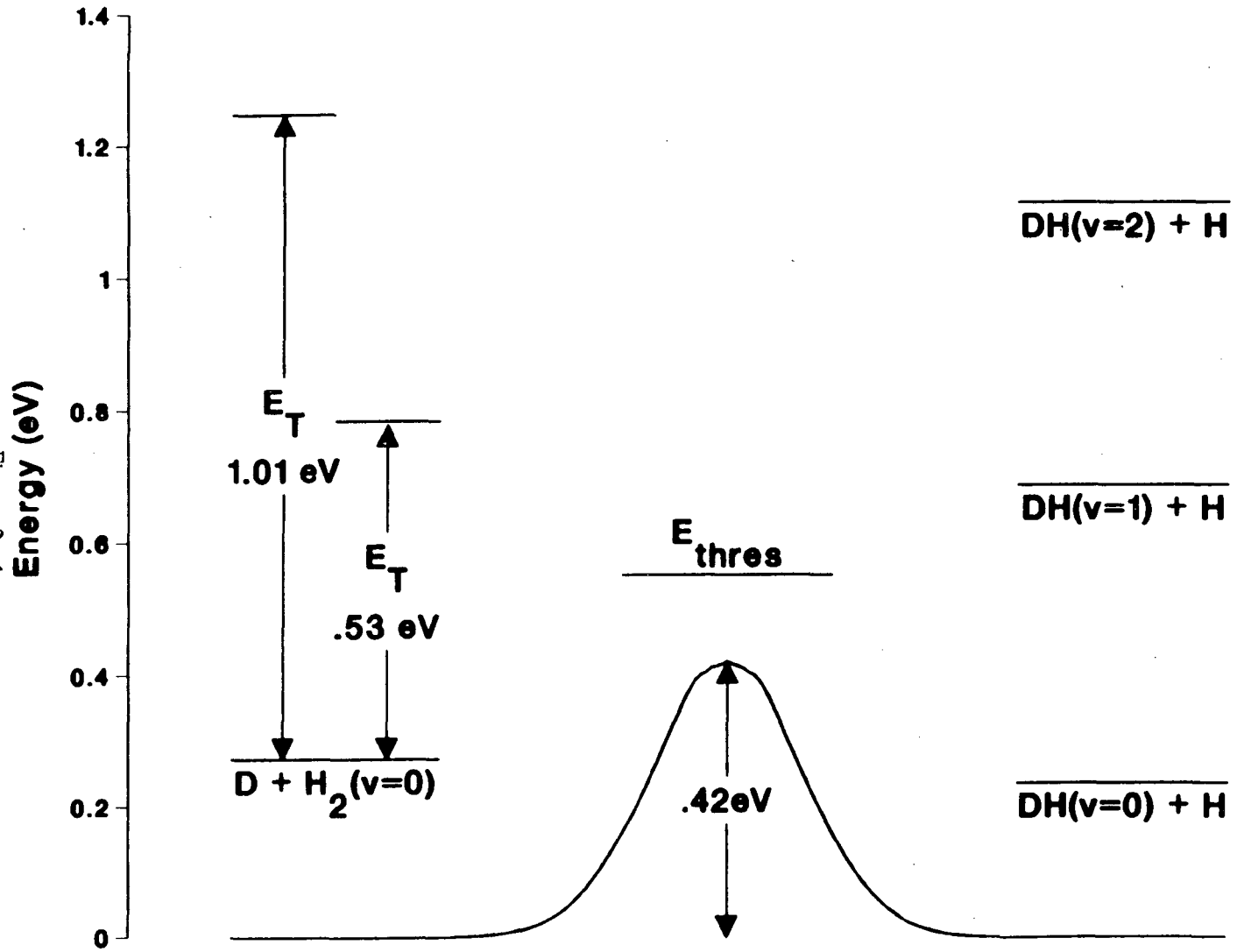

XBL 8911-4032

Figure 3 - 1

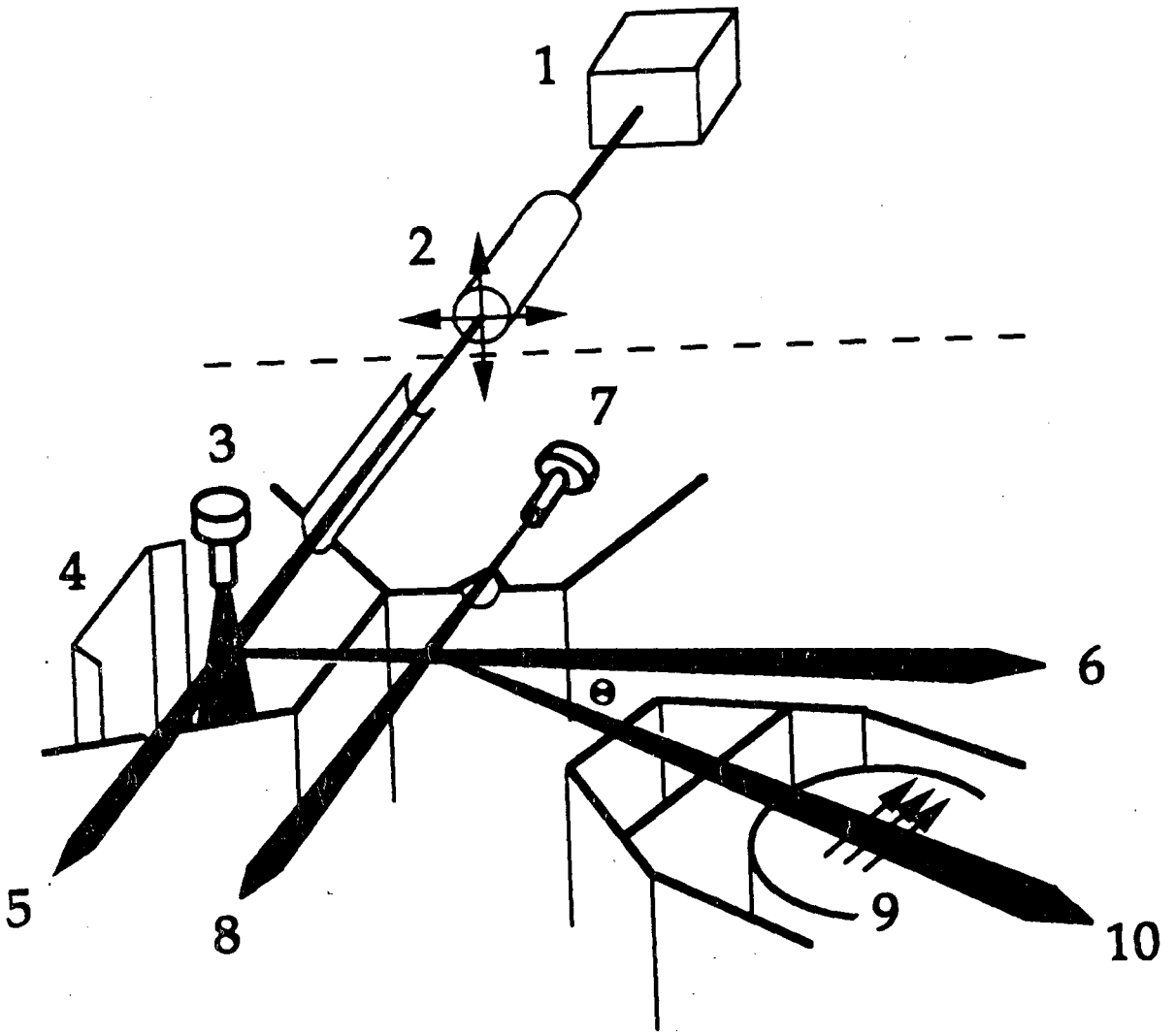

XBL 8911-4202

Figure 3 - 2

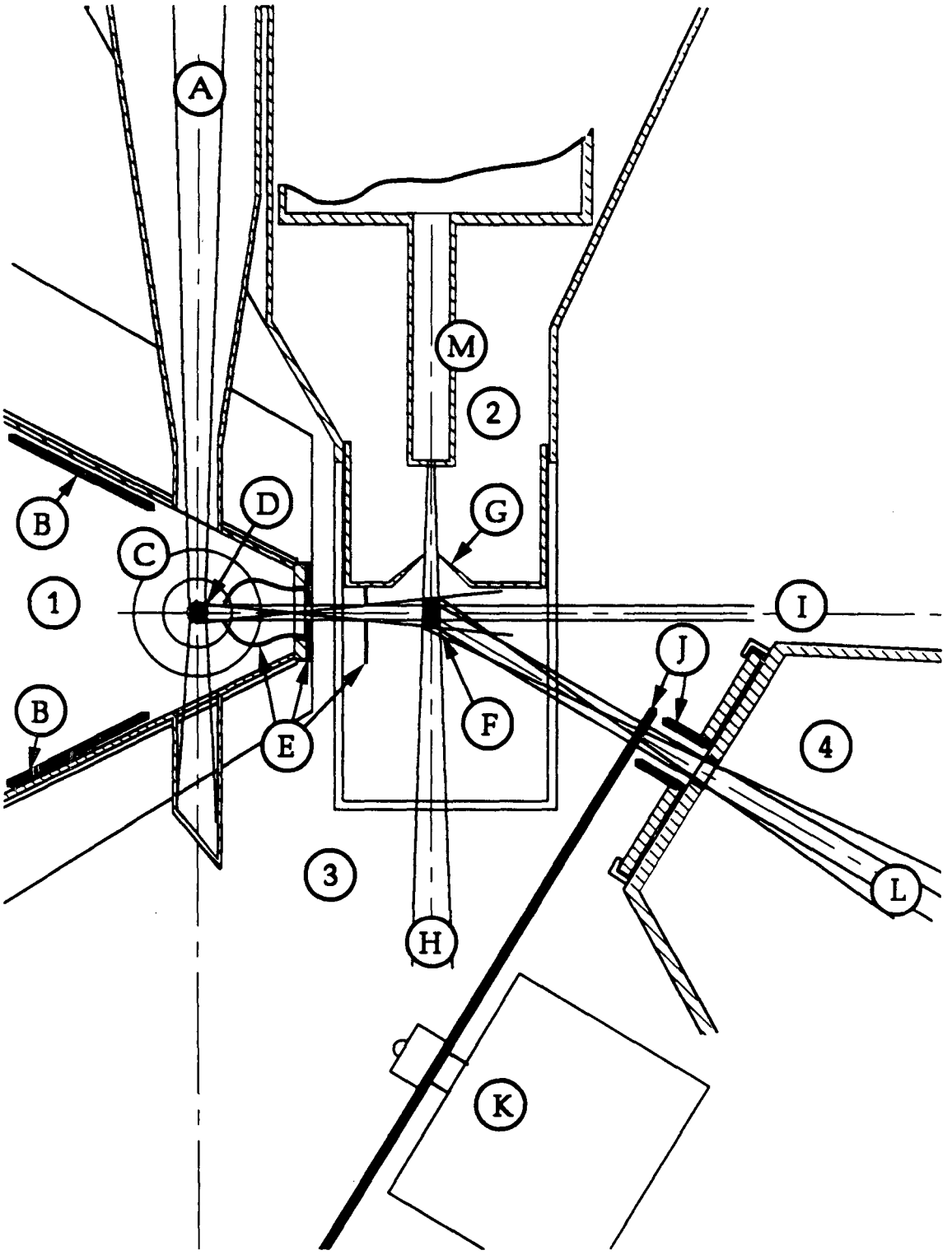

XBL 8911-4201

Figure 3 - 3

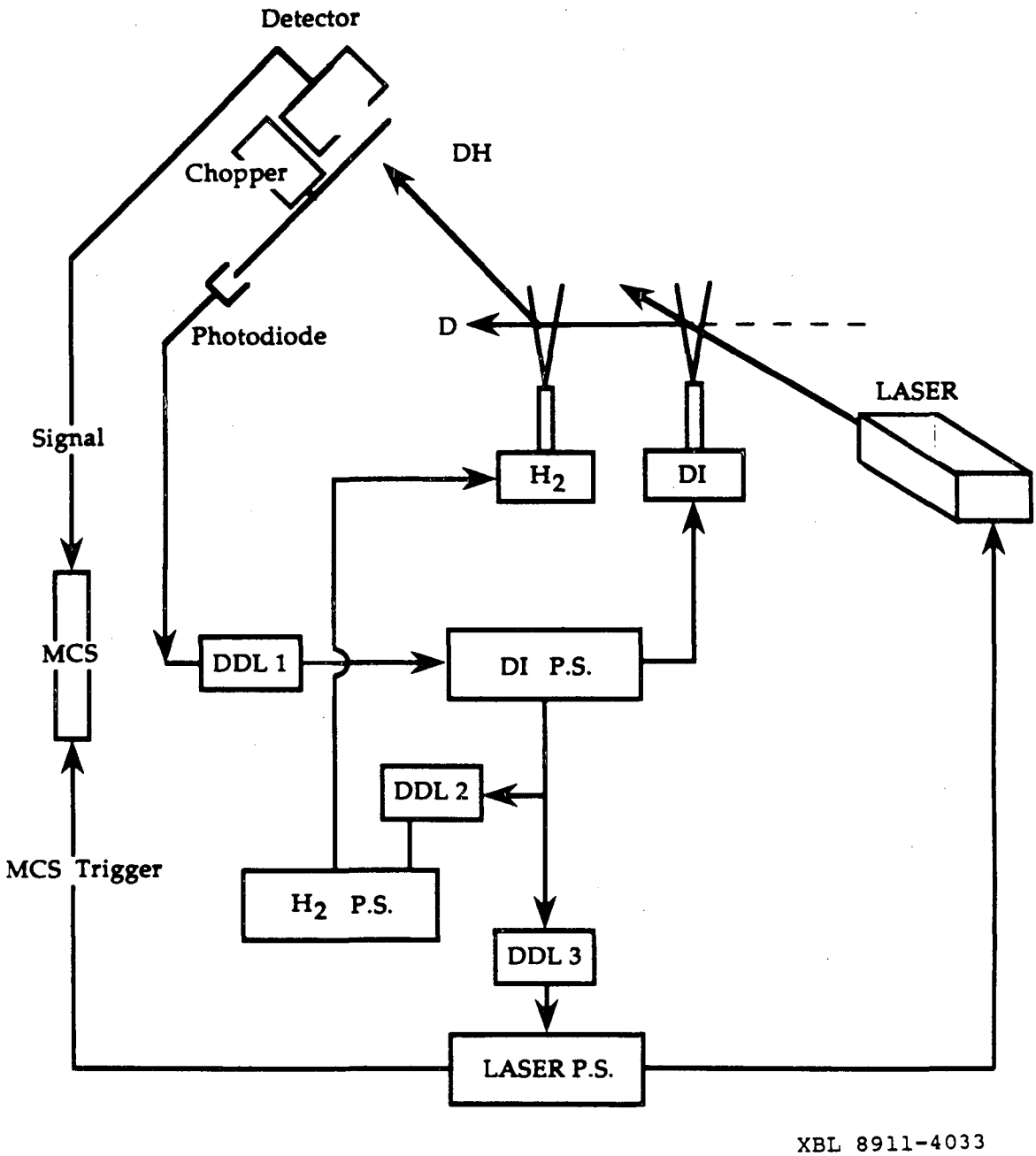
Detector
Chopper
DH
Photodiode
D
LASER
Signal
H_2
DI
MCS
DDL 1
DI P.S.
DDL 2
MCS Trigger
H_2 P.S.
DDL 3
LASER P.S.
XBL 8911-4033

Figure 3 - 4

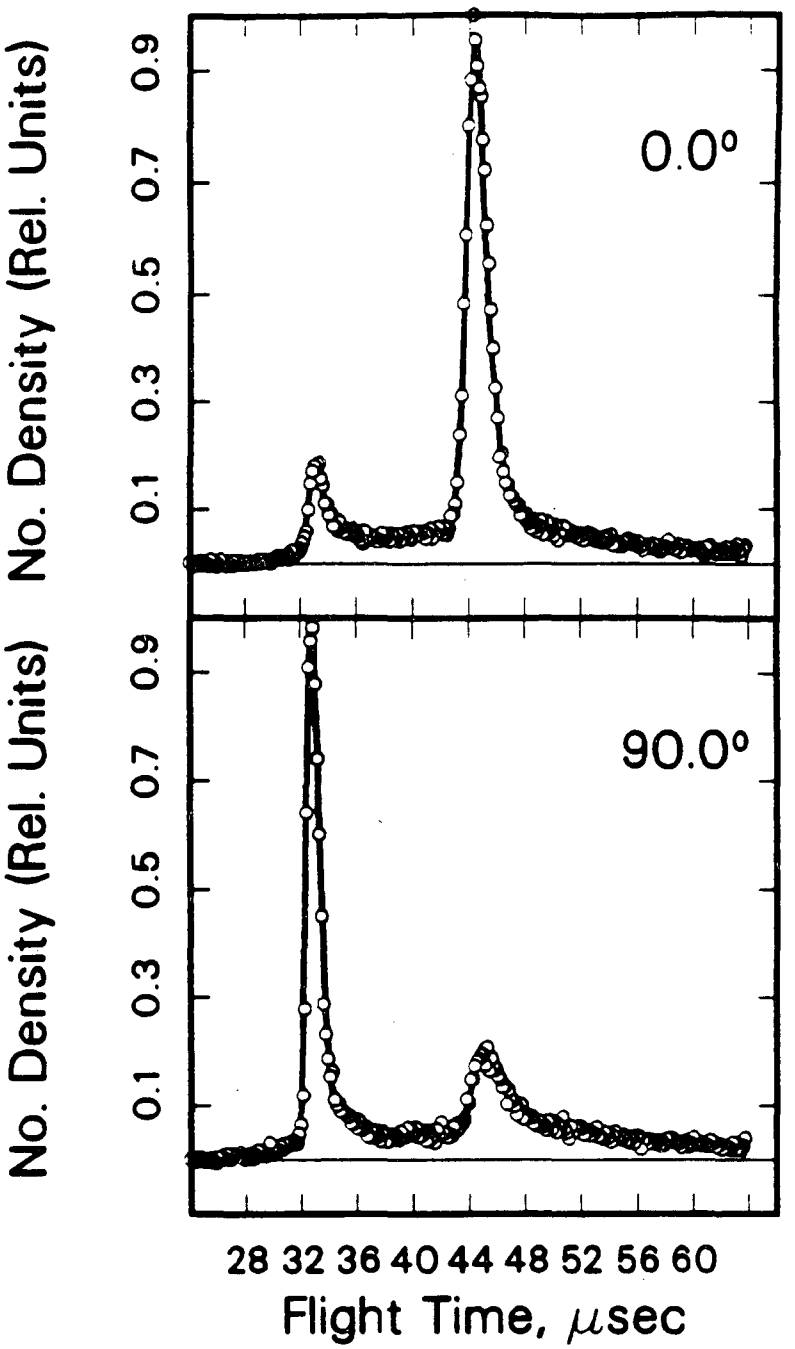

XBL 8911-4034

Figure 3 - 5

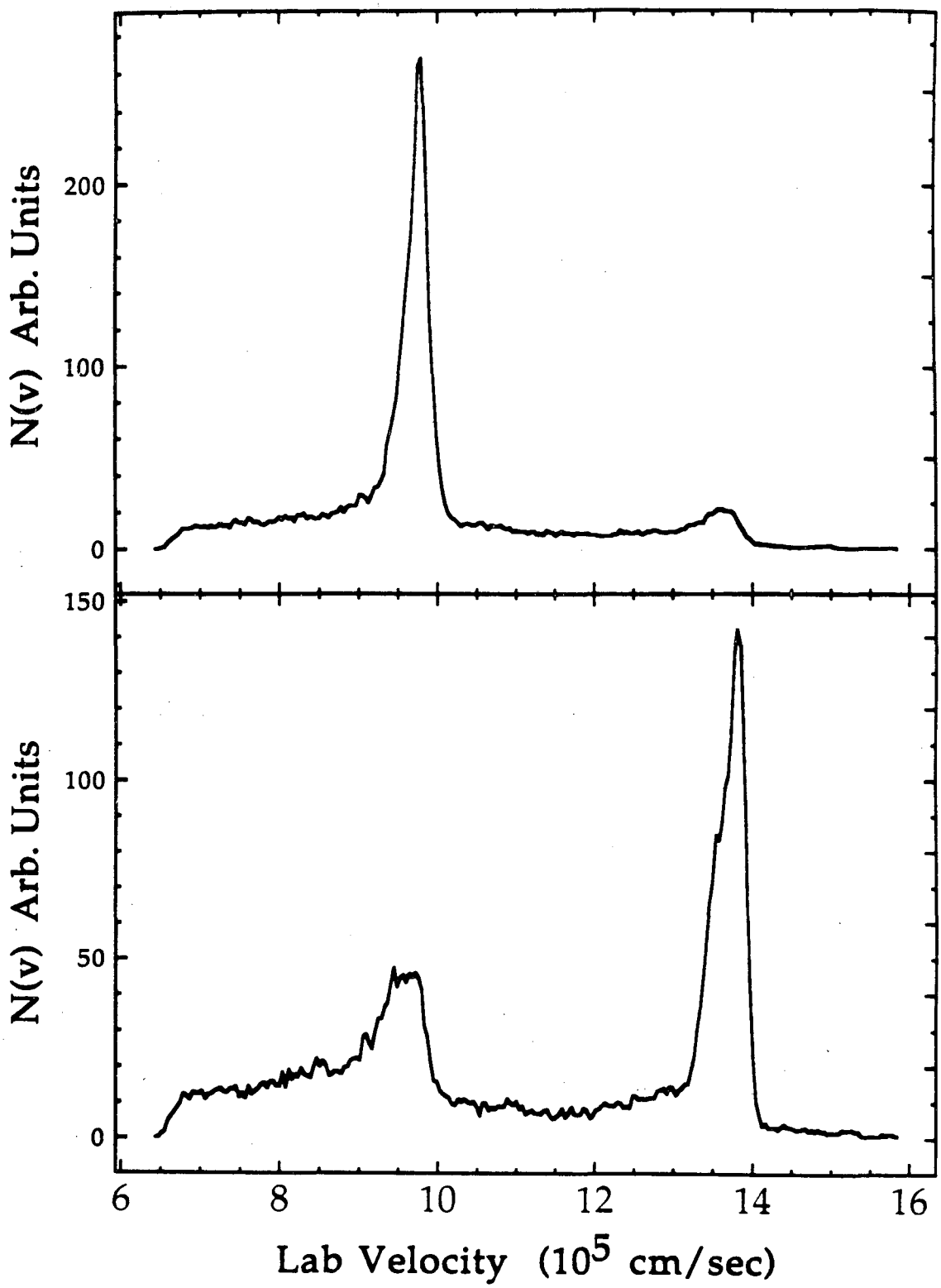

Figure 3 - 6 XBL 8911-4035

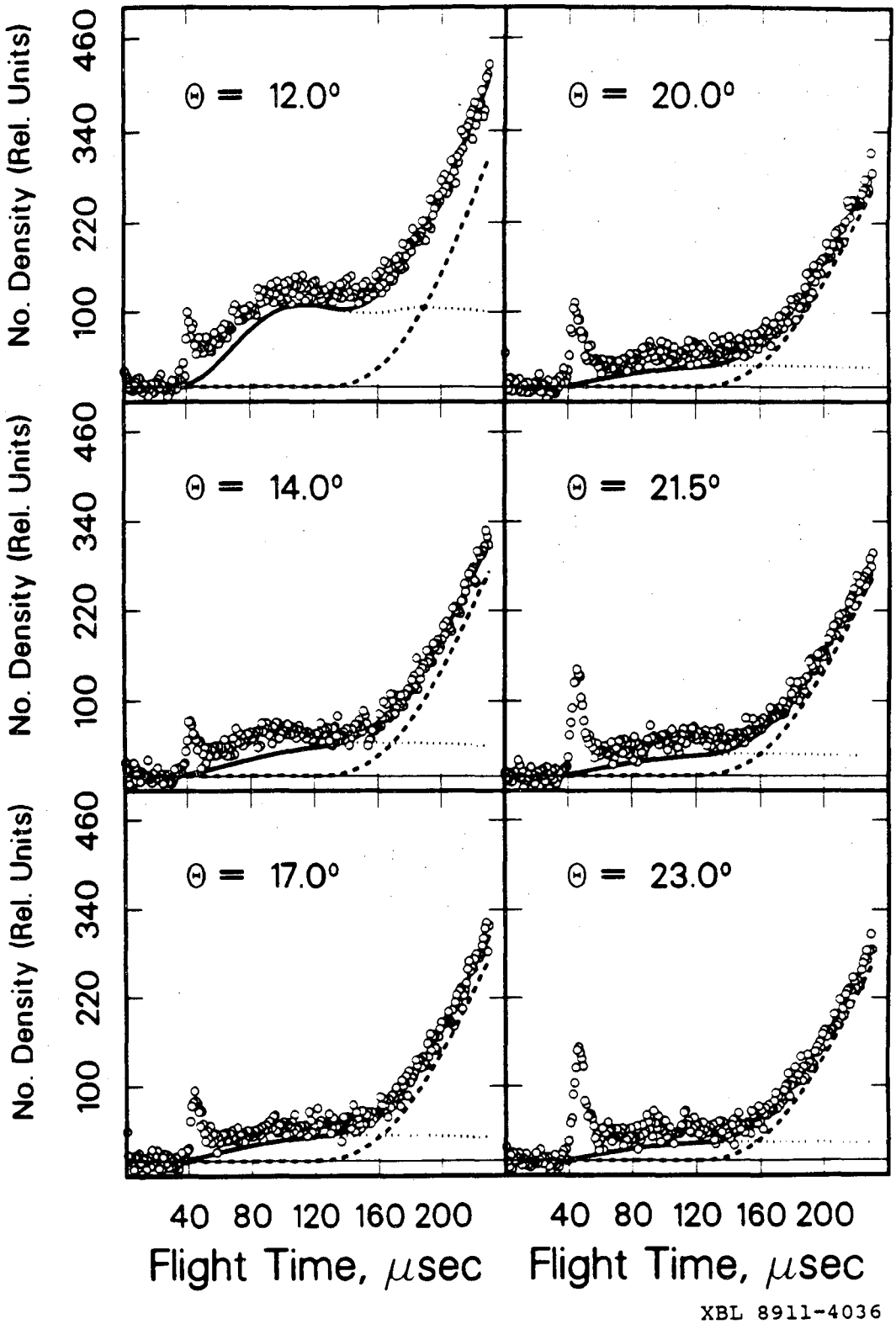
No. Density (Rel. Units)
100
220
340
460
Θ = 12.0°
Θ = 20.0°
Θ = 14.0°
Θ = 21.5°
Θ = 17.0°
Θ = 23.0°
40 80 120 160 200
Flight Time, μsec
XBL 8911-4036

Figure 3 - 7a

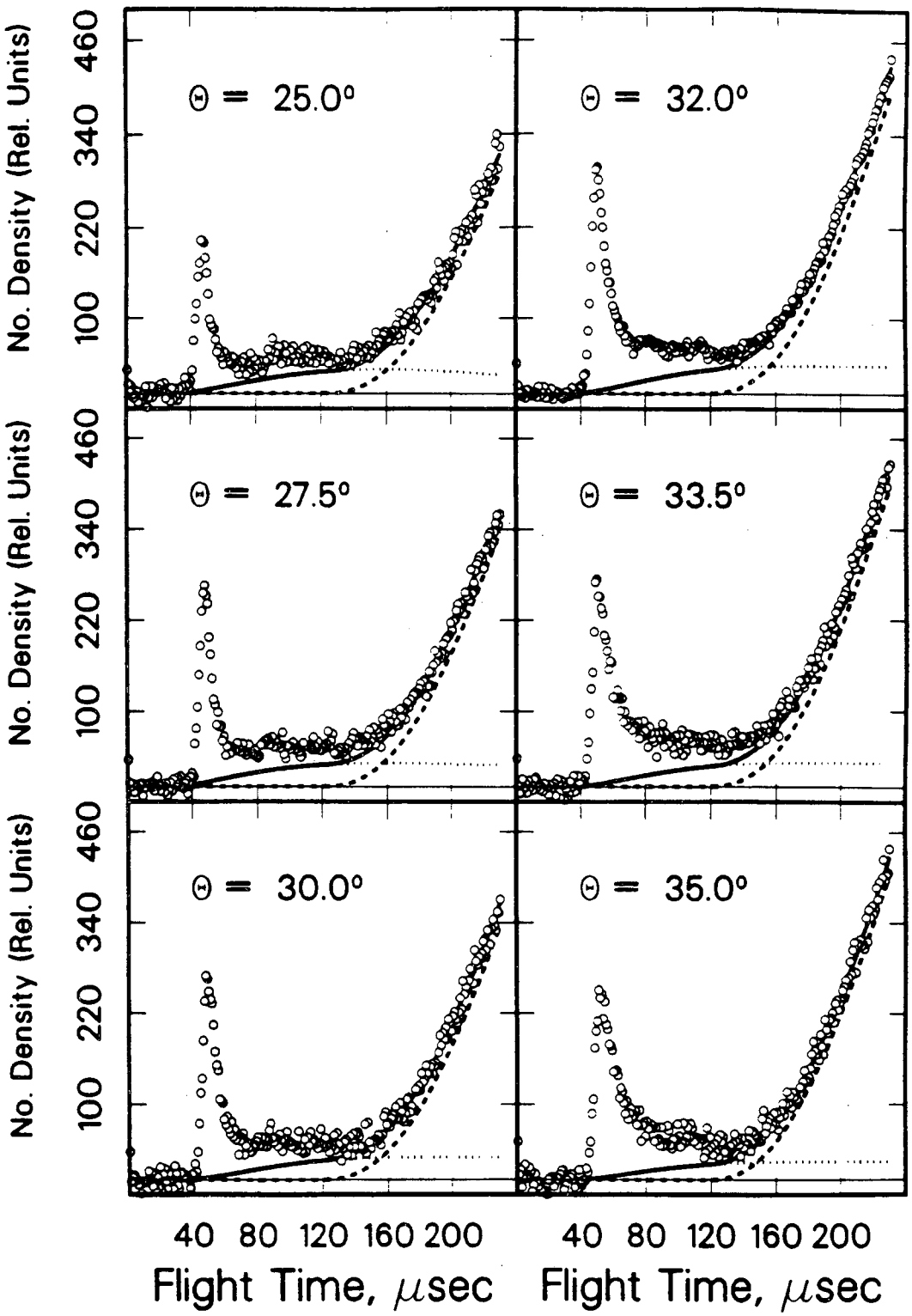
No. Density (Rel. Units)
100
220
340
460
Θ = 25.0°
Θ = 32.0°
Θ = 27.5°
Θ = 33.5°
Θ = 30.0°
Θ = 35.0°
40 80 120 160 200
Flight Time, μsec
XBL 8911-4037

Figure 3 - 7b

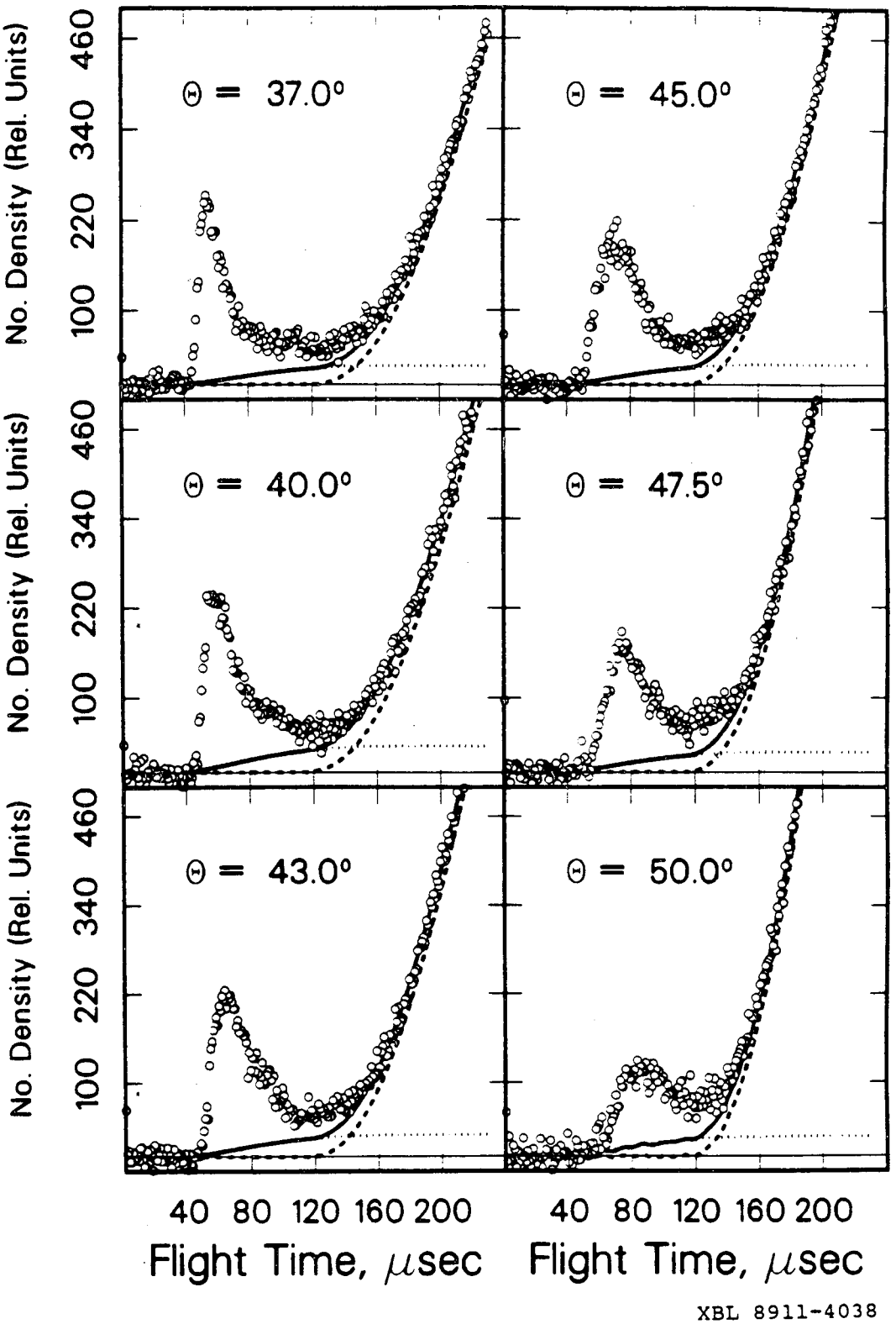
No. Density (Rel. Units)
100
220
340
460
Θ = 37.0°
Θ = 45.0°
Θ = 40.0°
Θ = 47.5°
Θ = 43.0°
Θ = 50.0°
40 80 120 160 200
Flight Time, μsec
XBL 8911-4038

Figure 3 - 7c

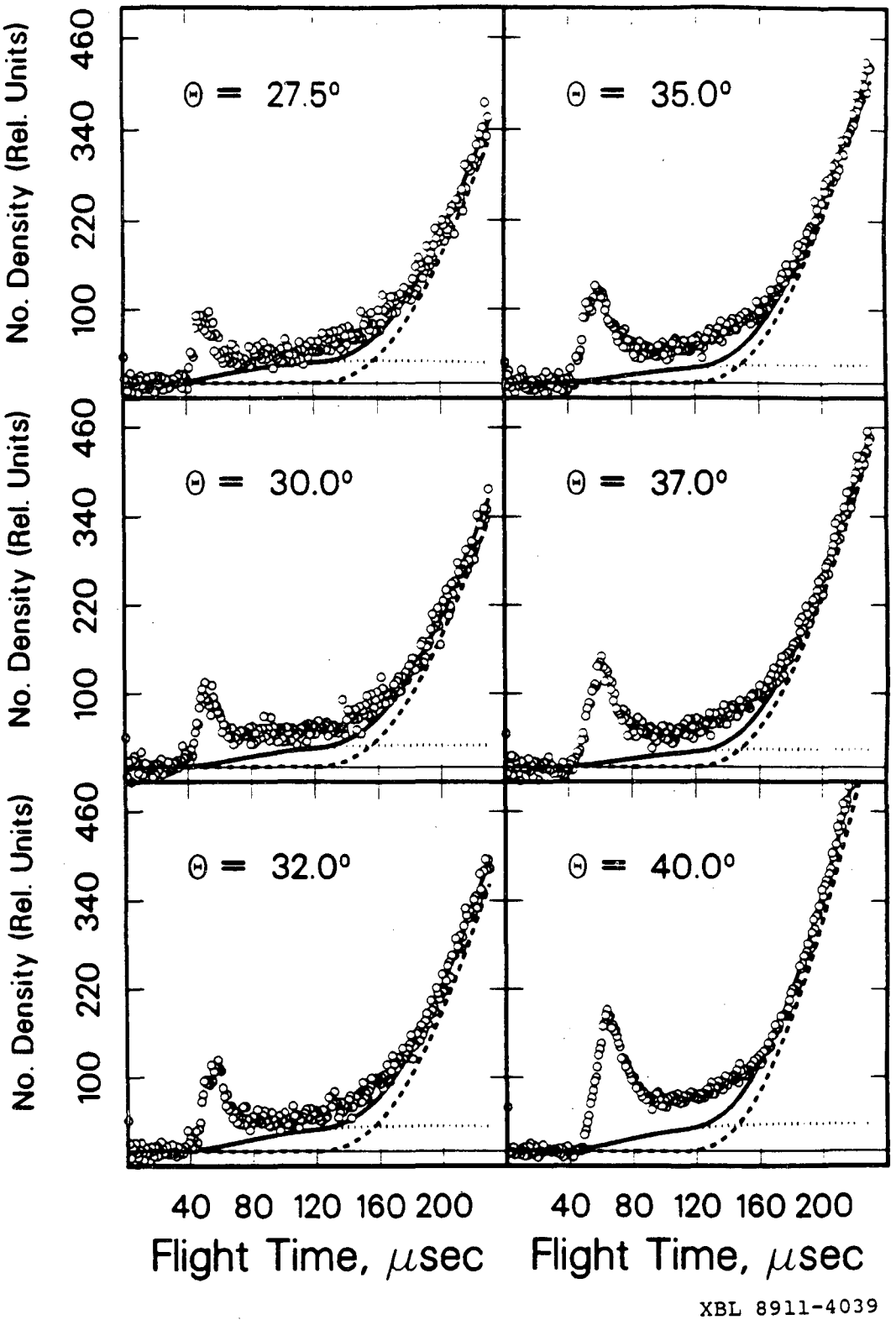
No. Density (Rel. Units)
100
220
340
460
Θ = 27.5°
Θ = 35.0°
Θ = 30.0°
Θ = 37.0°
Θ = 32.0°
Θ = 40.0°
40 80 120 160 200
Flight Time, μsec
XBL 8911-4039

Figure 3 - 8a

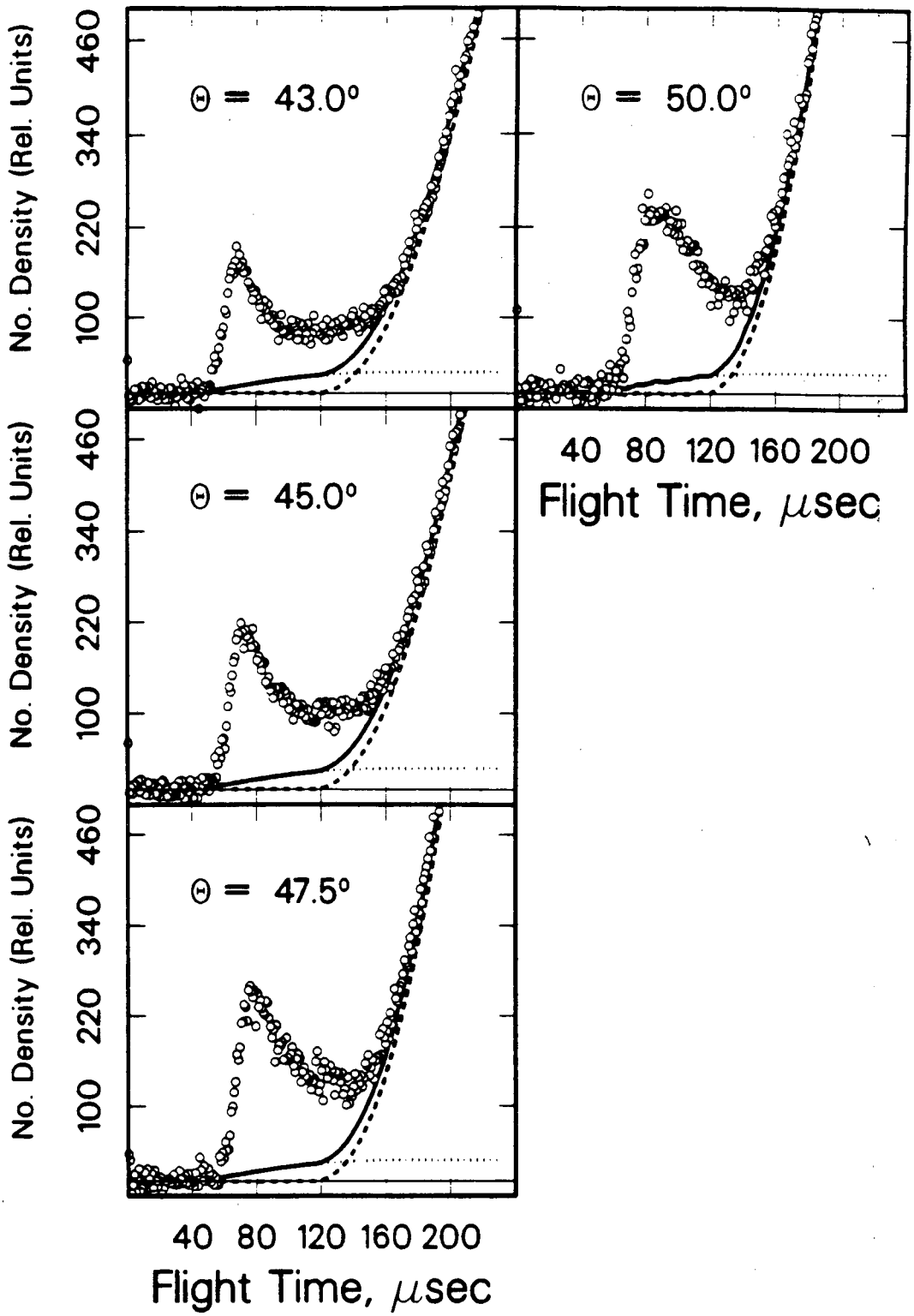

XBL 8911-4040

Figure 3 - 8b

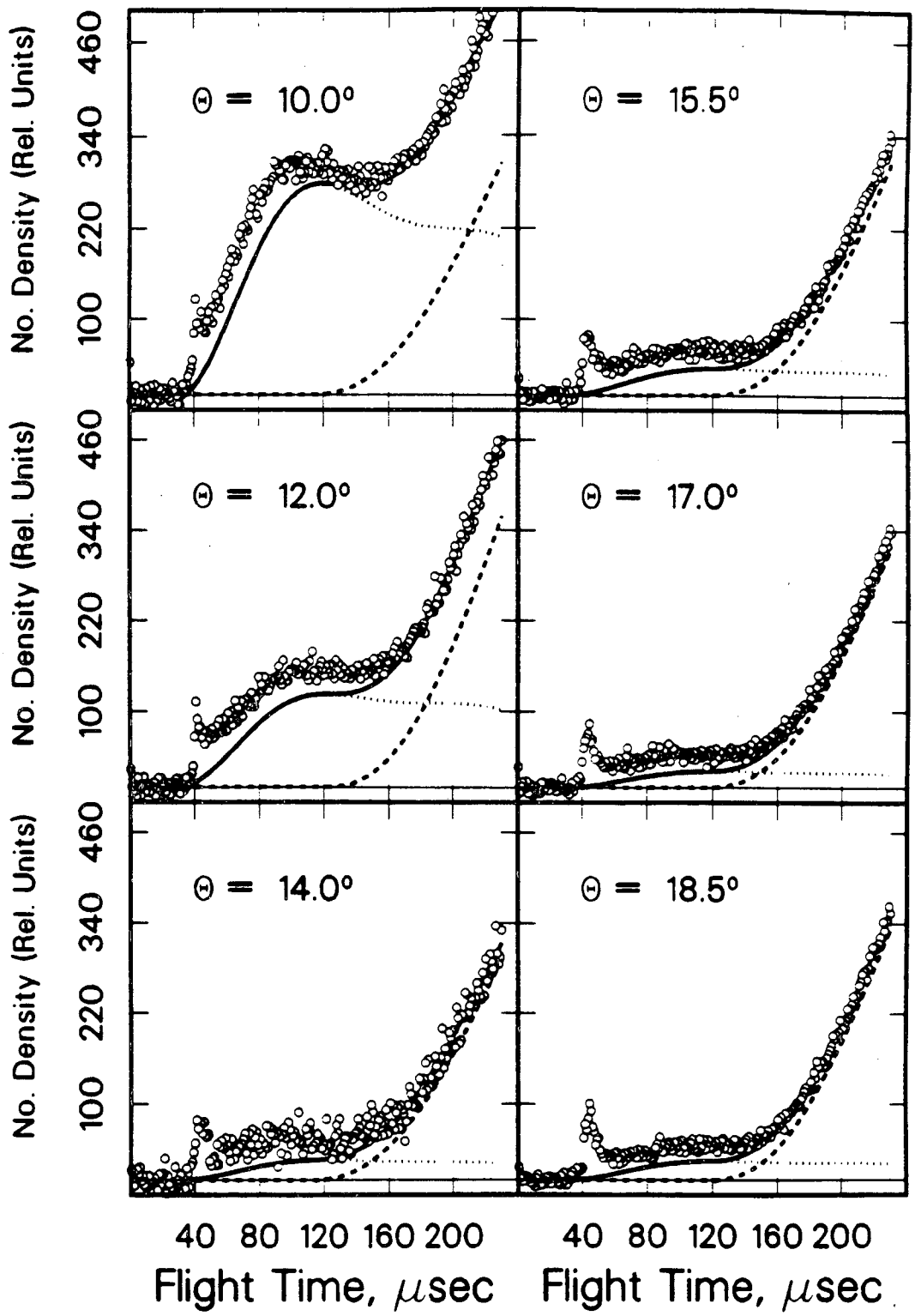
No. Density (Rel. Units)
100
220
340
460
Θ = 10.0°
Θ = 15.5°
Θ = 12.0°
Θ = 17.0°
Θ = 14.0°
Θ = 18.5°
40 80 120 160 200
Flight Time, μsec
XBL 8911-4041

Figure 3 - 9a

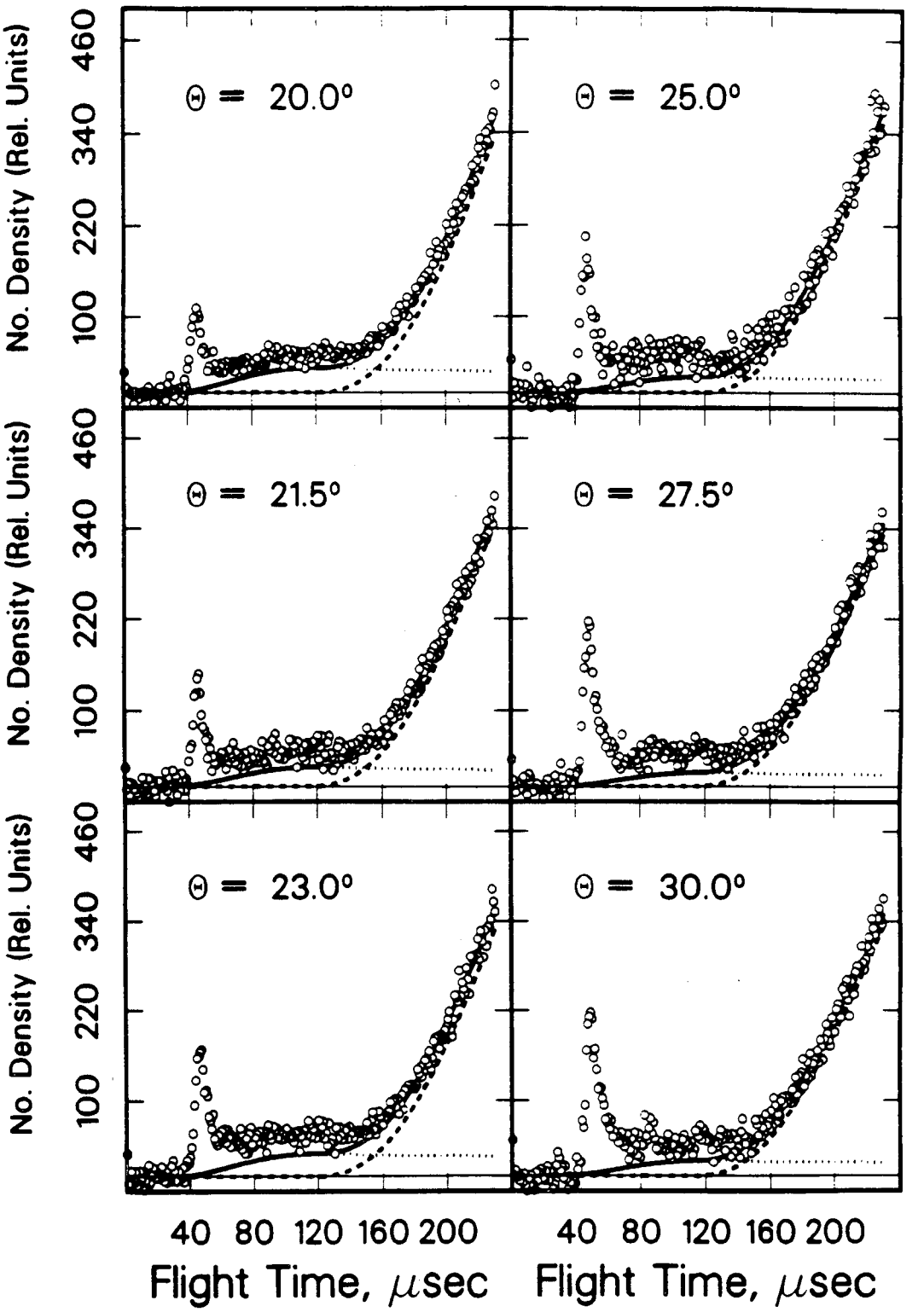
No. Density (Rel. Units)
100
220
340
460
Θ = 20.0°
Θ = 25.0°
Θ = 21.5°
Θ = 27.5°
Θ = 23.0°
Θ = 30.0°
40 80 120 160 200
Flight Time, μsec
XBL 8911-4042

Figure 3 - 9b

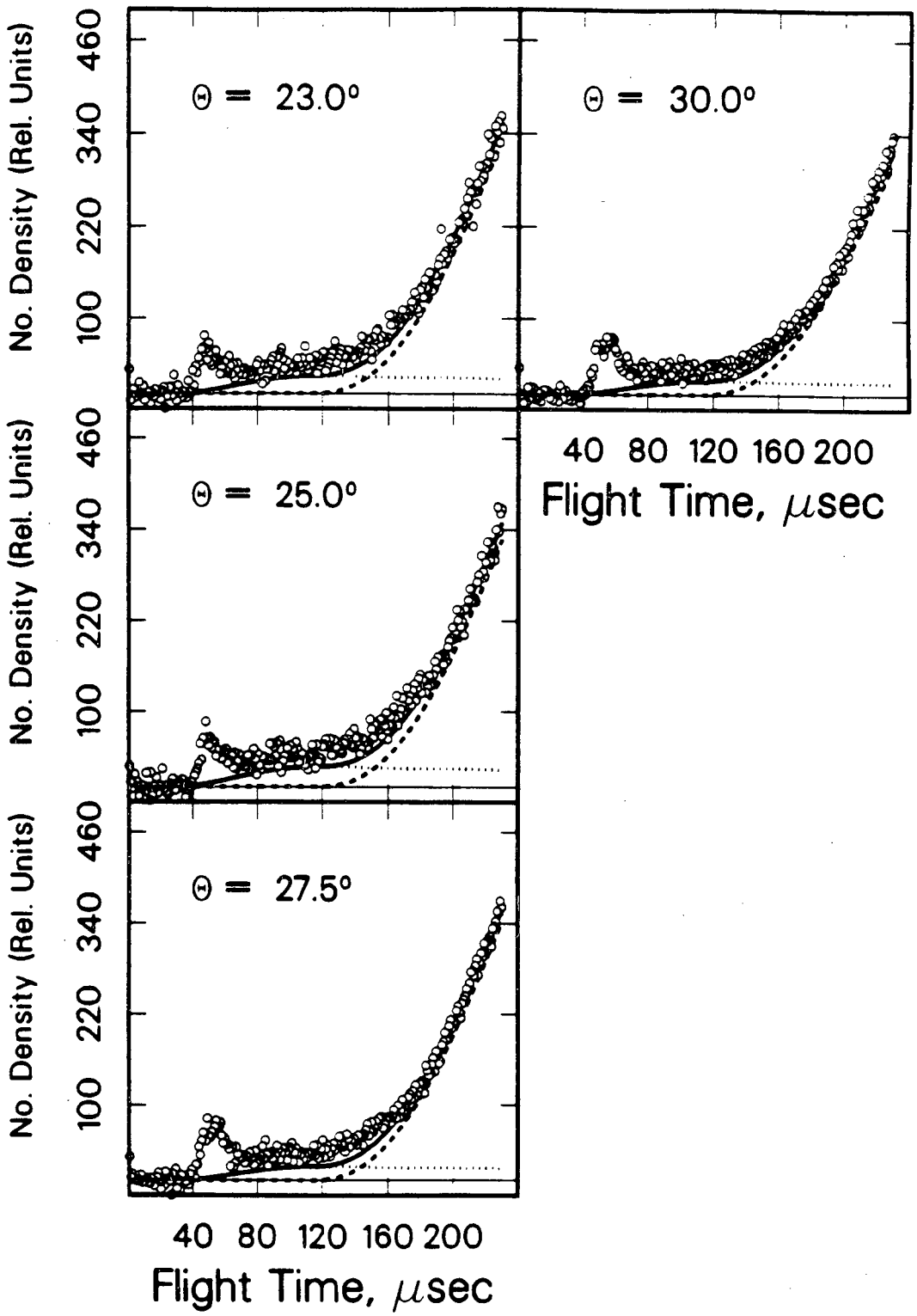

XBL 8911-4043

Figure 3 - 10

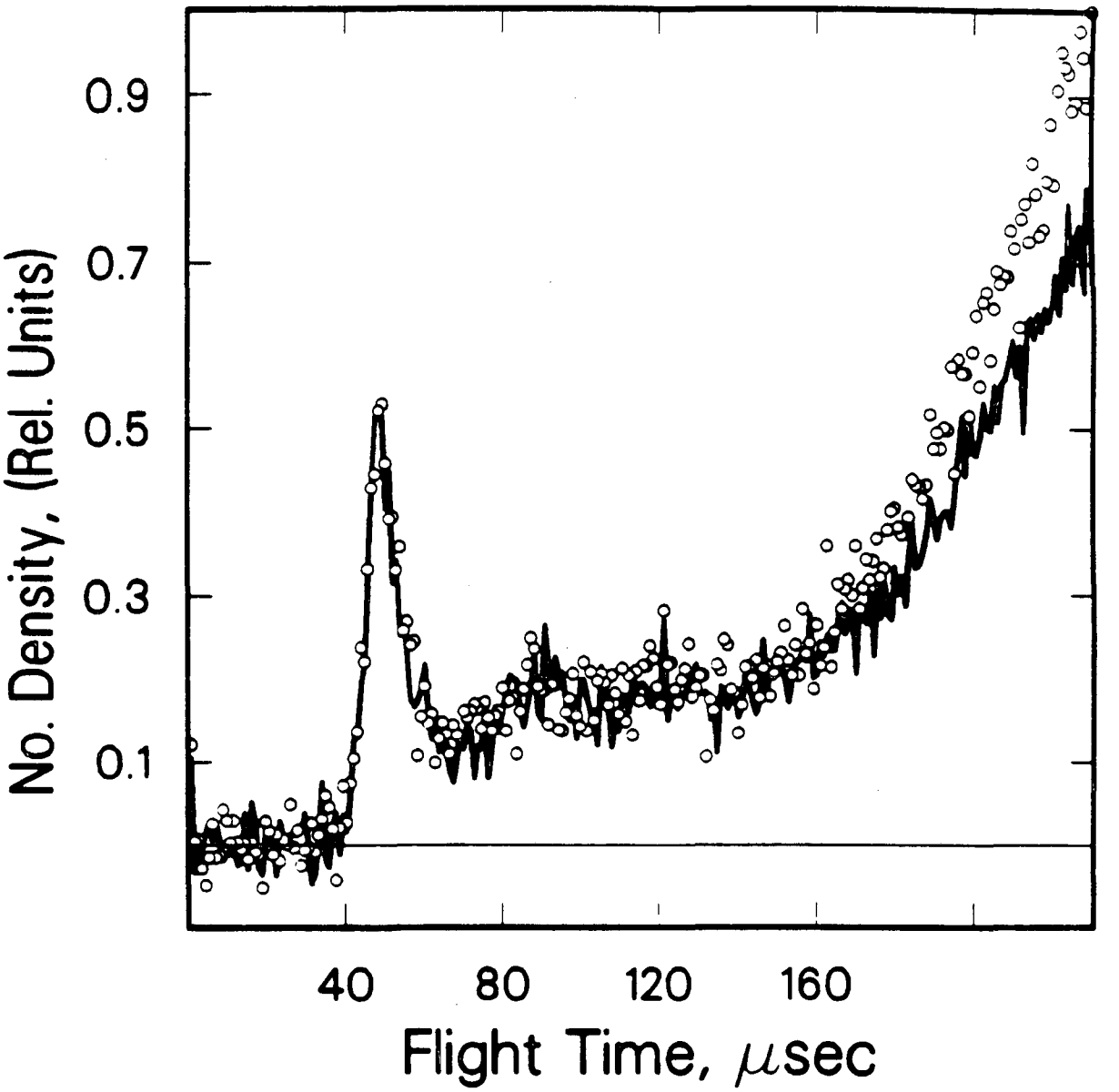

XBL 8911-4044

Figure 3 - 11

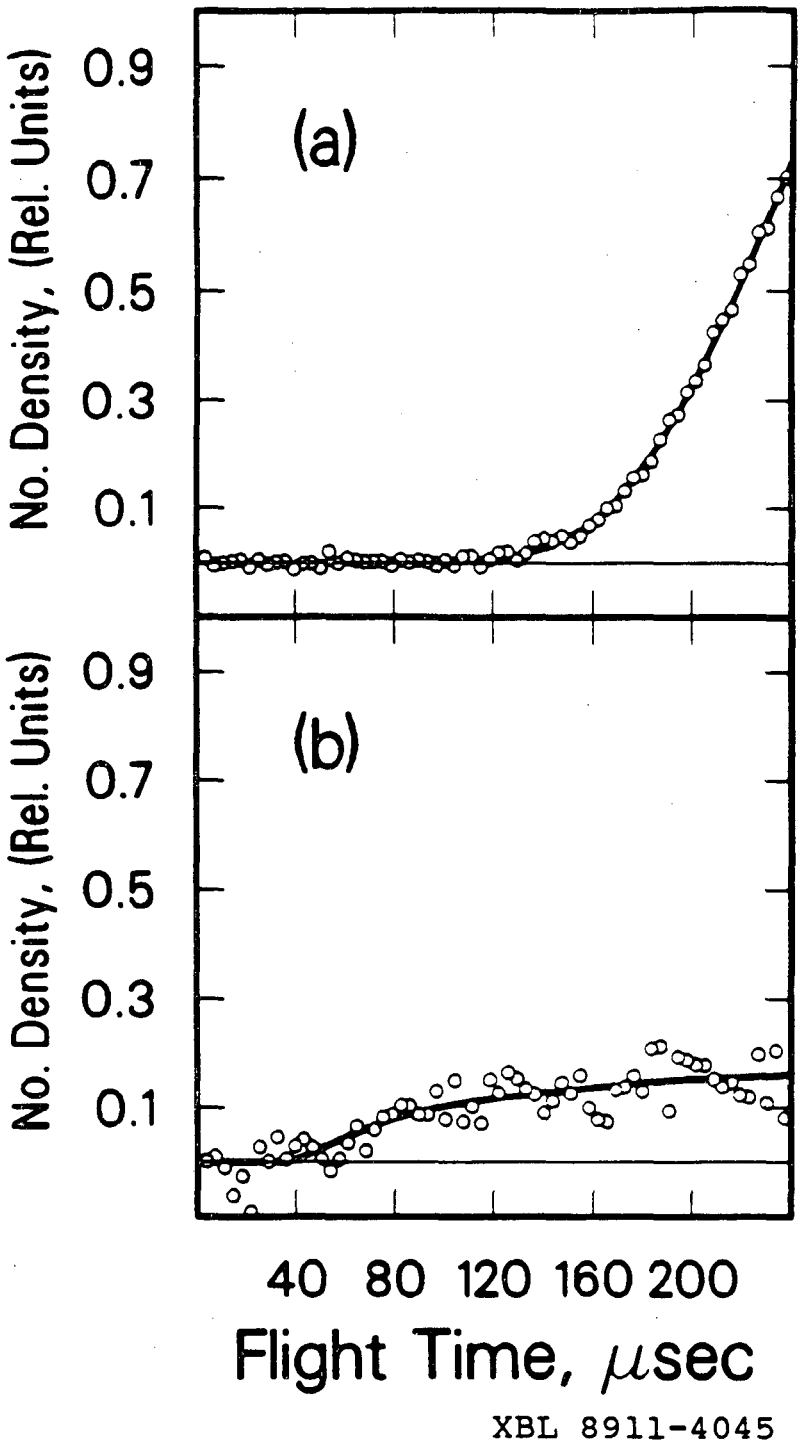
(a)
(b)
No. Density, (Rel. Units)
0.9
0.7
0.5
0.3
0.1
40 80 120 160 200
Flight Time, μsec
XBL 8911-4045

Figure 3 - 12

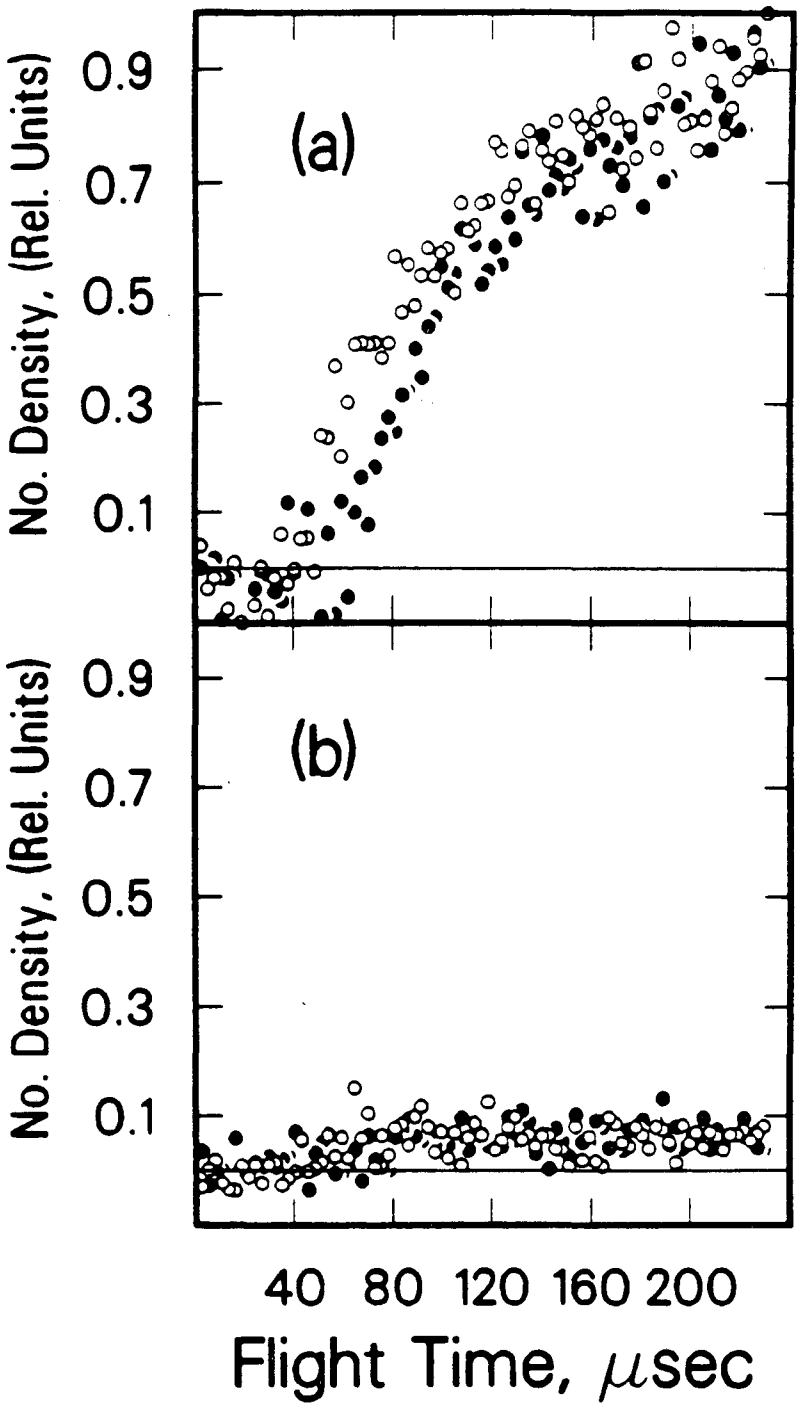

XBL 8911-4046

Figure 3 - 13

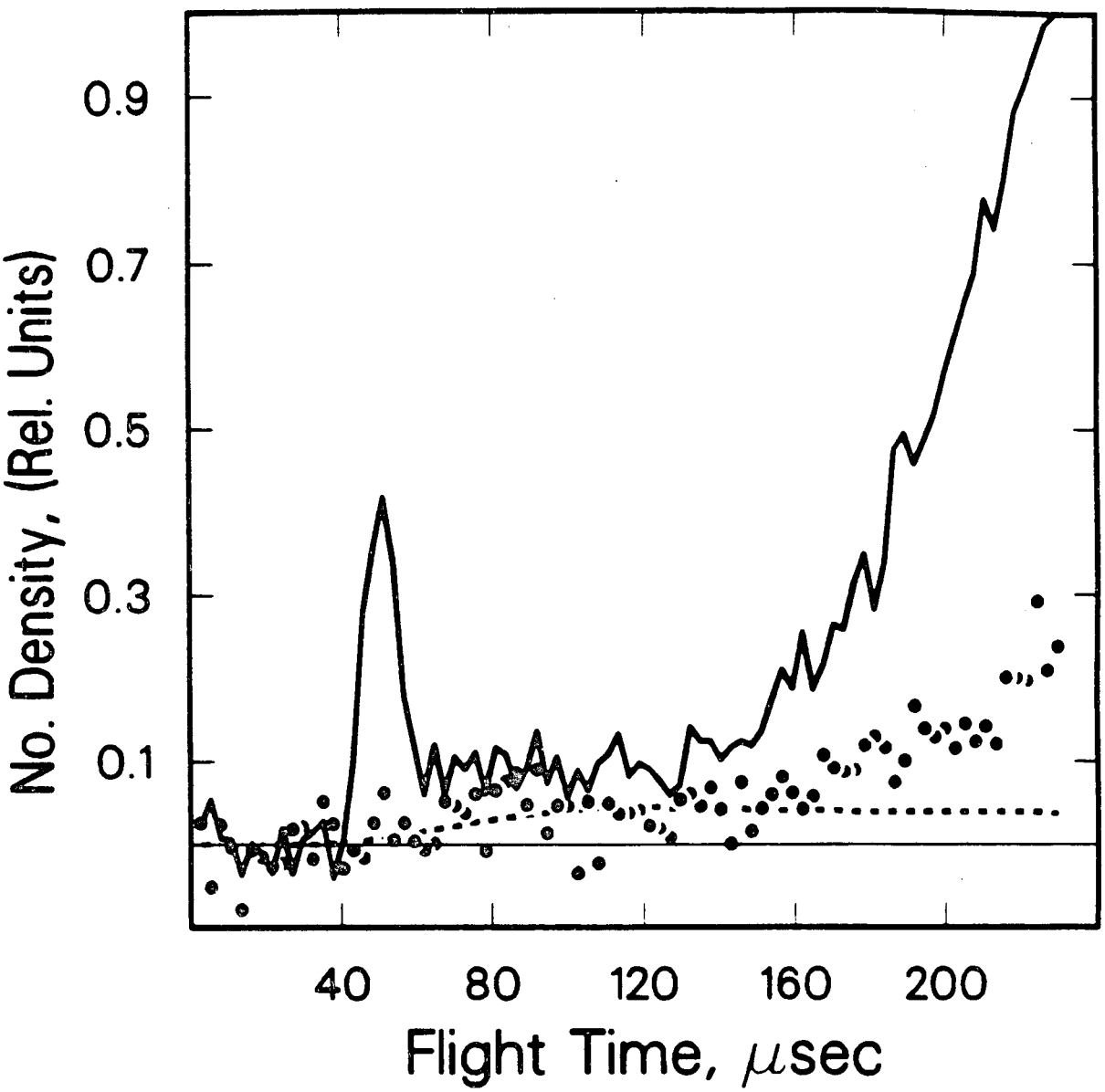

XBL 8911-4047

Figure 3 - 14

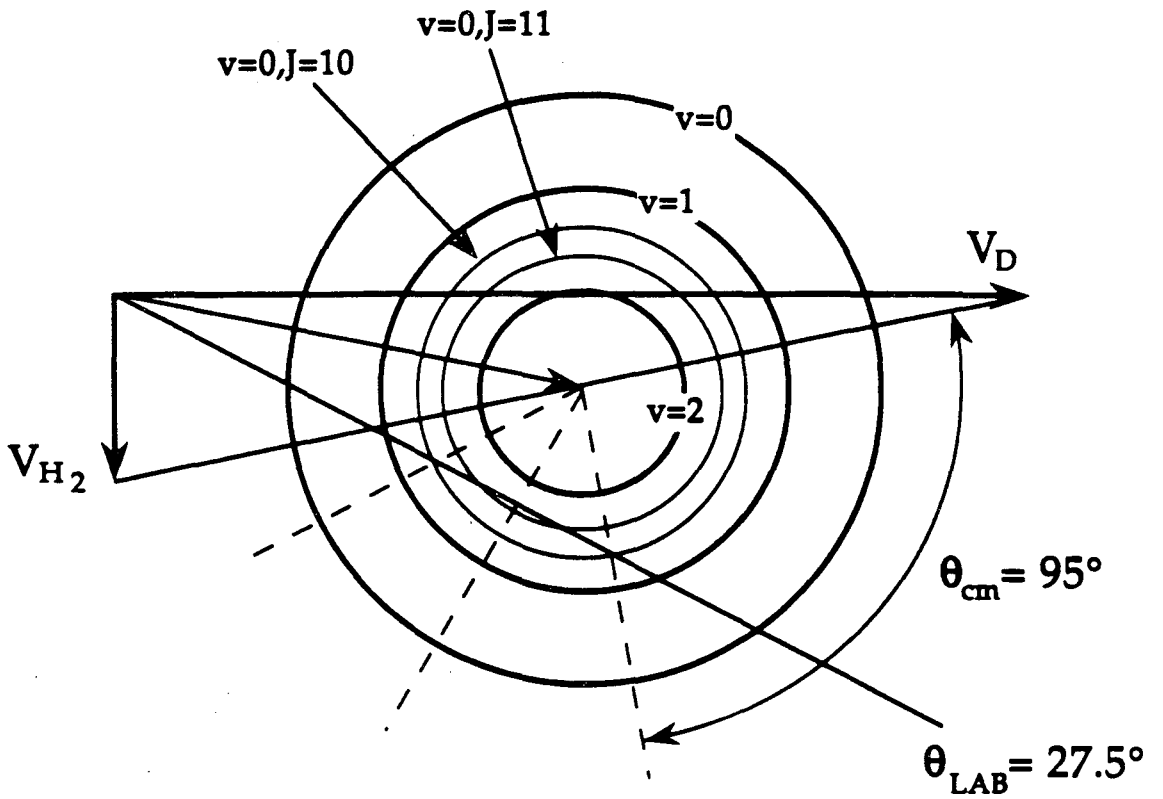

XBL 8911-4048

Figure 3 - 15

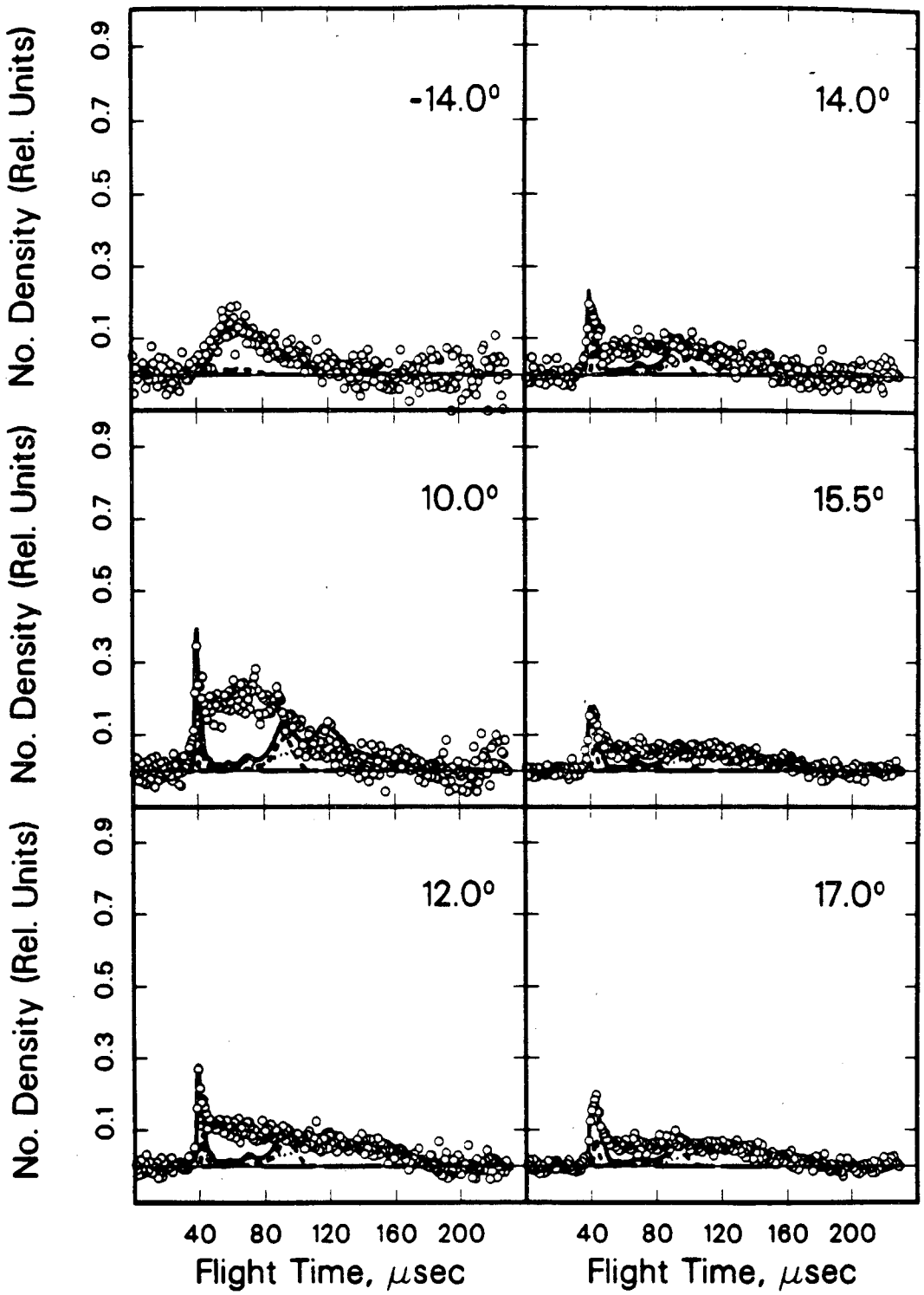

XBL 8911-4049

Figure 3 - 16a

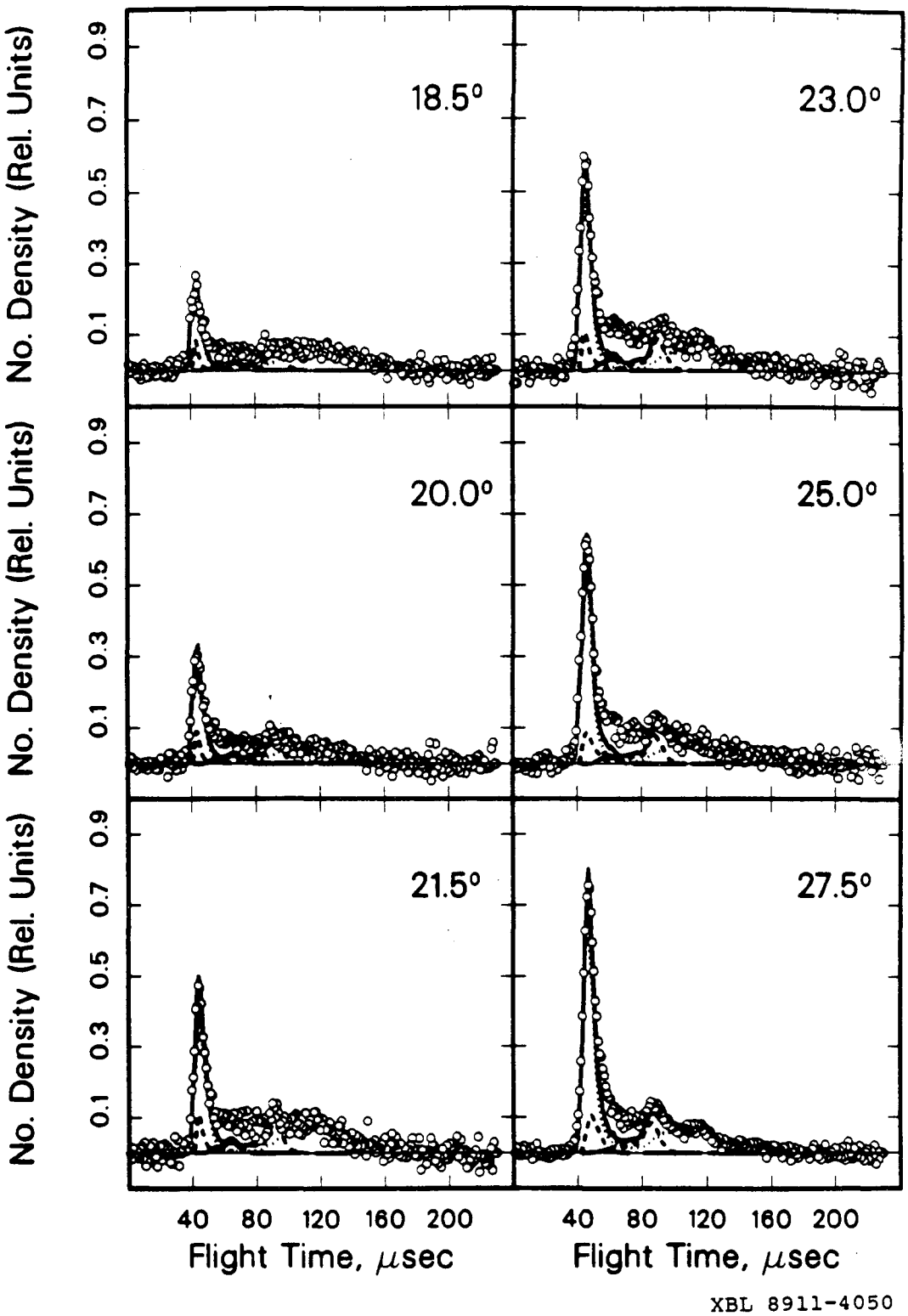
No. Density (Rel. Units)
0.1
0.3
0.5
0.7
0.9
18.5°
23.0°
20.0°
25.0°
21.5°
27.5°
40
80
120
160
200
Flight Time, μsec
XBL 8911-4050

Figure 3 - 16b

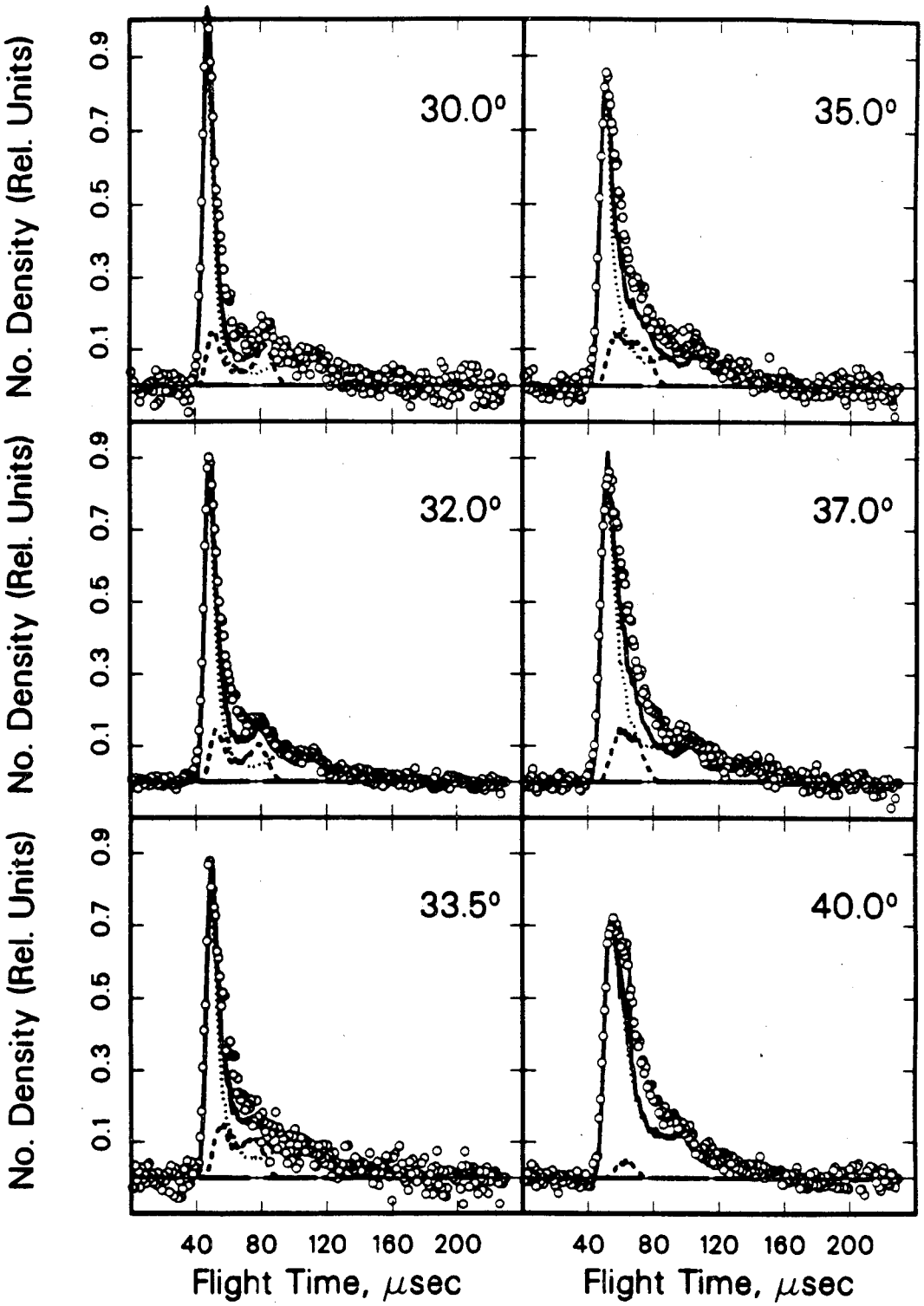
No. Density (Rel. Units)
0.1
0.3
0.5
0.7
0.9
30.0°
35.0°
32.0°
37.0°
33.5°
40.0°
40
80
120
160
200
Flight Time, μsec
XBL 8911-4051

Figure 3 - 16c

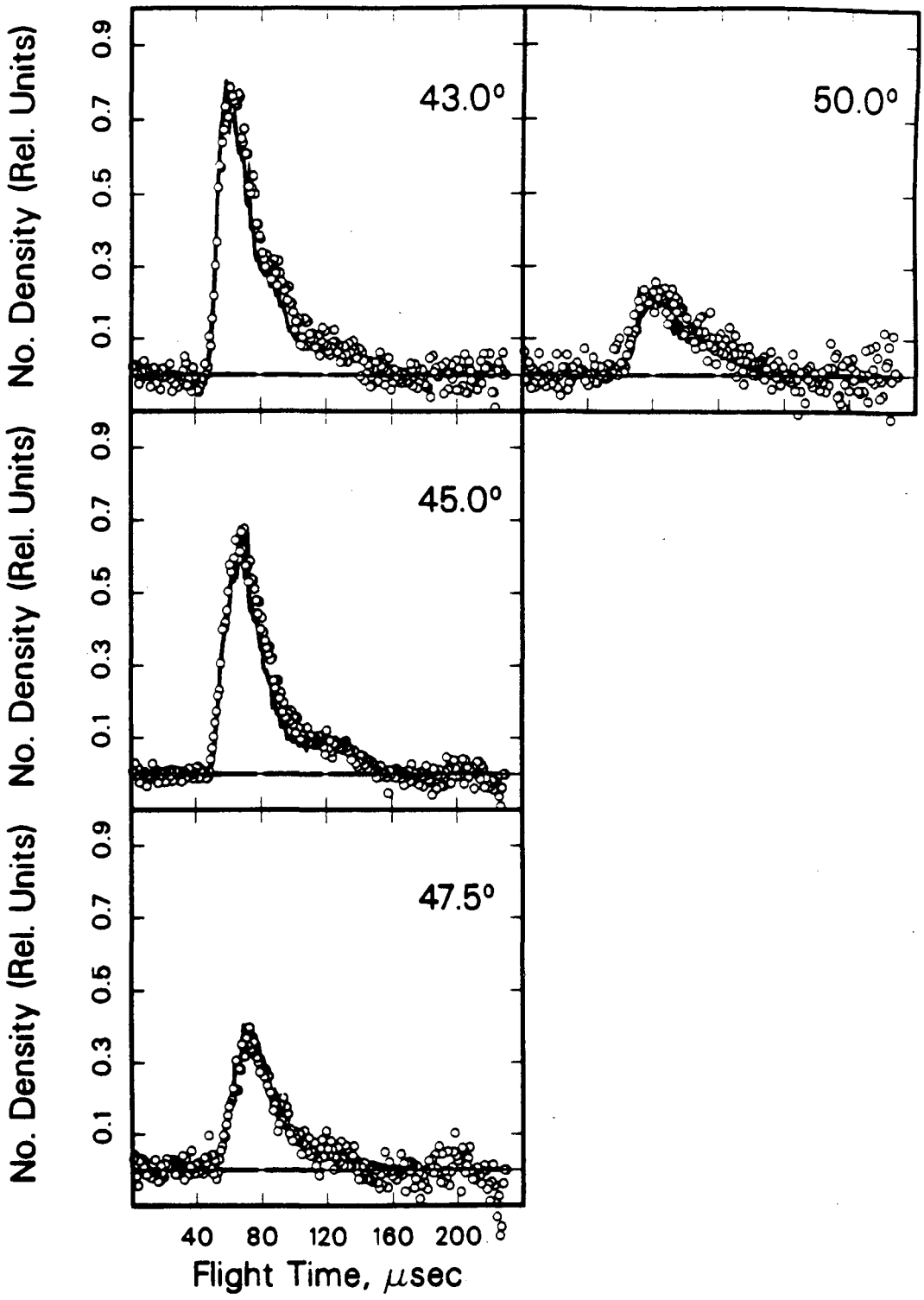

XBL 8911-4052

Figure 3 - 16d

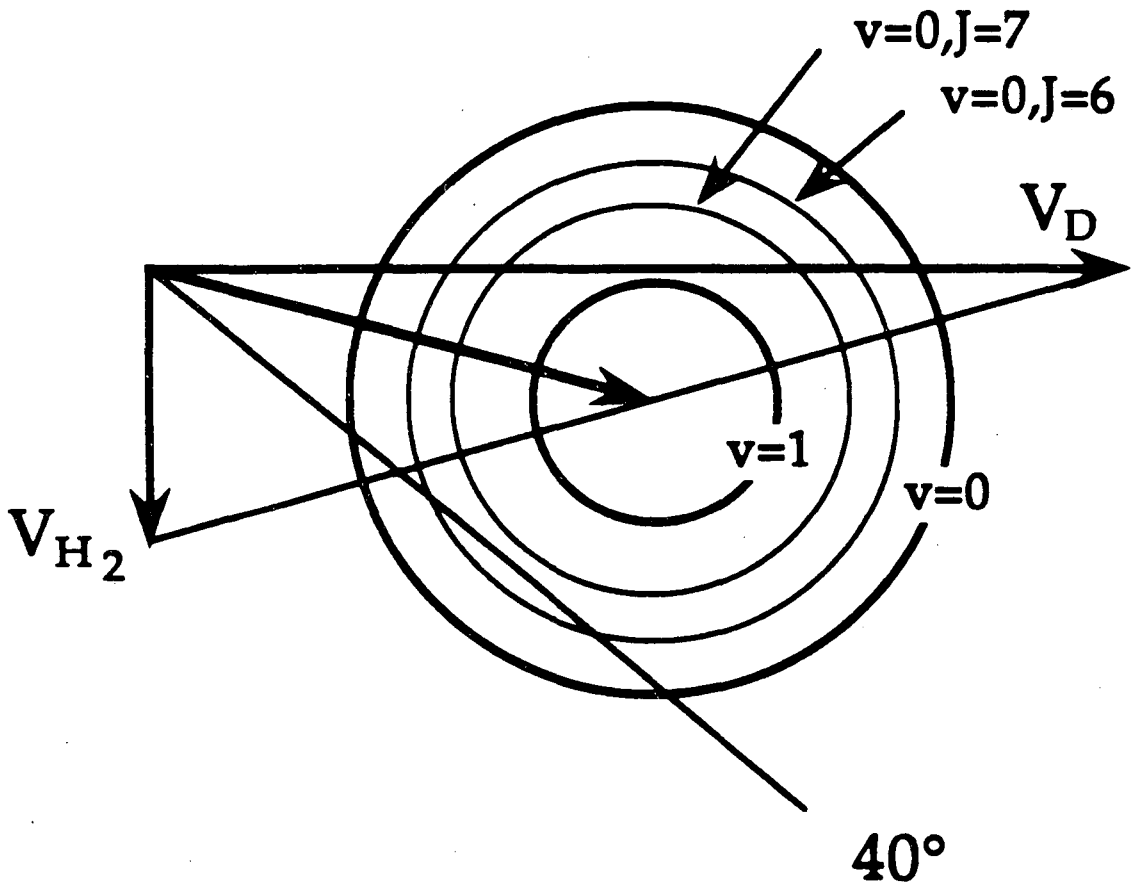

XBL 8911-4053

Figure 3 - 17

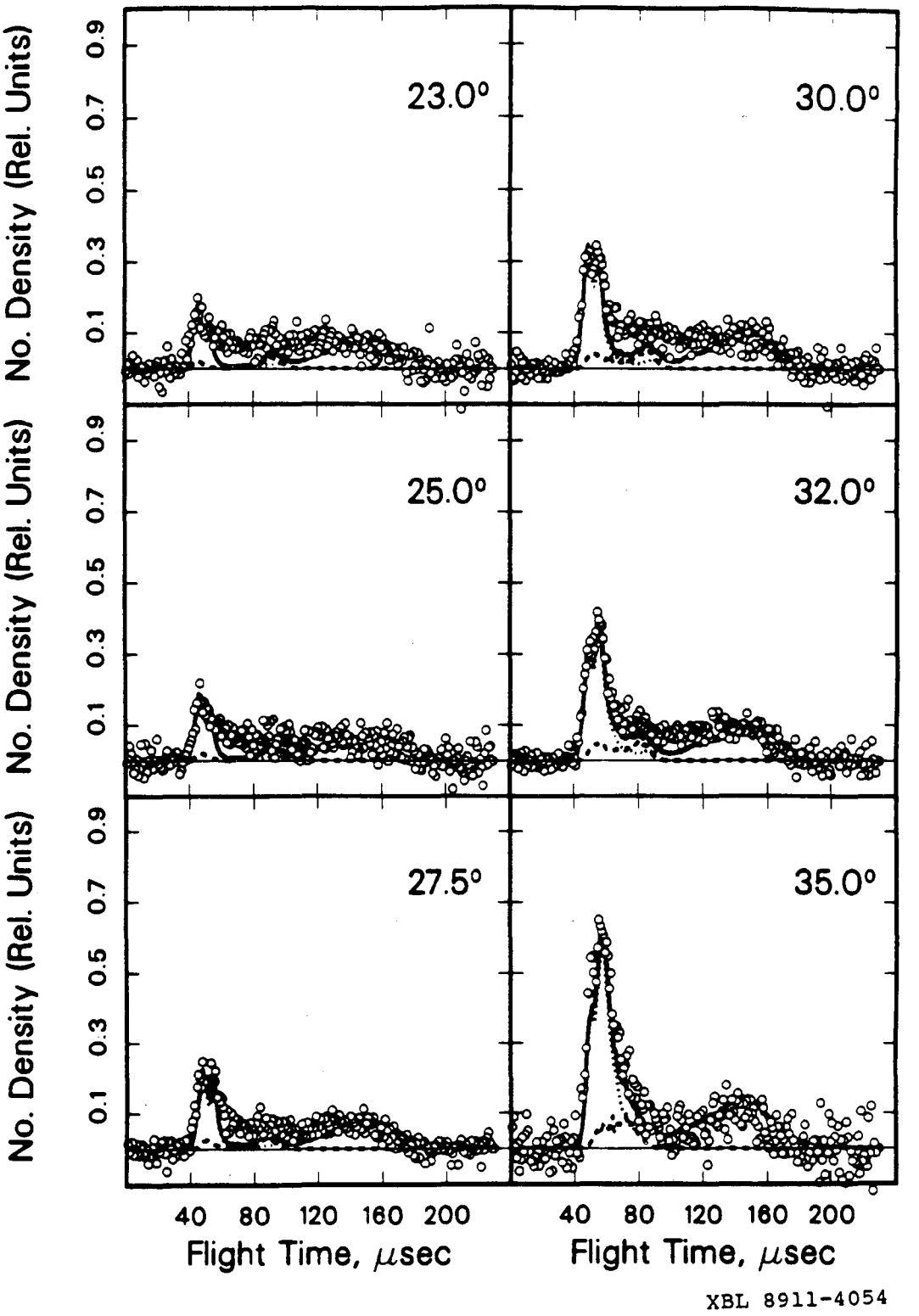
No. Density (Rel. Units)
0.1
0.3
0.5
0.7
0.9
23.0°
30.0°
25.0°
32.0°
27.5°
35.0°
40
80
120
160
200
Flight Time, μsec
XBL 8911-4054

Figure 3 - 18a

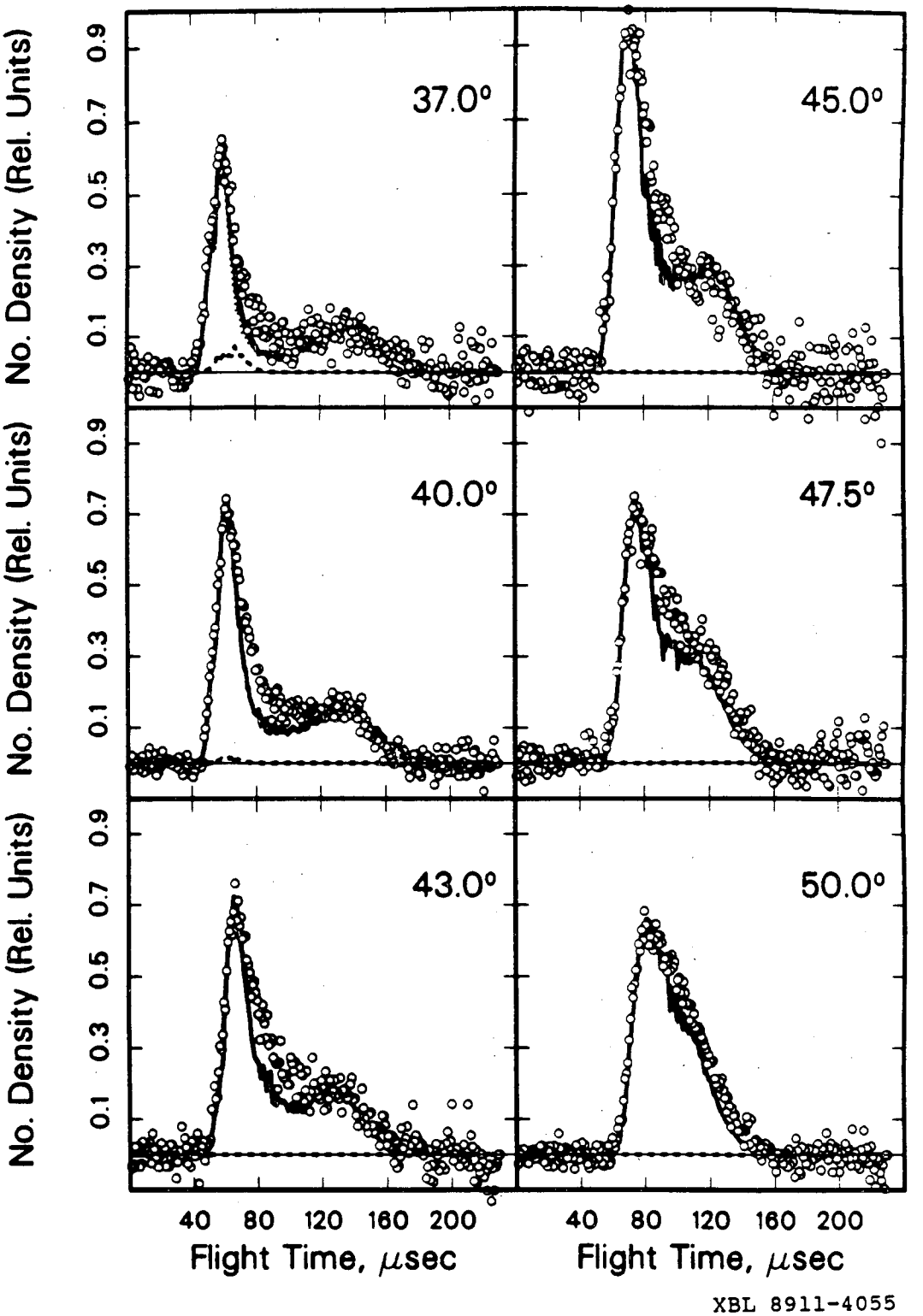
No. Density (Rel. Units)
0.1
0.3
0.5
0.7
0.9
37.0°
45.0°
40.0°
47.5°
43.0°
50.0°
40
80
120
160
200
Flight Time, μsec
XBL 8911-4055

Figure 3 - 18b

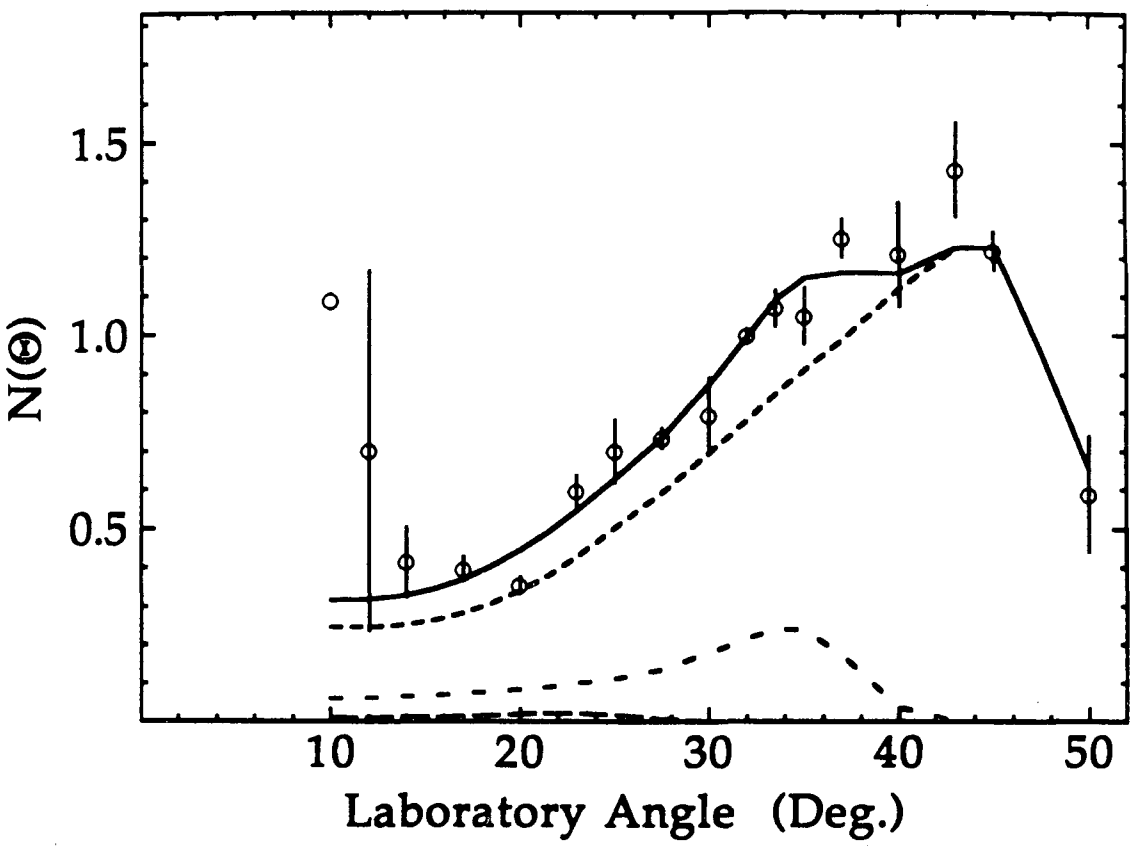

XBL 8911-4199

Figure 3 - 19

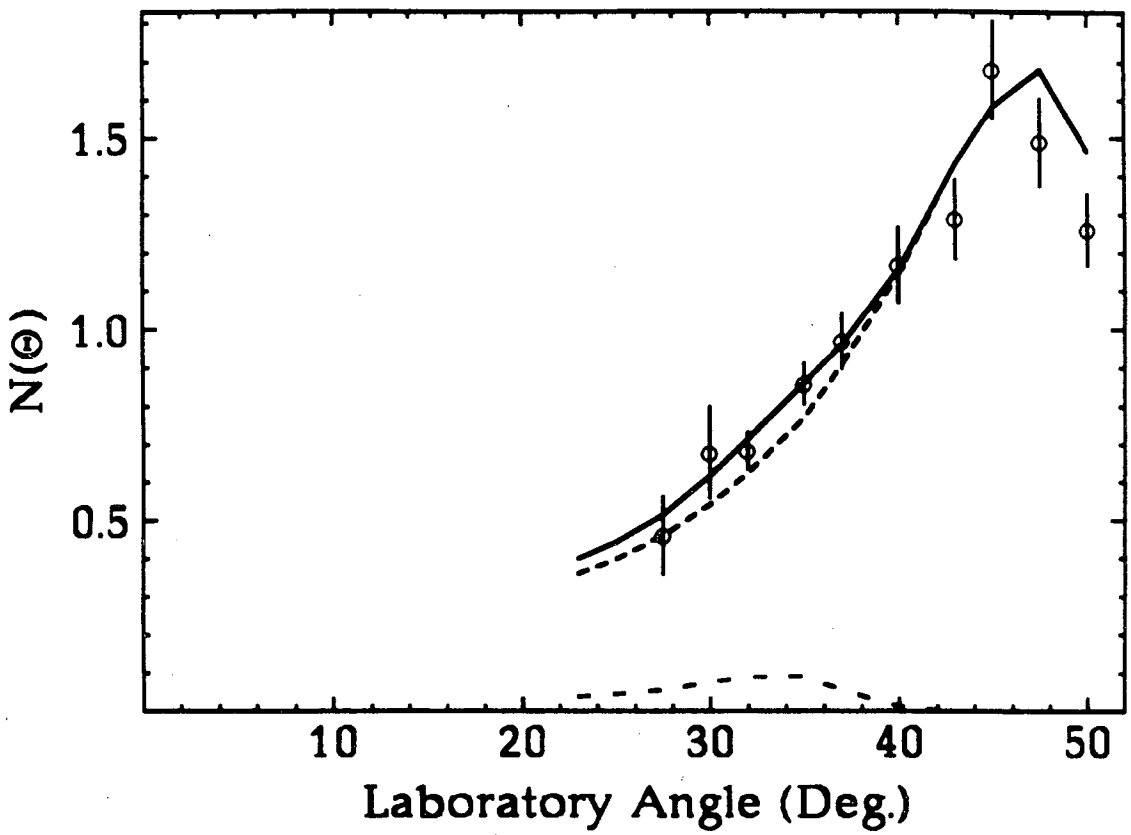

XBL 8911-4057

Figure 3 - 20

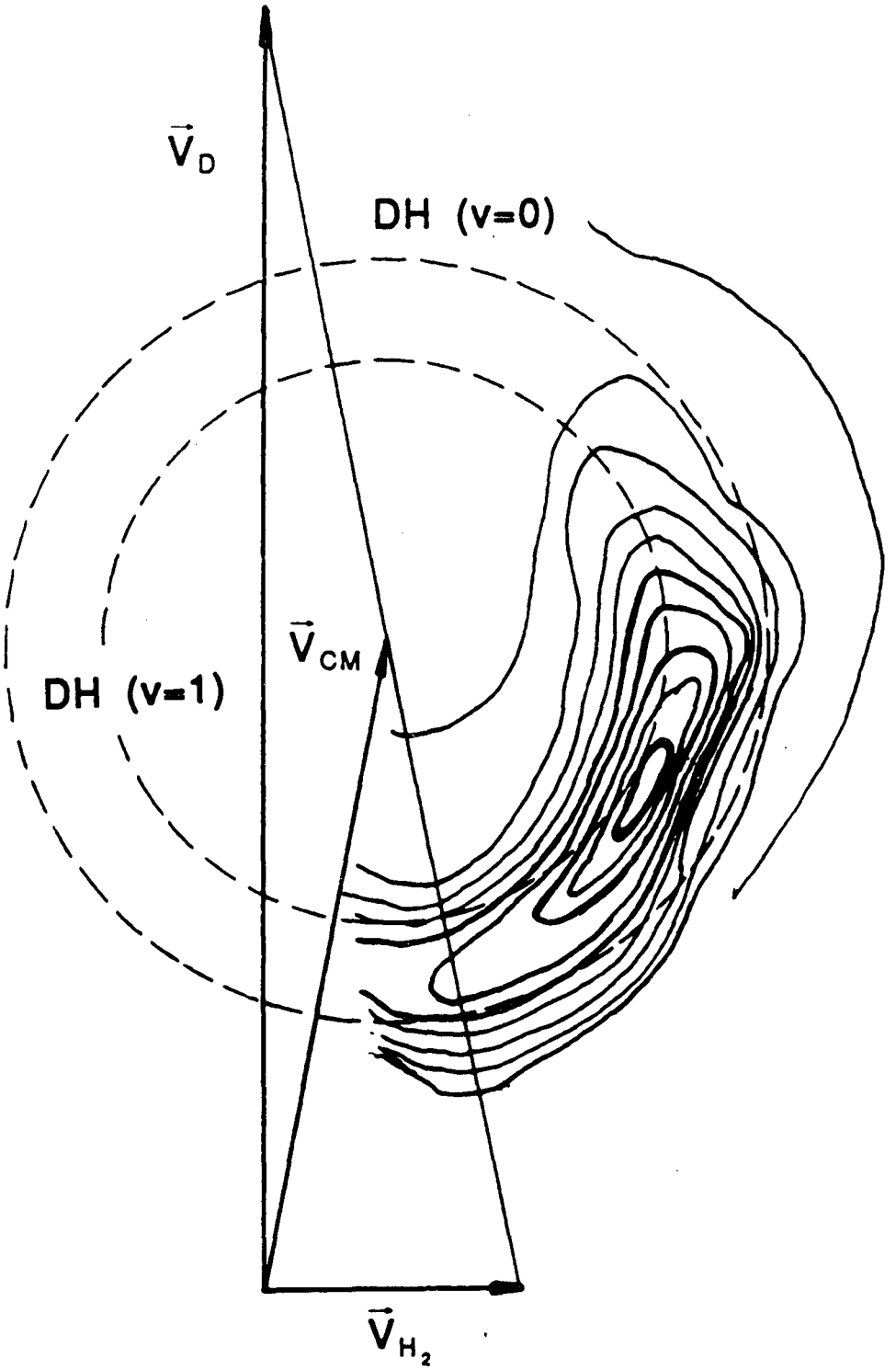

XBL 8911-4058

Figure 3 - 21

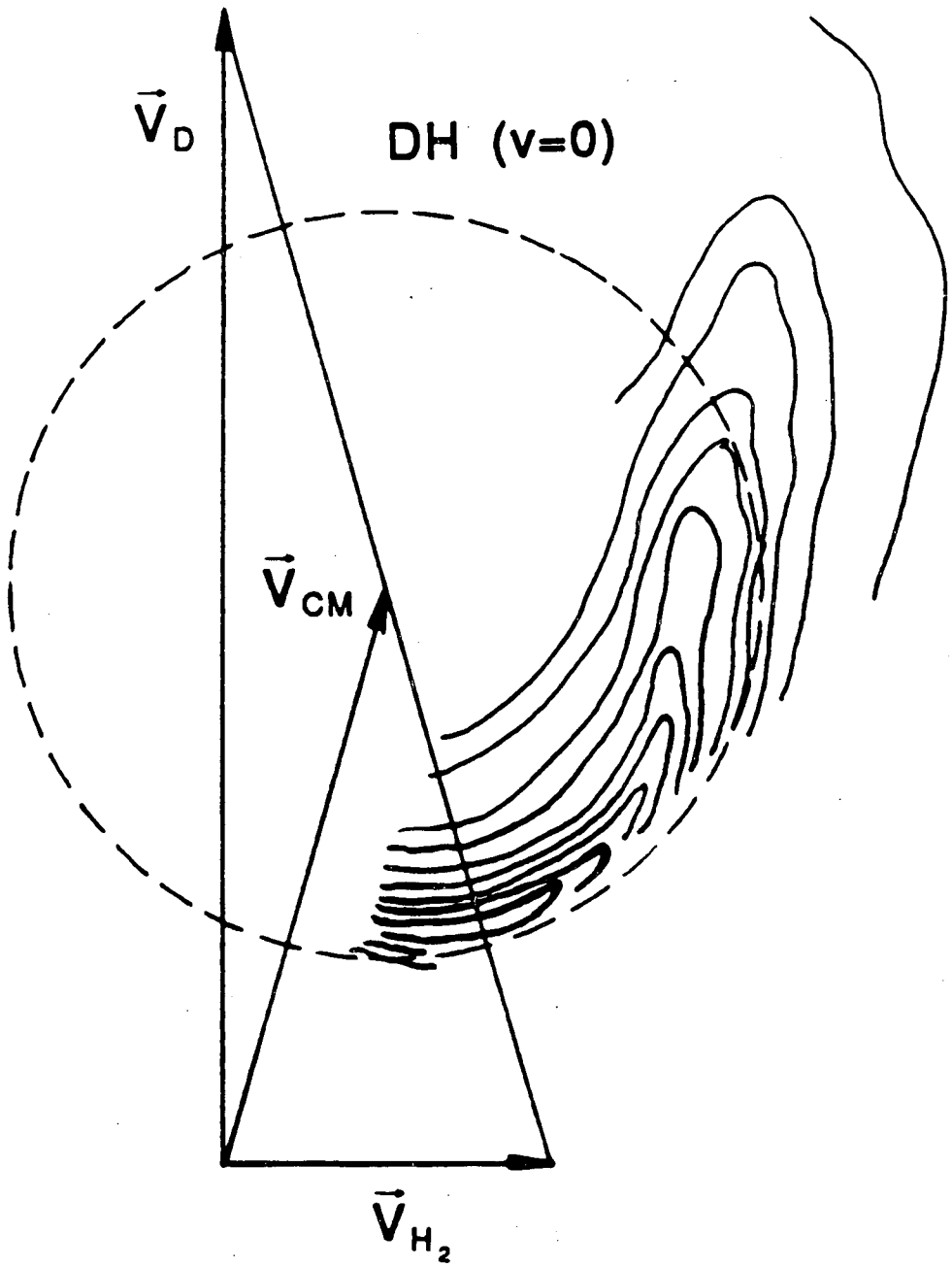

XBL 8911-4059

Figure 3 - 22

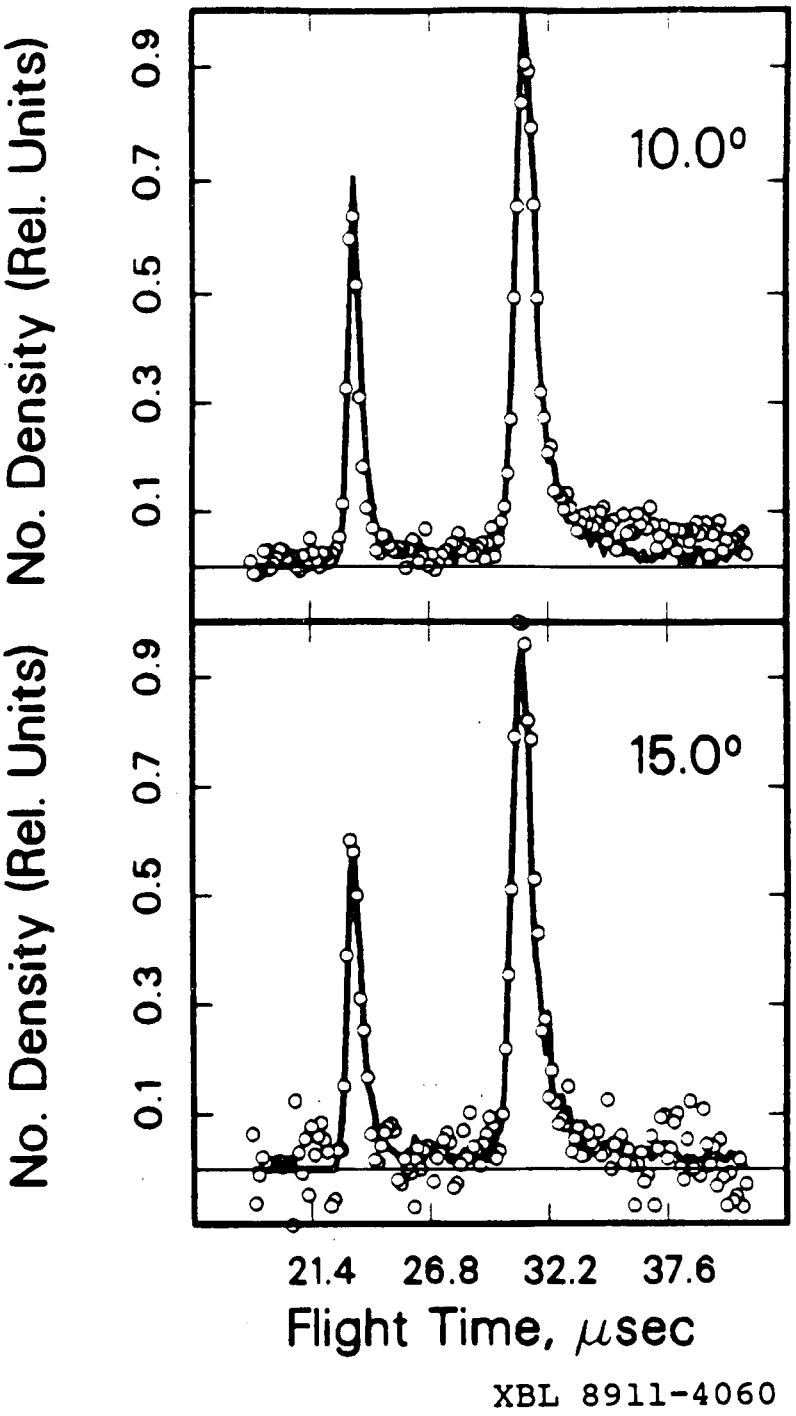
No. Density (Rel. Units)
0.1
0.3
0.5
0.7
0.9
10.0°
15.0°
21.4
26.8
32.2
37.6
Flight Time, μsec
XBL 8911-4060

Figure 3 - 23

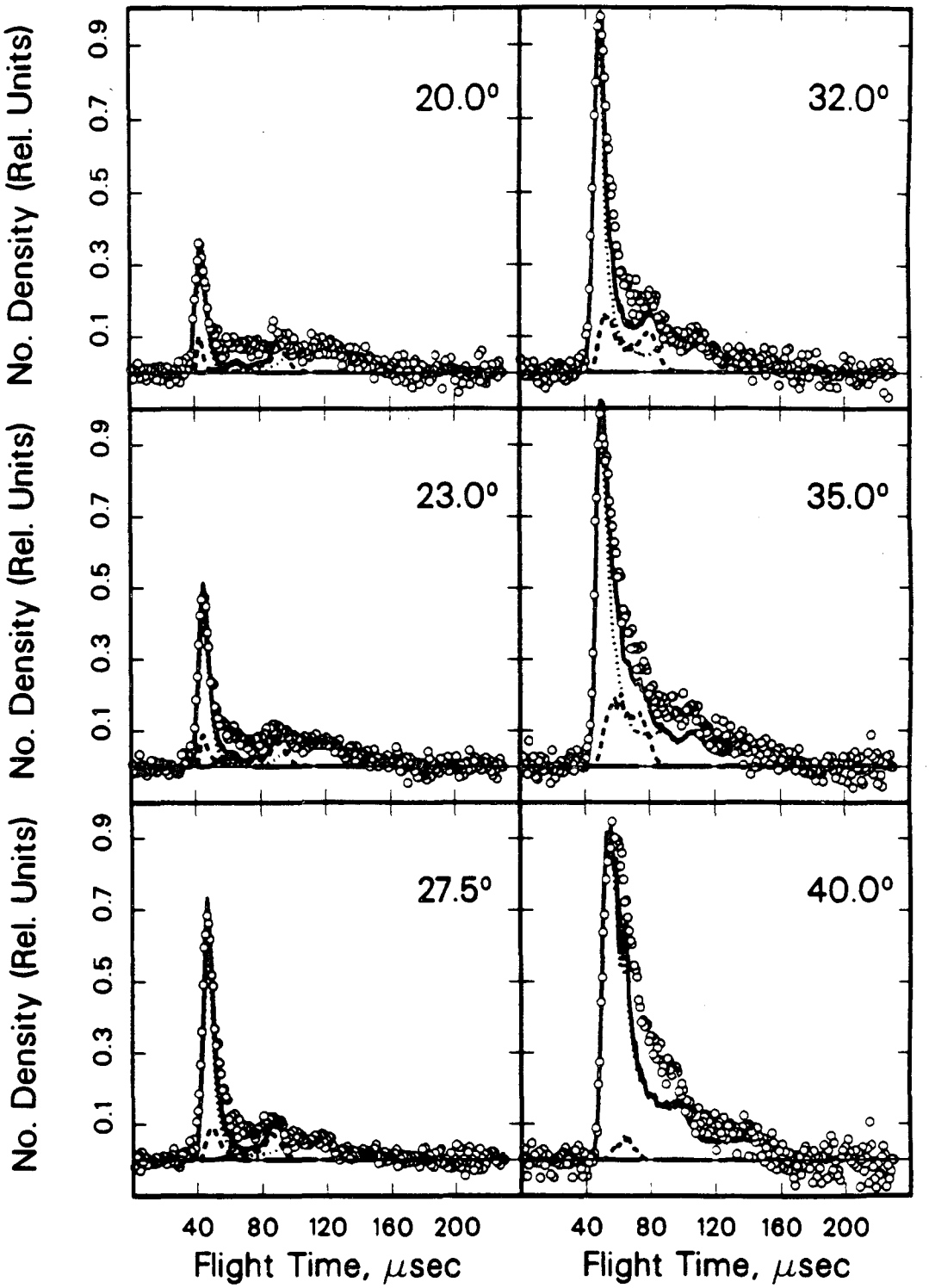
No. Density (Rel. Units)
0.1
0.3
0.5
0.7
0.9
20.0°
32.0°
23.0°
35.0°
27.5°
40.0°
40
80
120
160
200
Flight Time, μsec
XBL 8911-4061

Figure 3 - 24

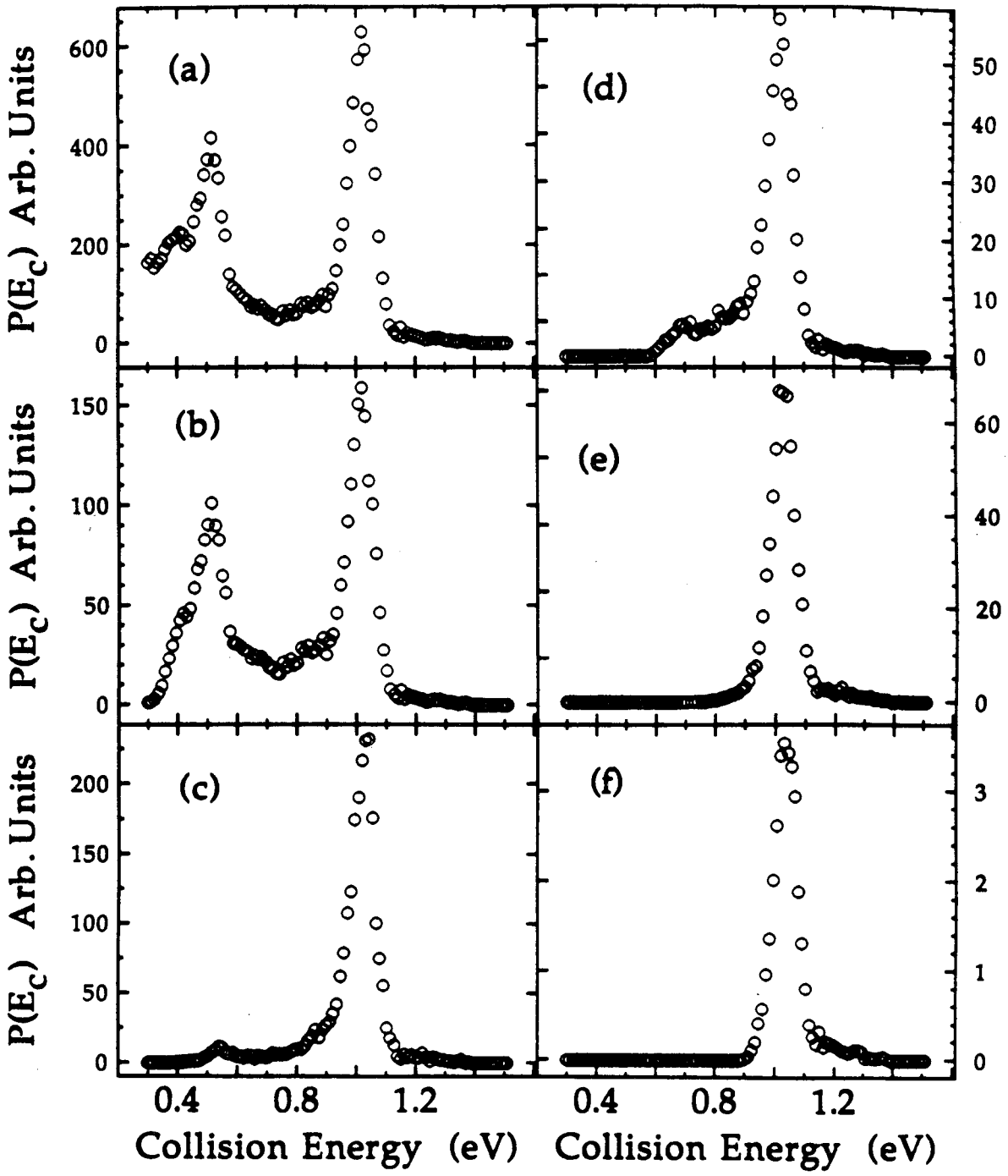
(a)
(b)
(c)
(d)
(e)
(f)
P(E_c) Arb. Units
Collision Energy (eV)
Collision Energy (eV)
XBL 8911-4062

Figure 3 - 25

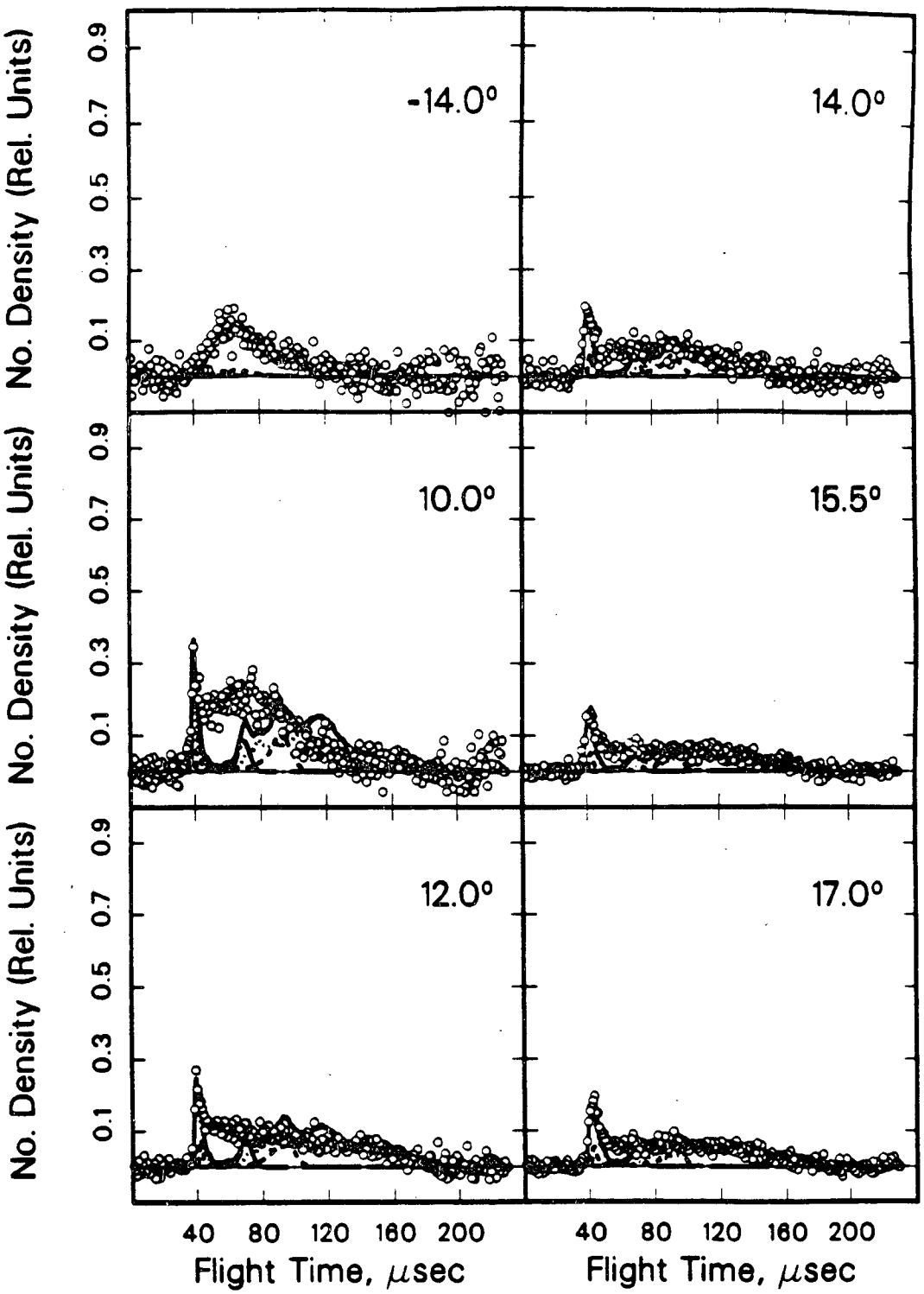
No. Density (Rel. Units)
0.1
0.3
0.5
0.7
0.9
-14.0°
14.0°
10.0°
15.5°
12.0°
17.0°
40
80
120
160
200
Flight Time, μsec
XBL 8911-4063

Figure 3 - 26a

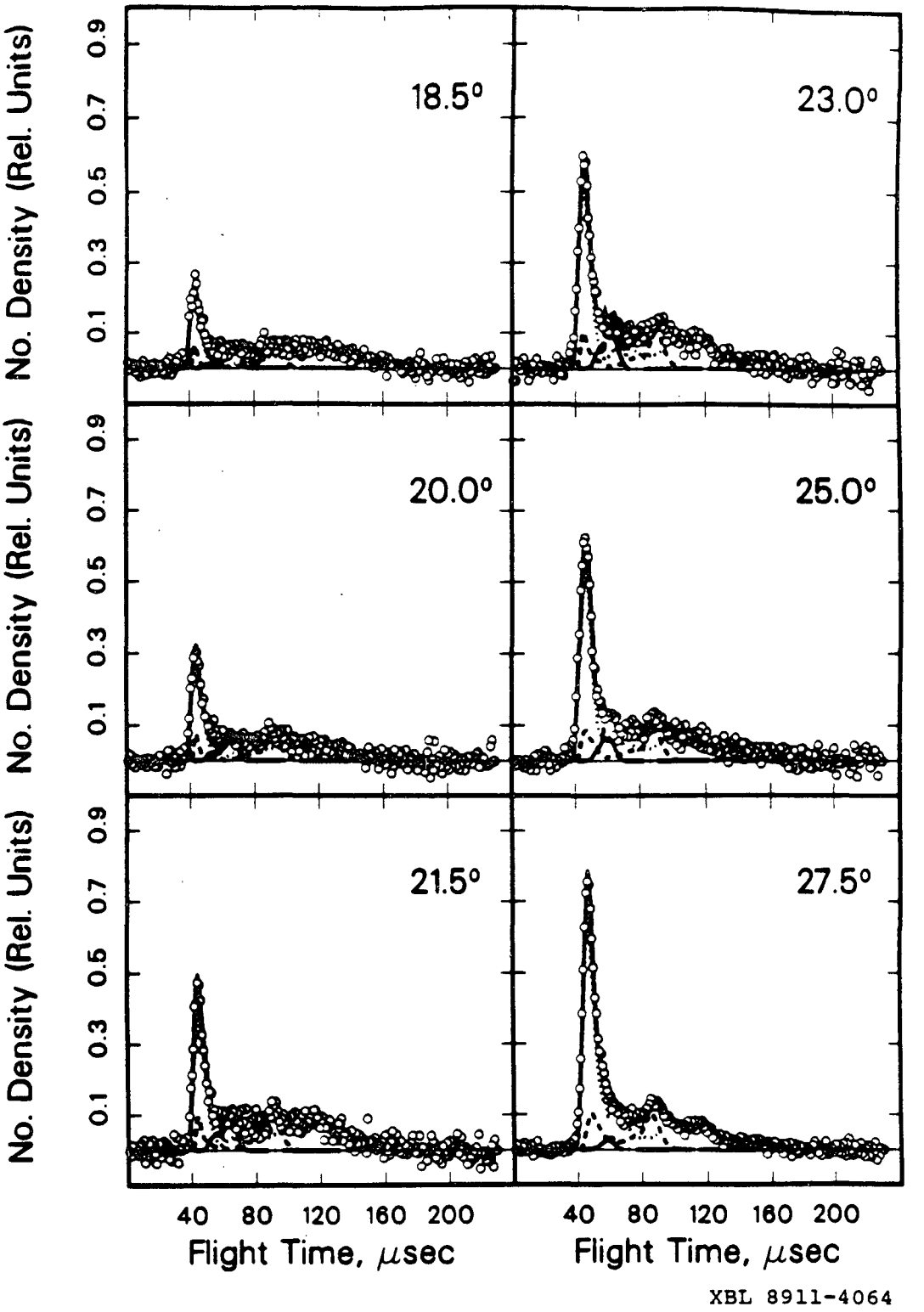
No. Density (Rel. Units)
0.1
0.3
0.5
0.7
0.9
18.5°
23.0°
20.0°
25.0°
21.5°
27.5°
40
80
120
160
200
Flight Time, μsec
XBL 8911-4064

Figure 3 - 26b

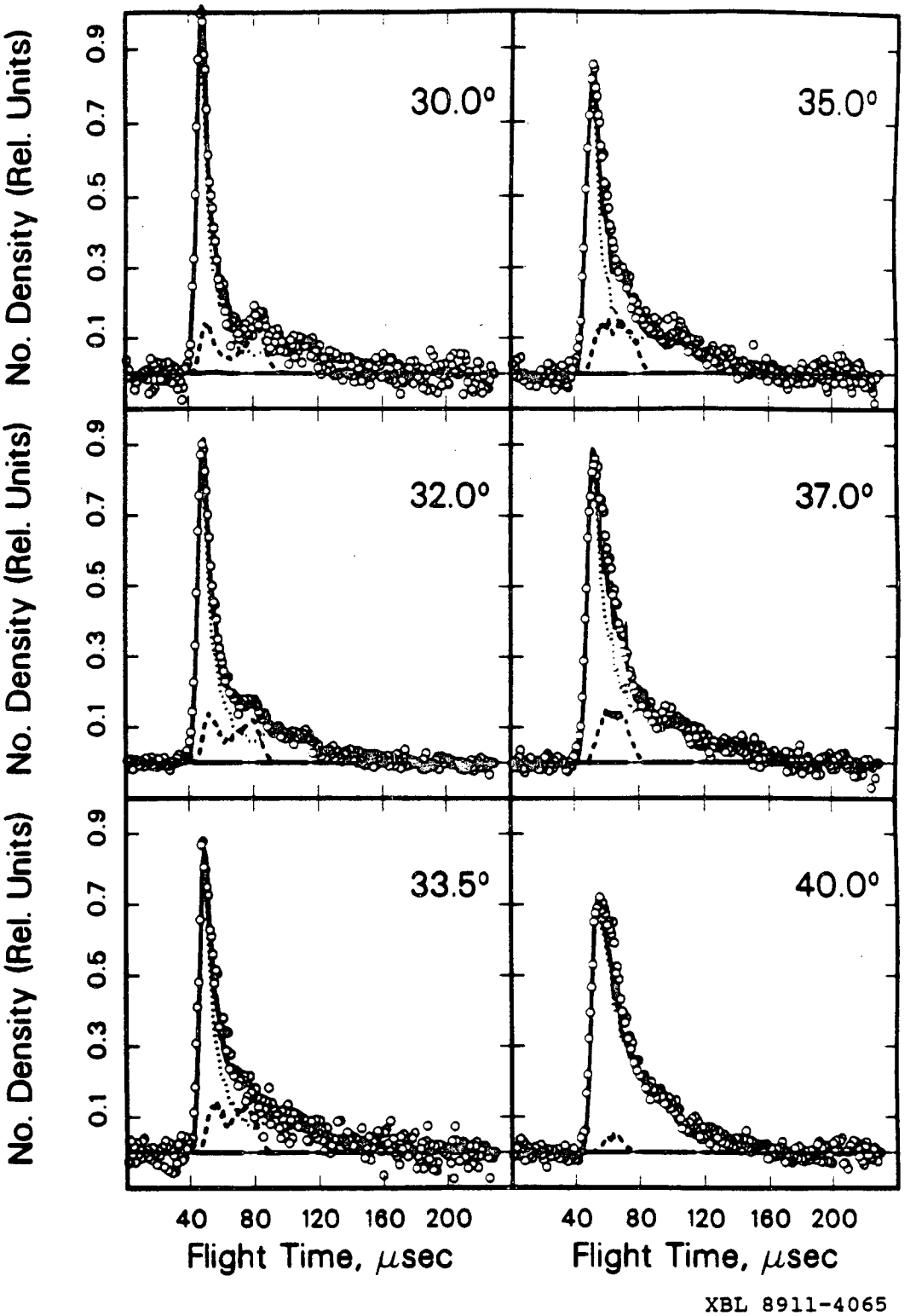
No. Density (Rel. Units)
0.1
0.3
0.5
0.7
0.9
30.0°
35.0°
32.0°
37.0°
33.5°
40.0°
40
80
120
160
200
Flight Time, μsec
XBL 8911-4065

Figure 3 - 26c

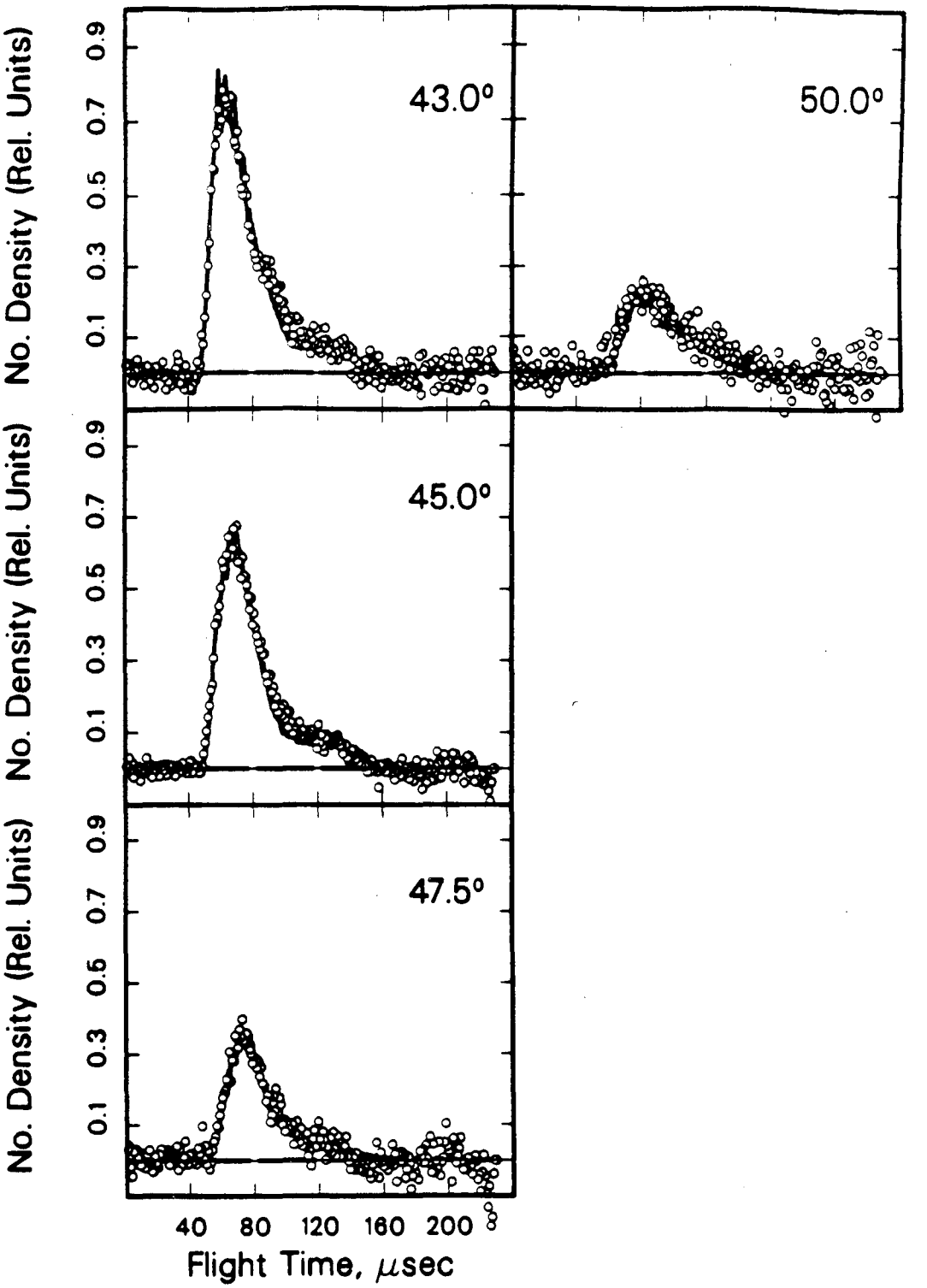

XBL 8911-4066

Figure 3 - 26d

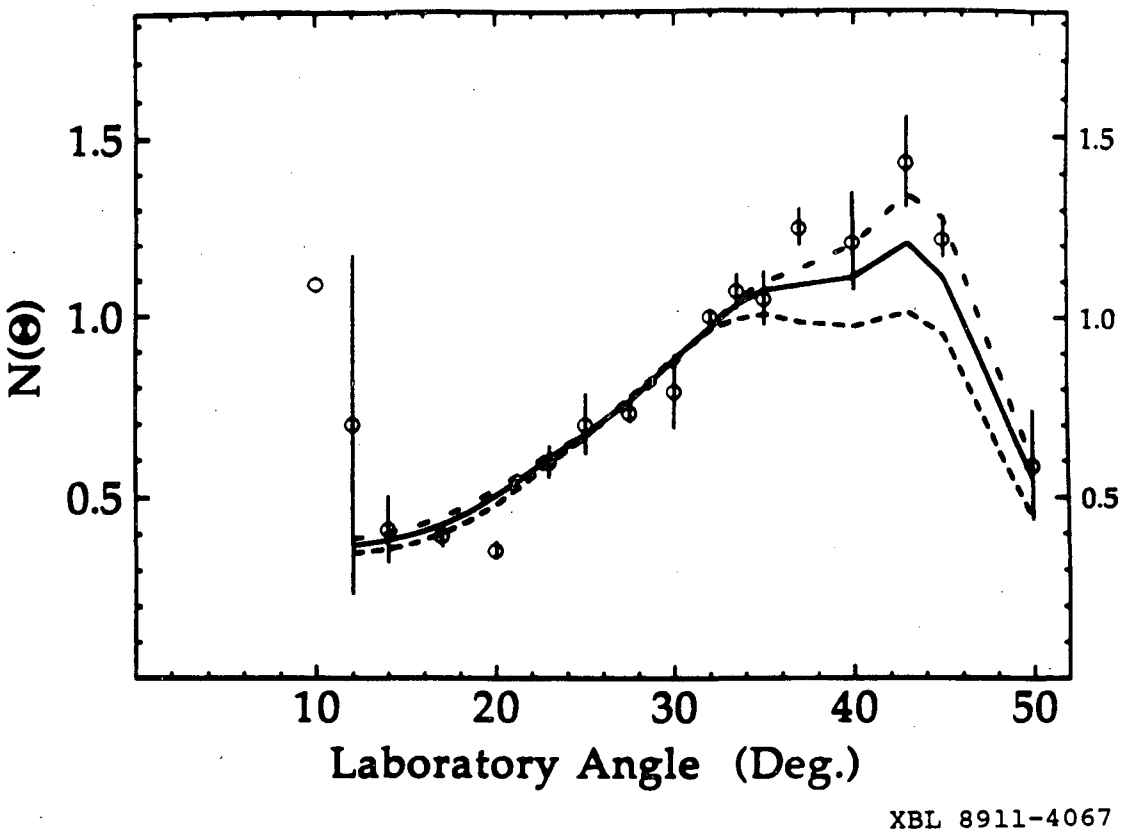

Figure 3 - 27

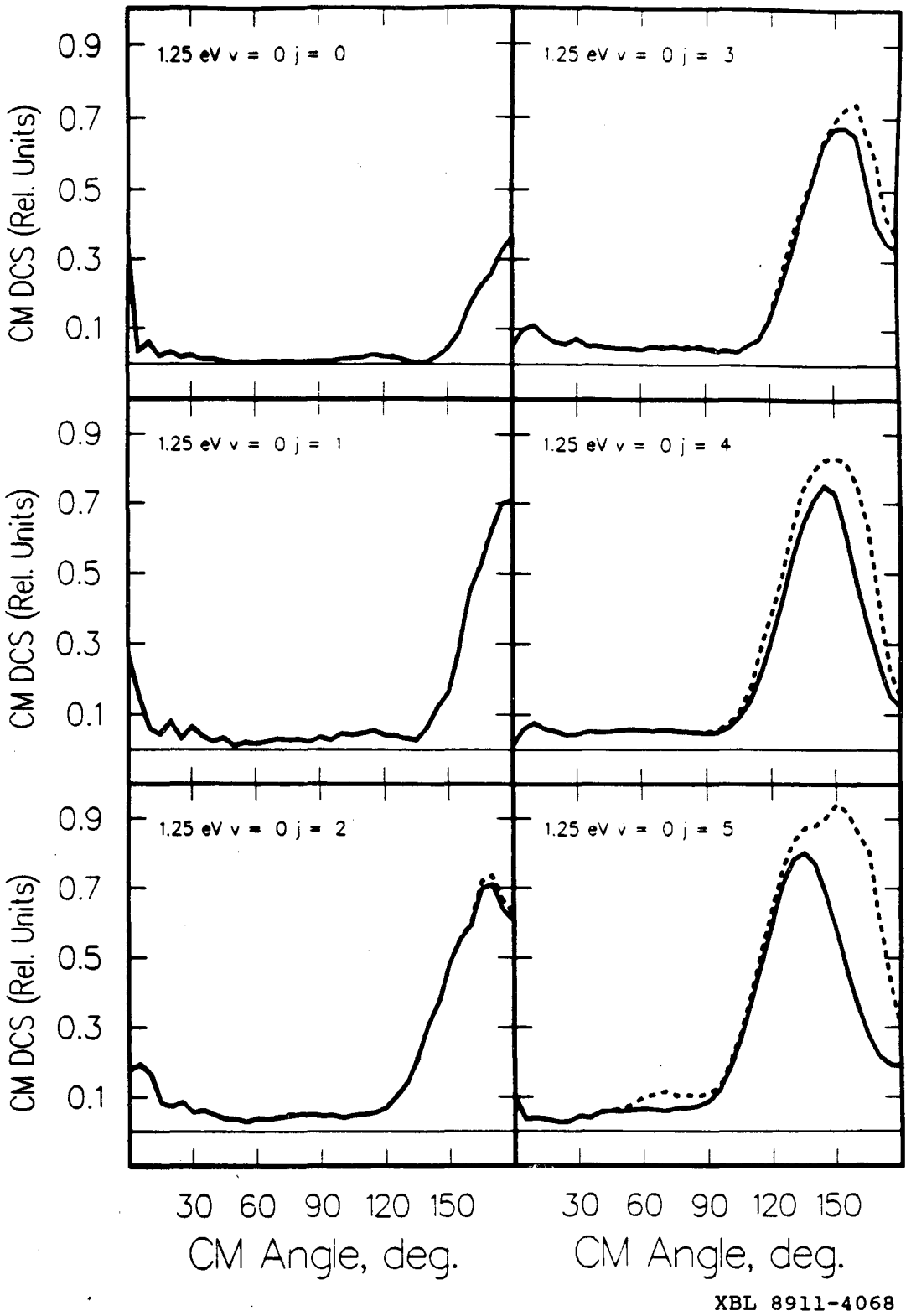
1.25 eV v = 0 j = 0
1.25 eV v = 0 j = 3
1.25 eV v = 0 j = 1
1.25 eV v = 0 j = 4
1.25 eV v = 0 j = 2
1.25 eV v = 0 j = 5
CM DCS (Rel. Units)
0.9
0.7
0.5
0.3
0.1
30 60 90 120 150
CM Angle, deg.
XBL 8911-4068

Figure 3 - 28a

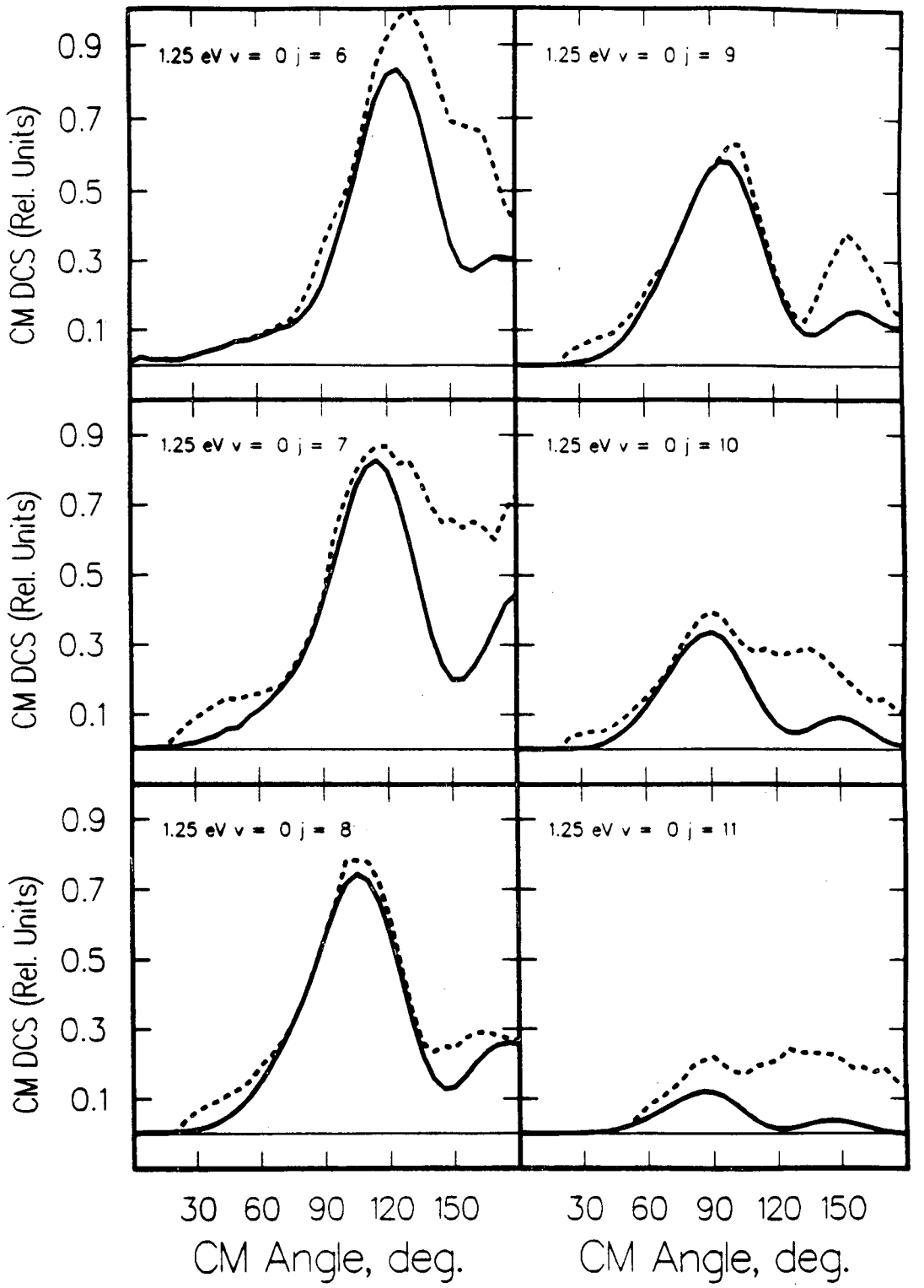

XBL 8911-4069

Figure 3 - 28b

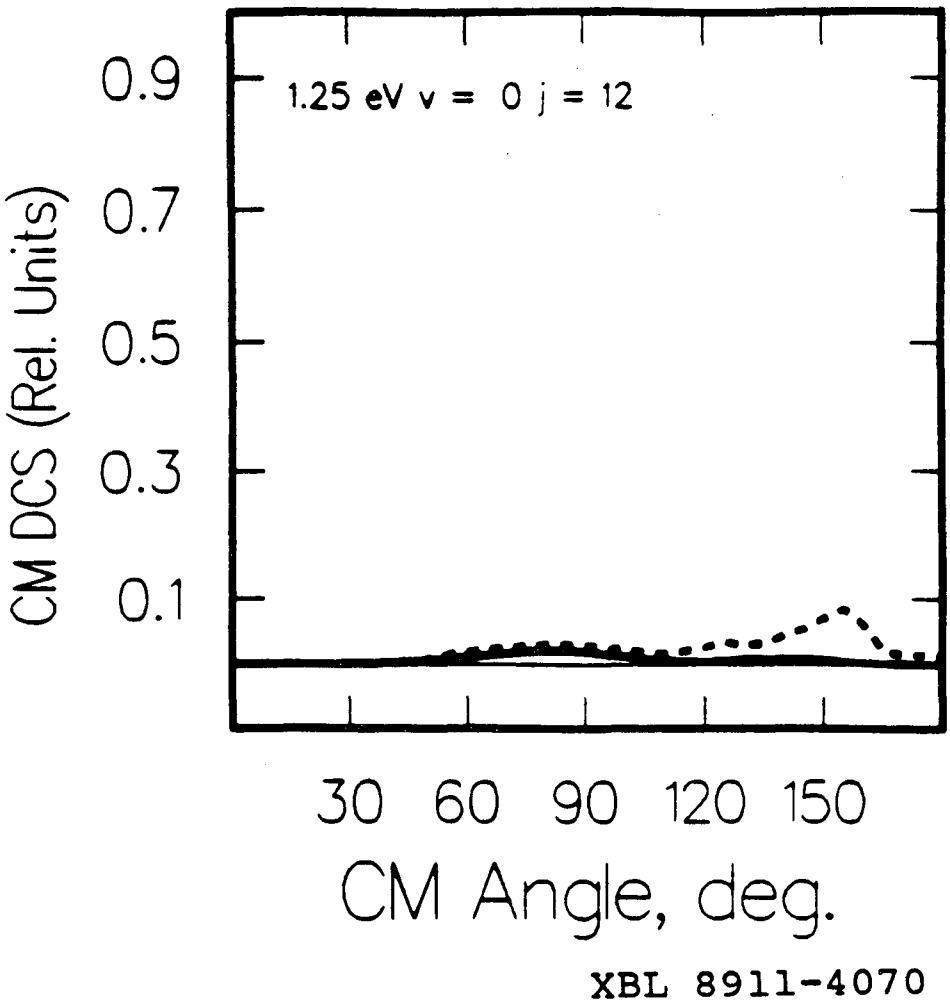
1.25 eV v = 0 j = 12
0.9
0.7
0.5
0.3
0.1
CM DCS (Rel. Units)
30 60 90 120 150
CM Angle, deg.
XBL 8911-4070

Figure 3 - 28c

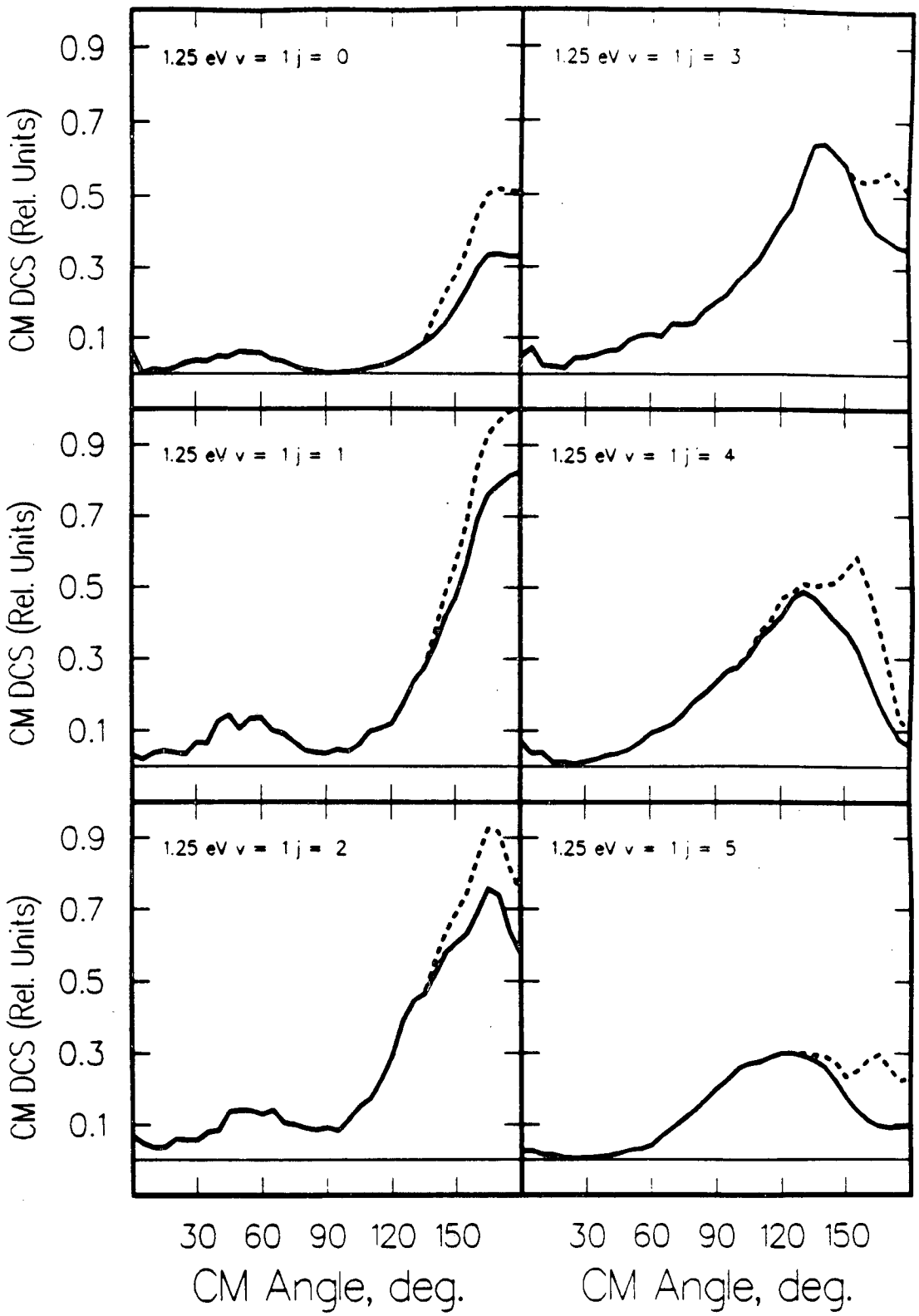

Figure 3 - 28d

XBL 8911-4071

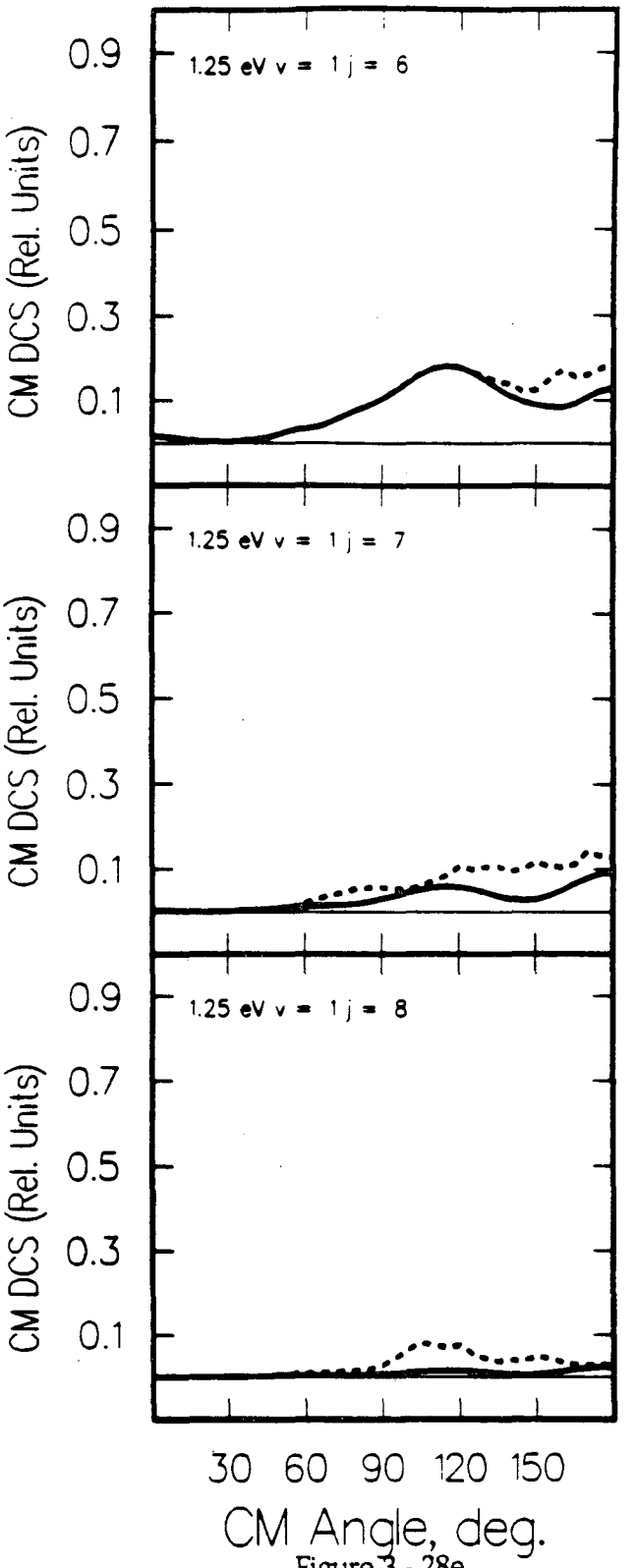

Figure 3 - 28e
XBL 8911-4072

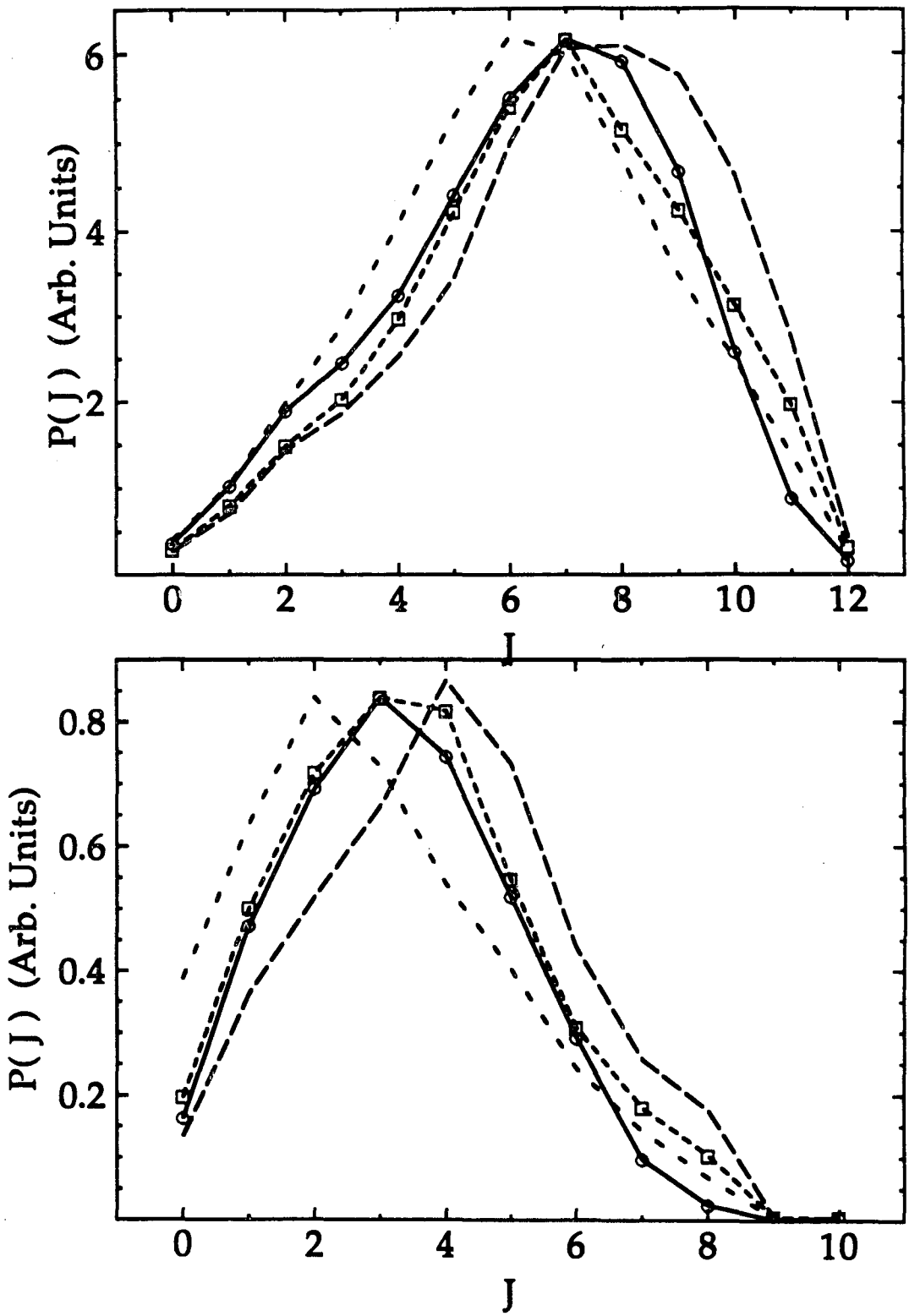

Figure 3 - 29 XBL 8911-4073

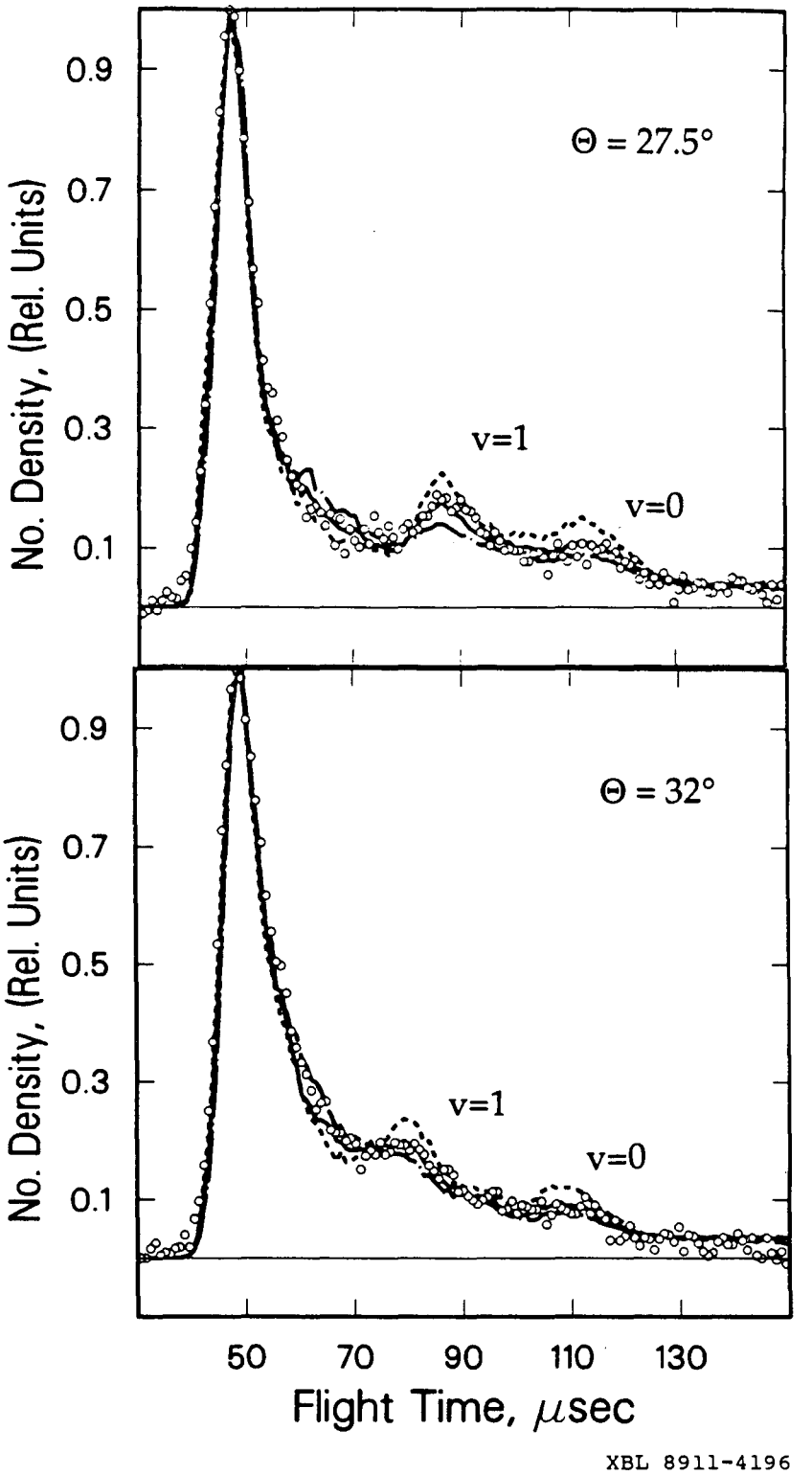
0.9
0.7
0.5
0.3
0.1
No. Density, (Rel. Units)
Θ = 27.5°
v=1
v=0
0.9
0.7
0.5
0.3
0.1
No. Density, (Rel. Units)
Θ = 32°
v=1
v=0
50
70
90
110
130
Flight Time, μsec
XBL 8911-4196

Figure 3 - 30

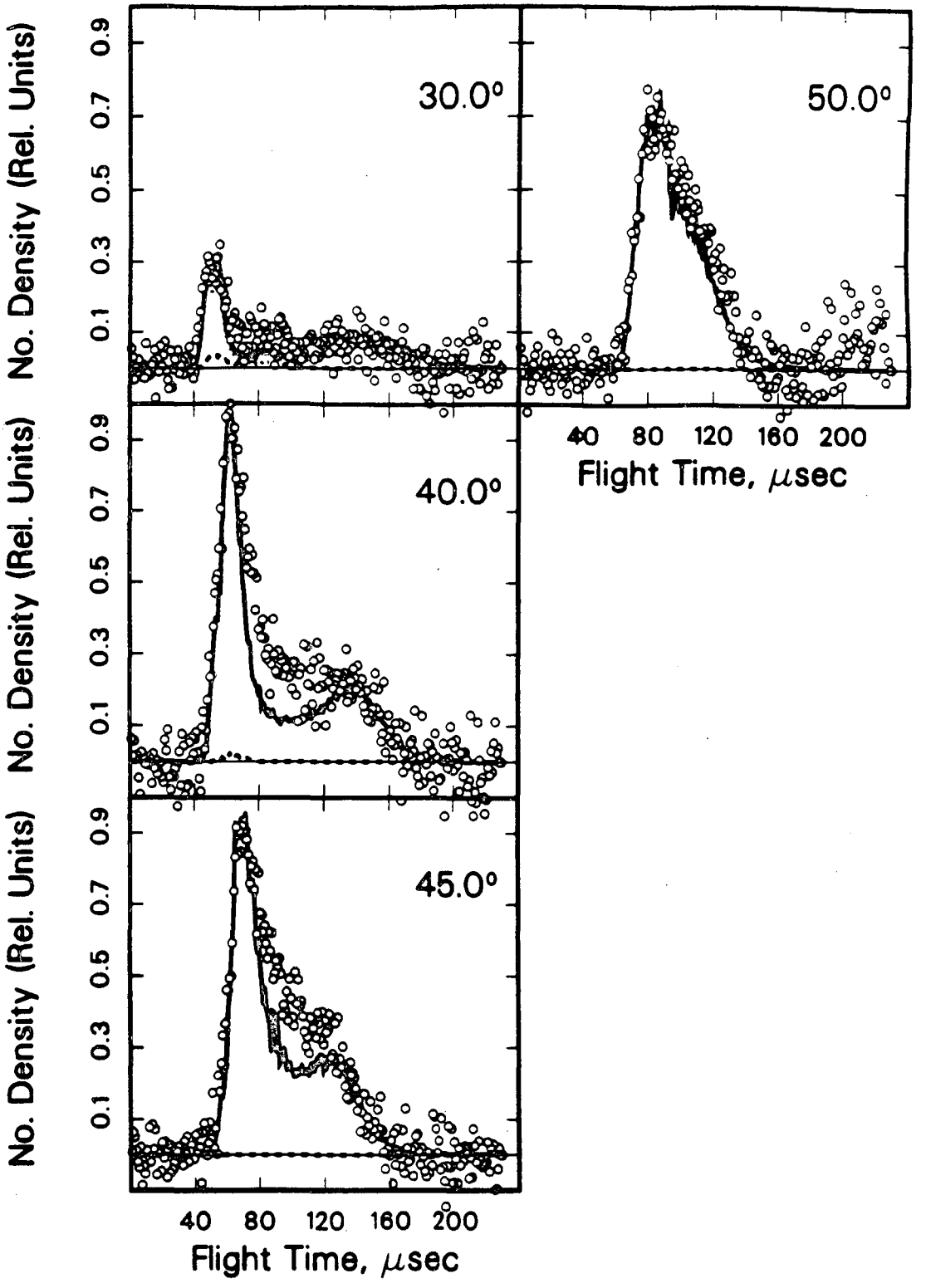

XBL 8911-4075

Figure 3 - 31

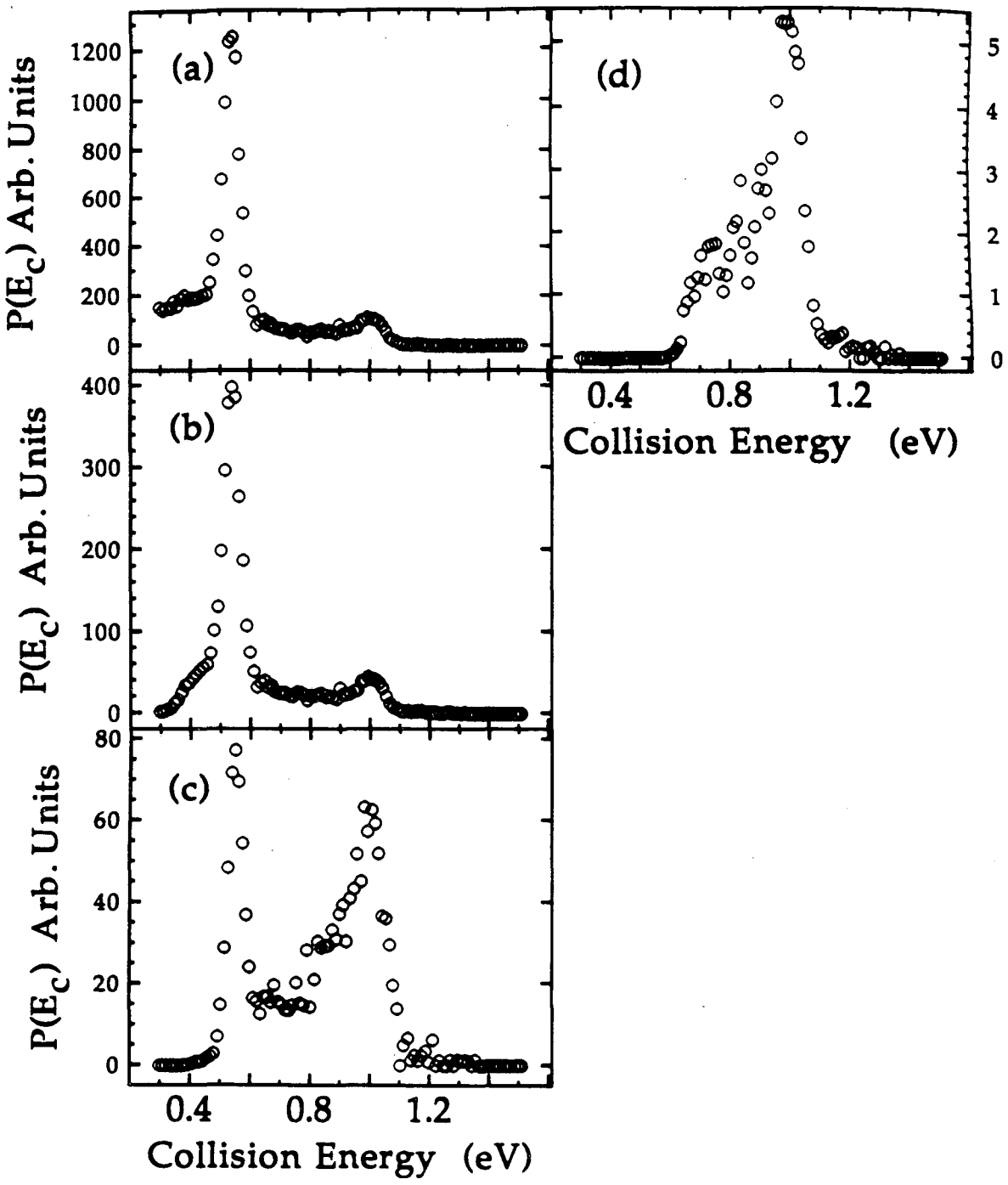

XBL 8911-4076

Figure 3 - 32

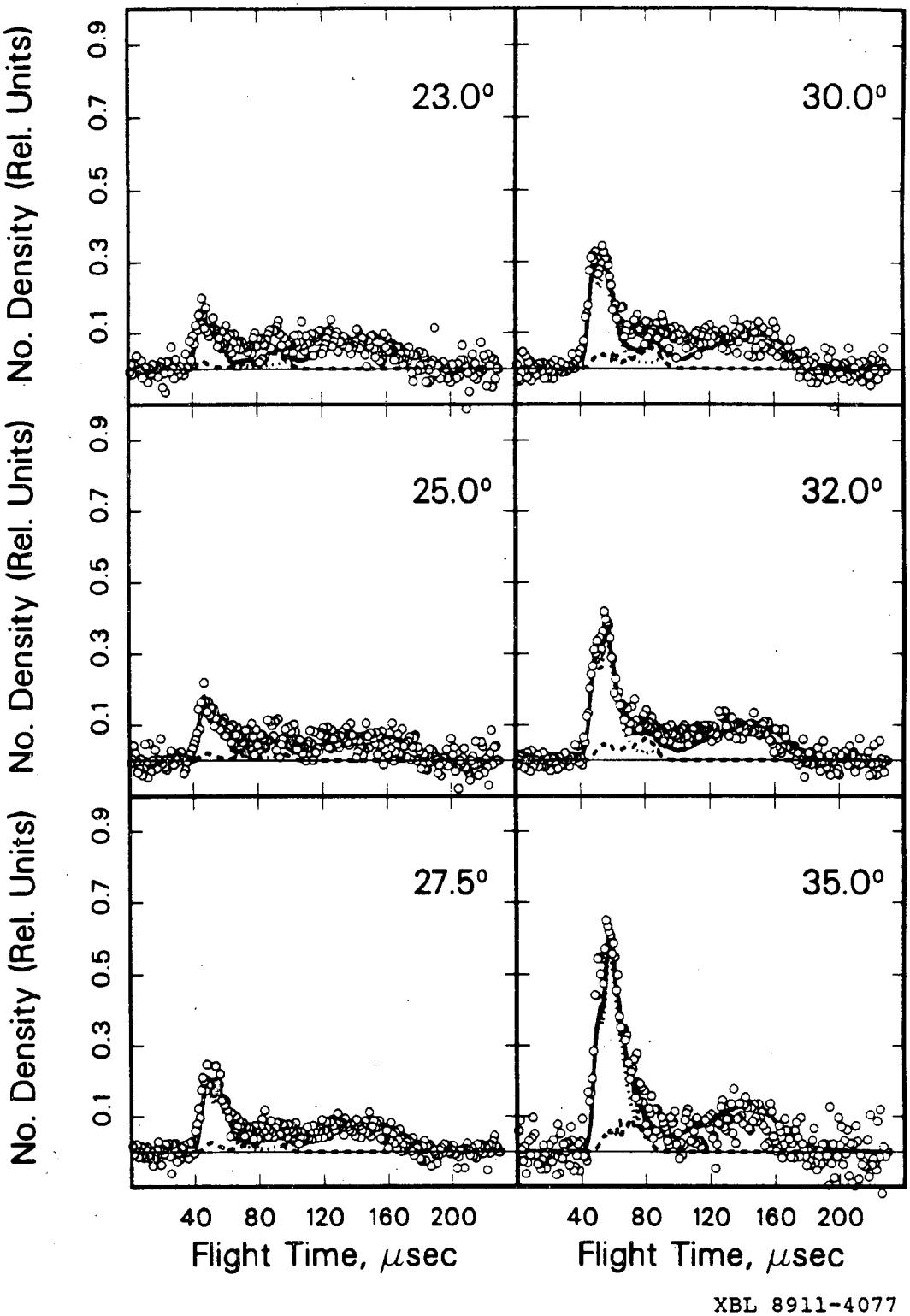
No. Density (Rel. Units)
0.1
0.3
0.5
0.7
0.9
23.0°
30.0°
25.0°
32.0°
27.5°
35.0°
40
80
120
160
200
Flight Time, μsec
XBL 8911-4077

Figure 3 - 33a

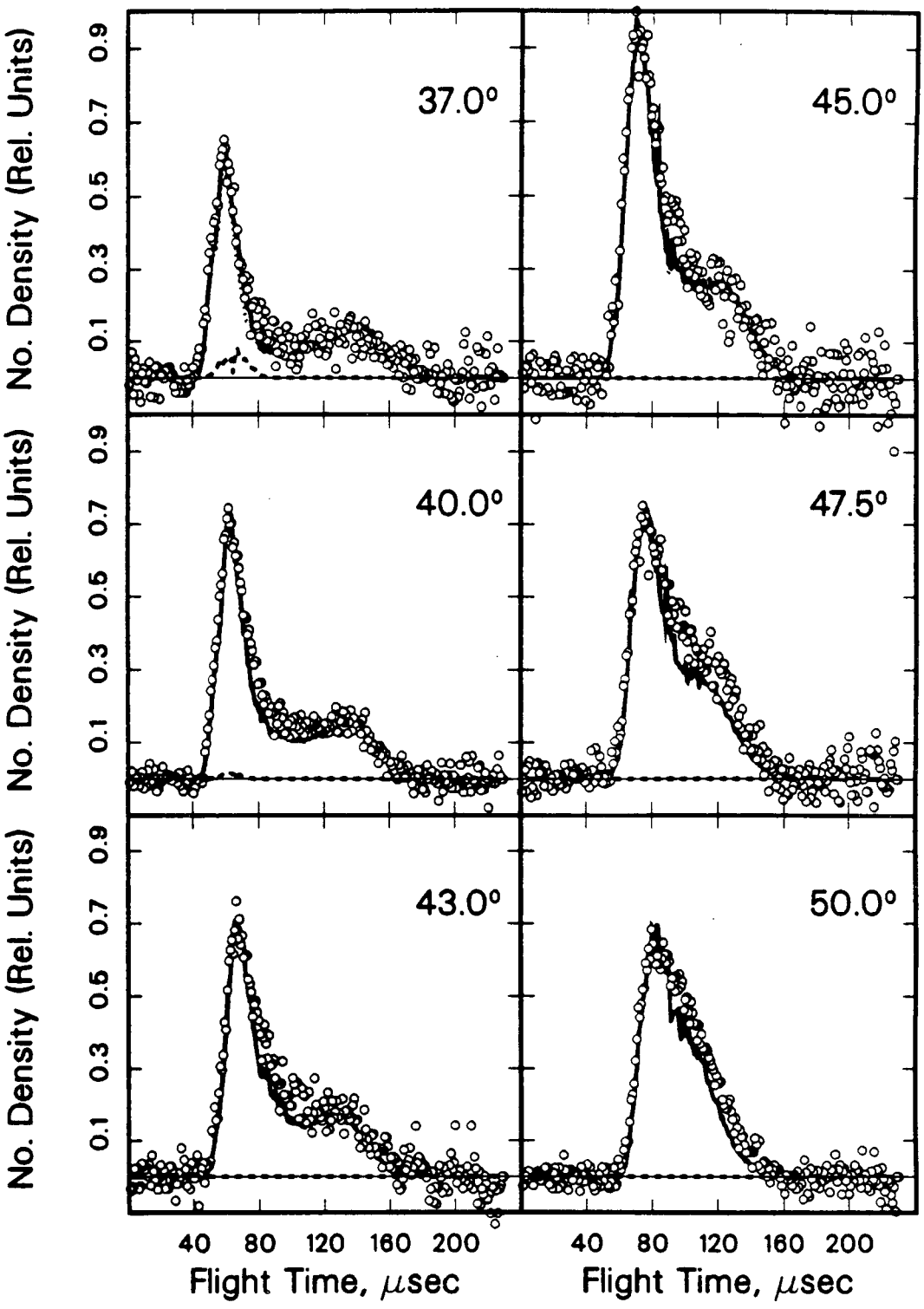
No. Density (Rel. Units)
0.1
0.3
0.5
0.7
0.9
37.0°
45.0°
40.0°
47.5°
43.0°
50.0°
40
80
120
160
200
Flight Time, μsec
XBL 8911-4078

Figure 3 - 33b

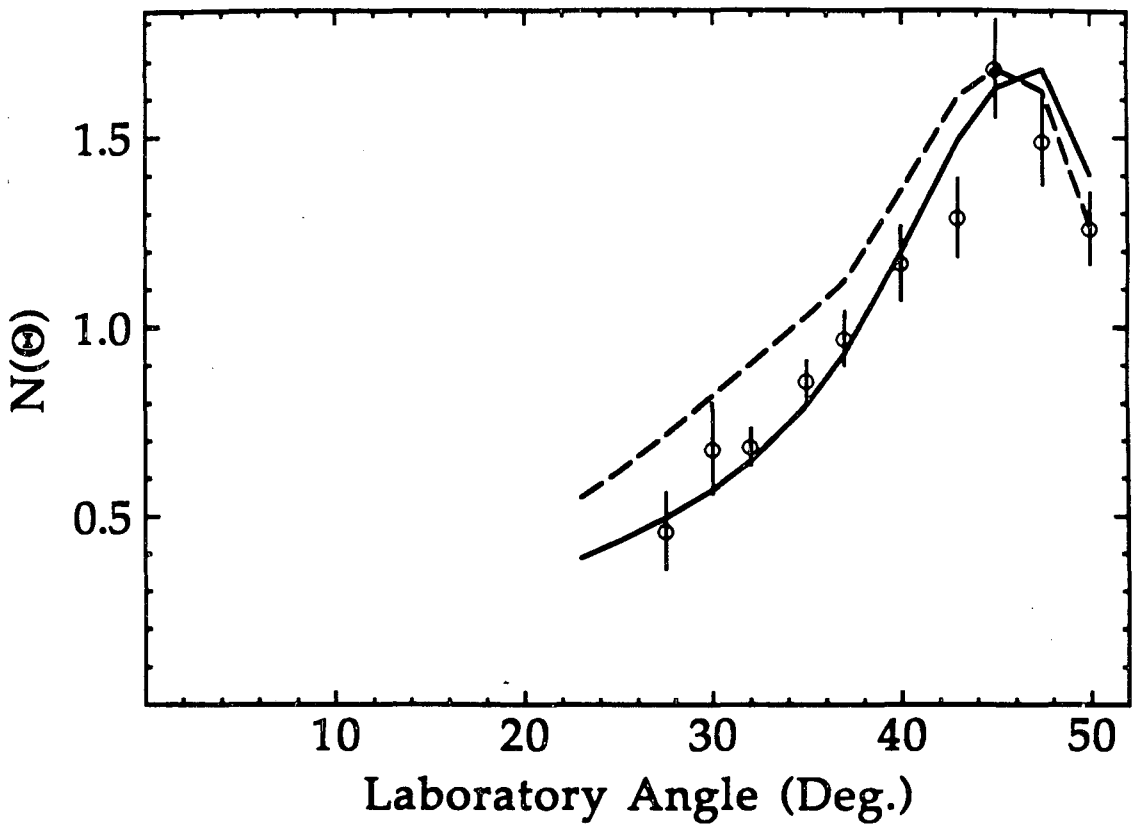

XBL 8911-4074

Figure 3 - 34

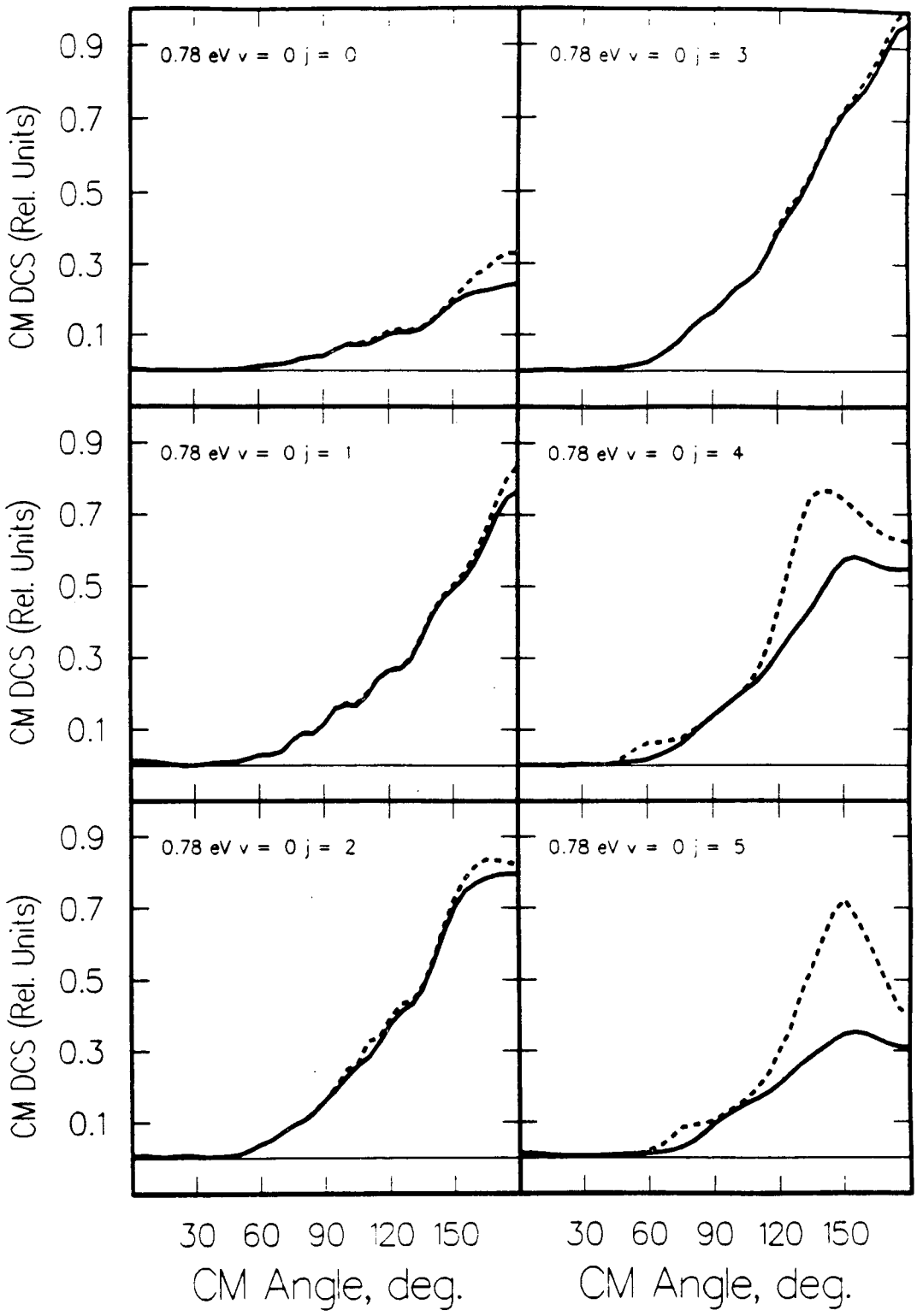

XBL 8911-4079

Figure 3 - 35a

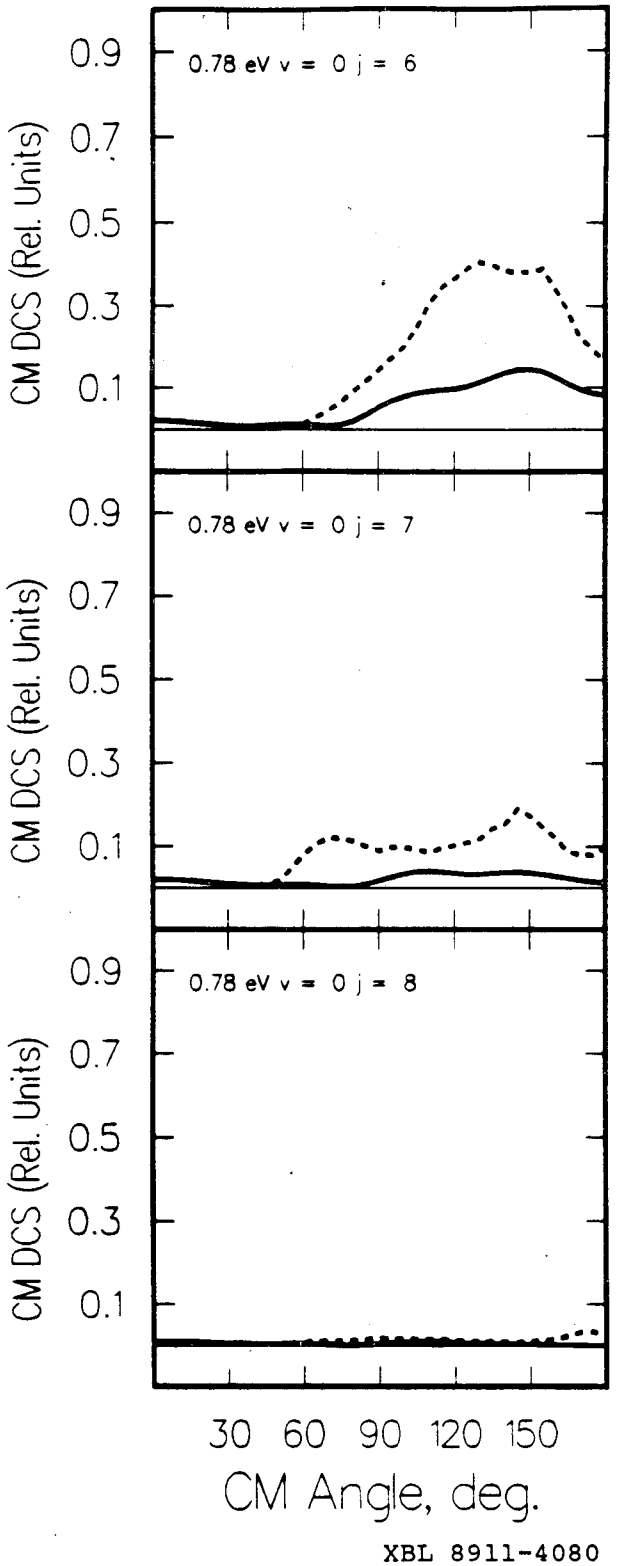
0.78 eV v = 0 j = 6
0.78 eV v = 0 j = 7
0.78 eV v = 0 j = 8
CM DCS (Rel. Units)
0.9
0.7
0.5
0.3
0.1
30 60 90 120 150
CM Angle, deg.
XBL 8911-4080

Figure 3 - 35b

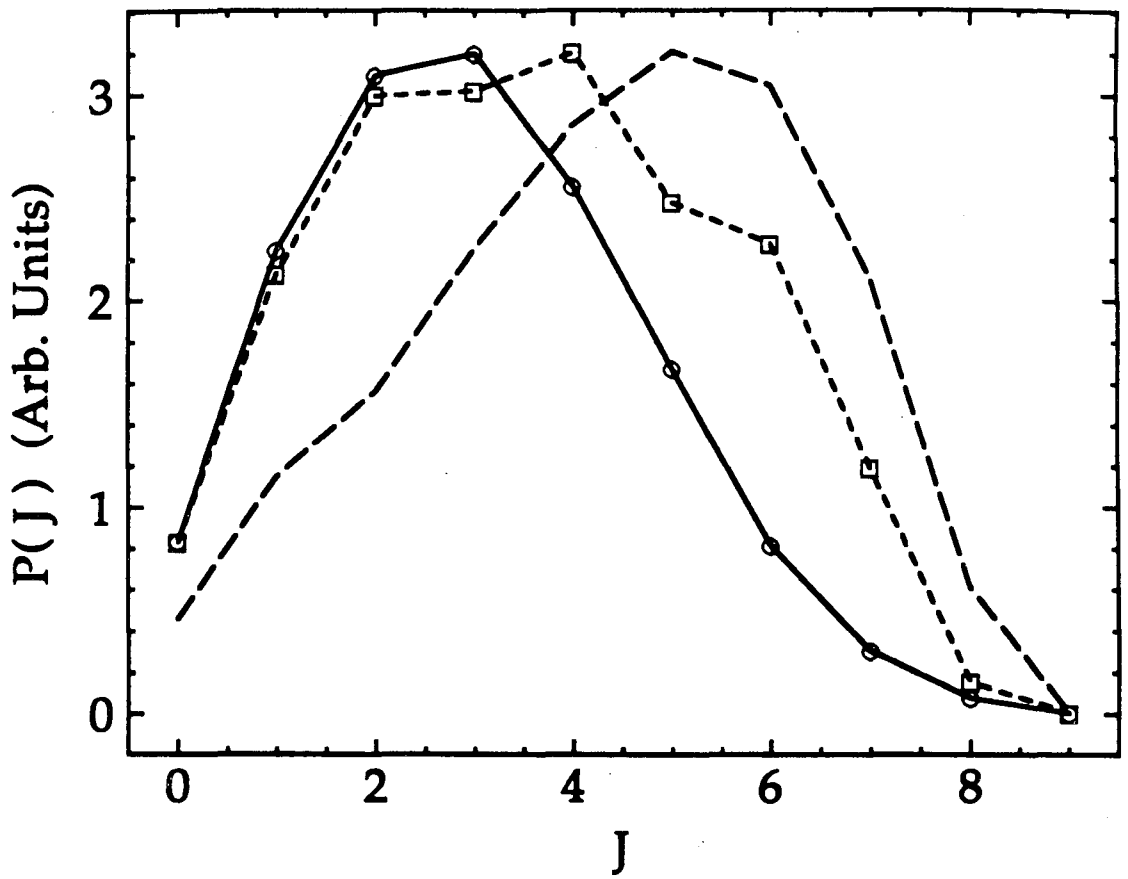

XBL 8911-4081

Figure 3 - 36

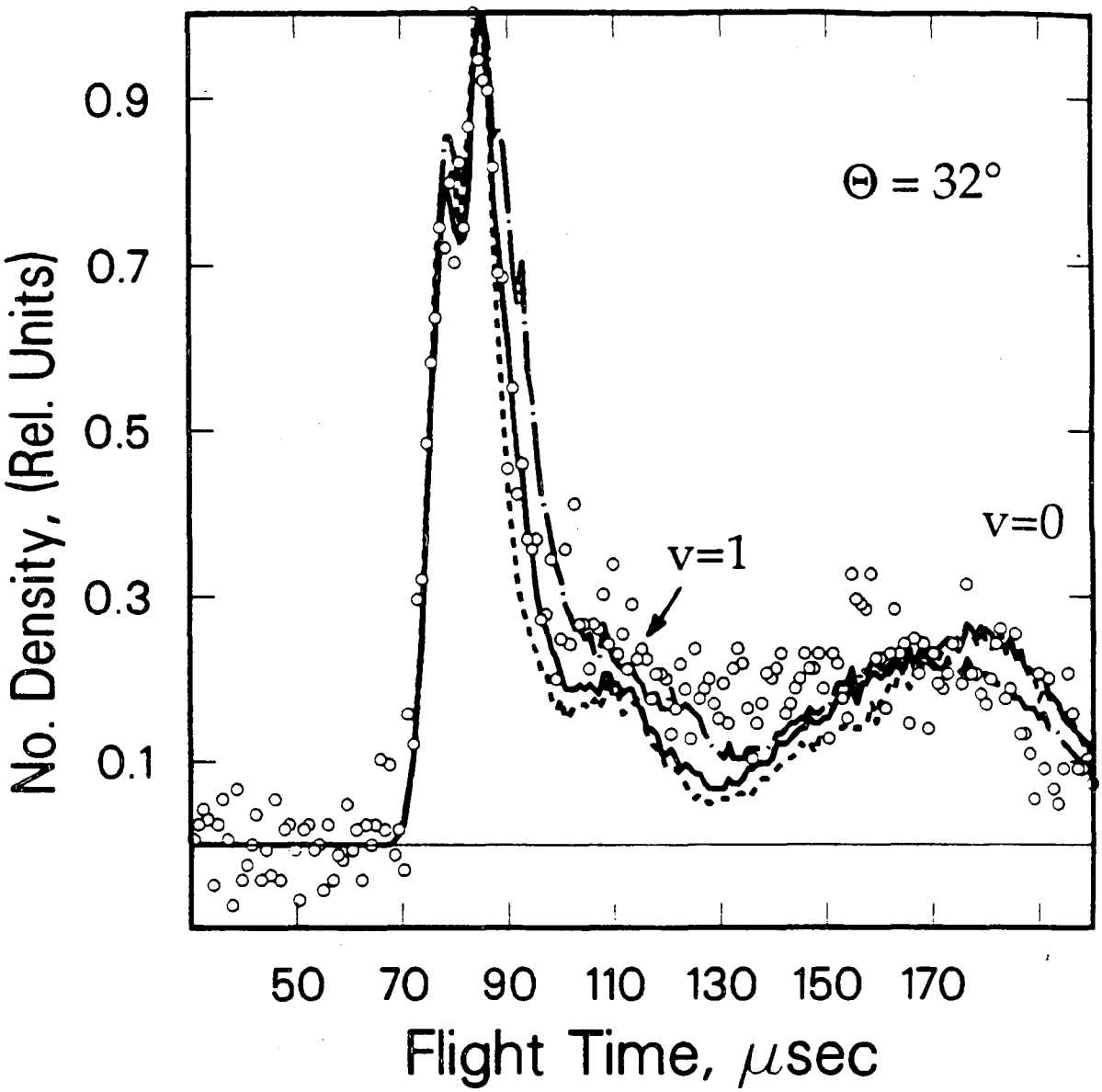

XBL 8911-4197

Figure 3 - 37

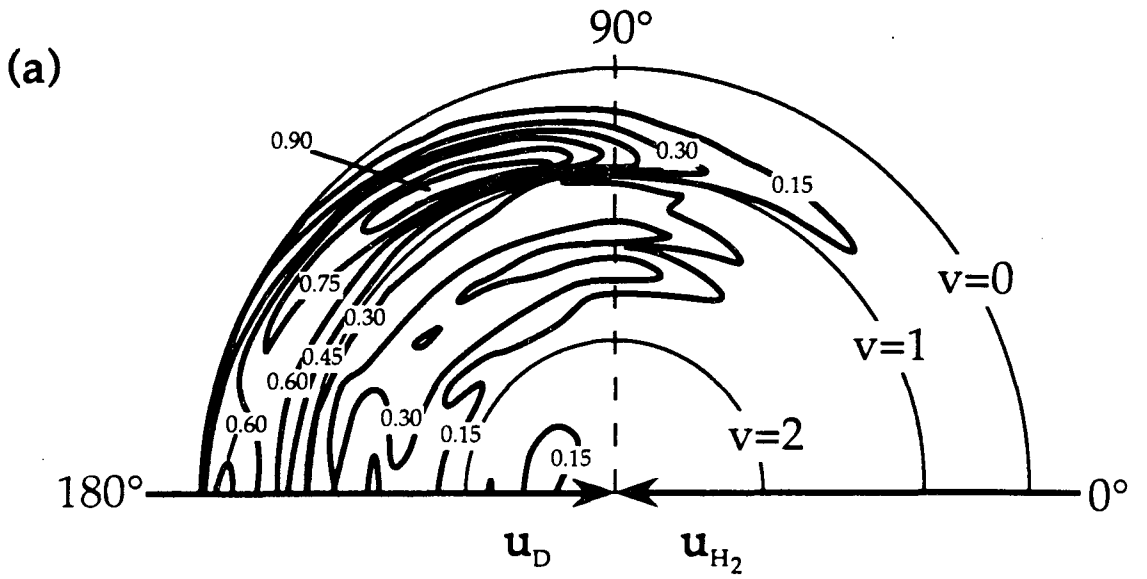

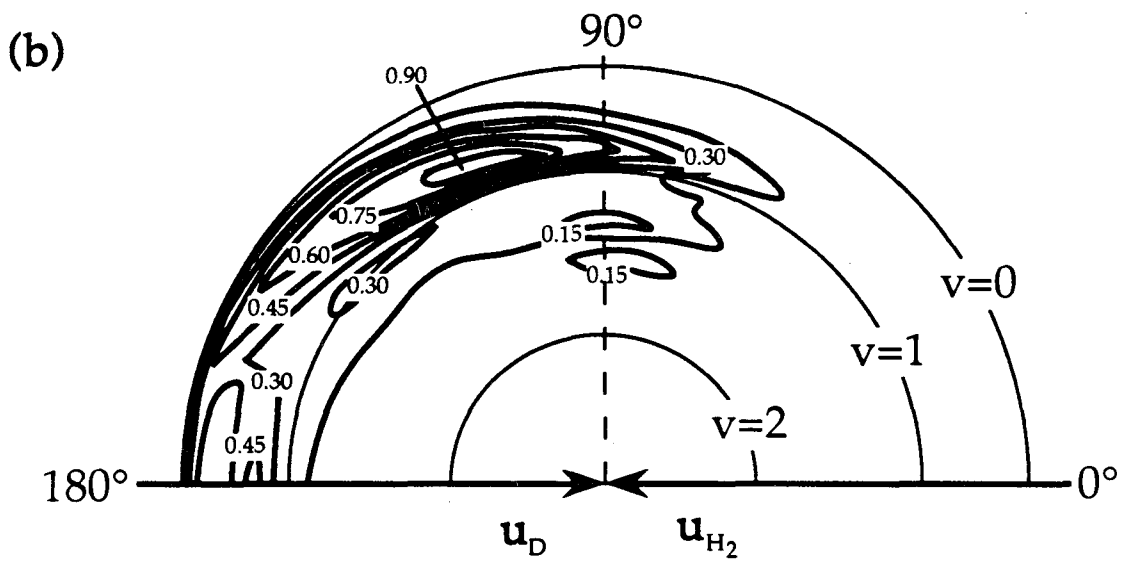

XBL 8911-4203

Figure 3 - 38

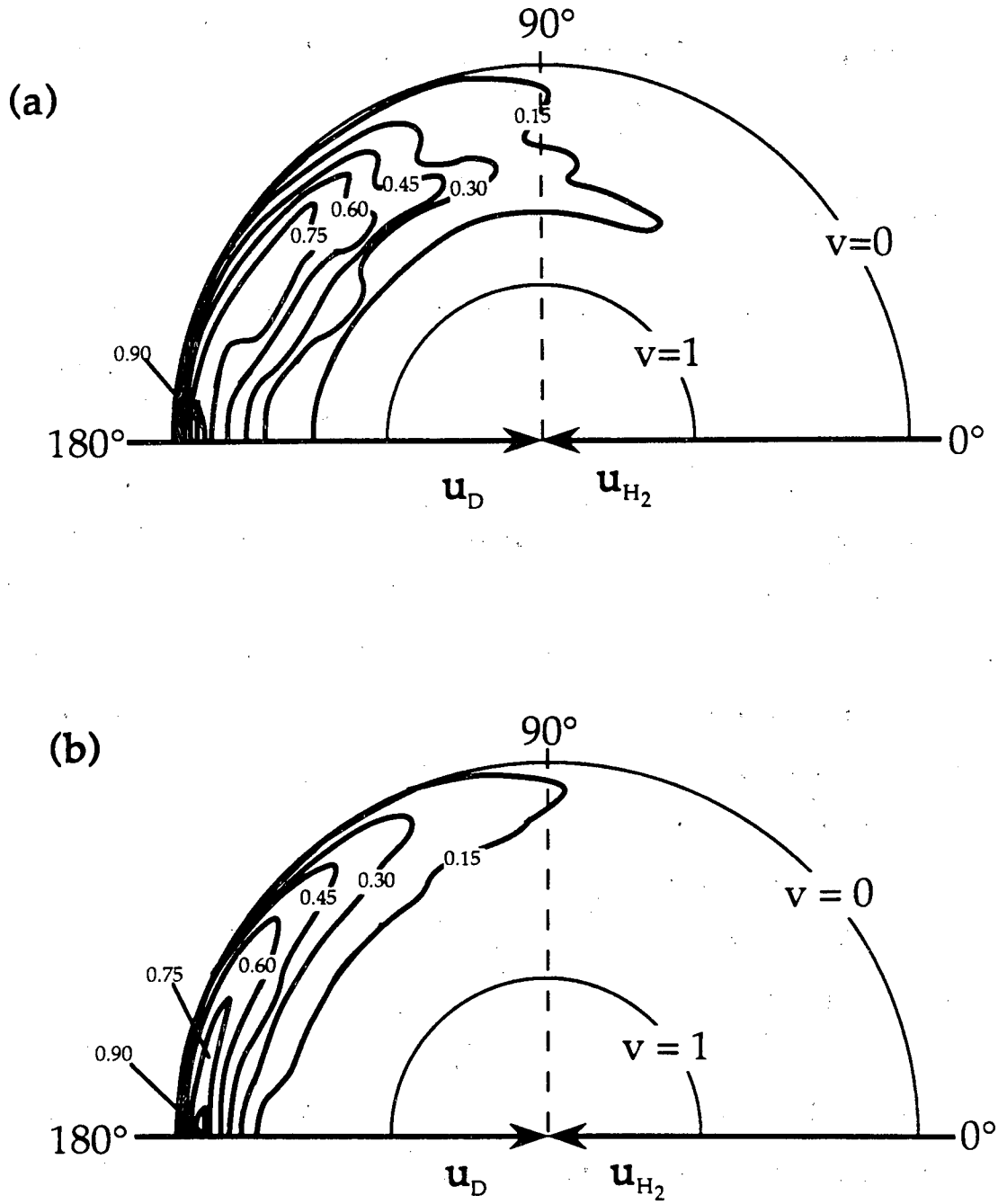
(a)
90°
0.15
0.45
0.30
0.60
0.75
0.90
v=0
v=1
180°
0°
u_D
u_{H_2}
(b)
90°
0.15
0.30
0.45
0.60
0.75
0.90
v = 0
v = 1
180°
0°
u_D
u_{H_2}
XBL 8911-4204

Figure 3 - 39

Appendix A

Transformation of Center-of-Mass Differential Cross Sections to the Laboratory Frame

1. Introduction

The analysis of differential-cross-section measurements for an elementary reaction like $D + H_2 \rightarrow DH + H$ involves either the determination of the center-of -mass differential cross sections (CM-DCS), or in the case where detailed predictions are available, the accurate comparison of the theoretical predictions with the experimental data. Direct inversion of the laboratory (LAB) data can provide qualitative insight into the form of the CM-DCS[1], however, due to the various experimental distributions which broaden the measured data, quantitative information is difficult to derive in this manner. The typical approach to the problem is to perform a 'forward convolution' of a predicted or guessed CM-DCS to the appropriate laboratory observables, (velocity and angular distributions in this case).

Several papers concerning the details of the CM→LAB transformation have been published, deriving the various transformation Jacobians and kinematic relationships.[2] The commonly used approach in our laboratory has been based on the kinematic analysis algorithm originally developed by Entemann[3] in Herschbach's group. A commonly used variant of this algorithm is described by Buss[4]. This program convolutes assumed product energy and angular distributions over the beam velocity and angular spreads and calculates laboratory angular distributions and TOF distributions averaged over the electron impact ionizer length. The version of this

program in use assumes that the product translational energy ,$P(E_T)$, and angular distributions, $T(\Theta)$, are uncoupled. In many cases this is a good assumption, especially for reactions which proceed through a long-lived complex. The use of parameterized functional forms for $P(E_T)$ and $T(\Theta)$ greatly facilitate fitting the data, as large changes in the CM quantities can be made by changing a small number of parameters. Parameterization in this manner also allows the possibility of using iterative least squares optimization of the fitting function.

The vibrational state-resolved differential cross sections which were obtained on the $F + H_2$, HD, and D_2 reactions demanded a slightly different approach to data analysis[5]. As discrete vibrational states were observed, the $P(E_T)$ could no longer be treated as a continuous function. Also, the product energy distribution was found to be strongly coupled with CM recoil angle, a feature that many direct elementary reactions may display. To handle this, a point form $T(\Theta)$ and a parameterized functional form for $P(E,\Theta)$ at each CM angle for each vibrational state were used. In this approach, within a given vibrational state, the $P(E_T)$ was taken to be a continuous function, i.e. the rotational energy of the products was treated classically. In all other respects, this program treated the kinematic averaging problem following Entemann's algorithm.

Initial efforts on the data analysis for $D + H_2 \rightarrow DH + H$ were made with this program, which was modified to allow the input of a continuous E_T representation of the theoretical DH(v,J) DCS's at the nominal collision energy. The distribution P(v,J) was converted to $P(v,E_T)$ by noting the following relationships between the (fictitious) continuous J space and E space;

$$E(J) = B \cdot J \cdot (J + 1) \tag{1}$$

and

$$dE_J \approx B \cdot (2J + 1) \cdot dJ \tag{2}$$

thus,

$$P(E_J) \approx P(J) \cdot \frac{dJ}{dE_J} \approx \frac{P(J)}{(2J + 1)} \tag{3}$$

This approximate treatment is not very good for high-J DH product, as the rotational spacing is large and the high-J products have small CM recoil velocities. Consideration of the Jacobian for the CM→LAB transformation[2] for these continuous distributions,

$$I(v) = \left(\frac{v^2}{u^2}\right) \cdot I(u) \tag{4}$$

shows that products with small CM recoil velocities, u, will be observed with high sensitivity in the LAB ("Jacobian enhancement"). Since the DH(v, J) have discrete u's, a continuous distribution will not give the same results as the discrete one, particularly for products with small u. In other words, the continuous representation of the rotational distribution is probably alright in cases where the Jacobian does not change drastically from one J to the next, which, for high J DH, is not true. Thus, when discrepancies were noted in the initial comparison of the theoretical DCS's with the TOF data, it was felt that an effort should be made to accurately transform the discrete DH(v,J)

theoretical CM-DCS's to the LAB for comparison with the experimental results.

The kinematic analysis programs described above are limited with respect to treatment of the affects the apparatus geometry may have on the observed data. In the coupled P(E,Θ),T(Θ) program, for example, beam speed and angular spreads, detector angular acceptance, and the distribution of product flight lengths were considered. No explicit account was made for finite beam interaction volume. In many cases, such parameters as the finite collision volume are of little significance. For the reactive scattering experiments described here, the effects of the apparatus geometry, including the finite D-atom source volume, crossed-beams interaction volume, and the variation of D-atom flight times from source to interaction volume, are not necessarily negligible. An effort was therefore made to model the effects of all of these experimental distributions accurately.

2. The Monte Carlo Approach

An approach to the forward convolution problem was presented in a paper by Dr. R.T. Pack[6] in which the treatment of apparatus averaging of the discrete CM→LAB transformation was set up in a rigorous manner. Dr. R.B. Walker adapted Pack's treatment to an importance sampling Monte Carlo algorithm which could accurately sample all of the apparatus distributions. The original LabAvg code, as received from Walker, was set up to calculate only laboratory angular distributions given input theoretical CM-DCS data. The program assumed two beams emanating from some virtual source points crossing in a specified volume, with products detected by a rotatable

detector with an aperture some distance from the crossing point. To use this program for D + H_2 reactive scattering data analysis, several modifications had to be made to allow generation of TOF spectra and to handle the details of the apparatus geometry. It was very easy to build on the foundation of the original LabAvg code, due to the modular subroutine construction of the program.

The data recorded in the D + H_2 reactive scattering experiments was in the form of laboratory time-of-flight (TOF) spectra of the products relative to an experiment-dependent time marker. Laboratory angular distributions were generated by integrating the appropriate TOF spectra. For our purpose, the firing of the photolysis excimer laser was used as the time marker. This then triggered the 4096 channel MCS, and at some later time ion signal at the selected mass of interest was recorded by the MCS, with a temporal resolution (dwell time) down to 150 nsec. To simulate the TOF spectra, then, first the laboratory velocities of the products had to be calculated, then averaged over the various spatial and temporal functions which the apparatus introduced in some manner. The important distributions for D + H_2 were the D-atom source volume ($\mathbf{r}_S$), the collision volume ($\mathbf{r}_C$), the ionizer volume ($\mathbf{r}_D$), the D-atom speed distribution (v_1), and the H_2 speed distribution (v_2). The beam angular distributions and detector angular resolution are naturally taken into account by the explicit treatment of the crossed-beams interaction volume and detection volume, and the probability of events as a function of position in these volumes. In addition, as the collision volume of the beams in these experiments was larger than the nominal 'viewing volume' of the detector apertures, it was desirable to be able to correct exactly for these effects by constraining the detected particle trajectories to be only those that passed

through the detector apertures. The Monte Carlo technique is well suited to handling these distributions in explicit detail, as it basically involves following the particle of interest from its inception to its detection, choosing these initial and final conditions from the various experimental distribution functions and keeping track of any particle properties that are of interest along the way.

Monte Carlo methods have seen considerable application to the simulation of a wide variety of phenomena, including neutron transport[7], molecular dynamics studies[8,9], and, increasingly, in quantum chemistry[10]. The neutron transport problems in particular are very similar to the transport through our scattering chamber under consideration here. At this point we will provide a quick introduction to the implementation of the Monte Carlo technique used. This is followed by a more detailed discussion of the various parameters averaged over in the program.

The Monte Carlo technique receives its name from the fact that it is fundamentally a game of chance. Random numbers are generated which are used to pick the initial variables, the result of the game is evaluated, and these results are accumulated in some manner. The rate of convergence of a 'crude' Monte Carlo calculation is relatively slow ($O(N^{1/2})$, where N is the number of iterations), however, numerous variance-reduction techniques exist which generally work by biasing the selection of the initial conditions in such a way that the region of space which is believed to contribute most to the integrals in question is sampled more thoroughly than other regions. The importance sampling technique used in this program[7] basically consists of taking the (presumably) known probability distribution functions (pdf's) for the various distributions of interest, normalizing them, and keeping track

of a table of the integral of the distribution function (the importance function). Given a pdf, p(x), and the independent variable, x, the distribution is fit by a cubic spline function, integrated, normalized, and a table of the form

$$\int_0^x p(x)dx \quad , x \ , \ p(x) \qquad (5)$$

is generated. Since the pdf has been normalized, the integral ranges in value from 0 to 1. Thus, when a random number [0,1] is picked, it may be used to select a value of x and p(x) from the table. In this way the regions of x space that have the greatest probability p(x) can be thoroughly sampled. This approach significantly improves the efficiency of the Monte Carlo technique over blindly picking x,p(x) values from the entire x range, with the amount of improvement depending on the functional form of p(x).

3. The LabAvg Program

Armed with the Monte Carlo 'technology' we can now consider the calculations that must be performed to accurately transform the discrete DH(v,J) CM-DCS to the laboratory frame. As noted in Pack's paper[6] the appropriate equation for transforming a discrete CM-DCS to a LAB number-density DCS at a nominal laboratory solid angle Ω_0 is

$$N_{fi}^{lab}(\vec{v}_1,\vec{v}_2,\Omega_0) = \frac{v_{rel} \cdot v_{lab}}{u_3^2 \cdot |\cos \zeta|} \cdot I_{fi}^{cm}(v_{rel},\theta_{cm}) \qquad (6).$$

As illustrated in Figure A-1, θ_{cm} is the CM scattering angle, and $I_{fi}^{cm}(v_{rel},\theta_{cm})$ is the CM-DCS for the given relative velocity and CM scattering angle. The relative velocity of the reactants, v_{rel}, weights the cross section by the number of collisions according to the well known relation for the collision frequency,

$$\dot{n} = n_1 \cdot n_2 \cdot v_{rel} \cdot \sigma(v_{rel}) \cdot \Delta V \tag{7}$$

where n_1, n_2 are the number densities of the reactants, $\sigma(v_{rel})$ is the velocity-dependent cross section and ΔV is the volume in which the reactants collide. Referring once again to Figure A-1, v_{lab} is the detected particle LAB velocity, u_3 is the detected particle CM velocity, and ζ is the angle between v_{lab} and u_3. The magnitude of the detected particle LAB velocity is implicitly determined by the incident particle velocities, and any energy consumed or released in the specific state-to-state $f \leftarrow i$ process under consideration. These factors take into account the transformation Jacobian from the CM→LAB for the case of discrete exit channel velocities with number-density detection.[6]

In practice equation (6) must now be averaged over the various apparatus functions mentioned previously. Product TOF distributions must also be calculated. Figure A-2 provides a physical picture of the problem at hand, the details of which will invariably differ somewhat according to the specific experiment being performed. Taking into account the important apparatus distributions previously mentioned, we can write an equation giving the LAB signal for a given nominal detector angle (after Pack)[6],

$$\overline{N}_{fi}^{lab}(\Omega_0) = \int d\vec{v}_1 \int d\vec{v}_2 \int d\vec{r}_c \int d\Omega \cdot P_1(\vec{r}_c,\vec{v}_1) \cdot P_2(\vec{r}_c,\vec{v}_2) \cdot P_{det}(\vec{r}_c,\vec{v}_f) \cdot N_{fi}^{lab}(\vec{v}_1,\vec{v}_2,\Omega) \quad (8).$$

As a matter of practice this equation may be recast into a form more suitable for the calculation under consideration. First we assume that the beam speed and angular distributions are uncoupled, i.e., $P_1(\mathbf{v}_1) = p(v_1)p(\theta,\phi)$ where θ and ϕ are the polar and azimuthal angles of the vector. We can then generate the interaction region density function $P_c(\mathbf{r}_c) = p_1(\theta,\phi) \cdot p_2(\theta,\phi)$. This distribution is assumed for convenience to be composed of three separable one-dimensional Cartesian pdf's, i.e., $P_c(\mathbf{r}_c) = P(x_c)P(y_c)P(z_c)$. The D-atom beam angular distribution was characterized by a trapezoidal distribution in the x-z plane and the H_2 beam was characterized by a Gaussian distribution in the y-z plane. The further assumption was made that the beams did not diverge considerably over the length of the interaction volume, i.e., the 'perpendicular' temperature of the beams was ≈ 0 K, as discussed by Pack.[6] The D-atom source-volume density function was also assumed to be a separable Cartesian distribution, with an added density gradient along the DI free-jet propagation direction. The x-y plane was governed by a Gaussian angular distribution, the x-z plane by a homogeneous laser-beam distribution, and the density decreased as $1/r^2$, where r is the distance from the free jet source to the source point $\mathbf{r}_S$. The DI beam velocity distribution was not taken into account explicitly in LabAvg, but was used in the calculation of the input D-atom laboratory velocity distribution with a version of this program modified to treat photodissociation processes. The H_2 beam was assumed to emanate from a point source over which no integration was required. The

ionizer volume was treated as three separable Gaussian pdf's in a manner similar to the crossed-beams interaction volume.

An importance-sampling correction is necessary for the weighting of the three-dimensional distributions to correct for the change of variables made in the importance sampling procedure.[7] In the interaction volume, for example, the true weight due to this importance sampling normalization correction is

$$P_{corr}(\vec{r}_S) = \frac{p(x_S)\cdot p(y_S)\cdot p(z_S)}{P(\vec{r}_S)} \qquad (9).$$

This correction is typically quite small (≈ 1-2 %). Since the various one-dimensional pdf's are normalized to unity, they need no correction of this sort.

The program supports several different forms for the beam speed distributions, including supersonic, thermal, velocity-selected and explicit point form input. The D-atom speed distribution was put in explicitly, with the distribution being found by simulation of the D-atom TOF's with the photodissociation version of this program, as mentioned previously. The H_2 speed distribution was characterized as a supersonic beam, using the common functional form

$$N(v) = (v^2)\cdot e^{-((v/\alpha)-S)^2} \qquad (10)$$

where the fitting parameters $\alpha = (2kT/m)^{1/2}$ and the speed ratio $S = v_s/\alpha$ were obtained with a non-linear least squares fit to beam TOF data as described in Appendix C.[11]

Using the above treatment of the various experimental pdf's, we may rewrite eqn. (8) into the form used by the program LabAvg:

$$\overline{N}_{fi}^{lab}(\Omega_0) = \int dv_1 \int dv_2 \int d\vec{r}_S \int d\vec{r}_C \int d\vec{r}_D \cdot \\ P_1(v_1)\cdot P_2(v_2)\cdot P_S(\vec{r}_S)\cdot P_C(\vec{r}_C)\cdot P_D(\vec{r}_D)\cdot N_{fi}^{lab}(\vec{v}_1,\vec{v}_2,\Omega) \qquad (11).$$

As noted above, in this formulation the integrals over beam velocity vectors and detector angles are now taken into account in the explicit coordinate space integrals. Equation (11) must be slightly modified to reach the final form used in the generation of TOF spectra from a given CM-DCS. Knowing the MCS dwell time, or bin width, and time zero we may assign the detected particle trajectory, with its known velocity and flight distance, to the appropriate MCS bin. For comparison with the laboratory data, we must add an ion flight time τ_{ion}, which takes into account the time it takes for the detected particle to travel from the ionizer to the ion counter and then to the MCS. In addition, since the MCS is triggered off of the excimer laser pulse we must also add to the calculated flight time the time it takes for the primary beam (laser-generated) particle to fly from the source to the interaction region τ_{flt}, a time which varies from 3.5 to 6.0 μsec for the two nominal D-atom LAB velocities produced by the 248 nm photodissociation of DI. Thus, for each reactive trajectory, the laboratory flight time t_f can be explicitly calculated, taking into account all of the above factors. The modified version of Pack's equation 18[6] can now be written, which gives the signal in an MCS channel n centered in time at t_n, with a width of $t_{n+} - t_{n-}$;

$$\overline{N}_{fi}^{lab}(\Omega_0,t_n) = \int dv_1 \int dv_2 \int d\vec{r}_S \int d\vec{r}_C \int d\vec{r}_D \cdot$$
$$[U(t_{n+} - t_f) - U(t_{n-} - t_f)] \cdot$$
$$P_1(v_1) \cdot P_2(v_2) \cdot P_S(\vec{r}_S) \cdot P_C(\vec{r}_C) \cdot P_D(\vec{r}_D) \cdot N_{fi}^{lab}(\vec{v}_1,\vec{v}_2,\Omega) \qquad (12).$$

In this equation the U's are Heaviside step functions, which simply indicate that the signal goes in channel n if the time is between the two limits t_{n+} and t_{n-}. To generate a complete simulation of the experimental TOF's we need to sum this expression (12) over the initial and final states under consideration, i.e.,

$$\overline{N}(\Omega_0,t_n) = \sum_f \sum_i P_i \, \overline{N}_{fi}^{lab}(\Omega_0,t_n) \qquad (13),$$

where P_i is the probability of the initial state i.

A schematic flow chart of the implementation of the LabAvg code is shown if Figure A-3. The internal energies of the reactant particles 1 and 2, of mass m_1 and m_2 are input, as well as the internal energies of the product particles 3 (the detected particle) and 4, of mass m_3 and m_4, for the state-to-state process under consideration. The distribution functions are tabulated using cubic-spline routines developed at Los Alamos National Laboratory which are included in the LabAvg code. The product DCS, which was supplied by Zhang and Miller at 15 energies from 0.40 to 1.35 eV total energy[12], is fit by a two-dimensional spline routine to give a surface in CM angle-energy space. Plots of the CM-DCS surfaces generated by the routine indicated that no significant deviations from the input DCS were introduced

by the spline fit. Figure A-4(a) shows the energy dependence of the CM-DCS for DH(v=0,J=7) at a CM scattering angle of 120°. Figures A-4(b) and A-4(c) show the CM-DCS for DH(v=0,J=7) at total energies of .78 and 1.25 eV. As the plots show, the spline routine does an excellent job of fitting the theoretical predictions. Finally, Figure A-5 shows the CM-DCS surfaces generated in CM scattering angle/energy space. Generation of the CM-DCS surfaces allowed accurate modelling of the effects of the entire D-atom velocity distribution, since for this direct reaction there is a strong coupling of CM scattering angle with energy and quantum state.

As the Monte Carlo simulation proceeds, the detector is rotated to the appropriate LAB angle and the Monte Carlo iteration cycle for the particular scattering process A + BC(v,J) → AB(v,J) + C is begun. The integration parameters $\mathbf{r}_C$, $\mathbf{r}_S$, $\mathbf{r}_D$, v_1 and v_2 are then selected as discussed earlier. The trajectories are then checked to ensure that they pass through all apparatus slits. If the trajectory makes it all the way to the detector, the kinematics for this particular collision, the CM-DCS, and the resultant angular and TOF signals are calculated. The results are tabulated in the appropriate arrays. In Pack's paper the kinematic calculations required to fully specify the post-collision velocity vectors were addressed for the case of elastic/inelastic scattering, and that treatment also applies to reactive scattering when the calculation of the final CM velocities is modified to include the change in reduced mass which occurs in a reactive collision. In the Monte Carlo code, once $\mathbf{r}_C$, $\mathbf{r}_S$, $\mathbf{r}_D$, v_1 and v_2 are picked, the incident particle LAB velocity vectors, the collision energy, and the direction of the detected particle LAB velocity vector are determined. The post-collision velocity vectors of the

products are then calculated, if the energetics and kinematics permit this particular event to occur.

When a cycle of Monte Carlo iterations has been completed the calculation is done for the next LAB angle. When the results for all the desired LAB angles have been calculated, the program either stops, or reads in a new CM-DCS and repeats the calculation for another scattering process, accumulating the total TOF signal for all the processes chosen. In this way, one can calculate the signal due to a given DH(v,J) state, or perform the calculation for a given DH(v) state by summing over the product J states. Utility programs were written for plotting the calculated results versus the experimental data.

4. Conclusions

The advantage of using the Monte Carlo approach as implemented in the program LabAvg is that it allowed an accurate transformation of the theoretically predicted CM-DCS for a bimolecular collision to the laboratory, sampling all experimental distributions of any significance in a legitimate, thorough way. Due to the modular construction of the program it is easily modified to handle various forms of DCS input, new apparatus distributions, etc. The two major disadvantages of the Monte Carlo approach are: (1) it is usually more computationally expensive, and (2) the simulations have statistical noise associated with the random sampling of the various pdf's. For the D + H_2 reactive scattering simulations good simulation 'signal to noise' ratio could be generated for DH (v=0,J=0-13) (14 CM-DCS's) at 26 LAB angles in ≈ 4 CPU hours of VAX 8600 computer time with 8192 Monte Carlo

iterations per state per LAB angle. It would not be difficult to modify the program further to completely emulate the usual separable CM $T(\Theta)$,$P(E_T)$ inputs commonly in use in our laboratory. This may prove useful in cases with extreme scattering kinematics where various apparatus distributions that are difficult to treat with the Entemann algorithm become important

In summary, the Monte Carlo code LabAvg was modified to accurately simulate the D + H_2 reactive scattering experiments . This code treats the various apparatus distributions in a rigorous fashion, and may be easily modified to treat specific experimental arrangements or physical processes. In most cases the Monte Carlo approach is not the fastest computationally, but in certain cases it is almost the only tractable approach, and in any case provides an excellent consistency check for faster, more approximate schemes.

[1] R. Wolfgang and R.J. Cross, Jr., J. Phys. Chem., **73**, 743 (1969).

[2] a). R.K.B. Helbing, J. Chem. Phys., **48**, 472 (1968).

b). T.T. Warnock and R.B. Bernstein, J. Chem. Phys., **49**, 1878 (1968).

c). G.L. Catchen, J. Husain and R.N. Zare, J. Chem. Phys., **69**, 1737 (1978).

[3] E. A. Entemann, Ph. D. thesis, Harvard, 1967.

[4] R. J. Buss, Ph. D. thesis, Univ. Cal. Berkeley, 1979.

[5] a) D.M. Neumark, Ph. D. thesis, Univ. Cal. Berkeley, 1984.

b) D.M. Neumark, A.M. Wodtke, G.N. Robinson, C.C. Hayden and Y.T. Lee, J. Chem. Phys., **82**, 3045 (1985).

[6] R.T. Pack, J. Chem. Phys., **81**, 1841 (1984).

[7] Several excellent treatments of such problems have been published, including:

a) G. Goertzel and M.H. Kalos, "Monte Carlo Methods in Transport Problems" in Prog. in Nuc. Energy, Ser. 1, Physics and Mathematics, vol. 2, Pergamon Press, New York (1958), pp. 315-369.

b) E.D. Cashwell and C.J. Everett, A Practical Manual on the Monte Carlo Method for Random Walk Problems, Pergamon Press, New York (1959).

c) L.L. Carter and E.D. Cashwell, Particle-Transport Simulation with the Monte Carlo Method, ERDA Critical Review Series, Tech. Info. Ctr., US Energy Res. and Devel. Admin., (1975).

[8] N. Metropolis, A.W. Rosenbluth, M.N. Rosenbluth, A.H. Teller and E. Teller, J. Chem. Phys., **21**, 1087 (1953).

[9] Reviewed by L.M. Raff and D.L. Thompson, "The Classical Trajectory Approach to Reactive Scattering", in Theory of Chemical Reaction Dynamics, vol. 3, ed. M. Baer, CRC Press, Boca Raton, Fla., USA (1985), pp. 1-121.

[10] R.N. Barnett, P.J. Reynolds and W.A. Lester, Jr., J. Chem. Phys., **82**, 2700 (1985).

[11] M.F. Vernon LBL report #12422, (1981). v_S is the stream velocity of the beam.

[12] J.Z.H. Zhang and W.H. Miller, J. Chem. Phys., **91**, 1528 (1989).

Appendix A Figure Captions

Figure A-1. Kinematic diagram used in the Monte Carlo program for determination of the collision kinematics. The initial particle velocity vectors $\mathbf{v}_1$ and $\mathbf{v}_2$ and the direction of the detected particle laboratory velocity vector $\mathbf{v}_{lab}$ are determined by picking the source,collision, and detection volume coordinates and the incident particle speeds v_1 and v_2. With these initial laboratory conditions specified, the relative velocity $\mathbf{v}_{rel}$ and the initial velocity of the CM, $\mathbf{v}_{cm}$ are determined. Since the initial and final energies of $D + H_2(v,J) \rightarrow DH(v,J) + H$ are all specified, the magnitude of the final detected particle velocity u_3 is determined. This may be then used to determine $\mathbf{u}_3$ and the detected particle lab velocity $\mathbf{v}_{lab}$. γ is the crossing angle of the incident velocities, Θ_0 is the nominal LAB in-plane scattering angle, χ_0 is the out-of-plane scattering angle, and θ_{cm} is the CM scattering angle for the detected particle.

Figure A-2. Schematic diagram of the geometry of the $D + H_2 \rightarrow DH + H$ reactive scattering experiments. As the figure shows, the size of the D atom source volume is comparable to the size of the beam interaction volume. The LabAvg program takes explicit account of all the apparatus dimensions. The distance from the beam interaction volume to the ionizer volume is not to scale.

Figure A-3. Schematic flowchart of the LabAvg Monte Carlo CM→LAB transformation and averaging program. In the Monte Carlo iteration cycle any finite apparatus viewing volume effects are explicitly checked by

noting whether or not the chosen trajectories can pass through the appropriate source or detector defining apertures. As the figure shows, the calculation is done for a given D + H_2(v,J) → DH(v,J) + H reaction, then either repeated, with results summed up to give the DH(v) results, or output for examination of the given final state TOF and LAB angular distribution results.

Figure A-4(a). Energy dependence of the CM-DCS for DH(v=0,J=7) product at a CM scattering angle of 120°. The squares show the points calculated by Zhang and Miller, with the solid line giving the spline fit to the points performed in the generation of the CM-DCS surface in the LabAvg program.

Figure A-4(b). CM-DCS for DH(v=0,J=7) product at a total energy of 0.78 eV showing the comparison of Zhang and Miller's calculation (squares) with the spline fit given by the solid line.

Figure A-4(c). CM-DCS for DH(v=0,J=7) product at a total energy of 1.25 eV showing the comparison of Zhang and Miller's calculation (squares) with the spline fit given by the solid line. Note the difference in CM-DCS scales between A-4(b) and A-4(c).

Figure A-5. CM-DCS surfaces for DH(v,J) product states plotted as a function of CM scattering angle and total energy. These surfaces were generated with a bicubic-spline interpolation of the theoretical results of Zhang and Miller, supplied at 15 energies and every 5° in the CM. The scale of the z -

axis is in units of a_0^2/steradian, and there is no scaling of the plots relative to one-another.

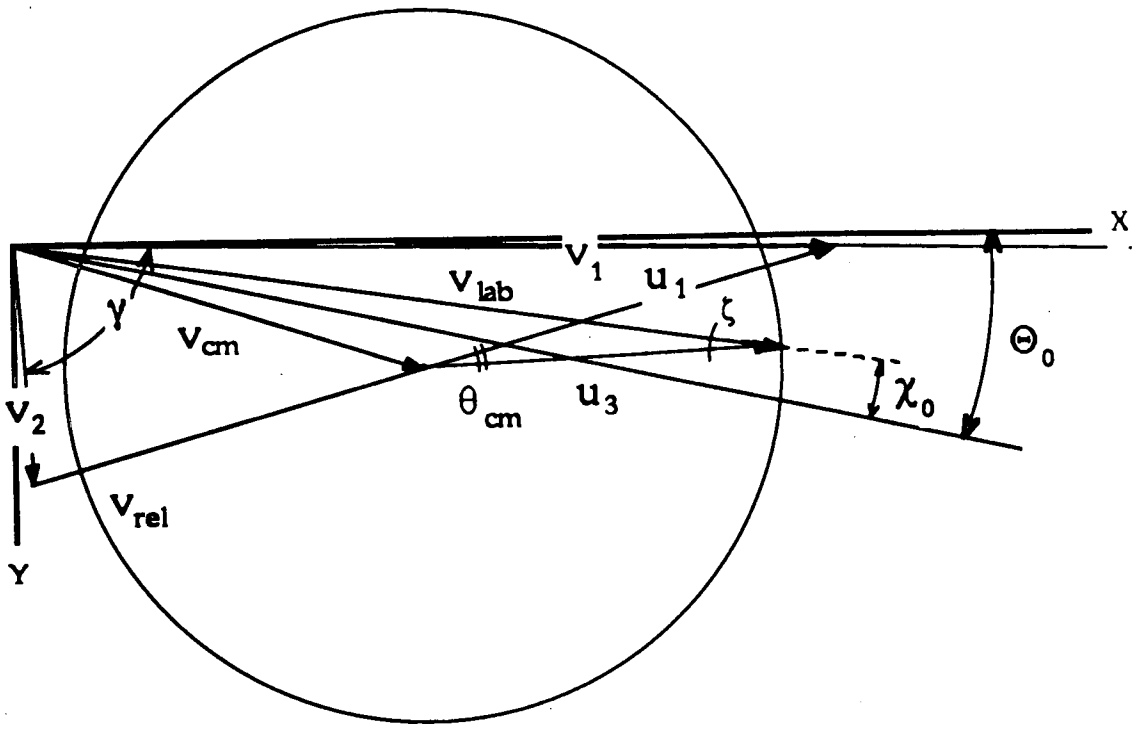

XBL 8911-4082

Figure A - 1

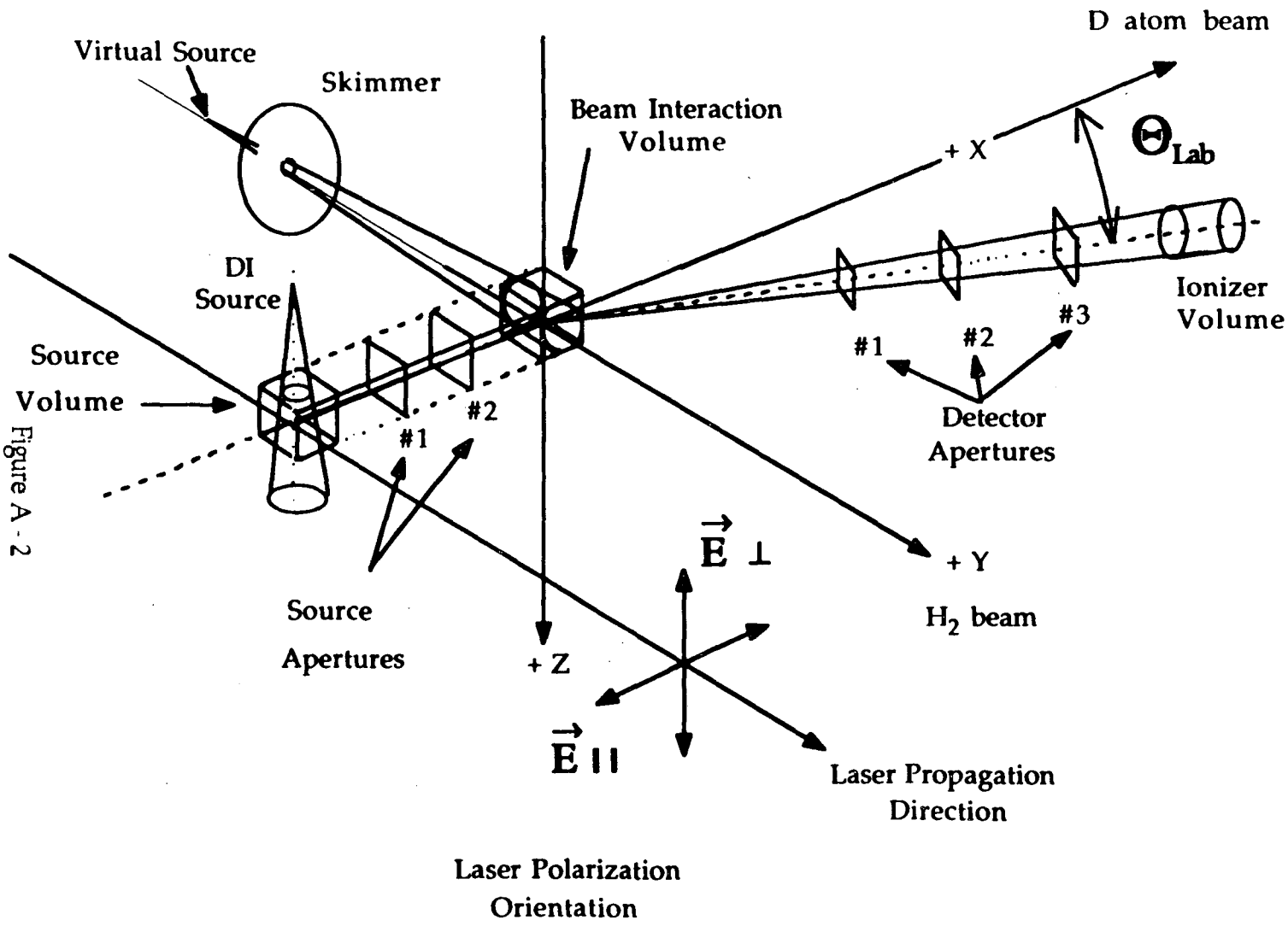

XBL 8911-4083

Figure A - 2

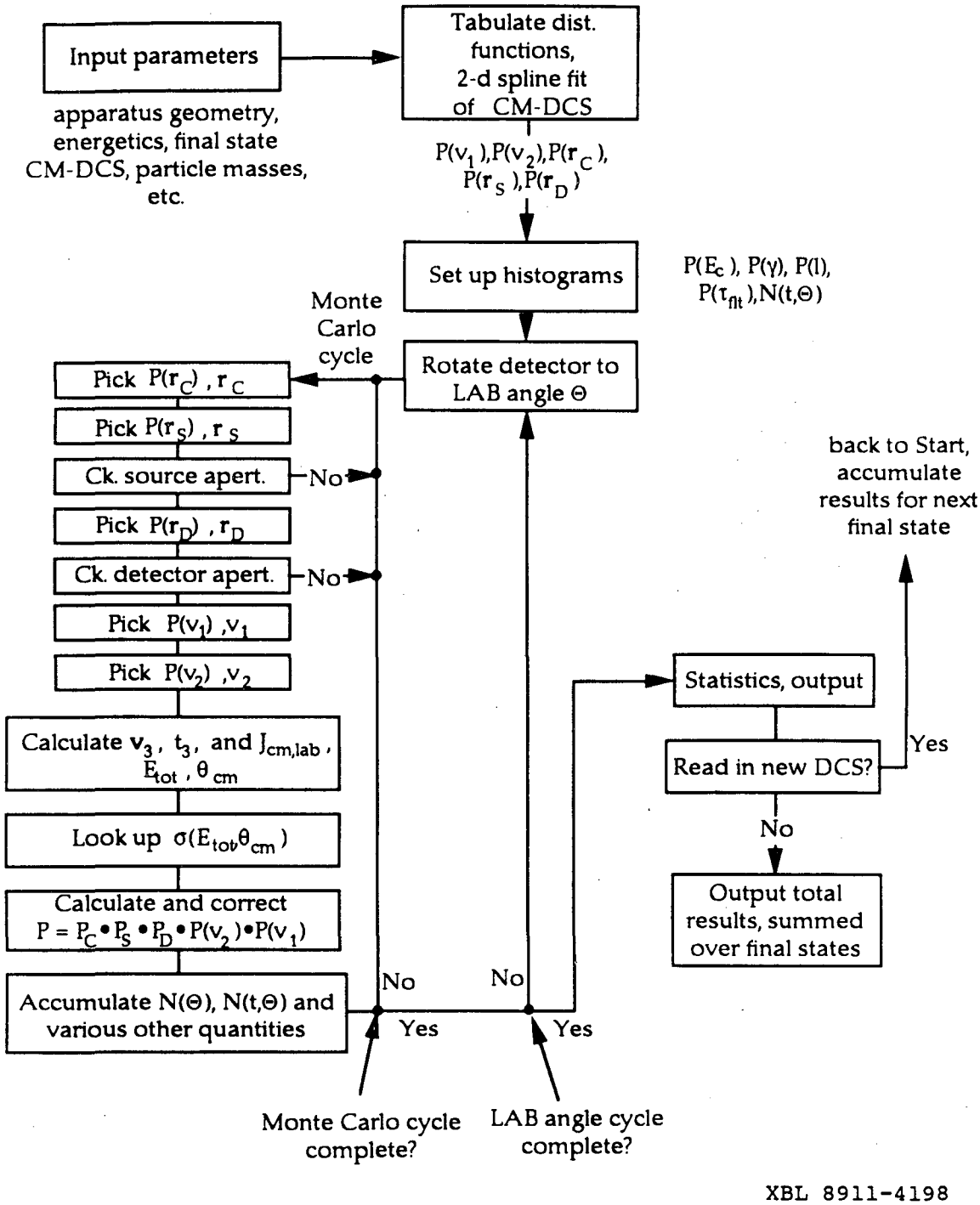
Input parameters
apparatus geometry, energetics, final state CM-DCS, particle masses, etc.
Tabulate dist. functions, 2-d spline fit of CM-DCS
P(v1),P(v2),P(rC), P(rS),P(rD)
Set up histograms
P(Ec), P(γ), P(l), P(τflt),N(t,Θ)
Monte Carlo cycle
Rotate detector to LAB angle Θ
Pick P(rC), rC
Pick P(rS), rS
Ck. source apert.
No
Pick P(rD), rD
Ck. detector apert.
No
Pick P(v1), v1
Pick P(v2), v2
Calculate v3, t3, and Jcm,lab, Etot, θcm
Look up σ(Etot,θcm)
Calculate and correct P = PC•PS•PD•P(v2)•P(v1)
Accumulate N(Θ), N(t,Θ) and various other quantities
No
Yes
No
Yes
Monte Carlo cycle complete?
LAB angle cycle complete?
Statistics, output
Read in new DCS?
Yes
No
Output total results, summed over final states
back to Start, accumulate results for next final state
XBL 8911-4198

Figure A - 3

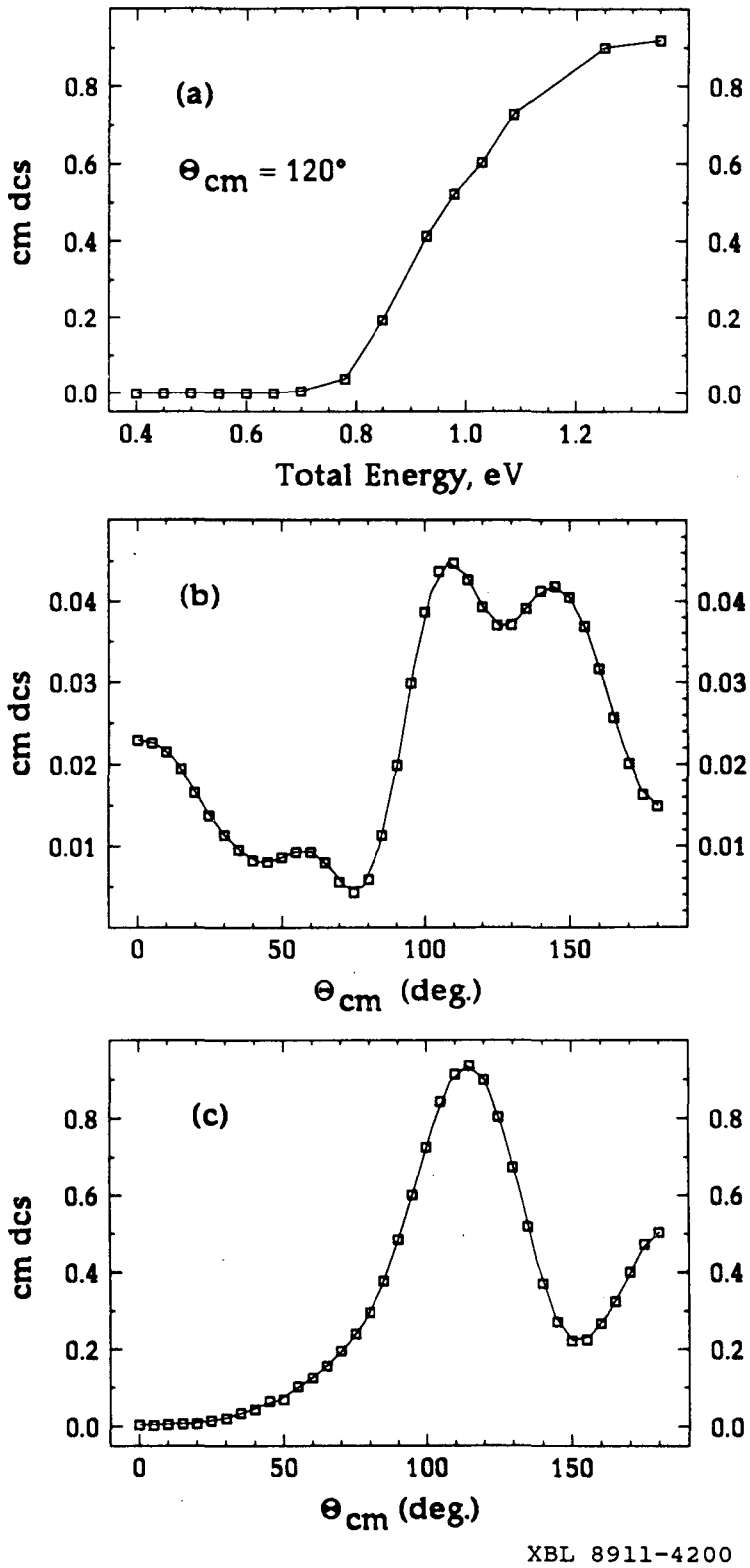
(a)
Θcm = 120°
cm dcs
Total Energy, eV
(b)
cm dcs
Θcm (deg.)
(c)
cm dcs
Θcm (deg.)
XBL 8911-4200

Figure A - 4

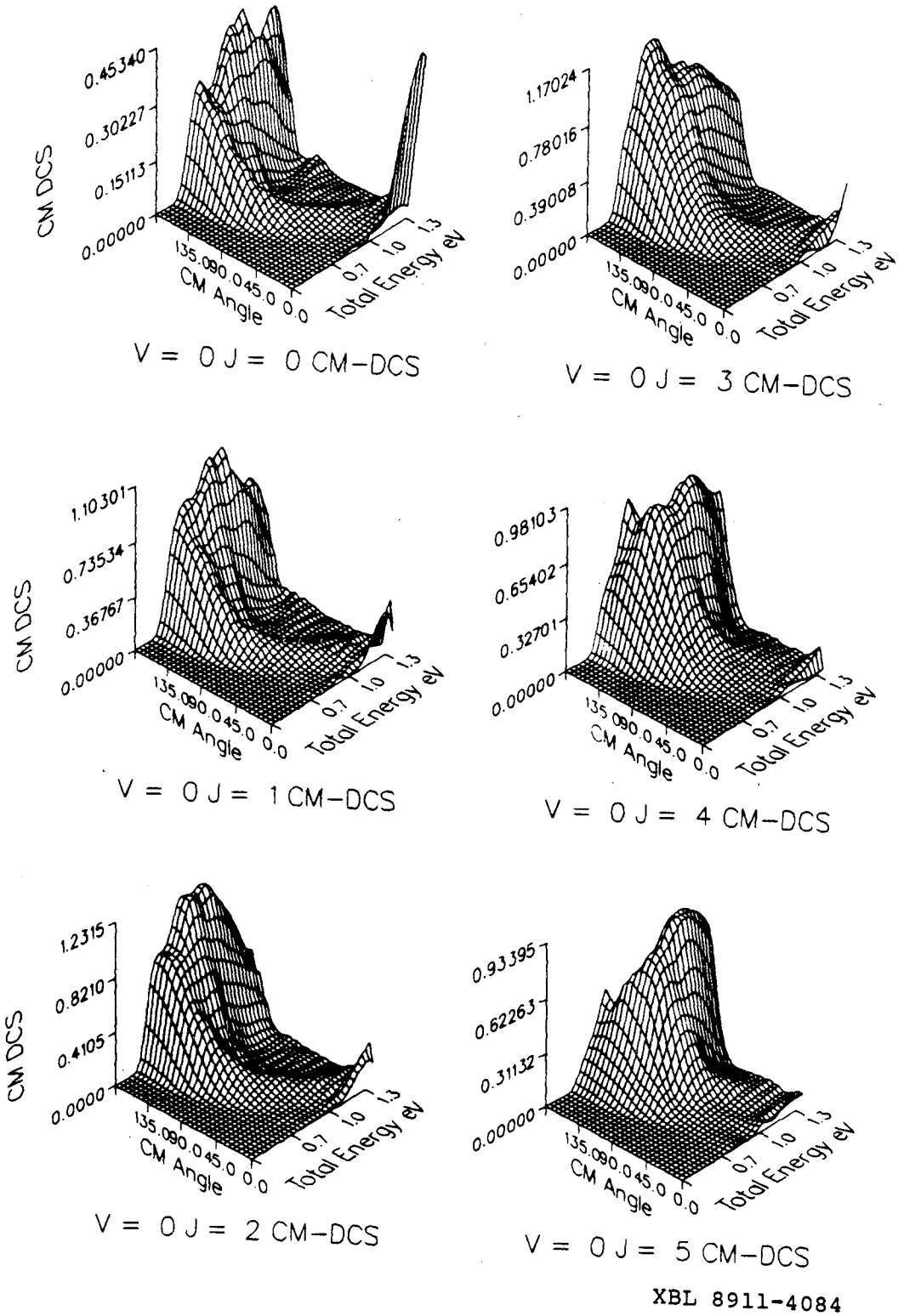
CM DCS
0.45340
0.30227
0.15113
0.00000
135.0 90.0 45.0 0.0
CM Angle
0.0 0.7 1.0 1.3
Total Energy eV
V = 0 J = 0 CM-DCS
1.17024
0.78016
0.39008
0.00000
V = 0 J = 3 CM-DCS
1.10301
0.73534
0.36767
0.00000
V = 0 J = 1 CM-DCS
0.98103
0.65402
0.32701
0.00000
V = 0 J = 4 CM-DCS
1.2315
0.8210
0.4105
0.0000
V = 0 J = 2 CM-DCS
0.93395
0.62263
0.31132
0.00000
V = 0 J = 5 CM-DCS
XBL 8911-4084

Figure A - 5a

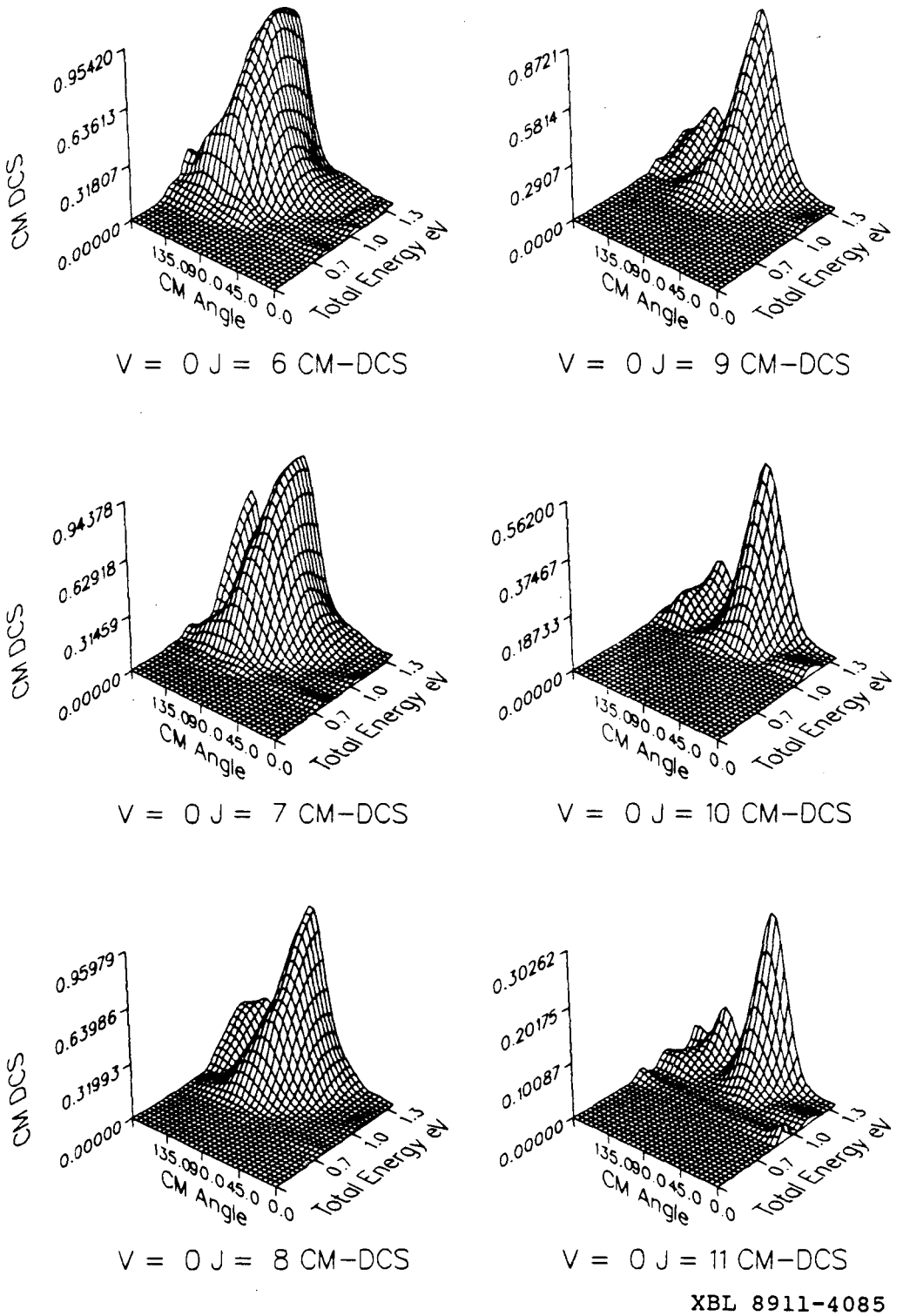
CM DCS
0.95420
0.63613
0.31807
0.00000
135.0 90.0 45.0 0.0
CM Angle
0.0 0.7 1.0 1.3
Total Energy eV
V = 0 J = 6 CM-DCS
0.8721
0.5814
0.2907
0.0000
V = 0 J = 9 CM-DCS
0.94378
0.62918
0.31459
0.00000
V = 0 J = 7 CM-DCS
0.56200
0.37467
0.18733
0.00000
V = 0 J = 10 CM-DCS
0.95979
0.63986
0.31993
0.00000
V = 0 J = 8 CM-DCS
0.30262
0.20175
0.10087
0.00000
V = 0 J = 11 CM-DCS
XBL 8911-4085

Figure A - 5b

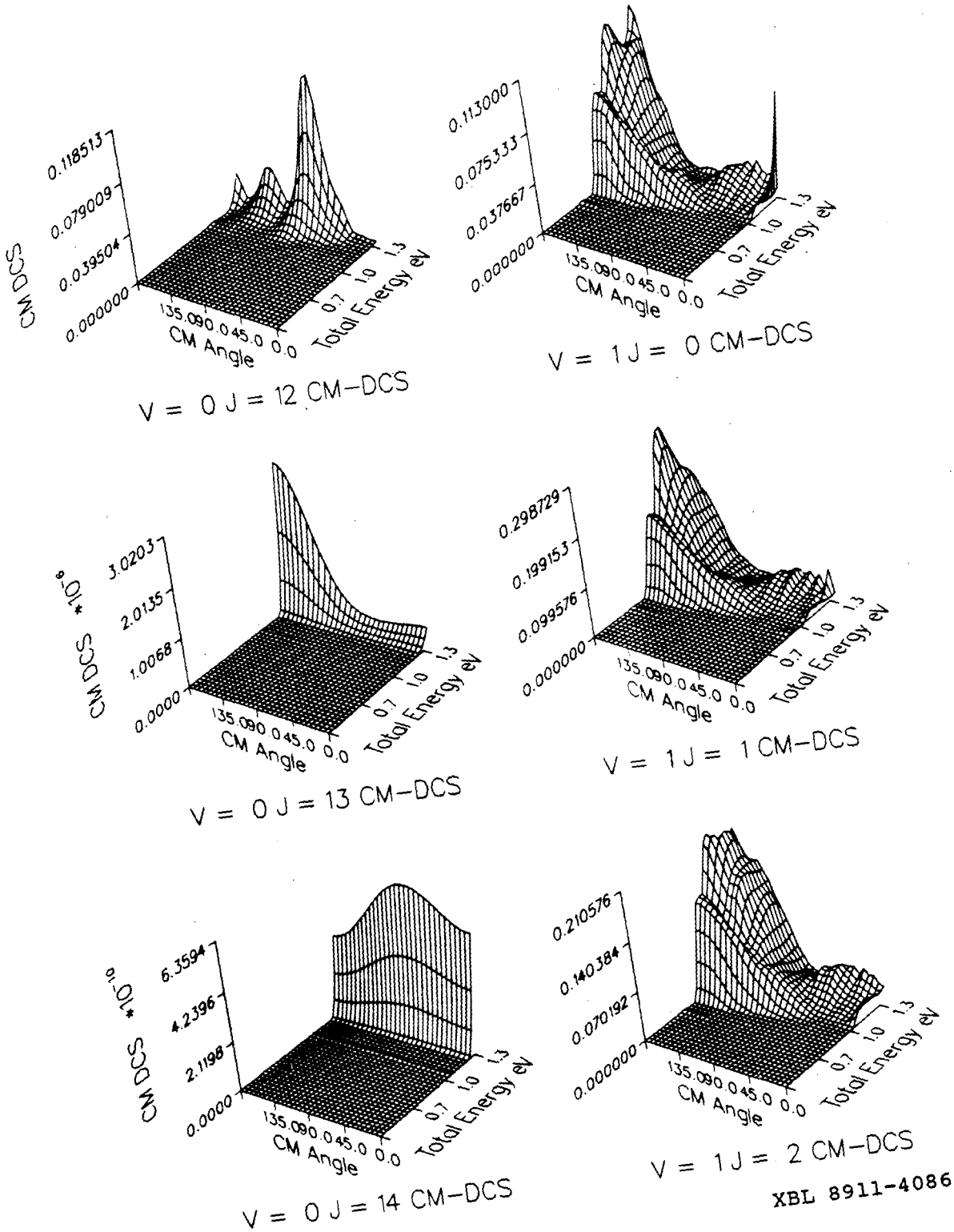
CM DCS
0.118513
0.079009
0.039504
0.000000
135.0 90.0 45.0 0.0
CM Angle
0.0 0.7 1.0 1.3
Total Energy eV
V = 0 J = 12 CM-DCS
0.113000
0.075333
0.037667
0.000000
V = 1 J = 0 CM-DCS
CM DCS *10^-6
3.0203
2.0135
1.0068
0.0000
V = 0 J = 13 CM-DCS
0.298729
0.199153
0.099576
0.000000
V = 1 J = 1 CM-DCS
6.3594
4.2396
2.1198
0.0000
V = 0 J = 14 CM-DCS
0.210576
0.140384
0.070192
0.000000
V = 1 J = 2 CM-DCS
XBL 8911-4086

Figure A - 5c

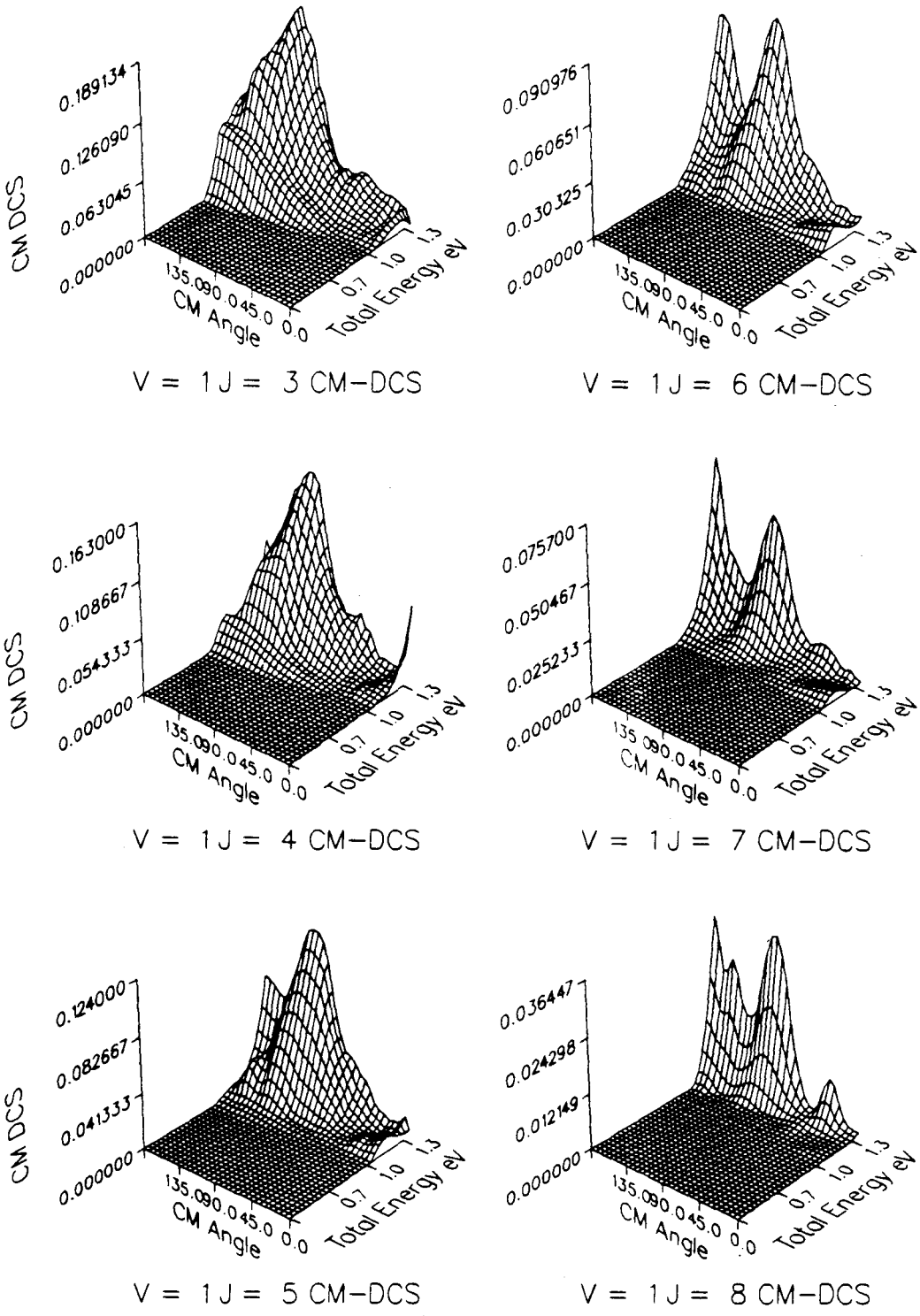

XBL 8911-4087

Figure A - 5d

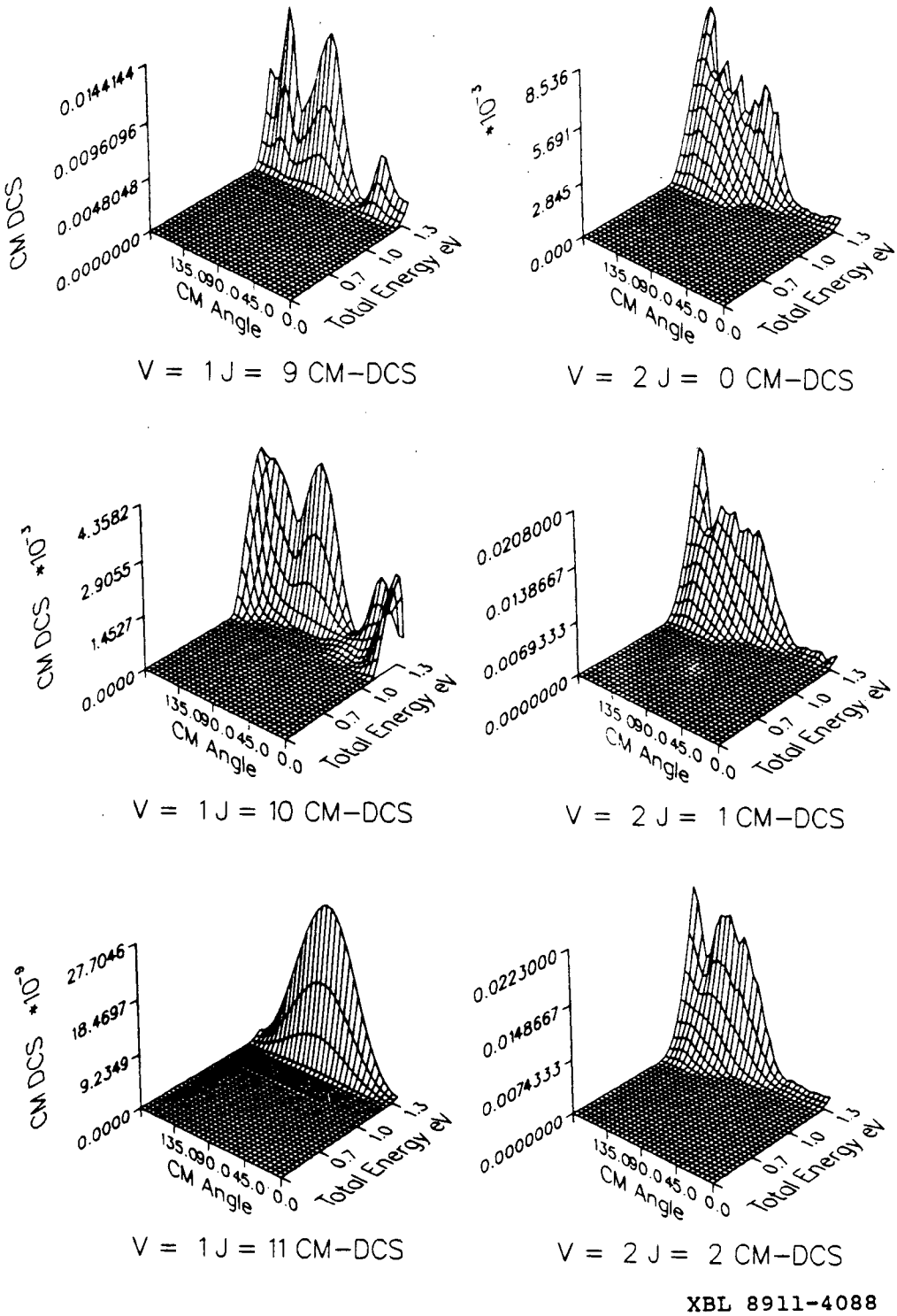

XBL 8911-4088

Figure A - 5e

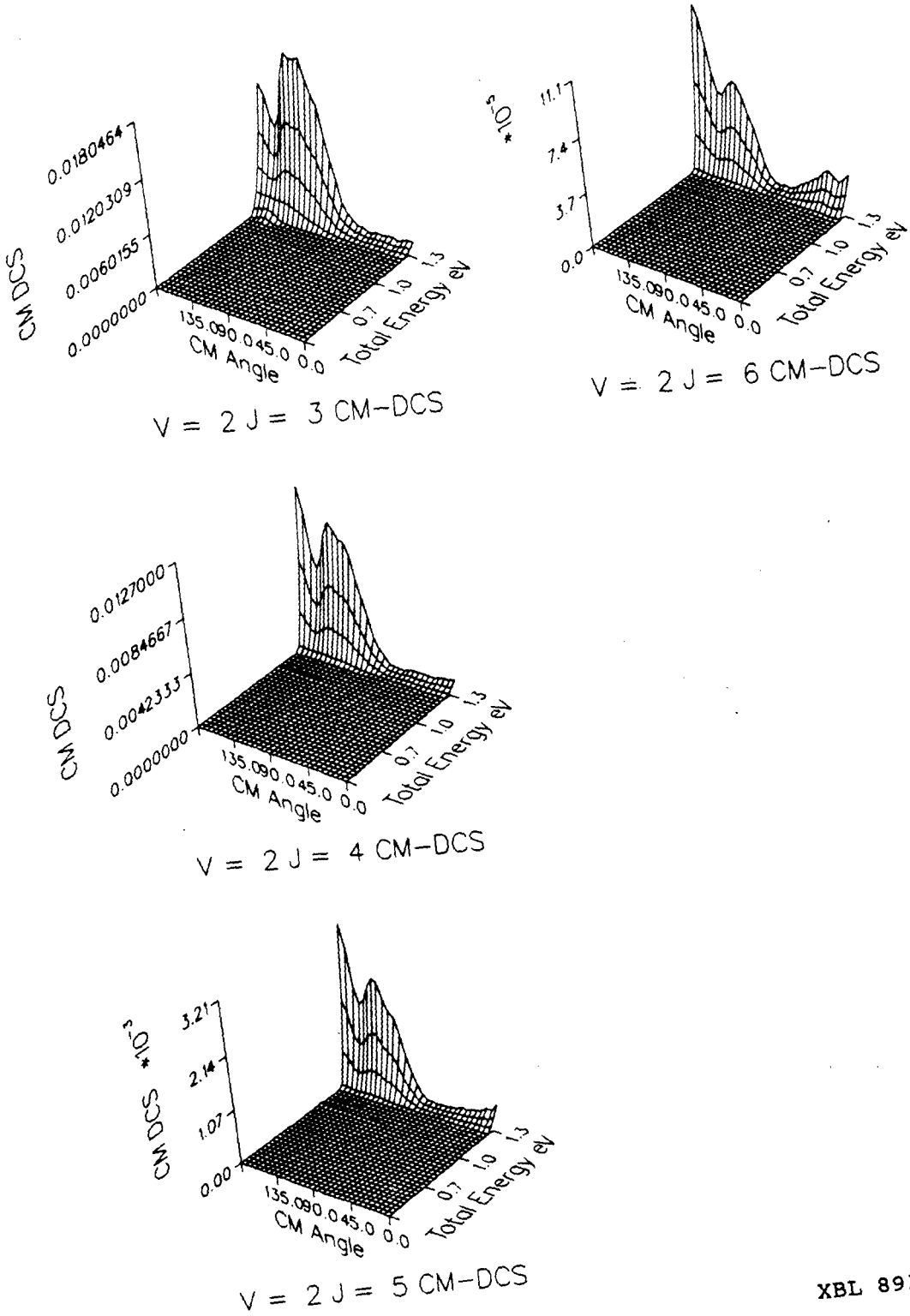

XBL 8911-4089

Figure A - 5f

Appendix B

Pulsed Molecular Beams

1. Introduction

Pulsed molecular beam techniques have become an increasingly important tool for physical chemists. The increased molecular or atomic number density that such beams provide have allowed many experiments to be done that were not possible with conventional continuous supersonic beam technology. The ideal pulsed molecular beam would produce gas pulses of the minimum duration required to achieve supersonic flow, and would be able to match the repetition rate of any pulsed laser used in the experiment. These two features have yet to be simultaneously achieved. Saenger and Fenn[1] have performed calculations that indicate that even in pulses as short as 10 μsec, supersonic flow results. Experimental results have confirmed this, with high speed ratios being observed for the extremely short gas pulses which may be generated with current loop pulsed valves.[2] An excellent review of the current status of pulsed molecular beam technology has recently appeared[3], however a brief review will be given here of the current state of the art and a discussion of the efforts we have taken in the direction of pulsed beam development.

Gentry's current loop valve can produce pulses of 10 μsec FWHM, however, the design depends on the switching of high currents, dissipating significant power in the valve, thereby limiting the possible repetition rate of such a device. The short pulse widths obtainable with this design permits experiments to be performed with an extremely high increase in signal-to-noise ratio for systems in which there is no inherent detector background. As

pointed out in Gentry's review[3] the key to this enhancement is that for a large enough chamber with a high enough pumping speed, no beam/wall collisions will occur while the measurement is under way for a given pulse, and at a sufficiently low repetition rate, the chamber will be entirely evacuated before the next pulse. For the D + H_2 reactive scattering studies, however, this approach is not necessarily the best, although Gentry's group has used it with success[4], since in these experiments the background level is limited by the detector DH partial pressure.

Other approaches based on fast solenoids, such as fuel injectors, have seen considerable use. A more sophisticated push-pull solenoid approach was developed by Ed Grant and coworkers, and is commercially available.[5] The commercial version of this valve is limited to ≈ 50 Hz operation, however higher rep rates may be possible with a modified power supply. Pulse durations on the order of 100 μsec are accessible with this design.

The other important family of pulsed valves currently in use are those based on piezoelectric translators (PZT's). PZT-based valves were first described by Auerbach and McDiarmid[6] and Cross and Valentini[7]. The advantage of the PZT based valves is very low power consumption, offering high repetition rate operation. The pulse duration can be as short as ≈ 100 μsec FWHM, however for the commercially available valve marketed by Lasertechnics it appears that such pulse durations can only be achieved by restricting the gas flow through the nozzle. In addition, when the valve has been adjusted for large throughput, significant secondary opening, or 'bouncing' of the poppet due to inadequate damping of the crystal motion was observed, increasing the effective duty cycle of the valve and thereby decreasing its overall utility.

2. Experimental

2.1 Commercial Piezoelectric Pulsed Valves

In early experimental efforts on the D + H_2 reaction, described in Chapter 2, the Lasertechnics LPV pulsed valve was used to pulse the hydrogen molecular beam, using a 1.0 mm orifice. The H_2 densities obtainable with this valve were insufficient to allow successful reactive scattering studies. The main disadvantages inherent in the LPV are a result of the small translation which the PZT produces, only ≈30 μm. This makes adjustment of the seal quite difficult, as the difference between a fully opening, yet sealed valve and a leaky one is very small. In addition, the sealing mechanism of the valve uses a flat viton sheet mounted on a small poppet, which tends to score rapidly and generally does not produce a reliable seal for long periods of time. The basic poppet adjustment is performed by screwing in the front face of the valve, which makes it quite inconvenient to perform 'dynamic' adjustment of the valve in a vacuum chamber with a Fast Ion Gauge (FIG) or other diagnostic technique.

2.2 Custom Piezolectric Pulsed Valve

In response to the deficiencies inherent in the LPV design, Proch and Trickl[8] at the Max Planck Institute for Quantum Optics developed an optimized design based on the robust PZT's marketed by Physik Instrumente[9]. The P-286 disc translator has a quoted movement of 100 μm

with an applied voltage of -1 kV, and can move loads of up to 5 kg with no loss of performance. The design of Proch and Trickl improved on the LPV by using a reliable O-ring seal mounted on the poppet, with improved damping of the crystal, allowing full opening of the valve with a minimum of secondary bounces. The design also makes reproducible adjustment of the valve easy, since all valve adjustments may be made from the back side of the valve. This allows use of a fast-ion-gauge equipped test chamber as described in Appendix C for convenient fine-tuning of the valve performance.

For the reactive scattering experiments described in this thesis, it was critical that we be able to bring the two pulsed beam sources quite close together. This was a bit of a problem with Trickl's original design, as the valve body is rather large, (6.6 cm diameter). This would have made it quite difficult to get the two beam sources, in their differential pumping chambers, very close together. Since the Physik Instrumente PZT is so powerful, we designed a nozzle/poppet combination which extended the orifice up to 8 cm from the valve body. Valve throughput and pulse rise time were not significantly reduced with this setup. The advantages inherent in applying such a design in close quarters are easily seen. The diameter of the valve 'face' is now only 1 cm, as opposed to 6.6 cm, which increases the conductance out of the source region considerably. With this design, the two pulsed beams can be put as close together as desired. With the exception of the long nozzle/poppet feature, this design is essentially the same as that described in ref. 8.

2.3 Corrosive Gas Applications

The D + H_2 experiments required production of a pulsed beam of deuterium iodide (DI), which is a highly corrosive gas. The PZT's are quite sensitive, and, as supplied by Physik Instrumente, are not in any way protected from corrosive environments. As shipped, they are potted with a reactive rubber material, which rapidly degraded upon contact with DI and I_2. The best and final solution to such problems would be to physically isolate the crystal from the corrosive gas reservoir/nozzle. This could perhaps be accomplished by using some sort of steel diaphragm mounted on the poppet to separate these two regions. The chief problem with such a solution would be to devise a setup which would not significantly dampen the motion of the crystal.

A simpler approach was taken in our experiments, which was to coat the crystal with an inert substance which, while protecting the crystal, would not dampen it excessively. The first material tried was RTV silicone rubber. This was applied to the PZT after first carefully removing the original rubber potting. This material did not prove to be especially inert, however, and rapid failure of the PZT after exposure to DI resulted. A flexible epoxy sealant[10] was then tried, which proved to be much more inert, however, after long periods of exposure to DI, this sealant also proved to be vulnerable. Coating with this sealant had to be done very carefully, as application of a thick coat would result in overdamping the crystal, to the point where the valve could not be adjusted to open reasonably without a large steady leak. The final approach taken was to use an extremely thin coating of the epoxy

sealant with a more generous coating of Fomblin perfluorinated grease, with great care taken to ensure that the grease covered the entire crystal, with no air pockets or crevices to allow penetration of the corrosive gas to the crystal. Use of this protective coating allowed only two PZT's to be used for DI beam generation in all of the final D + H_2 reactive scattering experiments described in Chapter Three.

2.4 Cryogenic Pulsed Valve

The first experiments we performed on D + H_2 which yielded product TOF results made use of a specially constructed Cryogenic Pulsed Valve (CPV). These experiments made use of a low-pressure, poorly collimated pulsed beam of H_2. Cooling of the beam source to 20K reduced the H_2 molecular velocity from its standard 300K value of 2.7×10^5 cm/sec to $\approx 7 \times 10^4$ cm/sec. It was essential to slow this relatively undefined H_2 molecular beam down to such speeds to maintain the well-defined kinematics which are essential to resolving the DH product vibrational states in a TOF experiment. To achieve a reliably operating cold pulsed beam with a good temporal profile, we recognized that it would be best to find a sealing mechanism which would operate at the temperatures of interest, thereby allowing the gas to be cooled behind the nozzle.

The PZT, however, cannot tolerate such temperature extremes, so a modified long nozzle tip like those described above was fabricated. The requirements of such a nozzle were that significant convective heat transfer should not occur between the cold gas at the nozzle tip and the PZT, and that the conductive heat load on the nozzle tip should be small enough to allow

cooling it to extremely low temperatures with a small closed cycle helium refrigerator. A special nozzle tip was made using a .95 cm tube, with a 2 cm length of thin walled (2.5 mm dia. x 0.2 mm wall) SS tube hard soldered to it, and a conical OFHC copper tip attached on the end. The thin walled SS tube had to be well centered, and great care taken to not bend it in installation, as the clearance between the ID of the tube and the composite Mg/SS 304 poppet was quite small. This effectively separated the cold gas at the nozzle tip from the warm gas reservoir behind. In addition, the conduction through both the SS tube and the 1.5 mm dia. SS/2 mm dia. Mg poppet was quite small (< 1 W at 20K).

The key question which remained was how to make a reliably operating seal at such temperatures. The initial approach taken was to use a polished steel ball tip seated into a smooth conical copper surface at the tip. When new, such an arrangement could be made to seal reliably, however, after ≈ 1 million cycles some of the Cu would invariably transfer to the SS tip, with a large leak rapidly developing thereafter. A better seal was finally found by replacing the SS ball with a screwed on Kel-F ball tip. This seal was very reliable, and in fact never developed any problems with leakage, even after operation at 20K. This Kel-F ball seal could probably even replace the conventional O-ring seals at room temperature. The valve was attached to the closed-cycle refrigerator by means of a Cu braid with a special clamping piece. This had to be installed very carefully as this nozzle was very fragile. Once this valve was perfected, an important problem arose due to the fact that a 40K surface acted as a quite effective cryopump, condensing diffusion pump oil onto the nozzle, eventually clogging the 1.0 mm orifice. This problem was eliminated by surrounding the nozzle by an 80K cold shield

which was cooled before the nozzle itself. Once all of these problems had been solved, operation of the valve without readjustment over a period of 20 x 10^6 cycles was demonstrated. A schematic of the final version of the CPV is shown in Figure B-1, with a detail of the seal design in Figure B-2. A discussion of the properties of the cold beams it produced is found in Appendix C.

3. Conclusions

In summary, the PZT-based pulsed valve introduced to our laboratory by Dr. T. Trickl proved to be quite versatile, and was successfully adapted to our special needs as described above. The pulse repetition rates available with this valve can easily match any excimer laser available, which is a nice feature when low S/N reactive scattering experiments are being done. It would be desirable to reduce the duty cycle of the valve, though, as currently pulses of shorter than 100 μsec FWHM are difficult to generate. The use of differentially pumped beam sources reduced the impact of this limitation on our experiments. The cryogenic pulsed valve described, as well as a similar, teflon-sealed one constructed by Dr. Trickl for operation at 77K[8], proved to be quite successful, the only shame being that after its perfection the decision was made to revert to a room temperature pulsed H_2 source to improve the kinematics for DH vibrational state resolution.

---

[1] K.L. Saenger and J.B. Fenn, J. Chem. Phys., **79**, 6043 (1983).

[2] W.R. Gentry and C.F. Giese, Rev. Sci. Inst., **49**, 595 (1978).

[3] W.R. Gentry ,"Low Energy Pulsed Beam Sources", Atomic and Molecular Beam Methods, ed. G. Scoles, Oxford Univ. Press, London, (1988), ch. 3, pp. 54-82.

[4] S.A. Buntin, C.F. Giese, and W.R. Gentry, J. Chem. Phys., **87**, 1443 (1987).

[5] J.E. Adams, B.H. Rockney, R.J.S. Morrison, and E. R. Grant, Rev. Sci. Inst., **52**, 1469 (1981). Model BV-100 , Newport Corporation, Fountain Valley, CA.

[6] D.J. Auerbach and R. McDiarmid, Rev. Sci. Inst., **51**, 1273 (1980).

[7] J.B. Cross and J.J. Valentini, Rev. Sci. Inst., **53**, 38 (1982). Model LPV, Lasertechnics, Albuquerque, NM.

[8] D. Proch and T. Trickl, Rev. Sci. Inst., **60**, 713 (1989).

[9] Physik Instrumente GmbH & Co., Siemenstrasse, D-7517 Waldbronn, Federal Republic of Germany. U.S. supplier; Polytec Optronics, Costa Mesa, CA.

[10] Master Bond Epoxy #EP30-DP9T2, Master Bond, Inc., Hackensack, NJ.

Appendix B Figure Captions

Figure B-1. Assembly drawing of the cryogenic pulsed valve. The front and rear parts of the valve are shown separated here. The piezoelectric crystal C was held in place on the carrier O-ring by nuts on the threaded rods at A. The sealing tension of the poppet D was adjusted by the lock nut/screw assembly at B. The cryogenic pulsed valve used a composite poppet composed of a magnesium rod D with a threaded SS rod E screwed into it. A thin walled SS tube F was used to connect the OFHC Cu tip G to the valve body. The Kel-F ball tip H was seated in a 90° cone in the Cu tip.

Figure B-2. Close-up view of the OFHC Cu tip G showing the Kel-F ball tip H screwed onto the SS poppet E.

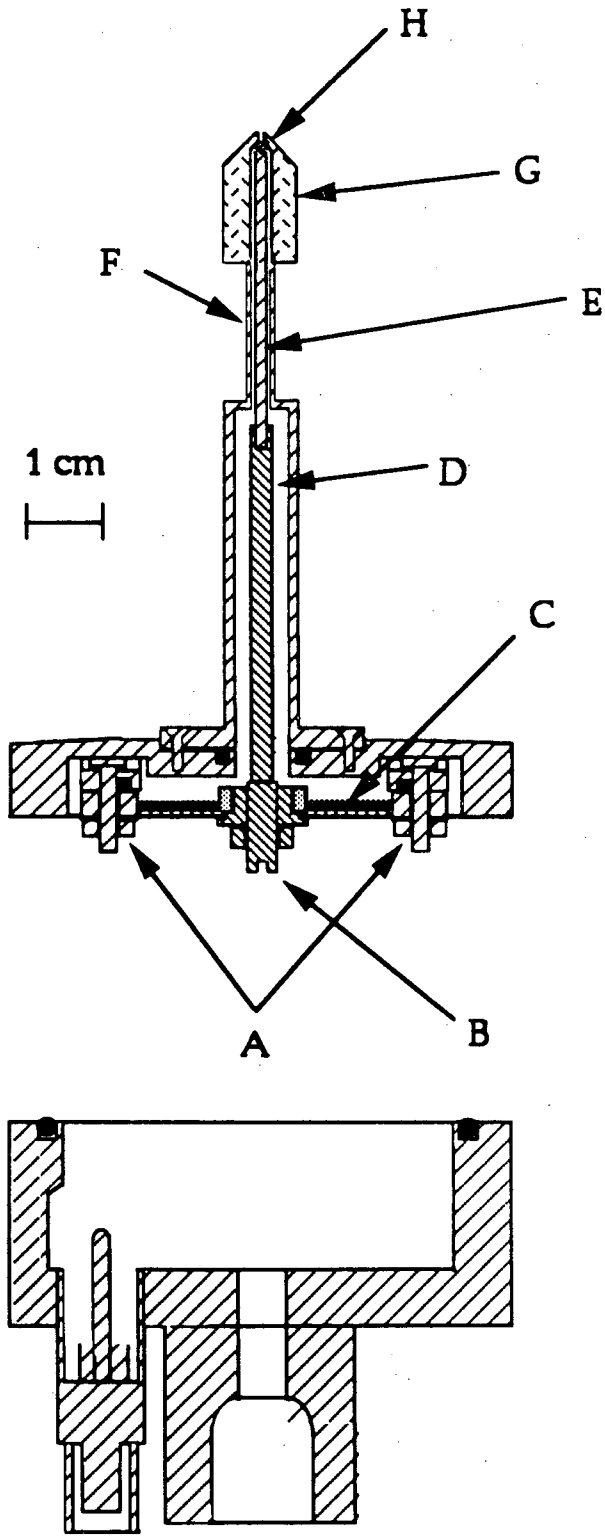

XBL 8911-4090

Figure B - 1

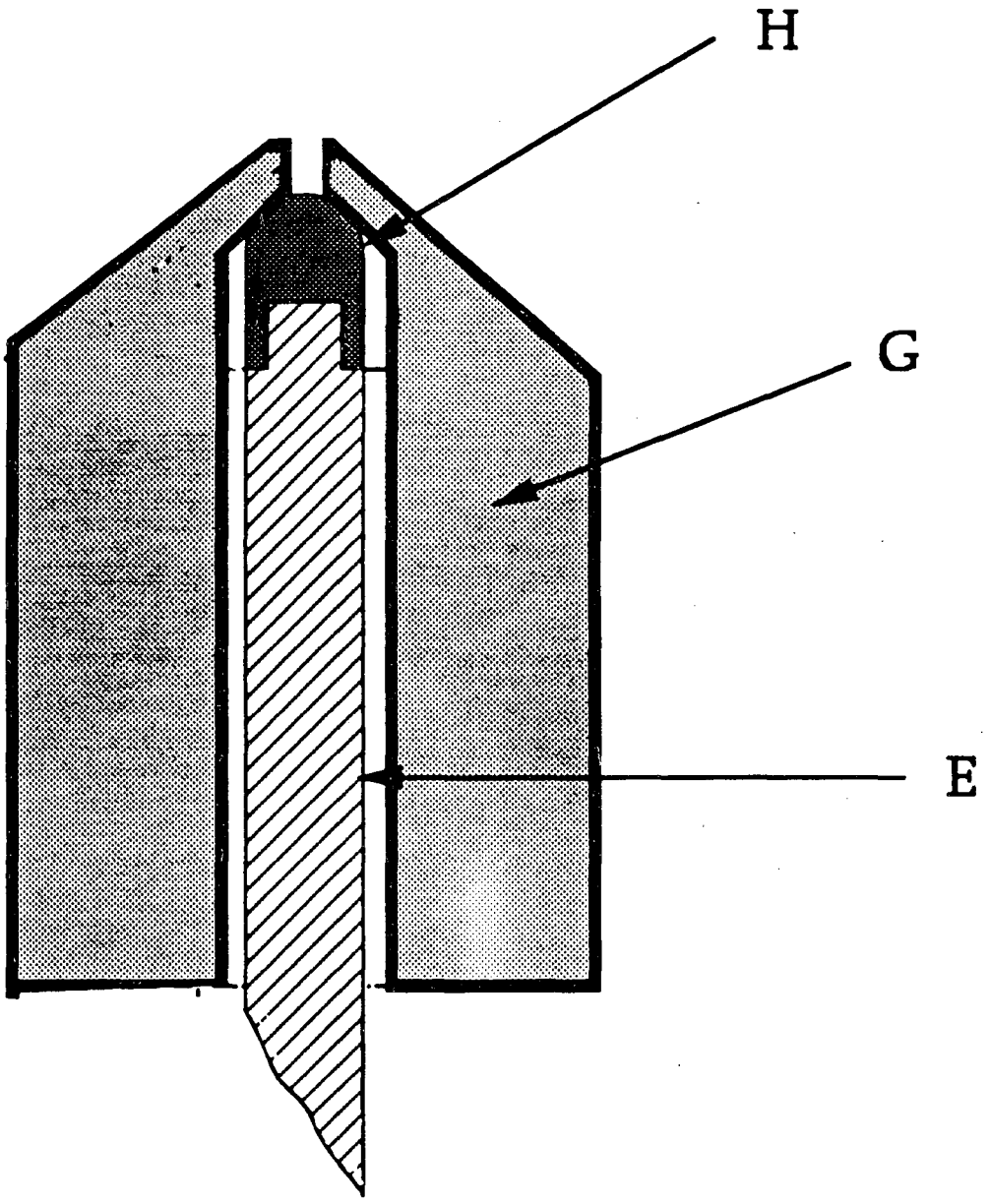

XBL 8911-4091

Figure B - 2

Appendix C

Pulsed Beam Diagnostics

1. Introduction

Pulsed-molecular-beam techniques add a new level of complexity to crossed-molecular-beams scattering experiments. Due to the time dependence of the beam density and velocity distributions, the beams must be crossed with a fixed relative phase. Successful optimization of the experiment requires information on these characteristics of the pulsed molecular beam. In a high duty-cycle experiment it is essential that the pulsed beam performance is not compromised by leaks or poor mechanical adjustment. In this appendix, the diagnostic procedures used to characterize the pulsed molecular beams are reviewed. Several pertinent papers on pulsed beams and pulsed beam diagnostics have been published[1,2,3,4,5], as well as a recent in-depth review of pulsed-molecular-beam techniques[6].

Two of the previously published papers are particularly pertinent to the problem of characterizing pulsed molecular beams produced with piezoelectric pulsed valves (PPV's). Time-of-flight (TOF) velocity distribution measurements and laser-induced fluorescence measurements of internal state distributions were made on pulsed beams generated with a commercial Lasertechnics piezoelectric pulsed valve (Lasertechnics Model LPV) in the work of Andresen, et. al. [3]. Kay and coworkers[4] also published a detailed study of the temporal behavior of the beam velocity distributions obtained with the Lasertechnics pulsed valve. The general characteristics of the high-

performance PPV's of the type used in these experiments have been discussed by Proch and Trickl[5]. The results presented in this appendix represent an extension of their work to the modified pulsed valves described in Appendix B.

The first problem facing the pulsed beam operator is to ensure that the PPV does not leak when it is 'closed', and that it produces intense gas pulses with the shortest possible width in time. A small test chamber equipped with a fast ion gauge (FIG)[1] and a conventional Bayard-Alpert ion gauge was assembled to allow routine measurement of the PPV performance. With the conventional ion gauge, the quality of the valve seal could be easily determined. The FIG allowed the measurement of the temporal density profile, which enabled the adjustment of the dynamic behavior of the pulsed valve. The FIG is described in section 2 of this appendix, along with some of the results obtained with it. The second important problem, particularly in scattering experiments, is the time dependence of the pulsed beam velocity distribution. To measure this, a technique involving the synchronization of a conventional single-shot TOF chopping wheel with the pulsed beam was employed. This allowed the probing of the velocity distributions at different times, and hence, spatial positions in the gas pulse. These efforts, including some interesting data concerning the velocity distributions in the cryogenic pulsed valve (CPV) are presented in section 3 of this appendix. Relative beam intensities and angular distributions were measured with an ion gauge manometer. This technique and the results obtained are presented in section 4 of this appendix. The laser-generated D-atom beam constitutes a far more ideal pulsed molecular beam (short pulse width, with a narrow velocity distribution) than the pulsed beams produced by the PPV. Measurements of

the characteristics of the D-atom beam were made with the UHV differentially pumped mass spectrometric detector, as described in Chapters 2 and 3.

With intense skimmed pulsed beams, care must be taken to ensure that interaction of the gas pulse with the skimmer does not perturb the beam intensity or velocity distributions considerably. If the nozzle-skimmer aperture distance is too short, a local region of high pressure can form at the skimmer orifice which will attenuate the transmitted skimmed molecular beam and broaden the beam velocity distribution.[7] The point at which beam attenuation phenomena become important depends on gas composition and density. For example, species with large collision cross sections will pose much more of a problem, as the critical density at the skimmer orifice at which cloud formation occurs will be lower. For these gases, the pressure at which attenuation begins will be lower, or, for a constant pressure, the minimum nozzle-skimmer distance at which attenuation occurs will be longer. All of the diagnostic techniques described in this appendix may be applied to the study of this phenomenon. The intensity of the transmitted pulse can be measured with either the FIG or the ion gauge manometer. Beam TOF measurements can reveal both the intensity and velocity distribution of the beam.

Maximum H_2 beam intensities with source stagnation pressures in the 1 to 2 atmosphere range were observed with a 2.0 cm nozzle-skimmer distance for 1.0, 0.75 and 0.50 mm nozzles. At shorter nozzle-skimmer distances a decrease in beam intensity and a broadening of the velocity distribution was observed, while at larger nozzle-skimmer distances, the beam intensity decreased. Larger nozzle-skimmer distances are required with

much higher stagnation pressures, however, for the purposes of our high duty cycle experiment such conditions were not desirable due to the limited pumping speed of the source chamber and the larger detector background which occurred under such operating conditions. Thus, the 2.0 cm nozzle-skimmer distance is not a universal 'best' value, but the optimum one for the $D + H_2$ scattering experiments.

2. Fast Ion Gauge Measurements

2.1 Method

A stainless-steel tee pumped by a 6" oil diffusion pump was equipped to provide a Pulsed Valve Test Chamber (PVTC) for routine adjustment of the pulsed molecular beams. The PVTC was equipped with both a Fast Ion Gauge (FIG) for time-resolved pressure measurements and a standard Bayard-Alpert ion gauge for background gas pressure measurements. Two test geometries were used, as shown in Figure C-1. Test geometry A was used for evaluating the pulsed valve performance in conjunction with various skimmers and various test gases, whereas test geometry B was routinely used for pulsed valve adjustment with the body of the pulsed valve open, using air as the test gas. The PPV was designed so that all adjustments could be made from the inside of the valve, making test geometry (B) particularly convenient for rapid, reproducible pulsed-beam adjustment.

The FIG was a home built version based on the design described by Giese and Gentry in 1975[1]. The specific electrometer circuit used and a schematic diagram of the FIG geometry is shown in Figure C-2.[8] The FIG is

basically a Bayard-Alpert style ion gauge, which makes use of small physical dimensions and a fast rise time electrometer circuit to make real time pressure measurements on the pulsed beams. The rise time of the electrometer circuit is very fast (≈ 100 nsec), so the chief limitation on the temporal resolution is the size of the grid (diameter ≈ 2 mm). Given air moving at about 8×10^4 cm·sec^{-1}, a grid of this size would give a flight-time uncertainty of ≈ 2.5 μsec. This is more than sufficient for our purpose, which is to measure the temporal profile of a pulsed beam with a full-width at half-maximum (FWHM) of ≈ 200 μsec.

2.2 Results

The FIG played an important role in both the development and routine readjustment of the pulsed-molecular-beam sources in the experiments described in this thesis. With FIG measurements under standard operating conditions, (20 μA emission current, +4V filament floating voltage and +220 V grid voltage), beam source performance could be accurately reproduced after disassembly and reassembly of a pulsed valve. As examples of the types of measurements performed with the FIG, temporal profiles for the PPV in different configurations will be presented. In addition, some interesting temporal profiles concerning the effectiveness of different skimmers will be shown.

The operation of the PPV is critically dependent on the mechanical adjustment of the O-ring seal and the carrier O-ring, which supports the piezoelectric element (see Figure B-1). The O-ring seal must be compressed enough to make a leak tight seal across a large pressure differential, yet it

must not be compressed so much that it will not open when the piezoelectric element actuates (the maximum excursion is < 100 μm). The carrier O-ring serves to dampen the motion of the piezoelectric element. If the carrier O-ring is compressed too much, the crystal will tend to 'ring', giving multiple gas pulses, and increasing the effective duty cycle of the supposedly low duty cycle pulsed valve.

In practice, these adjustments must be made by trial and error, and that is where the FIG serves so well. Several iterations of seal and carrier O-ring adjustment were typically required to achieve good performance. The optimum valve adjustment with respect to bouncing of the sealing O-ring is dependent on the excursion of the piezoelectric element, which is determined by the voltage supplied to the crystal and the driving pulse length. The Physik Instrumente P-286 disc translators are rated for operation with driving voltages up to -1 kV, however, for long term, reliable operation it was found that the valve performed better at -450 to - 600 V. Eventually, if the valve was run at voltages near the maximum of -1 kV for many cycles (millions) the crystal would crack, and need to be replaced.

To illustrate the behavior of the pulsed valve, Figure C-3 shows temporal profiles measured with a 1mm nozzle, 5.5 cm poppet and 80 psig of He , with two different O-ring sealing materials, Viton and Kalrez. Viton, which is familiar in UHV work, is a perfluorinated elastomer with good chemical resistance[9a]. Kalrez is the polymer of chlorotrifluoroethylene, and is noted for its superior chemical resistance.[9b] This sealing material was initially investigated because it was thought that Viton O-rings might crack shortly after exposure to DI, which did not turn out to be the case. Kalrez is stiffer than Viton, which is the cause for the considerable difference in the

two temporal profile traces. Kalrez seals caused the poppet to bounce considerably, a behavior which could not be solved by adjustment, whereas Viton seals allowed the valve to be adjusted such that the second bounce of the poppet was negligible as the figure shows. Note in all the FIG temporal profiles that the buildup of pressure in the chamber due to the pulse of gas at long times is seen as a long, slow baseline rise.

Figure C-4 shows the performance of the 5.5 cm poppet valve at the same driving voltage but with 100 and 150 μsec driving pulses. The figure shows that the 100 μsec driving pulse did not fully open the 1 mm nozzle with the valve adjustment used. The gas pulse width decreased from 200 μsec FWHM to 150 μsec FWHM as driving pulse length was decreased from 150 to 100 μsec. A small secondary pulse due to bouncing of the poppet can be seen with the 150 μsec driving pulse. With the poppet tension loosened, operating conditions exhibiting a 'bounce' with the 100 μsec driving pulse were achieved, with full nozzle flow resulting. In practice, to achieve maximum throughput, the valve was adjusted such that some bounce (≈ 10% of the main pulse) would occur at the highest driving voltages. This setting indicated that the poppet seal was just 'loose' enough, and would yield the highest gas throughputs under routine operation.

In the D + H_2 reactive scattering experiments, a 7.7 cm poppet with a 0.75 mm nozzle was used for the DI beam, while a 5.5 cm poppet with a 0.5 mm nozzle was used the H_2 beam. Typical operating conditions for the DI pulsed beam were 140 torr DI backing pressure, 500 V driving voltage and 100 μsec driving pulse width, with 35 μsec rise and fall times on the driving pulse. FIG measurements with air showed that the DI beam source produced pulses with a FWHM of ≈ 225 μsec. The H_2 beam was typically run with 1200 torr H_2,

400 volt driving pulse and only a 40 μsec driving pulse width. These operating conditions resulted in a simple impulsive kick being delivered to the disk translator, giving the shortest width gas pulse and no bounce. Under these conditions, the free-jet pulse width was ≈ 175 μsec as measured 15 cm from the nozzle. The m/e = 3 background in the detector was critically dependent on the H_2 beam source performance, and these settings gave the best signal/noise ratios in the experiment.

With the pulsed valve in position A, as shown in Figure C-1, the performance of several different skimmers was investigated. To make measurements of the part of the pulse transmitted through the skimmer, a deflector was placed between the PPV and the FIG, to prevent the great majority of molecules which did not travel through the skimmer from passing around it and arriving at a time only slightly delayed relative to the transmitted part of the pulse. The measurement of transmitted vs deflected beam could be made by measuring the temporal profiles with the various skimmers. This does not constitute an absolute measurement, as some of the deflected beam is pumped away before reaching the FIG. Keeping the deflector geometry the same, though, permitted reliable relative measurements to be made. Figure C-5 shows temporal profiles recorded with 80 psig of He. The skimmer in Figure C-5(a) was a simple 1.5 mm aperture the skimmer in Figure C-5(b) was a 1.4 mm-diameter machined-stainless-steel conical skimmer, and the 'skimmer' in Figure C-5(c) was a commercial 1.5 mm electroformed skimmer (Beam Dynamics)[10]. Of these, the electroformed skimmer gave the best performance, while the simple aperture gave the worst performance. Sharp-edged electroformed skimmers typically

caused the least amount of interference with the pulsed molecular beam, as Gentry has reported.[6]

3. Beam TOF Measurements

3.1 Method

A standard technique for the measurement of molecular beam velocity distributions involves mechanically chopping the beam and measuring the dispersion of the beam relative to the known shutter function of the chopper at some later time. This technique has been in use for some 35 years, and has been discussed in numerous papers[11]. For reactive scattering experiments, in particular, the beam velocity vector dispersion determines the spread in collision energies and a knowledge of this is essential to deconvolute the scattering data. The number-density velocity distribution of a supersonic molecular beam is typically assumed to be of the form

$$N(v) = (v^2)\cdot e^{-((v/\alpha)-S)^2} \qquad (1).^{12}$$

In this equation $\alpha = (2kT/m)^{1/2}$ and the speed ratio $S = v_s/\alpha$, where v_s is the bulk flow velocity of the gas. Frequently beam velocity distributions are also described in terms of the Mach number M, which is related to the speed ratio;

$$M = S\cdot(\gamma/2)^{-1/2} \qquad (2).^{13}$$

In a pulsed supersonic expansion, matters are complicated by the fact that α and S are both time dependent. In Kay's work[4], a model for the time dependence of these parameters was described. This formalism was not used in the analysis of beam TOF distributions in this appendix, since the velocity distribution of the part of the beam used in the scattering experiments was well described by fitting with equation (1).

When a continuous molecular beam is used, the TOF measurement is done by chopping the beam with a slotted disk and using a reference signal provided by a light/photodiode setup on the slotted disk to provide time zero for the subsequent measurement of the TOF of the particles. If such an arrangement is used for a pulsed molecular beam, with no synchronization between the pulsed beam and the chopping wheel a pulse-averaged measurement of the beam velocity distribution can be recorded. For scattering experiments, knowledge of the beam velocity distribution is critical, so it is important to measure the velocity distribution in the part of the pulse that is used. Bier and Hagena performed the first experiment in which the velocity distribution in a pulsed beam was analyzed with a synchronously operated chopper.[2] The later work in references 3 and 4 also made use of a synchronized chopper wheel/pulsed beam setup for measurement of the velocity distribution of the beam as a function of time in the pulse. A schematic of the synchronous TOF setup used here is shown in Figure C-6.

The free jet measurements in particular were difficult to perform with the mass spectrometer in pulse-counting mode, due to the large signals, but by turning the emission current down to very low levels ($\approx$ 0.5 mA), reliable measurements could be made. Initial efforts at lowering the count rate by reducing the secondary electron emission cathode voltage, reducing the

photomultiplier tube gain, or increasing the discriminator threshold were unsuccessful. Under such reduced gain conditions the detector became sensitive only to 'coincidence' events, i.e. only the simultaneous arrival of two or more ions would produce a large enough signal to be detected.[14] In retrospect it probably would have been worthwhile to perform these measurements in an analog mode.

The early pulsed beam work of Bier and Hagena in the 1960's used both synchronous TOF and a fast ionization gauge detector similar in principle to the FIG discussed in section 2.[2] The solenoid-based pulsed beam that they used produced pulses of ≈ 2 msec in length. Bier and Hagena found that 'quasistationary' conditions were reached within 100 - 200 μsec, with a maximum beam intensity occurring during this time , followed by a steady throughput for the rest of the pulse. With a 50 μm nozzle and a nozzle-skimmer distance of 80 nozzle diameters, they measured a speed ratio (S) for N_2 of 12 during the beam intensity maximum, with a steady state value of S = 9.6 at later times during the pulse.

Using a commercial piezoelectric pulsed beam with a nozzle diameter of 0.5 mm and a nozzle-skimmer distance of 136 nozzle diameters, (skimmer diameter = 0.5 mm) Andresen and coworkers[3] found that the peak speed ratios and peak beam intensities were observed simultaneously in the 0.5 msec gas pulse. The 'typical' speed ratios observed for He, Ar, Ne and N_2 in these studies were 19, 34, 34 and 20 respectively. These numbers were felt to be in good accord with the predictions made for continuous molecular beams if the 'effective' nozzle diameter was taken into account, due to the incomplete opening of the pulsed nozzle ($P_0 \cdot d_{eff}$ = 27 Torr·cm for He). Using the same commercial pulsed valve and a 0.05 cm diameter nozzle with a

nozzle-skimmer distance of 120 nozzle diameters and a nozzle diameter of 1.0 mm, Kay and coworkers[4] measured speed ratios of $S \approx 80$ for He in the middle of the gas pulse (P_0d = 270 Torr·cm). Lower values for S were measured at the leading and falling edges of the pulse. In their experiments, the gas pulse duration was 650 μsec. Using a short pulse length (≈ 15 μsec FWHM) electromechanical valve in $D + H_2$ reactive scattering experiments, Buntin et. al.[15] measured speed ratios of ≈ 16 for H_2 with a 0.58 mm nozzle, a rectangular skimmer of dimensions 0.36 cm by 0.51 cm at a distance of 100 nozzle diameters and a $P_0.d$ value of ≈ 7000 Torr·cm. In recent work, Gentry's group has reported a 'world record' speed ratio $S > 1000$ for a He expansion using a special new high pressure pulsed beam source.[16] These results give a general idea of the velocity distribution characteristics of the pulsed beams available today.

3.2 Results

In this section, the beam velocity measurements of most importance to the $D + H_2$ experiment, those of para-H_2 (p-H_2) and normal-H_2 (n-H_2), will be discussed first, followed by the measurements of the velocity distributions produced by the cryogenic pulsed valve.

To perform beam TOF measurements, all electronic and mechanical offsets must be determined as well as the flight path from the chopping wheel to the effective center of the electron-impact ionizer. The calibration of the flight path for continuous molecular beams has been previously discussed[12], and the procedure for the pulsed beam is very similar. Measurement of the 'mechanical offset' (MO) associated with the phase between the photodiode

trigger signal and the actual opening of the chopper shutter function is somewhat more difficult in a pulsed molecular beam. Measurement of this offset is typically made by simply spinning the wheel both clockwise and counterclockwise, and taking the MO to be half the difference between the peak flight times measured. With the pulsed beam, the peak velocity is also a function of time in the pulse, and thus the measured peak flight time is also a function of the phase of the chopper relative to the molecular beam. To solve this problem, careful measurement of the width and integrated intensity of the TOF spectra as a function of time in the pulse for both directions of wheel rotation were made, and the MO was determined from the measured peak velocities in TOF spectra of the same width and intensity for the two senses of wheel rotation. For skimmed beams of He (0.5 mm nozzle, 1.8 cm nozzle-skimmer distance, 1.5 mm diameter skimmer) the velocity distribution was characterized by (α, S) = (1.391,12.64) with a peak velocity of 1.78×10^5 cm/sec at 300 K.

3.2.1 300 K H_2 Beam Source

Skimmed beams of n-H_2 and p-H_2 have different velocity distributions. The reason for this is that H_2 can only undergo $\Delta J = 2$ transitions as it collisionally relaxes in the expansion, and n-H_2 is composed of $\approx$ 70% H_2 (J=1) at room temperature. At the peak of the pulsed-beam intensity, the n-H_2 beam was characterized by (α,S) = (1.98,13.9) with a peak velocity of 2.78×10^5 cm/sec, while the p-H_2 beam was described by (α,S) = (1.87,15.0) with a peak velocity of 2.82×10^5 cm/sec. TOF spectra for n- and p-H_2 showing the fit to eqn (1) are shown in Figure C-7. Figure C-8 shows several different TOF

spectra of a n-H_2 beam at different points in the gas pulse. Figure C-9(a) shows the integrated intensity of the n-H_2 beam TOF spectra in Figure C-8. The FWHM of the skimmed H_2 pulse as measured with the beam TOF method is ≈ 80 μsec. The temporal width of the skimmed pulse is shorter than that measured for the free jet of H_2, presumably due to interaction of the intense pulsed beam with the skimmer, attenuating the beam at longer times. The time-dependence of the peak beam velocities and speed ratios are shown in Figure C-9(b). The chopping wheel was located ≈ 7 cm from the nozzle in these measurements, which is a sufficient distance for a dispersion of the pulsed molecular beam, with the fastest molecules arriving at the chopper first. The peak beam intensity and peak speed ratios were observed to occur at the same point in the pulse.

A detailed study of the rotational relaxation of H_2 as a function of expansion conditions (P_0d) in continuous supersonic beams was performed by Pollard, et. al.[17]. For the pulsed molecular beams described here, the value of P_0d is (1200 torr)x(0.5 mm) = 600 torr-mm. Two factors may alter the actual rotational distribution from that expected for an expansion with P_0d = 600 torr-mm at 300K: 1) Interaction of the intense pulsed molecular beam with the skimmer may raise the effective rotational temperature of the beam, and 2) it is possible that the effective diameter of the pulsed beam source is less than the nominal 0.5 mm diameter of the nozzle, due to incomplete opening of the pulsed beam aperture. For this reason, the final rotational state distributions will be estimated from the work of Pollard, et. al. at P_0d = 100 torr-mm. Due to the inability of H_2 (J = 1) to relax in the expansion of n-H_2 from T = 297 K, the final rotational state distribution observed in Pollard's work was $H_2(J) = 0 : 1 : 2 : 3 = 18 : 75 : 7$. For the expansion of p-H_2 at 297 K,

the observed rotational state distribution was found to be $H_2(J) = 0 : 2 = 70 : 30$. In the scattering experiments no significant difference in reactivity was noted between D + n-H_2 and D + p-H_2.

3.2.2 Cryogenic H_2 Beam Source

The CPV was quite effective at producing slow beams upon cooling with a closed cycle refrigerator attached to it via a Cu braid. With the Air Products CS-202 displex, the nozzle could be cooled to temperatures as low as 20 K when it was shielded with 80K surfaces and mylar insulation. Measurements of the velocity distributions of both cold free jets and cold skimmed beams were made. In the free jet, a source temperature of 20 K produced peak intensity H_2 beams characterized by $(\alpha,S) = (.193,32.7)$ with a peak velocity of 6.32×10^4 cm/sec at 95 torr stagnation pressure, and $(\alpha,S) = (.291,21.8)$ with a peak velocity of 6.36×10^4 cm/sec at 45 torr stagnation pressure. When the CPV temperature was raised to 40 K, the peak velocity increased to 9.1×10^4 cm/sec with $(\alpha,S) = (.4933,18.40)$.

At the low temperatures achieved with the CPV it was easy to make H_2 clusters even though the P_0d values were quite low ($P_0d \approx 60$ Torr·mm for the .75 mm nozzle at 95 torr stagnation pressure; nozzle at 20K). Under such expansion conditions, significant velocity 'slip' occurred, with the H_2 monomers, dimers, etc. having considerably different velocities. This resulted in a significant dispersion of the clusters as the beam traveled. In Figure C-10 TOF spectra at m/e = 3 illustrating the velocity-dispersion of the hydrogen clusters are shown. In later parts of the pulse, a second, slower component is observed which results from the neutral clusters ionizing and

reacting to yield H_3^+ in the ionizer. Similar spectra were observed up to m/e = 9 (H_9^+), and probably extended to much higher masses, but no measurements were made. Figure C-11(a) shows the integrated intensity at m/e = 3, while Figure C-11(b) shows the time dependence of the peak velocities and speed ratios. These curves show clear manifestations of condensation occurring in the beam. The FWHM in time of the m/e = 3 spectrum is only ≈ 30 μsec, but since this does not represent the beam intensity for all m/e clusters, it is clear that a significant portion of the beam must be in the form of larger clusters. In Figure C-11(b), the peak velocity shows a steady decrease with time in the pulse, but in the speed ratio, a marked modulation is observed when clustering begins. Initially, the beam is heated by the energy released in the condensation, and these molecules reach the chopper first. The slower, cooled clusters then arrive at the chopper, with a corresponding dramatic increase in the speed ratio observed.

In practice, the final D-H_2 scattering experiments done with the CPV were performed using a crudely collimated beam. As Figure 2-8 shows, a thin aperture was mounted on an OFHC Cu cage attached to the nozzle. The temperature which this aperture reached was not independently measured, but was probably somewhat higher than the nozzle itself. In any case, a significant nozzle-skimmer interaction was observable with the beam in this geometry, resulting in a broadened velocity distribution. With a 20 K nozzle temperature, the best velocity distribution obtained was (α,S) = (.749,9.51) with a peak velocity of 7.28×10^4 cm/sec. With a 40 K nozzle temperature, the beam was characterized by (α,S) = (1.054,10.05) and a peak velocity of 10.8×10^4 cm/sec. The heating of the beam which occurred as a result of this nozzle-

skimmer interaction eliminated the significant condensation effects that were observed in the free jet.

4. Ion Gauge Manometer Measurements

4.1 Method

Using a standard Bayard-Alpert ionization gauge, a simple molecular beam detector may be assembled, as shown in Figure C-12. Such detectors have seen considerable use in the study of molecular beam work over the years.[18] A detector of this type was used to determine the molecular beam angular distributions.

The key feature of the ion gauge manometer (IGM) is that the directed molecular beam passes through the entrance orifice, collides with walls of the IGM and comes to equilibrium. The steady state pressure in the IGM is then determined by the rate of effusion back out of the aperture. By measuring the change in pressure, the rate at which molecules enter the IGM can be determined using the well known equation for the rate of molecular effusion through a thin aperture;

$$\dot{n} = \frac{1}{4}\Delta n_{ss}\bar{v}A_{ent} \qquad (3)$$

where n is the rate in molecules/sec, Δn_{ss} is the measured change in number density, v is the root mean square velocity of molecules in the IGM and A_{ent} is the area of the entrance aperture. For the measurements of the beam

angular distribution, the IGM was mounted on the rotatable detector, and therefore rotated about the center-of-rotation (COR) of the scattering chamber. The beam source is not at the COR, which is where the beams cross in the reactive scattering experiment, so a simple laboratory-angle-dependent geometry correction had to be made to the raw angular distribution measurements in order to correct for the changing effective aperture area the IGM presented to the molecular beam. When this correction, which is proportional to cos γ as shown in Figure C-12, is taken into account, the final equation for the beam intensity can be written as

$$I(\alpha) = \dot{n} \cdot \frac{4}{\pi d^2 \cos\gamma} \frac{\text{molec}}{\text{cm}^2 \cdot \text{sec}} \qquad (4)$$

or, in terms of the solid angle,

$$I(\Omega) = \dot{n} \cdot \frac{\pi d^2 \cos\gamma}{4R^2} \frac{\text{molec}}{\text{sr} \cdot \text{sec}} \qquad (5),$$

where R is the distance from the beam source and d is the diameter of the IGM aperture. The instantaneous density of the gas pulse may be determined given the duty cycle of the pulsed beam, $F = \nu\tau$, where ν is the valve operation frequency and τ is the pulse width. If the detailed temporal behavior of the valve is known, the beam density as a function of time in the pulse may be determined, but for the accuracy desired in these measurements it is satisfactory to simply consider a pulse with a 'square' temporal dependence of width τ. Given these assumptions, we can write the final equation for the gas flux during the pulse as

$$I(\Omega,t) = \frac{I(\Omega)}{F} \frac{\text{molec}}{\text{sr}\cdot\text{sec}} \qquad (5),$$

where t implies that this is the flux obtained while the gas pulse is on.

4.2 Results

Figure C-13 shows the angular distribution measured for the pulsed H_2 beam under the conditions of the D + H_2 experiment (nozzle-skimmer distance 1.80 cm, skimmer aperture 1.5 mm, skimmer height 0.64 cm). The alignment of the IGM was apparently off by ≈ 1.5 to 2.0 degrees, as measurements with the UHV rotatable mass spectrometer indicated that the center of the beam was not misaligned during the scattering experiments. The beam angular distribution was observed to have a FWHM of ≈ 8°. At higher stagnation pressures, the wide angle intensity of the beam was observed to increase, presumably due to cloud formation and scattering at the skimmer aperture. A key point that must be remembered with respect to these measurements is that they do not address the time dependence of the beam angular distribution. The wide angle components of the angular distribution probably result from cloud formation at the skimmer, with a resulting cosθ effusive angular distribution late in the pulse. For this reason, this part of the angular distribution of the H_2 beam was not considered in the reactive scattering simulation.

5. Conclusions

The three diagnostic techniques discussed in this appendix reveal many of the important properties of pulsed molecular beams pertinent to scattering experiments. The FIG is the most important tool for routine reassembly of the experiment, and should be useful in all pulsed molecular beam experiments. The beam velocity and angular distribution measurements are very important in scattering experiments, but in many spectroscopy experiments, for example, such information is not especially important. More detailed measurements of molecular rotational populations are now possible with many of the sensitive state-specific laser-based detection techniques available today, and will be necessary in future, higher-resolution experiments.

---

1. W.R. Gentry and C.F. Giese, Rev. Sci. Inst., **49**, 595 (1978).
2. K. Bier and O.F. Hagena, Rarefied Gas Dynamics, Proc. of 4th Int. Symposium, ed. J.H. de Leeuw , Academic Press, New York (1965), Vol. II, p. 260.
3. P. Andresen, M. Faubel, D. Haeusler, G. Kraft, H.-W. Luelf, and J.G. Skofronick, Rev. Sci. Inst., **56**, 2038 (1985).
4. Bruce D. Kay, T.D. Raymond, and J.K. Rice, Rev. Sci. Inst., **57**, 3266 (1986).
5. D. Proch and T. Trickl, Rev. Sci. Inst., **60**, 713 (1989).
6. W.R. Gentry, "Low Energy Pulsed Beam Sources", in Atomic and Molecular Beam Methods, ch. 3, ed. G. Scoles, Oxford Univ. Press, London, (1988), ch. 3, pp. 54 - 82.
7. a). U. Bossel, F.C. Hurlbut, and F.S. Sherman, Rarefied Gas Dynamics, Proc. of 6th Int. Symposium, ed. J.H. de Leeuw , Academic Press, New York (1969), Vol. II, p. 945.

b). G.A. Bird, Physics of Fluids, **19**, 1486 (1976).

8. Dr. T. Trickl, private communication.

9. a). Viton properties: F. Rosebury, Handbook of Electron Tube and Vacuum Techniques, Addison-Wesley, New York, (1965), p. 391.

b). Kalrez properties: Parker O-Ring Handbook, Parker Seal Group, Lexington, KY, (1982), pp. A 3-1 - A 3-17.

10. W.R. Gentry and C.F. Giese, Rev. Sci. Inst., **46**, 104 (1975).

11. a). O.F. Hagena and A.K. Varma, Rev. Sci. Inst., **39**, 47 (1968).

b). J.A. Alcalay and E.L. Knuth, Rev. Sci. Inst., **40**, 438 (1969).

12. a). M.F. Vernon, UC-LBL Report #12422, (1981).

b). D.J. Krajnovich, Ph. D. Thesis, University of California, Berkeley, (1983).

13. D.R. Miller, "Low Energy Pulsed Beam Sources", in Atomic and Molecular Beam Methods, ed. G. Scoles, Oxford Univ. Press, London, (1988), Ch. 3 p. 26.

14. H.R. Siddiqui, A. Khan and P.E. Siska, Rev. Sci. Inst., **53**, 1940 (1982).

15. S.A. Buntin, C.F. Giese and W.R. Gentry, J. Chem. Phys., **87**, 1443 (1987).

16. J. Wang, V.A. Shamamian, B.R. Thomas, J.M. Wilkinson, J. Riley, C.F. Giese, and W.R. Gentry, Phys Rev. Lett., **60**, 696 (1988).

17. J.E. Pollard, D.J. Trevor, Y.T. Lee, and D.A. Shirley, J. Chem. Phys., **77**, 4818 (1982).

18. F. Knauer and O. Stern, Zeits. f. Physik **53**, 766 (1929); see N. F. Ramsey, Molecular Beams, Oxford Univ. Press, London, New York (1956), ch. XIV, pp. 374-394 for a review of early molecular beam detectors.

Appendix C Figure Captions

Figure C-1. Pulsed Valve Test Chamber (PVTC). Two test configurations are shown. With the pulsed valve in position A, the skimmer/deflector S could be mounted on it for the study of pulsed beam/skimmer interactions. Routine pulsed valve adjustment was done with the valve in position B. The Fast Ion Gauge is marked FIG, and the standard Bayard-Alpert Ion Gauge is marked IG.

Figure C-2. (a) Schematic diagram of the Fast Ion Gauge (FIG) geometry and power supplies.

(b) Schematic diagram of the fast electrometer circuit used with the FIG.

Figure C-3. (a) FIG signal measured with Viton seals in the pulsed valve.

(b) FIG signal measured with Kalrez seals in the pulsed valve.

Figure C-4. (a) FIG signal measured with a 150 μsec driving pulse.

(b) FIG signal measured with a 100 μsec driving pulse.

Figure C-5. FIG signal measured with PVTC in configuration A (see Figure C-1) and skimmer/deflector in place.

(a) Simple 1.5 mm aperture, 1" nozzle-aperture distance.

(b) 19 mm high by 1.4 mm dia. machined SS skimmer, 25 mm nozzle-skimmer distance.

(c) 19 mm high by 1.5 mm dia. electroformed skimmer, 25 mm nozzle-skimmer distance.

Figure C-6. Schematic of pulsed-beam TOF beam velocity measurement scheme with synchronous chopping wheel modulation. The chopper is synchronously run at 250 Hz. Since the chopping wheel has 4 x .75 mm wide slots, the effective frequency is 1 kHz. The photodiode produces a timing signal when a slot passes the detector aperture, which is divided by 10. The divided 100 Hz signal then triggers the MCS, and, after a variable time delay, the pulsed beam is fired. This delay is set such that the pulsed beam will reach the chopper when the next 100 Hz pulse triggers the MCS and the chopper slot is in front of the detector aperture. The chopped beam molecules then fly to the detector and are measured with the MCS at time τ_{flt}.

Figure C-7. TOF spectra (m/e = 2) for skimmed molecular beams of (a) n-H_2 and (b) p-H_2 produced with a 300 K pulsed beam source. The solid line fit to the spectra are generated with equation 1.

Figure C-8. TOF spectra of a skimmed n-H_2 beam (m/e = 2) as a function of time in the pulsed beam. The spectra are shown scaled by the relative intensity. See Table 1 for velocity distribution parameters.

(a) ——— leading edge of the pulse, '0' μsec; scaled up 10 x

-------- 2 μsec; scaled up 5x

— — — 4 μsec

(b) ——— 10 μsec

--------	15 μsec
— — —	20 μsec
(c) ———	25 μsec
--------	57 μsec
— — —	62 μsec
(d) ———	72 μsec
--------	92 μsec
— — —	112 μsec
(e) ———	137 μsec
--------	202 μsec; scaled up 5x
— — —	362 μsec; scaled up 10x

Figure C-9 (a) Intensity of the skimmed n-H_2 beam obtained by integrating the TOF spectra in Figure 8.

(b) Time dependence of the peak velocity and speed ratio S for the TOF spectra in Figure 8.

Figure C-10. TOF spectra (m/e = 3) of a free jet of n-H_2 produced with the cryogenic pulsed valve at a stagnation temperature of 20 K with a stagnation pressure of 95 torr and a 0.75 mm nozzle. Note the H_2 cluster components with significantly slower velocity in (b), (c) and (d).

(a) ———	leading edge of the pulse, '0' μsec, scaled up 10x
--------	10 μsec; scaled up 5x
— — —	20 μsec
(b) ———	30 μsec
--------	35 μsec

— — —	40 μsec
(c) ———	45 μsec
- - - - - - - -	50 μsec
— — —	55 μsec
(d) ———	60 μsec
- - - - - - - -	70 μsec
— — —	80 μsec
(e) ———	100 μsec
- - - - - - - -	140 μsec
— — —	180 μsec
(f) ———	320 μsec; scaled up 5x
- - - - - - - -	340 μsec; scaled up 10 x

Figure C-11. (a) Intensity of the cryogenic n-H_2 beam obtained by integrating the TOF spectra in Figure 10.

(b) Time dependence of the peak velocity and speed ratio S for the TOF spectra in Figure 10.

Figure C-12. (a) Ion Gauge Manometer (IGM). A commercial Bayard-Alpert pyrex ion-gauge tube was modifed by adding a tube with a collimating aperture at the end.

(b) Diagram showing the geometric relationship between an IGM angular distribution measured as a $f(\Theta)$, with IGM rotating about C to $f(\alpha)$, where α is the angle with respect to the source, located a distance D from the COR at C.

Figure C-13. Angular distribution for the H_2 pulsed beam used in the final D + H_2 scattering experiments described in Chapter 3. The fit to the data is a Gaussian distribution with a FWHM of 8°.

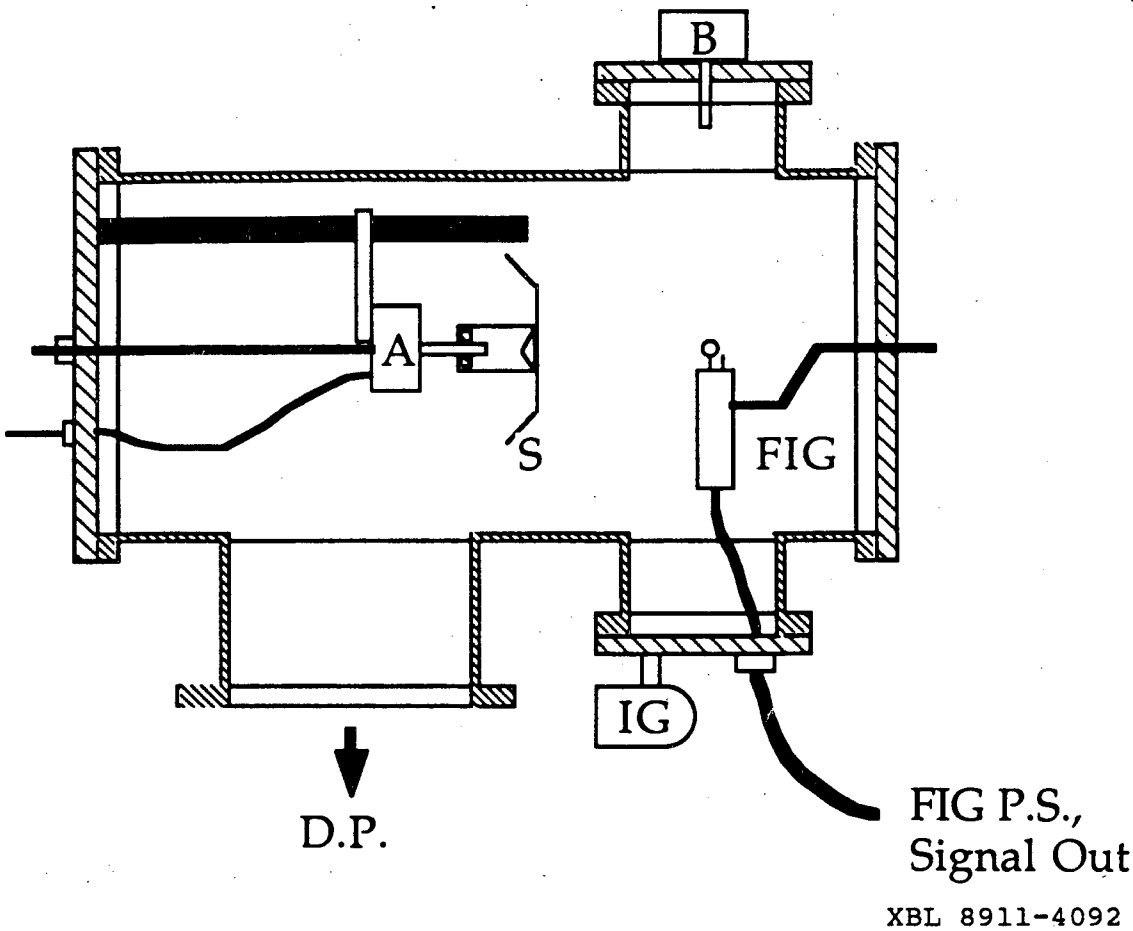

Figure C - 1

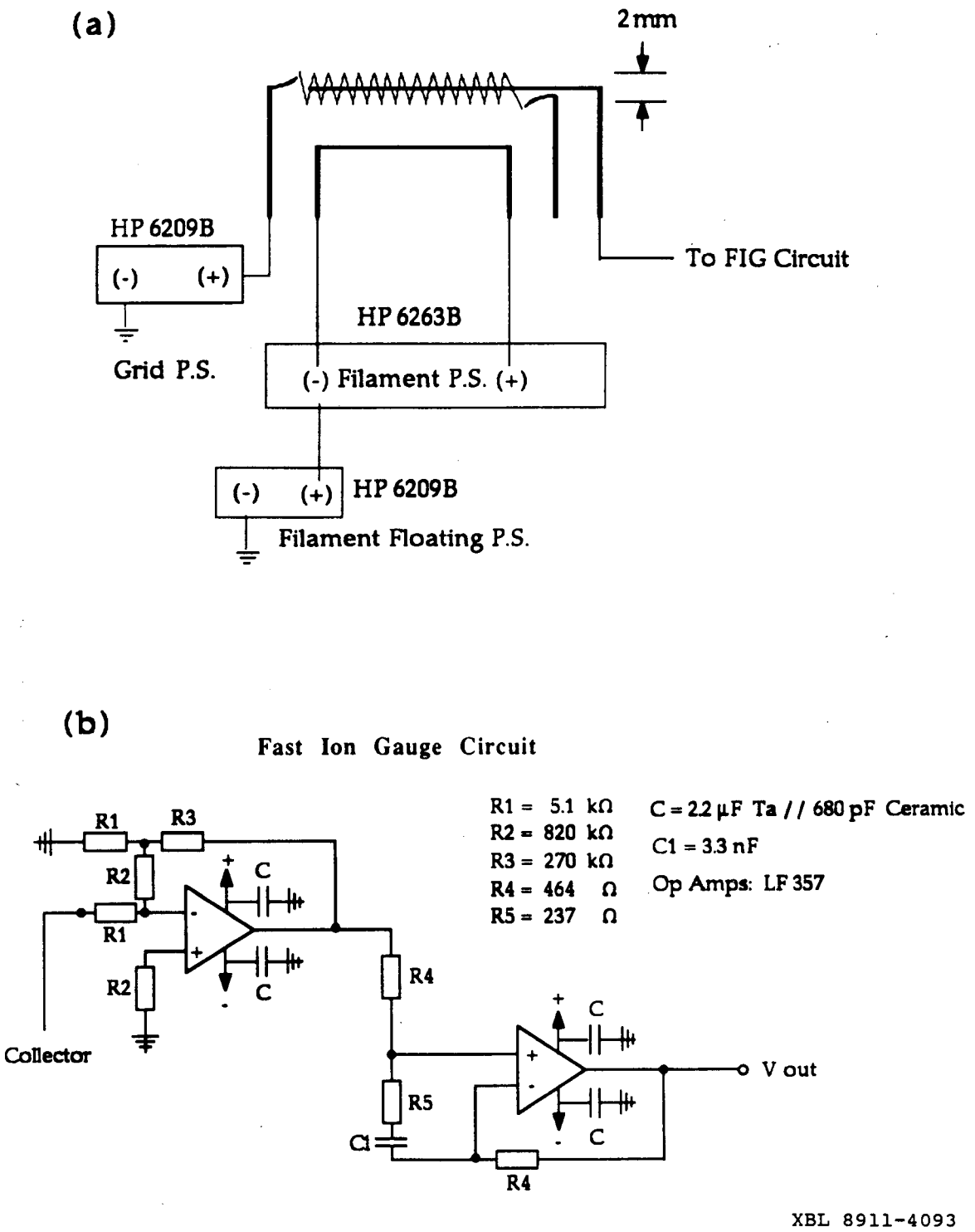
(a)
2mm
HP 6209B
(-) (+)
To FIG Circuit
HP 6263B
Grid P.S.
(-) Filament P.S. (+)
(-) (+) HP 6209B
Filament Floating P.S.
(b)
Fast Ion Gauge Circuit
R1 = 5.1 kΩ
R2 = 820 kΩ
R3 = 270 kΩ
R4 = 464 Ω
R5 = 237 Ω
C = 2.2 µF Ta // 680 pF Ceramic
C1 = 3.3 nF
Op Amps: LF 357
R1
R3
R2
R1
R2
C
C
R4
R5
C1
R4
C
C
V out
Collector
XBL 8911-4093

Figure C - 2

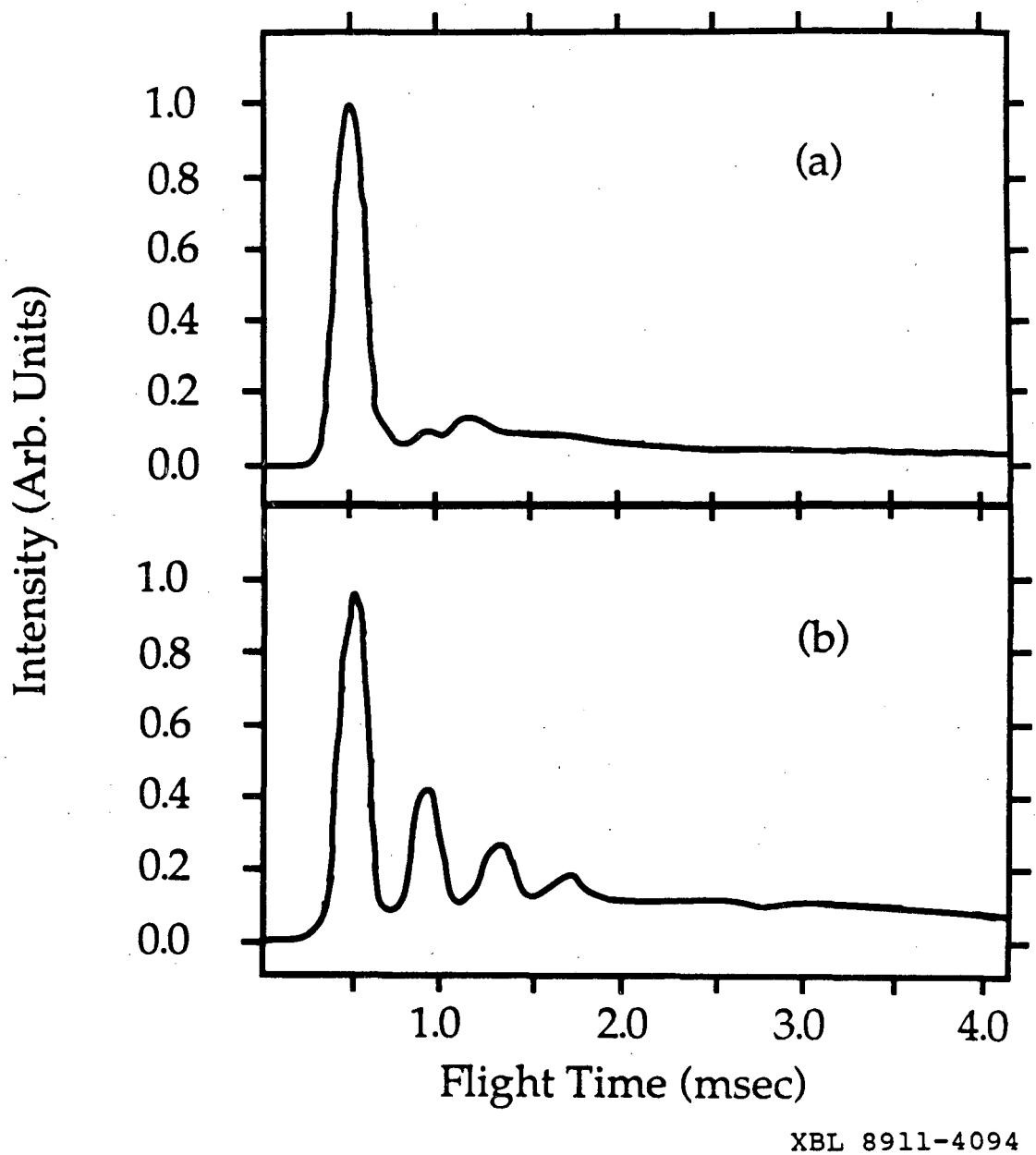
1.0
0.8
0.6
0.4
0.2
0.0
(a)
1.0
0.8
0.6
0.4
0.2
0.0
(b)
Intensity (Arb. Units)
1.0
2.0
3.0
4.0
Flight Time (msec)
XBL 8911-4094

Figure C - 3

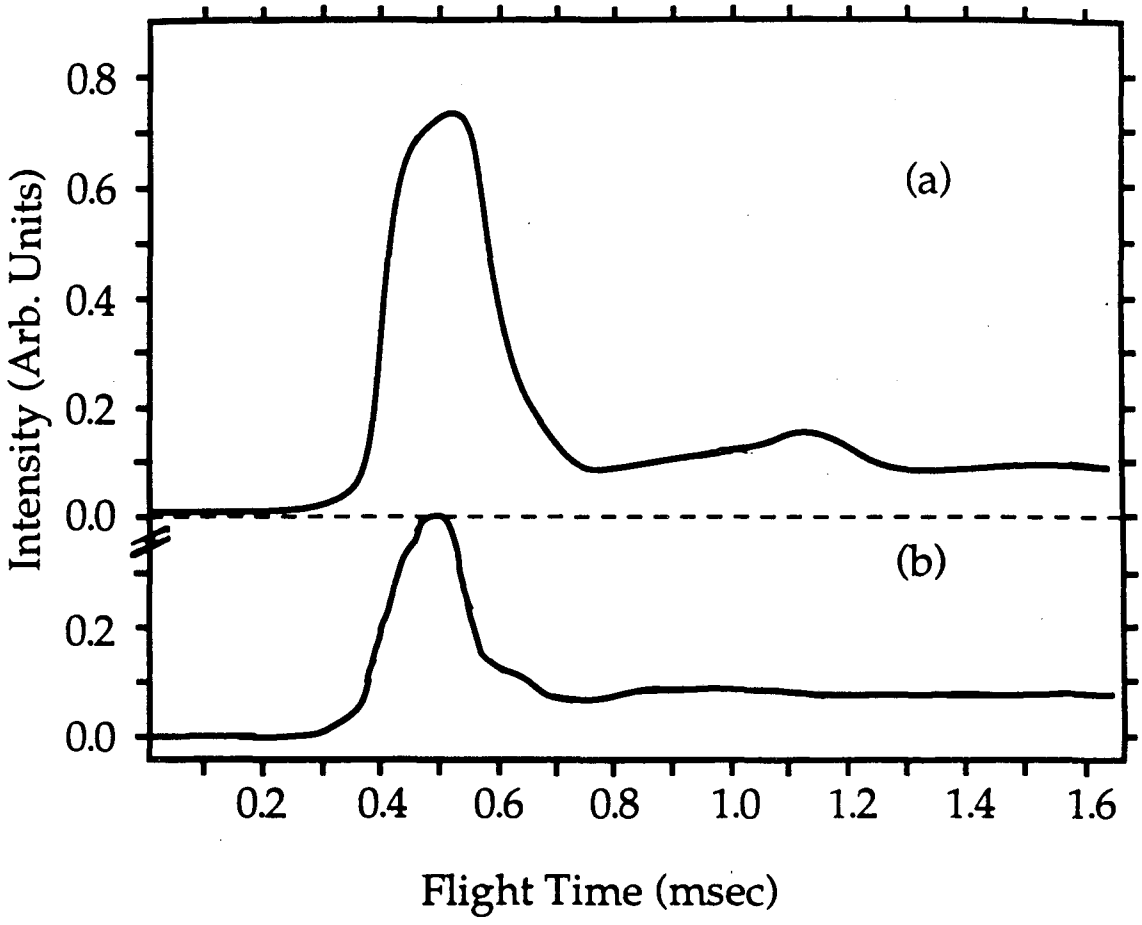

XBL 8911-4095

Figure C - 4

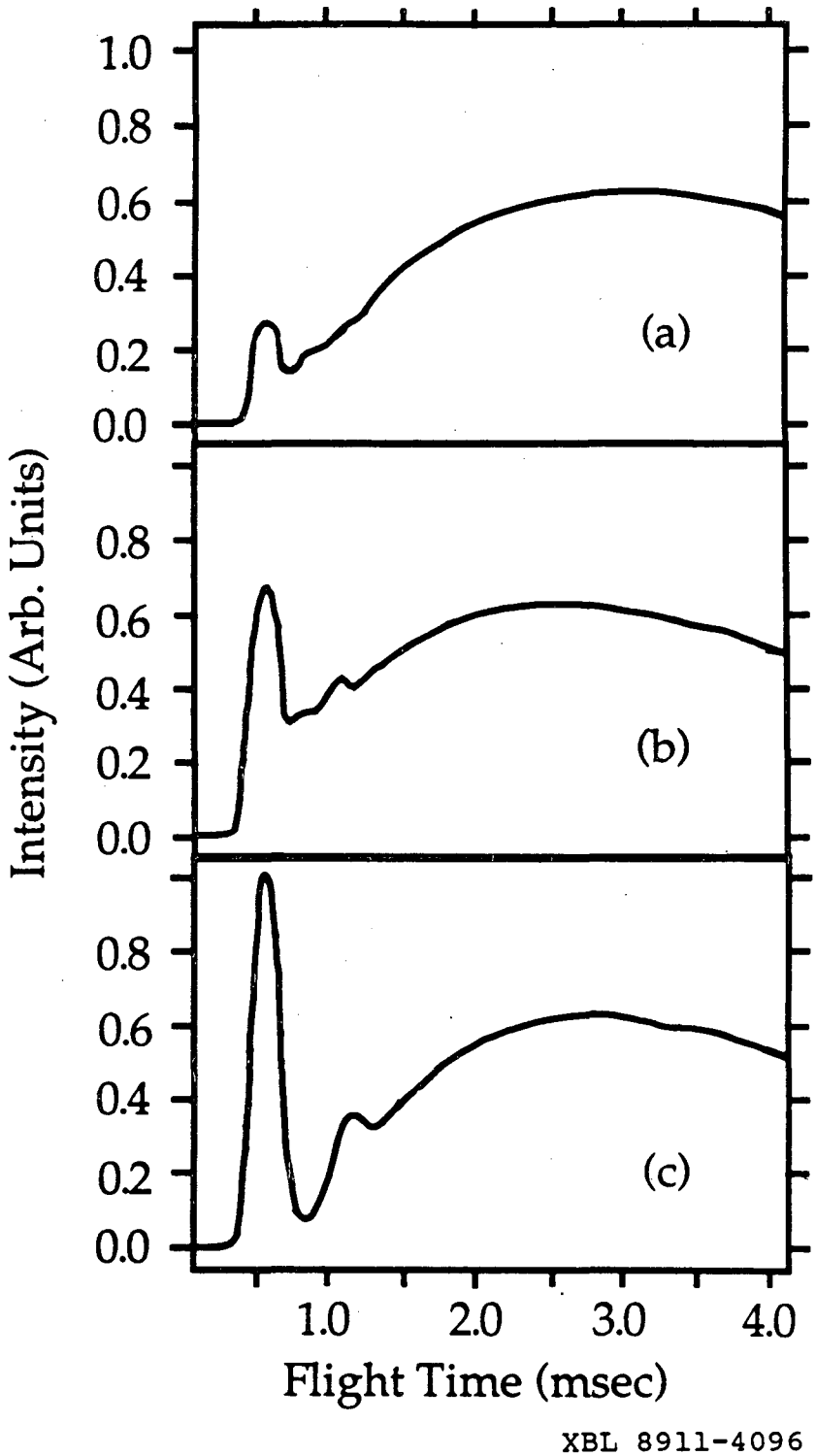
1.0
0.8
0.6
0.4
0.2
0.0
(a)
0.8
0.6
0.4
0.2
0.0
(b)
0.8
0.6
0.4
0.2
0.0
(c)
Intensity (Arb. Units)
1.0
2.0
3.0
4.0
Flight Time (msec)
XBL 8911-4096

Figure C - 5

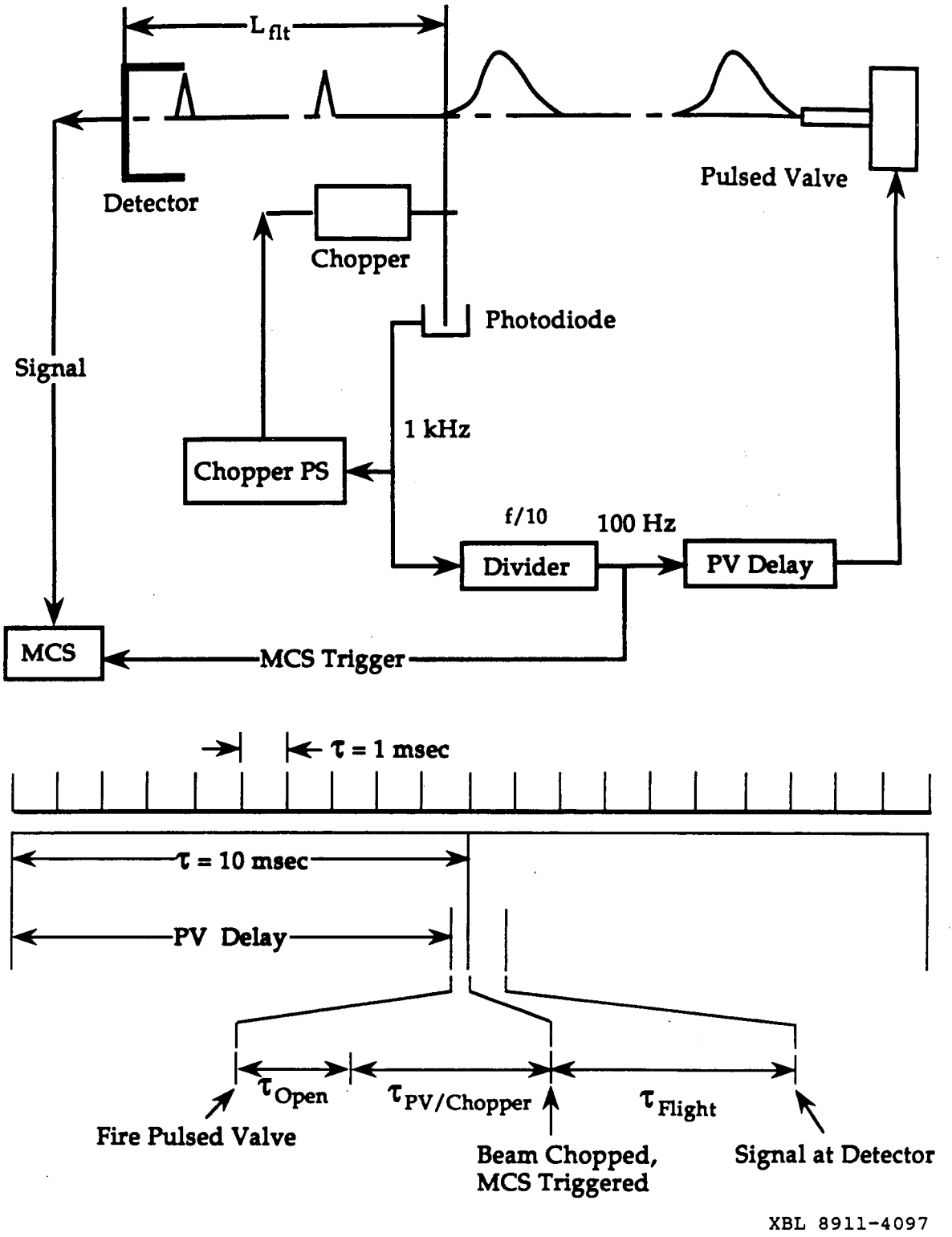
L flt
Detector
Chopper
Pulsed Valve
Photodiode
Signal
1 kHz
Chopper PS
f/10
100 Hz
Divider
PV Delay
MCS
MCS Trigger
τ = 1 msec
τ = 10 msec
PV Delay
τ Open
τ PV/Chopper
τ Flight
Fire Pulsed Valve
Beam Chopped,
MCS Triggered
Signal at Detector
XBL 8911-4097

Figure C - 6

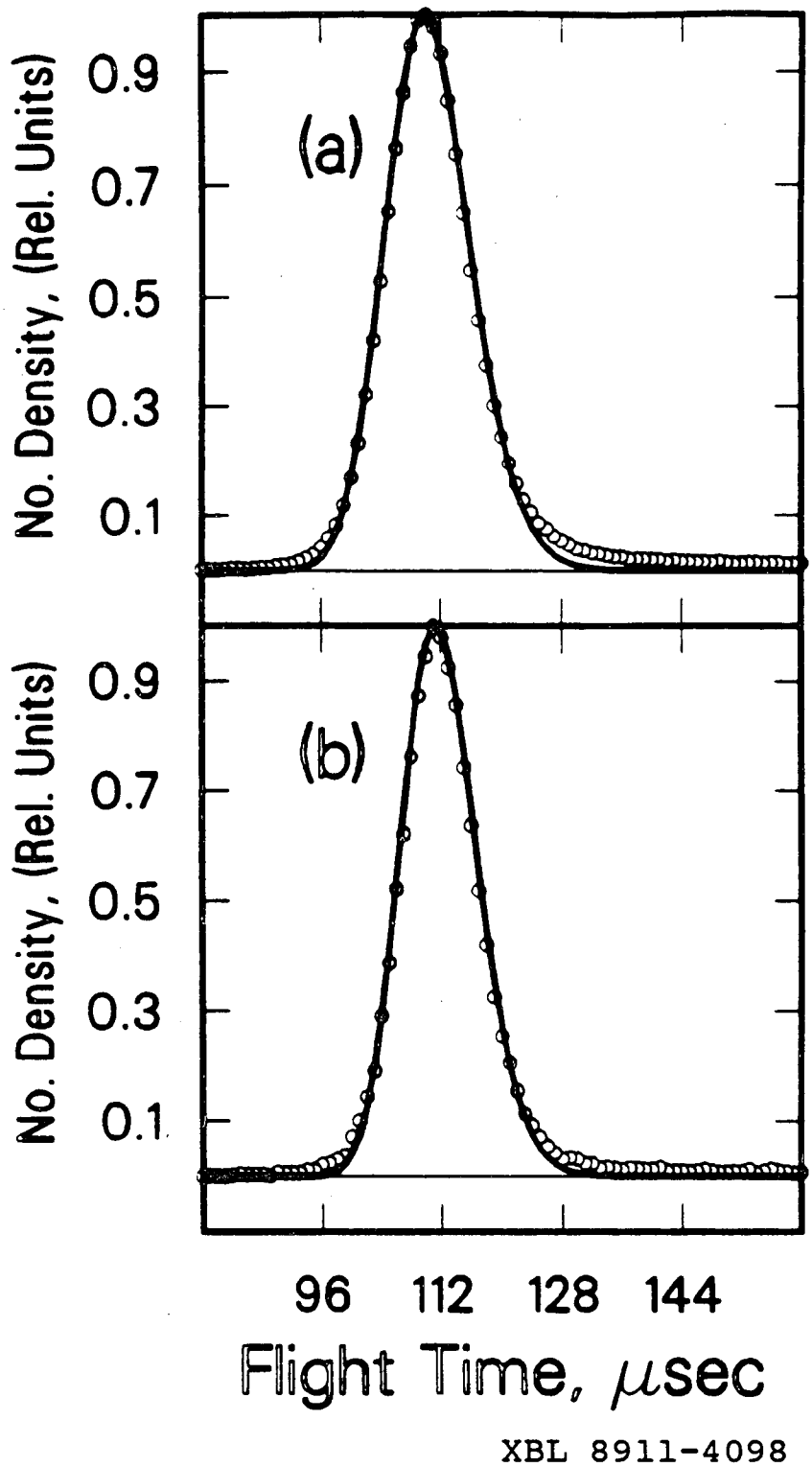
No. Density, (Rel. Units)
0.9
0.7
0.5
0.3
0.1
(a)
(b)
96
112
128
144
Flight Time, μsec
XBL 8911-4098

Figure C - 7

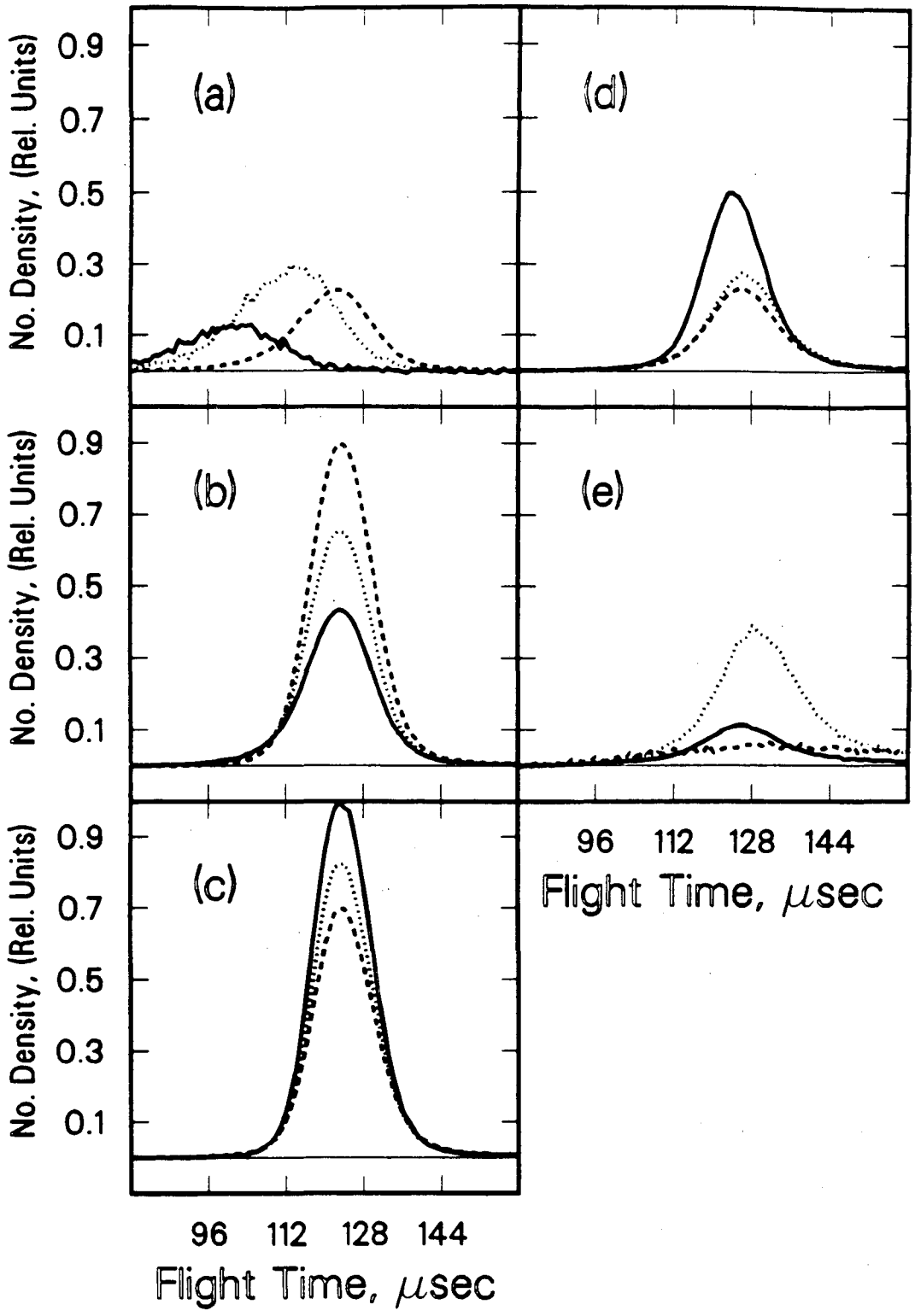

XBL 8911-4099

Figure C - 8

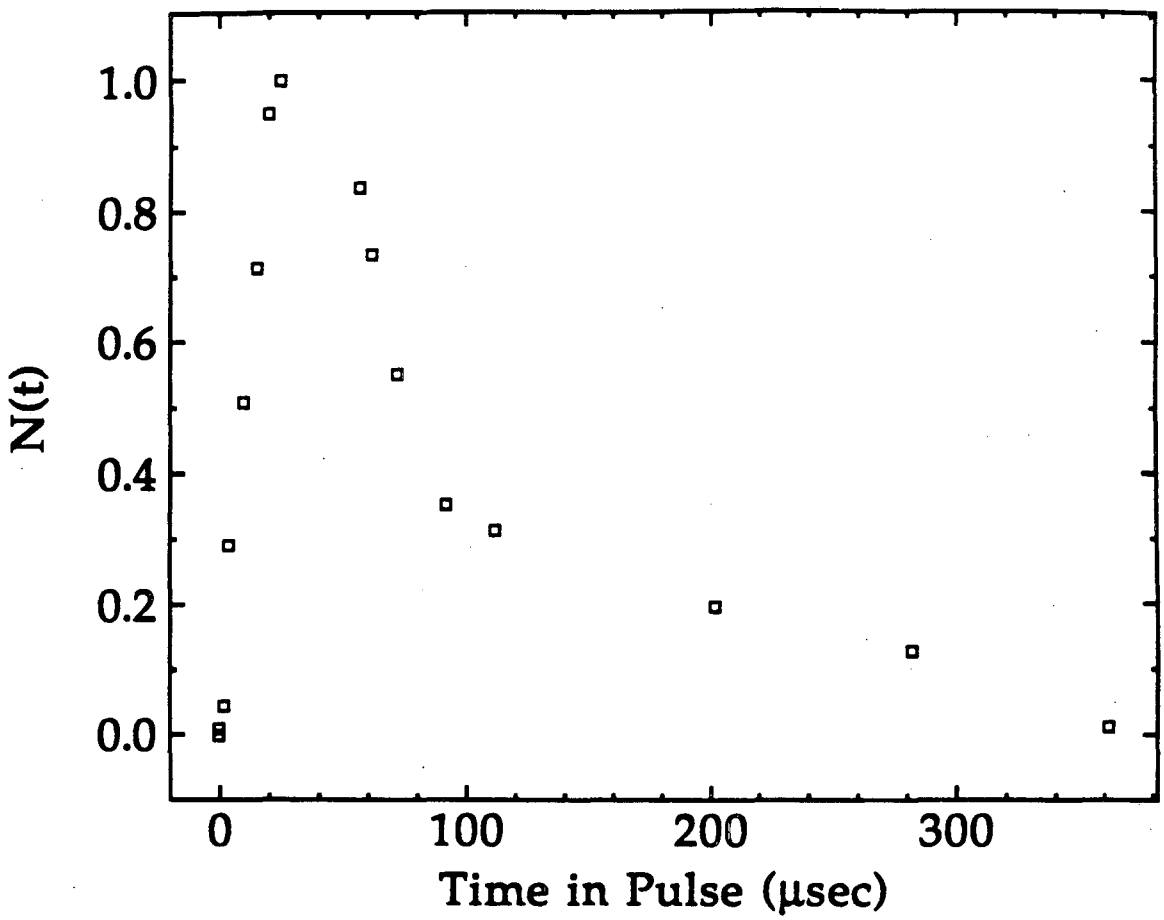

XBL 8911-4100

Figure C - 9a

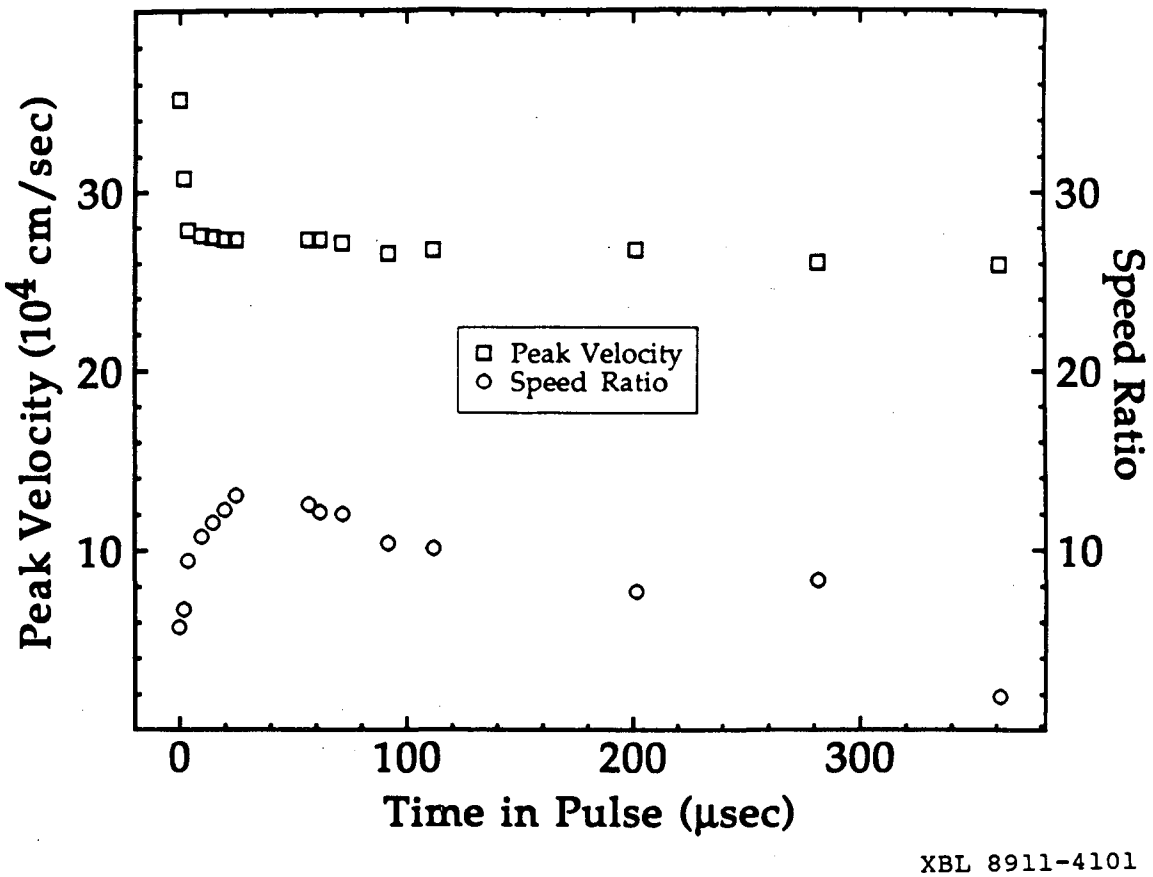
Peak Velocity (10^4 cm/sec)
30
20
10
Speed Ratio
30
20
10
Peak Velocity
Speed Ratio
0
100
200
300
Time in Pulse (μsec)
XBL 8911-4101

Figure C - 9b

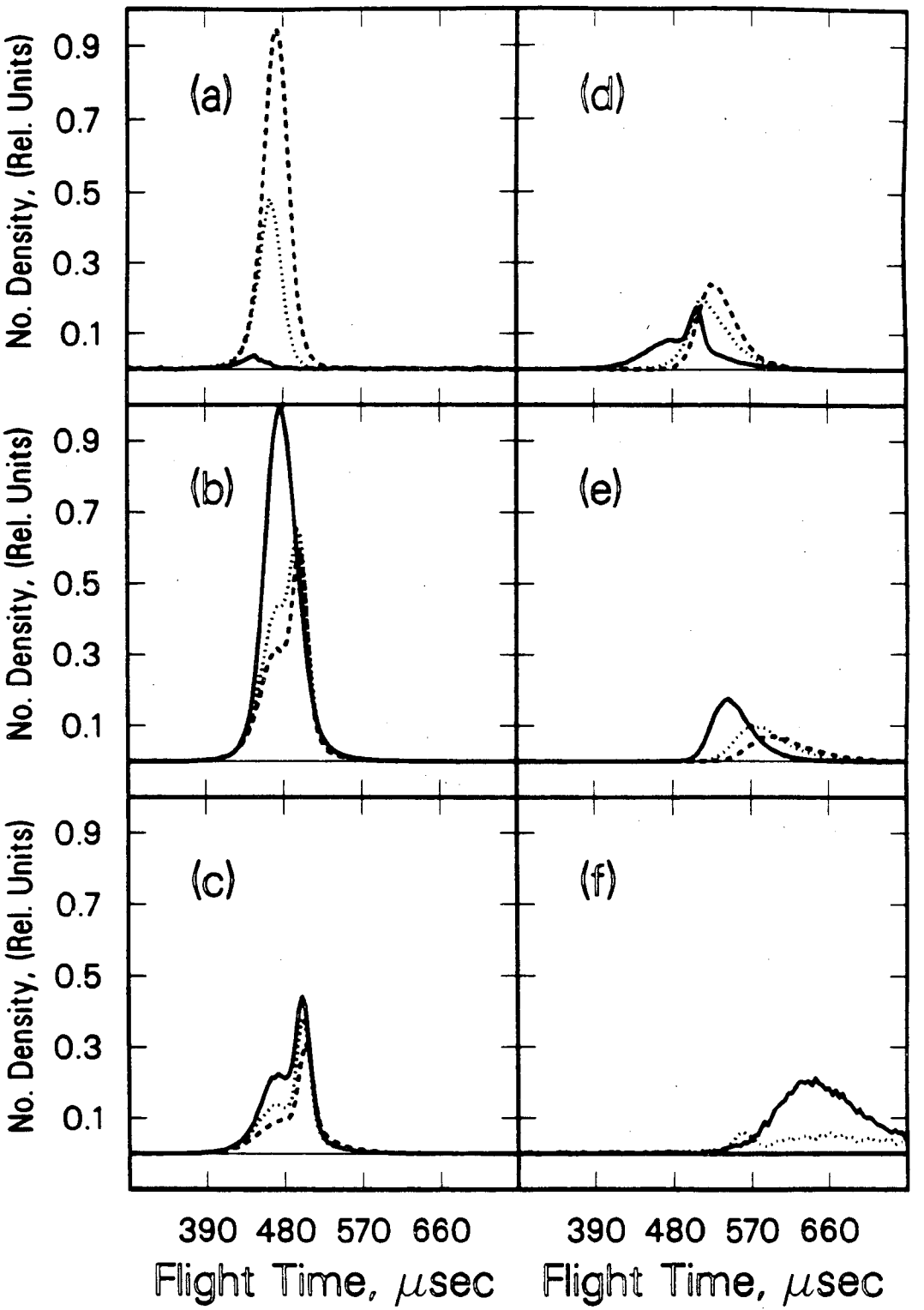

XBL 8911-4102

Figure C - 10

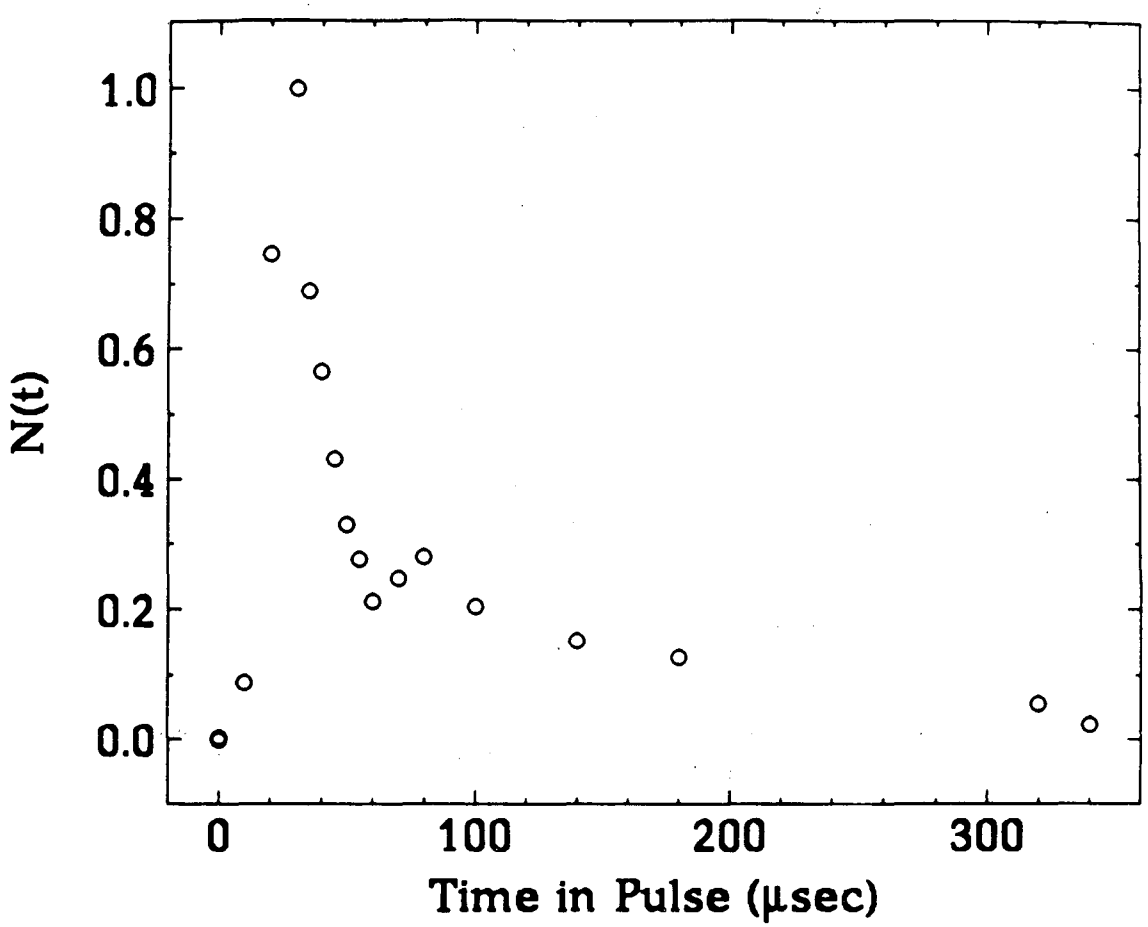

XBL 8911-4103

Figure C - 11a

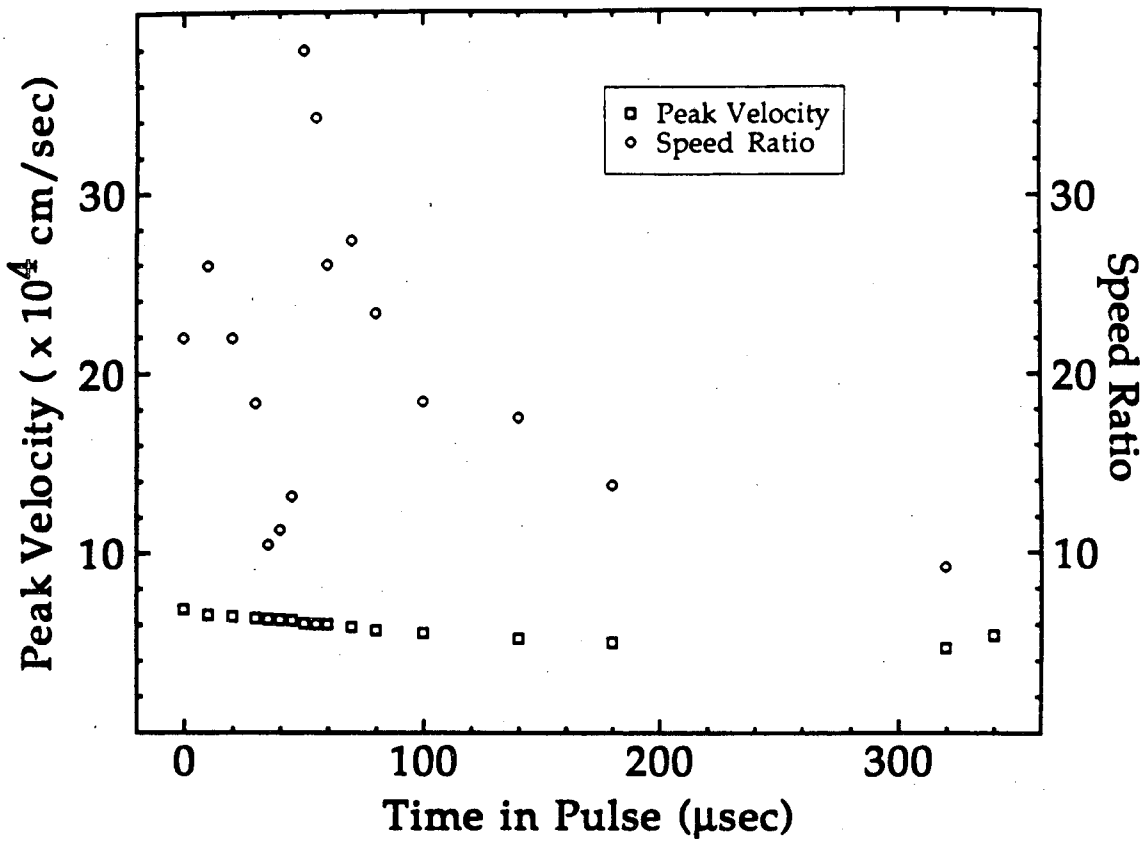

XBL 8911-4104

Figure C - 11b

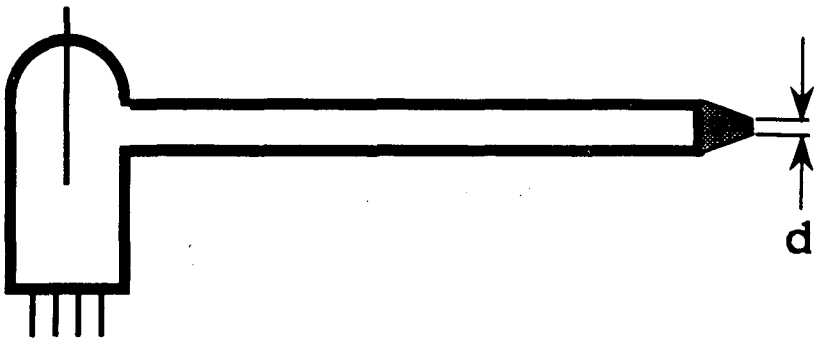

(a)

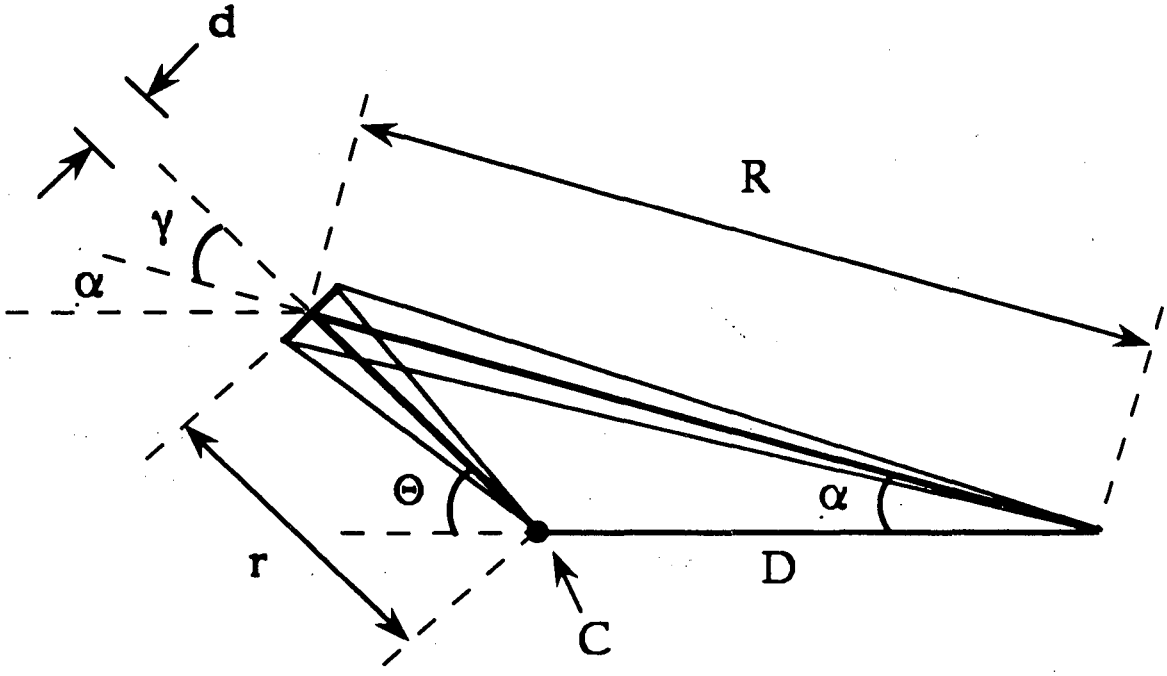

(b)

XBL 8911-4105

Figure C - 12

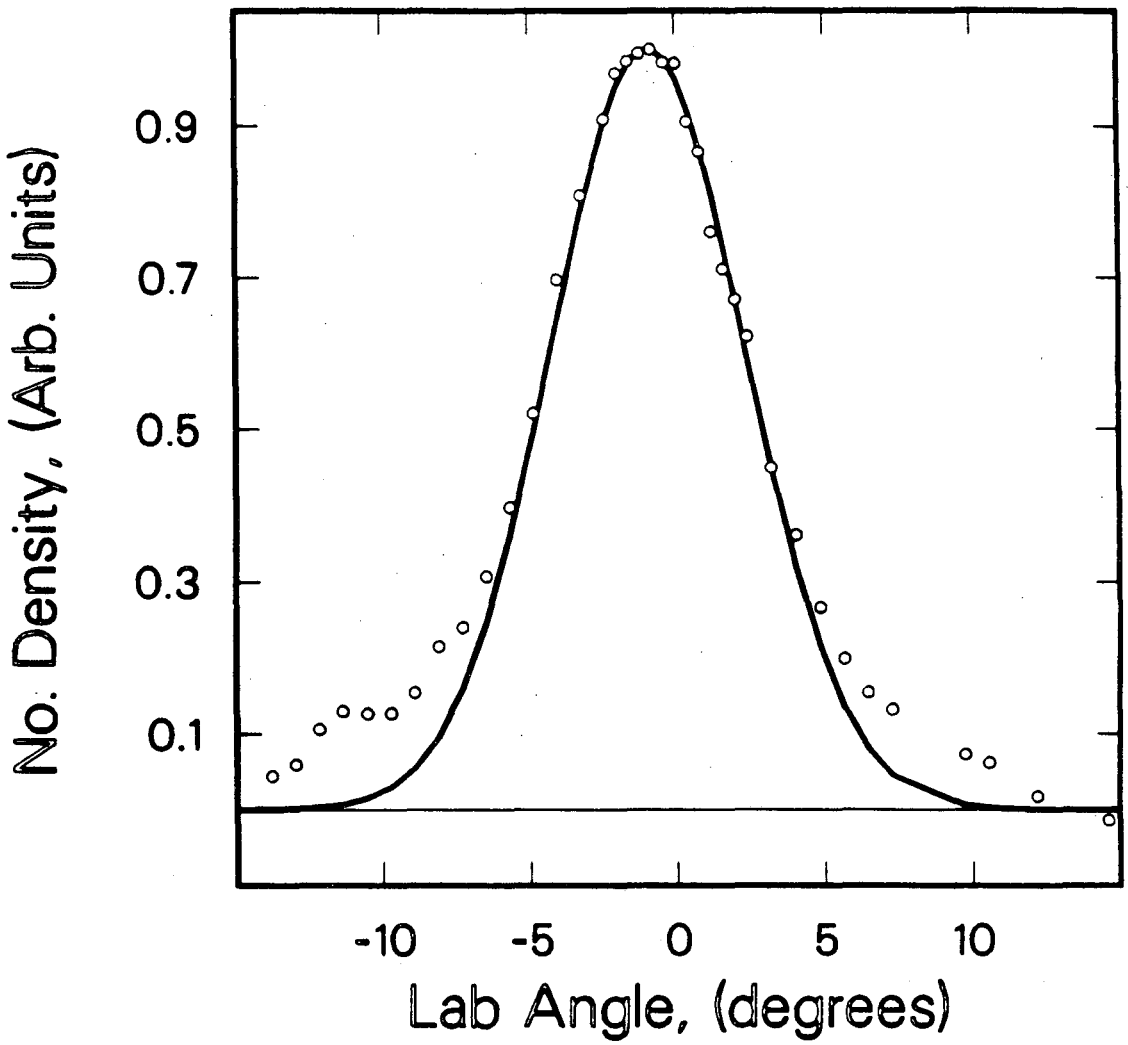

XBL 8911-4106

Figure C - 13

Appendix D

The Synthesis of Deuterium Iodide

1. Introduction

Due to the great expense and thermal instability of deuterium iodide (DI) this important D-atom precursor was synthesized for the reactive scattering experiments. The simplest synthetic approach is direct union of the elements, $D_2 + I_2$, over a platinum catalyst at elevated temperatures. This approach was first used by Bodenstein[1], and the specific approach we have followed is based on that described by Woodall.[2] Woodall's scheme involved an open flow system to allow large product yields, however, this approach was quite wasteful of D_2. The manifold described here made use of a metal bellows pump to allow recirculation of the D_2 reagent, increasing the efficiency of the synthesis considerably. An account of this procedure will be of use in future experiments involving large quantities of DI. Isotopically pure syntheses are by no means trivial; great care must be exercised in the choice of construction materials, reagents and synthetic protocol. These aspects of the synthesis are discussed below.

2. Materials of Construction

To achieve the highest isotopic purity possible in this synthesis it is critical to construct a clean, leak free synthetic manifold. To use the D_2 reagent in an efficient manner it is important that this be a closed flowing

system, as the reaction rate is relatively slow. A clean, leak free stainless steel/Pyrex/Quartz manifold was constructed using Viton O-ring seal joints in the glass manifold, Ultra-Torr (Cajon) unions + flexible stainless steel tubing for the glass/metal unions, and VCR (Cajon) metal gasket seals on the stainless part of the manifold. To achieve recirculation of the D_2 reagent, a Metal Bellows Corporation Diaphragm pump was used (model #MB-21). This pump worked very well recirculating the D_2 in the 0.5-1.5 bar pressure regime, and remained leak free. In assembly of the manifold great care was taken to insure that no grease or other hydrogen containing contaminants were present in any of the components. Where lubricants or pipe joints were required, Fomblin perfluorinated grease and teflon tape were employed to insure a hydrogen free environment.

The manifold was evacuated by a single-stage diffusion pump using Fomblin YVAC 25-6 pump fluid, backed by a small mechanical pump. To maintain the cleanliness of the manifold, a liquid N_2 cryotrap was employed between the diffusion pump and the synthetic manifold. Stainless-steel bellows valves (Nupro Series B and H) and teflon-body pyrex stopcocks (Kontes) were used on the manifold. The reaction tube was made of quartz, joined to pyrex on either side by graded seals. Such seals must naturally be treated with great care, as they are somewhat fragile. The reaction tube was heated with a .020"x.140" Nichrome ribbon wound on a silicate fiber mat wrapped around the tube, covered with more silicate fiber, and finally insulated with several layers of Al foil. In addition, the manifold was 'passivated' with ≈ 1 cc of D_2O , which was vaporized and recirculated through the manifold in Ar buffer gas after any major venting or modification of the manifold. In general, great care was taken to either keep

the manifold evacuated or under dry Ar or N_2 buffer gas to minimize atmospheric water contamination.

3. Reagents

Deuterium gas, iodine crystals and platinized asbestos catalyst comprise the reagents necessary for this synthesis. LBL 'stock' D_2 was used, with a quoted purity of 99.5 atom %. Analytical reagent grade I_2 (Fisher) was used. No DCl or DBr product was detectable via excimer laser photolysis. The platinized asbestos catalyst was prepared in the standard way, by soaking 4 g of asbestos fiber (this is actually somewhat difficult to obtain now) in ≈ 10 ml of 10% by weight Chloroplatinic acid (K_2PtCl_6 in deionized H_2O). The asbestos was then ignited at red heat to drive off all the chloride, leaving a high surface area dispersed platinum catalyst.[1b] The catalyst was then loaded into the reaction tube, with quartz fiber plugs at each end to contain it. Care had to be taken to not pack the catalyst and quartz fiber plugs too tightly, lest the D_2 flow rate be reduced too much. The reaction tube (25 mm id) was packed with around a 10 cm length of catalyst (≈ 8 g of platinized asbestos).

4. Synthetic Protocol

A schematic diagram of the DI synthetic manifold is shown in Figure D-1, and reference should be made to this diagram in the discussion that follows.

4.1 Manifold Preparation

The first step in an isotopically pure synthesis such as this is to ensure that the system was leak free and had little or no atmospheric water contamination. Since the system was typically closed off from the vacuum pump for up to 18 hours during a synthetic run, the leak rate had to be very small. In practice leak rates of ≈10 mT/hr were achievable. Stainless-steel tubing of the manifold was also baked out with heating tapes, and for the first operation of the system after assembly, the manifold was passivated by vaporizing and recirculating ≈ 1 cc of D_2O/inert gas. The manifold was always pumped with a liquid-nitrogen (LN_2) trapped single-stage diffusion pump to ensure a clean vacuum. The ultimate pressure obtained was never accurately measured, but the trapped diffusion pump should have easily reached 1×10^{-4} torr. In addition it was important to thoroughly degas the platinized asbestos catalyst by heating to operating temperature (≈ 800 C) for a couple of hours, and then leaving the catalyst at an elevated temperature (≈300C) during the loading of the manifold.

4.2 Loading of Reagents

At the beginning of a synthesis, then, the manifold was baked out and evacuated, with all regions of the manifold open and the system configured for diffusion pumping. The manifold was then filled with inert gas (Ar or N_2) to prevent atmospheric contamination of the manifold during reagent I_2 loading (up to 1.5 moles of I_2 could be used). To load the I_2 reagent, the

manifold was first carefully filled to atmospheric pressure with Ar or N_2. The bypass leading from the reaction flask through valve 6 was provided to prevent the pressure differential established during the filling of the manifold from forcing the loosely packed catalyst out of the reaction zone. When the manifold reached slightly in excess of 1 atm as indicated on the pressure gauge, the system was breached at PR2, and a brisk flow of inert gas was established using needle valve 19. To fill the round bottom reaction flask with I_2 the 25 mm O-ring seal at the entrance to the reaction flask was opened and moved out of the way. The inert gas flow rate was then increased appropriately with needle valve 19 to prevent air from entering the system. The iodine was then loaded into the round bottom flask, the reaction flask was closed, then PR-2 and the Ar cylinder were shut simultaneously. At this point the manifold was evacuated. While the system was being evacuated, a solid dry ice jacket was placed around the I_2 to prevent sublimation and facilitate pumpdown. Once the ultimate vacuum was reached the cryogenic traps were prepared and installed on the vacuum line. A dry ice/ethanol slush filled dewar was placed on trap A to remove unreacted I_2 from the product, and three LN_2 filled dewars were placed on traps B, C and D to collect the DI product.

4.3 Synthesis

Once the LN_2 traps were in place, the system was ready to be filled with D_2, and recirculation started. The catalyst was brought to its operating temperature (≈800 C) by supplying 250W with a variac. The evacuated sample bottle was isolated at the main shutoff valve 23 and 16. The ballast to

be used (1 or 4 liter) was left open, with the other one isolated at the appropriate valve (14 or 13). For syntheses with expensive isotopically enriched D_2 (99.95 atom%, Cambridge Isotope Laboratories) the small ballast was used, decreasing the total system volume and using the reagent more efficiently. In this configuration, the manifold had to be watched more closely in operation, as the D_2 pressure would fall quickly as the reaction progressed. The entire manifold was then slowly filled with D_2 through the appropriate needle valve 20 or 22 to ≈ 3 psig D_2. With the manifold filled, the system was then configured for D_2 recirculation by closing bypass 6, valves 18,19,20 and the main cylinder shutoff valves on the compressed gases. The bypass 11 on the flowmeter was typically left open, as the flow rate through the flowmeter was too slow for efficient reaction. D_2 flow was started by turning on the metal bellows pump. The dry ice jacket was then removed from the reagent I_2, a heating mantle put in its place, and the reagent vessel heating tape turned on, between the I_2 reagent and the reaction tube. (50W tape, 15W mantle). At operating temperature and flow rate, dark purple I_2 vapor could be seen entering the furnace, with little unreacted I_2 coming through, and no I_2 vapor backstreaming against the reagent D_2 flow. Care had to be taken to keep all regions of the reactor warmer than the I_2 reagent, to prevent I_2 condensation.

Large quantities of DI were synthesized in one run (up to 1.5 moles), so it was essential to use large (55 mm ID) glass traps, with 25 mm ID feeder tubes to inhibit system clogging. The use of three LN_2 traps in series allowed almost complete recovery of DI product. Most product condensed in the first trap (B). The traps were refilled approximately every 1/2 hour.

Whenever the D_2 pressure dropped to ≈ 0 psig, the D_2 was replenished to 3 psig. Care was also taken to ensure that D_2 flow rate was unimpeded by using the flowmeter and checking that a significant (3 psig) pressure drop was maintained across the reaction tube by the metal bellows pump. At flow rates too low, the reaction efficiency would drop as the residence time of the DI product in the catalyst increased, pushing the equilibrium back towards the molecular elements D_2 and I_2. At flow rates too high, the residence time of the reagents was too short over the catalyst to effect efficient reaction. The optimal condition on this manifold was, as noted, the maximum obtainable flow rate through 10 cm of catalyst packed in the 25 mm ID reaction tube.

4.4 Product Collection

Once all the I_2 reagent had reacted, the DI product had to be collected and transferred. To do this, bypass 6 was opened to equalize the pressure across the catalyst, the metal bellows pump was turned off and the entire system evacuated to 10 mT. Before evacuation, the ballast in use was isolated from the system, as the residual D_2 therein could be used in the future for passivation. When the system was evacuated, the product transfer section of the manifold was isolated by closing valves 6,9 and 15. The product was then isolated in the three traps B, C and D by closing 7. The LN_2 dewar on trap D was then removed, concentrating the product in traps B and C. After this was done, any noncondensibles would be removed by pumping through 7, and the process repeated by closing 8, removing the LN_2 dewar from trap C and collecting all the product in trap B at LN_2 temperature.

The impure yellowish-white DI was then ready for trap-to-trap distillation to produce a white, I_2 free product. The manifold was built to allow three such distillations, from traps B to C, C to D and D to the sample bottle. This procedure takes an extremely long time for 1.5 moles of DI subliming at -72C. For our purposes, I_2 contamination in the product was not a major problem, as the DI was kept at -55C during experimental runs, where the vapor pressure of any I_2 contaminant is much lower than the DI. For this reason, the experimental protocol was shortened by first concentrating all the product in trap B, then putting dry-ice ethanol dewars on traps C and D, cooling the sample bottle SB to LN_2 temperature, and distilling at -72C from trap B through traps C and D into the SB. A single distillation of 1.5 moles of DI could easily take 4-5 hours. When the distillation was complete, noncondensibles were removed by pumping, and the SB was isolated at 23 and 16, and removed from the manifold. Between syntheses, it is very important to keep the manifold dry and unexposed to air, as isotopic purity drops and the SS parts, especially the thin walled bellows, are subject to corrosion when exposed to moist iodine. As soon as possible, a new SB was put into place, the entire manifold kept evacuated, then baked and readied for the next synthesis.

5. Results

The efficiency of the synthesis relative to the I_2 reagent can easily pass 90%. For the D_2, however, the efficiency is probably only 60%, as significant quantities of D_2 must be pumped away at the end of the run. The DI produced liquefies at 300K at ≈ 90 psig.[3] DI will decompose into D_2 and I_2 at

room temperature, so if extended storage is planned, its best to keep the product cold. To remove excess D_2 after storage of DI it is essential to go through freeze-pump-thaw cycles to remove the noncondensible D_2. With a properly passivated gas delivery line, photofragmentation of the product showed purity nearly equivalent to the starting material D_2, however, it must be emphasized that DI undergoes isotopic exchange at surfaces, so great care had to be taken to passivate the feed line to achieve pure D atom beams. D_2O was used to accelerate this process, but it would often take in excess of one day to achieve reasonable feed line passivation, and great care was taken to preserve this once it was achieved. With this manifold > 3 moles of DI was synthesized over the course of this work as required experimentally.

---

[1]a) Bodenstein, Z. Phys. Chem., 13, 59 (1894), ibid., 29, 295 (1899).

b) Inorganic Syntheses, ed. H.S. Booth, McGraw-Hill, New York (1939).

[2] K.B. Woodall, Ph. D. Thesis, Univ. of Toronto, (1971).

[3] Matheson Gas Data Handbook, Matheson Gas Products, East Rutherford, NJ, (1971), pp. 311-314.

Appendix D Figure Caption

Figure D-1. Schematic diagram of the DI synthesis manifold. See text for details.

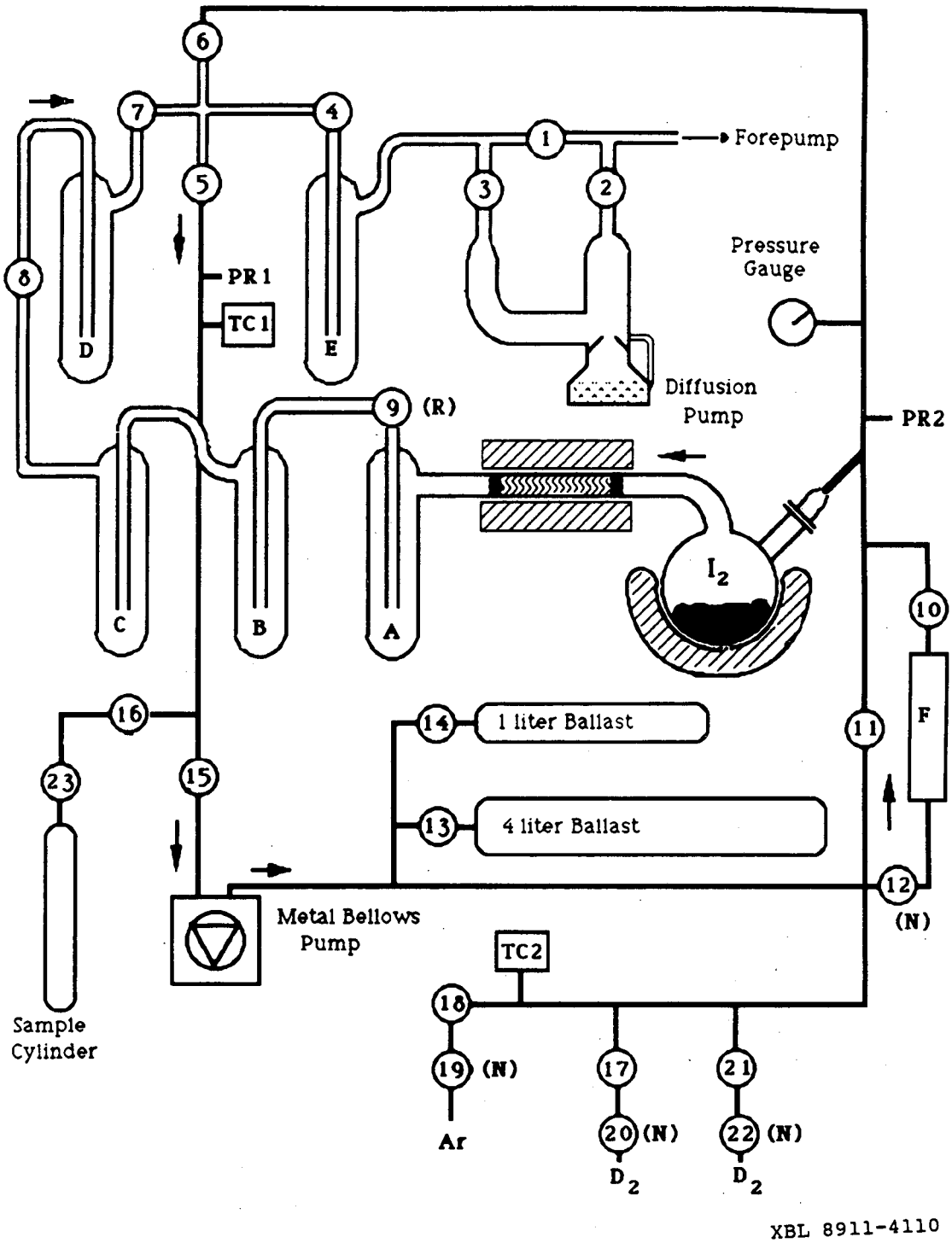
Forepump
Pressure Gauge
Diffusion Pump
PR1
TC1
PR2
(R)
I_2
1 liter Ballast
4 liter Ballast
Metal Bellows Pump
TC2
Sample Cylinder
(N)
Ar
D_2
D_2
XBL 8911-4110

Figure D - 1

LAWRENCE BERKELEY LABORATORY
TECHNICAL INFORMATION DEPARTMENT
1 CYCLOTRON ROAD
BERKELEY, CALIFORNIA 94720